Experimental and numerical investigation of three equispaced cylinders in cross-flow

by

Manpreet Singh Bansal

A thesis
presented to the University of Waterloo
in fulfillment of the
thesis requirement for the degree of
Master of Applied Science
in
Mechanical Engineering

Waterloo, Ontario, Canada, 2014

I hereby declare that I am the sole author of this thesis. This is a true copy of the thesis, including any required final revisions, as accepted by my examiners.

I understand that my thesis may be made electronically available to the public.

Abstract

Flow around a cluster of three equally spaced cylinders with a spacing ratio of $P/D = 1.35$ was studied experimentally and numerically. The main focus of this investigation is the effect of cluster orientation on flow characteristics. Two Reynolds numbers were investigated: $Re_D = 100$ and $Re_D = 2100$. Experiments were conducted at the University of Waterloo water flume facility at $Re_D = 2100$ for a range of cluster orientation angles $0° \leq \alpha \leq 60°$ using hydrogen bubble technique, particle image velocimetry, and laser Doppler velocimetry. The flow was modeled numerically at $Re_D = 100$ and $Re_D = 2100$ for $\alpha = 0°$ and $60°$. A laminar model was used for $Re_D = 100$ and a RANS model was used for $Re_D = 2100$. For the RANS case, four turbulence models were evaluated: SST, $k - \omega$, $k - \epsilon$, and LRR-IP.

For all cluster orientations, the experimental results show large scale vortex shedding, similar to single bluff body flows, beyond $x/D = 5$. Wide and narrow wakes are produced downstream of the cluster due to jets, that form in the passages between the cylinders, exiting the cluster. Small scale vortices are shed from shear layers bounding the narrow wake(s). For $\alpha = 0°$, a bistable wake development is present, in which the jet exiting the cluster is directed towards either one of the two downstream cylinders. The asymmetry in the wake development about $y = 0$ decreases as α increases from $0°$ to $60°$. For $\alpha = 60°$, the wake development is symmetric, consisting of two narrow wakes behind the two upstream cylinders and a wide wake behind the downstream cylinder. For all orientations, interactions between the inner shear layer of the wide wake and small scale vortices shed from the shear layers bounding the narrow wake occur. As a results, each large scale structure forming on this side of the wake axis encompasses smaller scale vortices with opposite vorticity sense, which reduces the coherence of the large scale vortices compared to that of their counterparts on the opposite side of the wake for $0° \leq \alpha < 60°$. The small scale vortex shedding frequency increases with increasing α for $0° \leq \alpha \leq 60°$. For all orientations, the large scale vortex shedding frequency, when scaled by the projected height of the cluster, is equal to that for a single cylinder at the same Reynolds number, suggesting that the cluster behaves like a single bluff body.

For $Re_D = 100$, the numerical results show a symmetric wake development for $\alpha = 0°$ and $60°$. No bistable wake development is present for $\alpha = 0°$. Also, there is no presence of small scale shedding in the near wake of the cluster for both orientations. The Strouhal number based on the projected height of the cluster is equal for both cluster orientations and to that expected for a single cylinder at the same Reynolds number. The total drag on the cluster for $\alpha = 0°$ and $60°$ is $C_P \approx 1.35$ and $C_P \approx 1.5$, respectively. The maximum drag occurs on the two upstream cylinders for $\alpha = 60°$, and is approximately 10% larger than that on a single cylinder. The drag coefficient on all other cylinders is at least 25%

lower than that on a single cylinder. Mean lift forces are produced on the two downstream cylinders for $\alpha = 0°$ and the two upstream cylinders for $\alpha = 60°$. The total RMS for the cluster for $\alpha = 0°$ and $60°$ is $C_L{}' \approx 0.3$ and $C_L{}' \approx 0.5$, respectively. The maximum lift RMS occurs on the downstream cylinder for $\alpha = 60°$ and is approximately 35% larger than that for a single cylinder.

Numerical results for $Re_D = 2100$ show that, out of the four turbulence models tested, the SST and $k-\omega$ models perform the best overall when compared to experimental results. Based on the results of the SST model, for $\alpha = 0°$ (i.e., the bistable case), the maximum drag occurs on the cylinder producing the narrow wake. For $\alpha = 60°$, the maximum drag occurs on cylinders 1 and 3. For both orientations, the total drag coefficient for the cluster is approximately 15% smaller than that for a single cylinder case. Also, the mean lift forces are generated only on the two downstream cylinders for $\alpha = 0°$ and the two upstream cylinders for $\alpha = 60°$.

Acknowledgments

I would like to express my deepest gratitude to my supervisor, Serhiy Yarusevych, for his support and guidance throughout my graduate studies. I am blessed to have worked closely with someone this intelligent. Without his leadership and supervision, this thesis would not have been possible.

I would like to thank Chris Morton, fellow Ph.D. student, for all of his help and guidance throughout my studies. Thank you for assisting me in troubleshooting multiple issues during experimentation.

I would like to thank my fellow graduate students, Tom Kirk, Holly Neatby, Jeff McClure, John Kurelek, Sahil Mahey, Andrew Lambert, Eugene Zivkov, Brian Kettlewell, Ajith Airody, and JiaCheung Hu for their kind support when required.

Thank you to all University of Waterloo machine shop staff who assisted me in the construction of parts for my experimental setup.

Thank you to my best friends, Diana Lam, Akshat Sehgal, Taniya Gupta, Hooman Safaee, Avish Buck, Adam Masood, Sam Rees, Anand Sundararajan, Hussein Hashi, and Siyaman Sadagopan, for all your motivational support throughout my studies.

I would also like to thank Natural Sciences and Engineering Research Council, Babcock and Wilcox Canada, and the University of Waterloo for their financial support for my research.

Dedication

I would like to dedicate this thesis to my loving parents, Gurmukh Singh Bansal and Amardeep Kaur Bansal, and brother, Amrit Singh Bansal. Your endless support and encouragement was always there with me throughout my entire studies. I will always appreciate everything you have done to help me complete my Master's.

I would also like to dedicate this work to all my family members in Canada and India for their moral support. Special thanks to my grandparents in Edmonton, Joginder Singh Bansal and Sarjeet Kaur Bansal, who always tell me that I can solve the hardest problems in the world, just need to approach it one step at a time.

Love you all!

Table of Contents

List of Figures

List of Tables

Nomenclature

a	POD temporal mode coefficient
b	Half wake width
C_p	Particle concentration
C_D	Mean drag coefficient
C_L	Mean lift coefficient
C'_L	Lift RMS coefficient
c	Proportionality constant
D	Single cylinder diameter
D_c	Cluster diameter
D_h	Projected height of the cluster
D_g	Projected height of the minimum gap between the cylinders
d_i	Interrogation window size
d_p	Seed particle diameter
d_s	Diffraction limited diameter
d_x	Camera sensor pixel size
d_τ	Particle-image diameter
f	Frequency
f_l	Focal length
$f^{\#}$	Focal ratio or f-stop
H	Object distance from lens
M	Magnification, $M = f_l/(f_l - H)$
N_i	Particle-image-density
n	Normal direction
P	Spacing between two cylinders
Re_D	Reynolds number based on a single cylinder diameter
Re_{D_h}	Reynolds number based on cluster blockage
S	Longitudinal spacing between two cylinders
St_D	Strouhal number based on a single cylinder diameter

St_{D_h}	Strouhal number based on cluster blockage
T	Transverse spacing between two cylinders
t	time
Δt	Time step
$\overline{U}$	Mean streamwise velocity
$\overline{U}_m$	Mean streamwise velocity measured by the LDV probe
U_0	Free-stream velocity
u	Streamwise velocity component
u'	RMS of the streamwise velocity component
u'_f	RMS of the band-pass filtered streamwise velocity signal
V	Mean velocity
v	Velocity
ΔX	Average particle displacement
x	Streamwise distance from the origin
y	Transverse distance from the origin
y^*	Yoke translation
Δz_0	Laser sheet thickness
α	Orientation of three cylinder triangular cluster relative to incoming flow
α_s	Angle of full-shielded flow
β	Orientation of two cylinders relative to the flow
ϵ	Measurement error
ϵ_t	Total measurement error
λ	Light wavelength
ϕ	POD spatial mode
ω	Light frequency
ω_D	Doppler frequency

Chapter 1

Introduction

Fluid flow interaction with cylindrical bodies is seen in multiple engineering applications and is important for their design and/or operation. These examples range from flow through tube bundles in heat exchangers to noise generation from flow over cylindrical structures on aircraft landing gears. Thus, flow over single uniform circular cylinders has been studied in vigorous detail over several decades (e.g., [1–5]). The vortex shedding phenomenon has been the primary focus of such investigations. The periodic pressure fluctuations in the flow field due to this phenomenon result in oscillating forces on the cylindrical body. Previous studies have shown that parameters such as Reynolds number [5, 6], free-stream turbulence [7, 8], and surface roughness [8] impact vortex shedding characteristics. There is numerous literature available present day to characterize flows around single uniform cylinder bodies.

There is only a limited number of studies, in comparison to those performed on flows over a single uniform cylinder, that have investigated flows over multiple cylinder configurations (e.g., triangular cluster of three cylinders). Such flows are seen in heat exchangers,

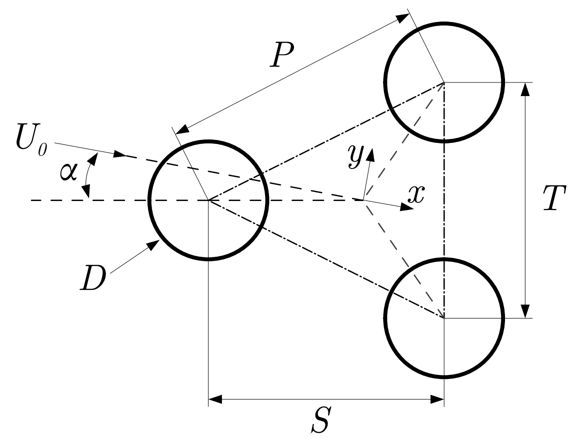

Figure 1.1: Triangular cluster geometry definition.

cluster of cooling towers, support structures, and chimney stacks. For the case of a triangular cluster of three cylinders (Figure 1.1), only a few studies have involved quantitative measurements (e.g., [9–12]). Previous results show that the characteristics of the vortex shedding phenomenon and forces exerted on the cylinders depend strongly on the spacing between the cylinders, cluster orientation relative to the flow direction, and Reynolds number.

Flows through a triangular cluster of three cylinders involve complex vortex interactions and multiple frequency-centered activities in the wake [9, 12]. For some combinations of the cylinder spacing, cluster orientation, and Reynolds number, vortex shedding can be suppressed behind one or more cylinders in the cluster. For example, at low Reynolds numbers ($60 < Re_D < 300$) and for $\alpha = 0°$, a single vortex street is produced behind the cluster for $2 \leq P/D \leq 6$ and three individual streets form for $P/D > 6$ [9]. Sayers [10] and Price & Paidoussis [11] investigated both the single and three individual vortex street regimes. They measured forces exerted on each cylinder and suggested that each cylinder behaved similar to an isolated cylinder for $P/D > 5$. Lam & Cheung [12] visualized the flow through an equispaced triangular cluster of three cylinders using dye injection and observed a bistable phenomenon at $Re_D = 2100$ for $\alpha = 0°$ and $1.27 \leq P/D \leq 2.29$. In this flow regime, the gap flow forming between the two downstream cylinders can be stably biased towards the wake of either of the two downstream cylinders, resulting in a narrow wake and a wide wake behind the cluster. Lam & Cheung [12] noticed that there was no intermittent switching in the gap flow direction and that the biased direction was dependent on the initial conditions of their experiment. This observation is different from the bistable mode detected for flow over two cylinders in a side-by-side arrangement [13], in which there is intermittent switching in the biased direction during operation.

For the case of $\alpha = 60°$, no bistable phenomenon occurs for the cluster [12]. The presence of the downstream cylinder prevents the formation of a bistable wake. The wake consists of a narrow wake behind each of the upstream cylinders which are symmetric about the $y = 0$ and equal in size and a wide wake behind the downstream cylinder.

Previous studies provide a detailed qualitative description of the flow topology for flow through an equispaced triangular cluster of three cylinders [9, 12]. However, quantitative flow field measurements are needed to gain further insight into the wake development. The present work aims to investigate flows through an equispaced triangular cluster of three cylinders, focusing on wake development and vortex dynamics. The aim of the study is to assess the effect of cluster orientation on the near-wake development via quantitative field measurements. To obtain such measurements, an experimental and numerical investigation at the University of Waterloo was conducted. The specific objectives of this work are as follows:

1. Experimentally investigate flow through an equispaced triangular cluster of three cylinders and effects of cluster orientation on the near-wake development, primarily focusing on wake vortex dynamics at $Re_D = 2100$ and $P/D = 1.35$. These operating parameters are common in various industrial applications.

2. Numerically model the flow through the cluster for (a) laminar and (b) turbulent flow conditions:

   (a) solve unsteady Navier-Stokes equations and analyze the vortex shedding phenomenon in the laminar flow regime ($Re_D = 100$), and

   (b) solve Reynolds-Averaged Navier-Stokes equations and evaluate the performance of various turbulence models at $Re_D = 2100$.

Chapter 2 provides an overview of the relative literature. The experimental and numerical setup details are described in Chapters 3 and 4, respectively. A comprehensive analysis of the results is given in Chapters 5 and 6, followed by concluding remarks and recommendations in Chapters 7 and 8, respectively.

Chapter 2

Background

This chapter provides a detailed overview of previous investigations and their findings related to flow over single and multiple cylinder configurations. The first section describes studies of flow past a single uniform circular cylinder, focusing primarily on vortex shedding in the cylinder wake and Reynolds number effects on the overall flow characteristics. Section 2.2 describes the flow topology when an additional cylinder is present. The main purpose of this specific part of the review is to highlight the effects of interactions between two cylinders on the flow. Lastly, previous investigations on flow through a triangular cluster of three cylinders are reviewed and discussed in Section 2.3.

2.1 Flow around a uniform circular cylinder

As a fluid flows past a single uniform circular cylinder, boundary layers form on both sides of the cylinder surface (Figure 2.1). Due to an adverse pressure gradient, the boundary layers

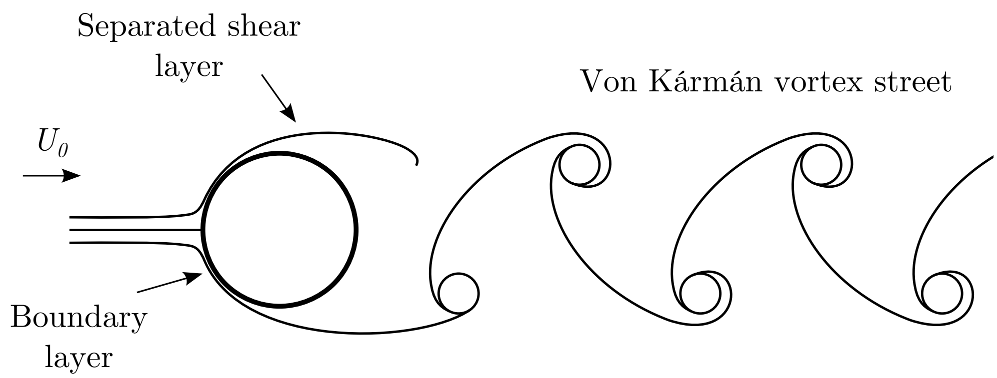

Figure 2.1: Flow over a single uniform circular cylinder.

separate from the surface and form separated shear layers. At sufficiently high Reynolds number ($Re_D > 50$) [5], these shear layers roll-up into large vortical structures which are shed downstream. This shedding process is periodic and occurs at a fixed frequency. Figure 2.1 shows a typical flow topology for flow past a uniform circular cylinder. The shedding phenomenon produces a notable structure in the wake of the cylinder, known as a von Kármán vortex street (Figure 2.1).

Flow around a uniform circular cylinder is strongly dependent on the Reynolds number, $Re_D = \rho U_0 D/\mu$. Williamson [5] and Zdravkovich [6] identify distinct flow regimes for a wide range of Reynolds numbers. For $0 < Re_D < 45$, the wake of the cylinder is steady, laminar, and two-dimensional. For $5 < Re_D < 45$, two steady counter rotating eddies are present in the near-wake [14]. These eddies grow in size in the streamwise direction with increasing Re_D. Oscillations in the wake are first visible far downstream when $Re_D \approx 45$ and a two-dimensional von Kármán vortex street is present for $45 < Re_D < 190$ (also knows as the periodic laminar regime) [5]. Gerrard [3] suggests that the continuous supply of vorticity from the shear layer to the growing vortex becomes strong enough to draw the opposite shear layer across the wake. The approach of this shear layer with oppositely-signed vorticity across the wake cuts off further supply of circulation to the vortex, and the vortex is then convected downstream by the flow. The streamwise extent of the vortex formation region is dependent on the Reynolds number [15, 16]. Griffin & Votaw [16] defined the vortex formation length to be the distance from the center of the cylinder to the location of the maximum fluctuations in the streamwise velocity component along the wake axis. The length of the formation region decreases with increasing Reynolds number in the periodic laminar regime [15,16].

Figure 2.2 schematically shows laminar and turbulent flow regions in the wake, separated shear layers, and boundary layers, occurring at higher Reynolds numbers. For $190 < Re_D < 350$, transition to turbulence takes place in the wake (Figure 2.2a) and three-dimensional deformations of the main spanwise rollers occur in two modes [5]. The first mode (Mode A) sets in at $Re_D \approx 190$ and is associated with the deformation of the shed vortices, resulting in the formation of streamwise vortex pairs with a spanwise spacing of approximately 3 to 4 diameters [5]. Mode B starts at $Re_D \approx 240$, and involves the formation of smaller scale streamwise vortices with a spanwise distance of approximately $1D$ [5]. At the onset of Mode A, there is a sudden drop in the Strouhal number, $St_D = fD/U_0$. As the Reynolds number increases, a gradual energy transfer from the first mode to the second mode leads to a rise in St_D [5]. In this regime, the separated shear layers and boundary layers are still laminar and two-dimensional.

Transition to turbulence in the shear layers occurs for $1 \times 10^4 < Re_D < 2 \times 10^5$ [5]. Transition moves upstream along the shear layers with increasing Re_D. The Kelvin-

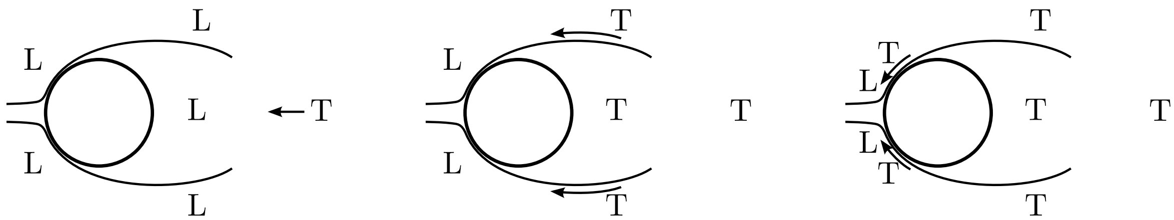

(a) Wake (b) Shear layers (c) Boundary layers

Figure 2.2: Transition from laminar to turbulent in the (a) wake, (b) shear layers, and (c) boundary layers. Reynolds number increases from (a) to (c). L = Laminar and T = Turbulent. Adapted from [6].

Helmholtz instability is present in the shear layers in this flow regime, as seen in Figure 2.3. Bloor [17] was the first to measure the frequency of these structures within the shear layers and found that the ratio of the shear layer instability frequency to the vortex shedding frequency is approximately proportional to $Re_D^{1/2}$. Prasad & Williamson [18] reanalyzed this relation and showed that the ratio scales more accurately with $Re_D^{0.67}$.

For $Re_D > 2 \times 10^5$, transition moves upstream along the boundary layer on each side of the cylinder surface (Figure 2.2c). For $2 \times 10^5 < Re_D < 7 \times 10^6$, a separation bubble exists on both sides of the cylinder surface due to the reattachment of the separated shear layers. The separation bubble forms at irregular intervals in this flow regime [6]. When the bubble forms, the boundary layer separates further downstream, resulting in a reduced wake width, as compared to the previous flow regime. Also, there is a sudden drop in the drag when the separation bubble is present. Beyond $Re_D \approx 7 \times 10^6$, periodic vortex shedding is present with separation occurring further upstream, resulting in a wider wake and increased drag, compared to the range of $2 \times 10^5 < Re_D < 7 \times 10^6$.

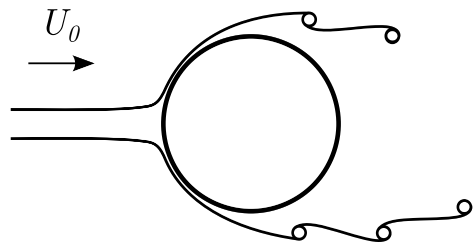

Figure 2.3: Shear layer transition vortices. Based on the results of [19]

2.2 Flow over two circular cylinders

Fluid flow over two circular cylinder geometries is seen in a wide range of engineering applications (e.g., pair of chimney stacks, structural members, electrical transmission lines, and twin cooling towers) and numerous investigations (e.g., [13, 19–23]) have been performed for this geometry. Figure 2.4 shows three relative arrangements of two cylinders commonly studied in various industrial applications. The spacing between the two cylinders and their orientation relative to the flow direction, β, play a significant role in the flow patterns for this geometry. Zdravkovich [23] defines four types of interference flow regimes observed for various arrangements of the two cylinders for $350 < Re_D < 2 \times 10^5$: (i) wake, (ii) proximity, (iii) wake and proximity, and (iv) no interference. For case (i), upstream separated shear layers or vortices shed from the upstream cylinder interact with the downstream cylinder. Proximity interference (case (ii)) occurs when the two cylinders are relatively close to each other such that there is interaction between the two inner shear layers. Case (iii) is a combination of (i) and (ii), in which both types of interference are present. For case (iv), the cylinders are spaced relatively far apart such that there is no interference between them and each cylinder behaves like a single isolated cylinder. For a detailed map of the

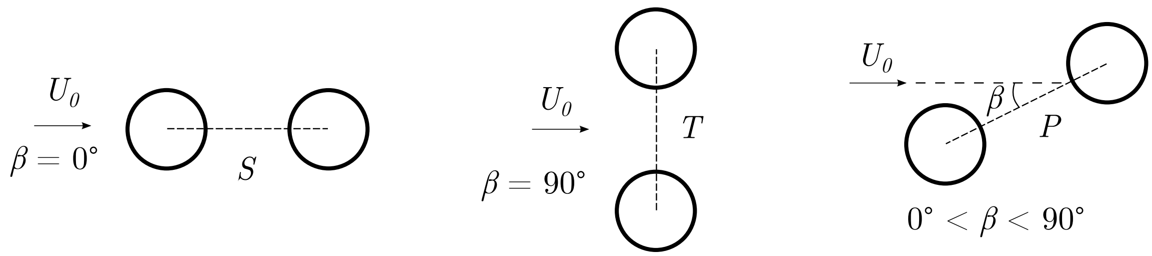

(a) Tandem (b) Side-by-side (c) Staggered

Figure 2.4: Definition of two cylinder arrangement.

interference flow regimes, the reader is directed to [23].

2.2.1 Tandem arrangement

Figure 2.5 shows typical flow topology observed for flow over two tandem cylinders in the wake interference flow regimes. For this geometrical configuration, two possible outcomes occurs, depending on Re_D and S/D: (i) suppression of vortex shedding behind the upstream cylinder (Figures 2.5a and 2.5b) or (ii) a vortex street behind each cylinder (Figure 2.5c) [23]. Reattachment of the upstream separated shear layers on the downstream cylinder surface is seen for a range of S/D within flow regime (i).

Single vortex street

Biermann & Herrnstein Jr. [13] were one of the first to study the impact of flow interference on the drag coefficient for each cylinder in a tandem arrangement. They performed experiments for $2.5 \times 10^4 < Re_D < 1.4 \times 10^5$ and $1 \leq S/D \leq 9$. The results showed significantly lower values of drag for the downstream cylinder, with respect to a single cylinder case.

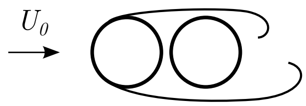

(a) Single vortex street

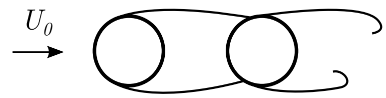

(b) Upstream shear layer reattachment

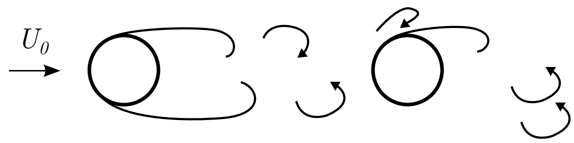

(c) Binary vortex street

Figure 2.5: Typical flow patterns for tandem cylinders. Based on the results of [23].

The drag coefficient on the upstream cylinder is not significantly affected by the presence of the downstream cylinder. For $S/D < 4$, the shedding behind the upstream cylinder is suppressed due to the presence of the downstream cylinder. The drag coefficient on the downstream cylinder decreases with decreasing S/D, and, for $S/D < 3$, the drag on the downstream cylinder is negative. The reason for the reduced drag is that the downstream cylinder is submersed in the wake of the upstream cylinder. Vortices forming from the shear layers of the upstream cylinder grow and impinge on the back surface of the downstream cylinder, producing a force opposite to the free-stream direction [13].

Kostic & Oka [24] performed surface pressure measurements on the tandem cylinders for $1.2 \times 10^4 < Re_D < 4.0 \times 10^4$ and $1.6 \leq S/D \leq 9$. They observed reattachment of the upstream separated shear layers on the surface of the downstream cylinder for $S/D < 3.8$. For this range of S/D, the surface pressure distribution for the downstream cylinder differs significantly compared to that on a single cylinder. The pressure distribution on the downstream cylinder shows a peak on both sides of the downstream cylinder surface indicating the locations of shear layer reattachment. The reattachment points move upstream along the downstream cylinder surface with decreasing S/D. Zdravkovich & Stanhope [25] supported the findings of Kostic & Oka [24] by obtaining velocity profiles in the gap region (i.e., wake of the upstream cylinder). They found that the flow in the gap region was stagnant in this flow regime.

For $S/D < 4$, Igarashi [26] used surface oil visualization and pressure measurements and classified four different types of shear layer reattachment behaviors: (i) no reattachment, (ii) alternate reattachment, (iii) quasi-steady reattachment and (iv) intermittent vortex shedding. For very small spacings (e.g., $S/D \approx 1.03$), the upstream separated shear layers do not reattach on the downstream cylinder surface (Figure 2.5a). The downstream cylinder is bound by the separated shear layers of the upstream cylinder. A single vortex street forms behind the tandem cylinders. For case (ii), only one of the two upstream shear layers reattaches on the downstream cylinder surface at a time. When one of the separated shear layers reattaches, the opposite one rolls into a vortex. Once the vortex is shed, the reattached shear layer detaches from the downstream cylinder and starts to rolls up into a vortex; whereas, the opposite separated shear layer reattaches on the downstream cylinder surface. This alternating process occurs at the vortex shedding frequency. As the spacing increases further, quasi-steady vortices form in the gap (case (iii)). For case (iv), near the critical spacing of $S/D \cong 3.8$, intermittent shedding in the gap region is present.

Despite the suppression of vortex shedding behind the upstream cylinder for $S/D < 3.8$, vortex shedding occurs for all S/D behind the downstream cylinder [26,27]. For $S/D < 3.8$, the Strouhal number for the downstream cylinder decreases with increasing S/D. At $S/D = 3.8$, there is vortex shedding present behind the upstream cylinder. Ishigai et al. [28] noticed that shedding in the gap region was bistable at $S/D = 3.8$ and it switched intermittently between shedding and no shedding. Ishigai et al., further investigated this behavior by comparing the Strouhal number values for the upstream cylinder to the case of a single cylinder with a splitter plate [29]. The results showed that both the splitter plate and the downstream cylinder in the tandem arrangement create a closed wake flow pattern directly behind the upstream cylinder, which suppresses vortex shedding [28].

Zdravkovich [30] performed smoke visualizations of the tandem wakes for $40 < Re_D < 250$ and $1 < S/D < 12$ and made comparisons to a single isolated cylinder. The results show suppression of transition to turbulence in the wake for $S/D < 4$. The transition to turbulence is delayed as the spacing between the tandem cylinders decreases. For a particular case of $S/D = 1$, the wake behind the two cylinders remains laminar until approximately twice the transition Reynolds number for a single cylinder. Zdravkovich [30] suggests that this delay is due to the increased base pressure on the downstream cylinder.

Dual vortex street

Thomas & Kraus [20] studied the interaction of the vortex streets for two cylinders in a tandem arrangement for $3.6 < S/D < 16$ at $Re_D = 62$. For $S/D > 10$, vortices shed from the upstream and downstream cylinders coalesce to form one street about $20D$ downstream. For $3.6 < S/D < 8.5$, the tandem wake expands and contracts (in the transverse direction) periodically at a lower frequency than the vortex shedding frequency. Also, when S/D is an odd multiple of half the longitudinal spacing of the vortices in the wake, contractions or cancellations of vortex streets occur downstream of the two tandem cylinders.

Koboyashi [31] performed flow visualization at $Re_D = 10^4$ for $3 < S/D < 8$ and used red and blue dye to trace vortices shed from the upstream and downstream cylinder. For $3.8 < S/D \lesssim 5$, the shed vortices from the upstream cylinder move around the downstream cylinder sides and pair with the vortices shed from the downstream cylinder, forming a binary vortex street [31, 32], as shown in Figure 2.5c. For $S/D > 5$, the vortices from the upstream and downstream cylinder are shed at different frequencies and do not form a binary vortex street behind the downstream cylinder [32].

Drag and lift forces on both cylinders in tandem arrangement depend on both S/D and Re_D [13, 24, 27]. For $S/D > 3.8$, the drag coefficient on the upstream cylinder is approximately equal to that of a single cylinder at the corresponding Reynolds number. Thus, the downstream cylinder has minimal effect on the drag of the upstream cylinder. There is, however, a strong effect of Re_D on the drag of the downstream cylinder. The drag of the downstream cylinder approaches that of the upstream cylinder for $Re_D \lesssim 10^4$. At high Reynolds numbers ($\sim 10^5$), the drag of the downstream cylinder decreases significantly with increasing Re_D [24, 27]. Also, as the spacing between the cylinders increases, the drag of the downstream cylinder increases [24]. The effect of Re_D and S/D on the drag of the downstream cylinder in a tandem arrangement is analogous to the effect of free-stream turbulence level on the drag of a single cylinder [8].

The transition Reynolds number in the tandem wake is different when compared to that for a single cylinder and is dependent on the spacing between the cylinders. Zdravkovich [30] notes that there is promotion of transition for $8 < S/D < 12$. For $4 < S/D < 8$, however, the transition occurs at the same Reynolds number as for the single cylinder case.

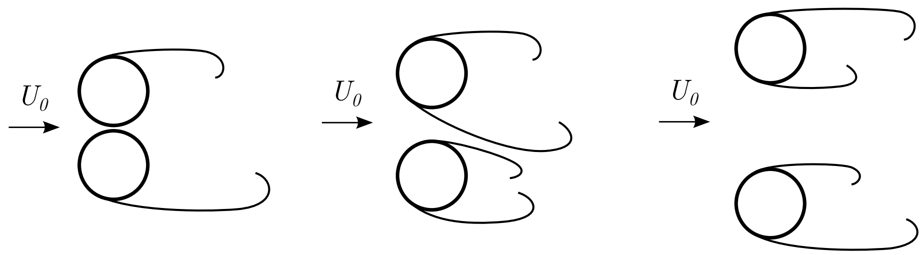

(a) Single vortex street (b) Bistable flow (c) Coupled vortex streets

Figure 2.6: Typical flow patterns for side-by-side cylinders. Based on the results of [23].

2.2.2 Side-by-side arrangement

Depending on the spacing between the two side-by-side cylinders (T/D), three different flow patterns occur due to proximity interference, as shown in Figure 2.6: (i) formation of a single vortex street, (ii) bistable gap flow, and (iii) parallel coupled streets [23].

Single vortex street

For relatively small spacing ratios ($1 < T/D < 1.1 - 1.2$), a single vortex street is present behind the two cylinders (Figure 2.6a) [23]. The velocity of the flow between the small gap is relatively low. Spivack [33] investigated the shedding frequency behind the tandem cylinders for $1 \leq T/D < 6$ at $5 \times 10^3 < Re_D < 9.3 \times 10^4$. At $Re_D = 2.8 \times 10^4$, only one vortex street is present in the wake for $1 \leq T/D < 1.09$. The Reynolds number and Strouhal number, based on the height of the projected area of the two cylinder arrangement (i.e., $\approx 2D$), is equal to that of a single cylinder whose diameter equals to the height of the project area at the given Reynolds number. Thus, in the regime, the geometry is analogous to a single bluff body, in terms of large scale shedding characteristics. Bearman

& Wadcock [21] supported the findings of Spivack [33] by measuring the base pressure for both cylinders simultaneously and found the same for both cylinders in this flow regime.

Bistable flow phenomenon

Biermann & Herrnstein Jr. [13] were the first to notice bistable flow behavior for a specific range of spacing ratios. For $1.1 < T/D < 2.2$, the flow through the gap between the two cylinders becomes biased towards one of the two cylinders, as seen in Figure 2.6b. The biased gap flow forms a narrow and a wide wake behind the side-by-side cylinders. The direction of the gap flow is bistable (i.e., it switches irregularly) [23]. The different size of wakes results in different size of shed vortices and shedding frequency behind the cylinders. The small vortices shed from the narrow wake coalesce with the vortices shed from the wider wake [23]. The vortices from the narrow wake are shed at a frequency higher than that of the vortices shed in the wide wake. However, far downstream, a single Strouhal number value is present corresponding to the frequency of the large scale structures [34]. The narrow wake produces larger Strouhal number. Also, the drag and lift forces on the cylinder producing the narrow wake is larger, relative to the values for the opposite cylinder [23]. Bearman & Wadcock [21] noticed that the low and high drag values always add up to less than twice the value for the single cylinder case.

The source of this biased gap flow has been hypothesized in several previous studies, but is still uncertain. Ishiqai et al. [28] suggests that the bistable flow phenomenon is a consequence of the Coanda effect [35], which is seen in the case of a jet deflecting when attached to a curved surface. This hypothesis was proven incorrect by Bearman & Wadcock [21] who used side-by-side flat plates and observed bistable flow even though the surface of the objects were not curved. Zdravkovich [36] proposed that this phenomenon occurs due to the initial stage of the interference in the gap. He suggested that a small deflection or disturbance in the gap flow disrupts the balance of opposite sign vorticity in the inner shear layers which causes one of the shear layers to start rolling up. This imbalance leads to an increase of vorticity towards the bias side. The random switching can also be explained by observing the behavior at the initial stage of gap interference. If a small disturbance at the initial stage of the gap interference causes an imbalance towards the opposite side of the bias, the shear layer on that side will start to roll up and shift the bias to the other side of the wake.

Parallel vortex streets

For $2.2 < T/D \lesssim 5$, bistable flow behavior disappears and the two vortex streets behind the side-by-side cylinders are coupled (Figure 2.6c) [23]. The coupled streets are synchronized in frequency and phase. Figure 2.7 shows the two possible modes of flow patterns in this regime. Landweber [37] proposed a model for two parallel vortex streets based on Kármán's single vortex street theory and specified two conditions: (i) transverse-induced velocity component must be zero for the four vortex rows to be aligned and (ii) the streamwise velocity of the vortices in each row must be the same. These conditions must hold for a stable flow pattern to convect downstream. Applying these requirements results in two possible flow patterns, as seen in Figure 2.7. Landweber [37] also showed that the strength of the outer and inner vortices cannot be equal. For the out-of-phase case, the strength of the vortices in row (2) must be greater than that of row (1). For the other case (Figure 2.7b), the strength of the vortices in row (1) must be greater than that of row (2). Williamson [19] used flow visualization techniques to study the flow development in the wake of two side-by-side cylinders and showed the occurrence of both modes. The out-of-phase mode is predominant; however, it is possible for the flow to intermittently switch to the other mode. Both modes behave differently far downstream. The out-of-phase streets keep its form for large distances downstream, however, for the in-phase case, the parallel streets are in-phase only in the near-wake region. In this mode, both parallel wakes combine to form a single binary vortex street far downstream, similar to the case of two tandem cylinders for $3.8 < S/D \lesssim 5$ [31]. The single street is similar to a Kármán street, however, each row of vortices consists of a pair of vortices of equal sign.

2.2.3 Staggered arrangement

According to [38], three main types of flow development over two cylinders in a staggered arrangement are as follows: (i) single bluff body shedding, (ii) shear layer reattachment, and (iii) synchronized vortex shedding. Figure 2.8 shows the typical flow patterns for each of these cases. The most common observation for such flows is the presence of a narrow and wide wake behind the upstream and downstream cylinder, respectively [28]. The degree of bias in the gap flow and difference in size of the two wakes both decreases with increasing spacing (P/D).

Single bluff body shedding

For $1 < P/D < 1.25$ and at all values of β, the two staggered cylinders behave similar to a single bluff body [38]. A single vortex street is present behind the pair of cylinders. For

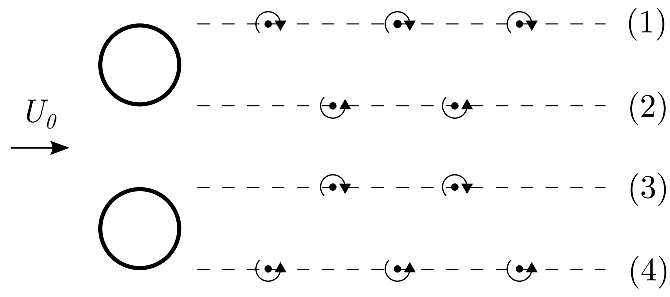

(a) Out-of-phase

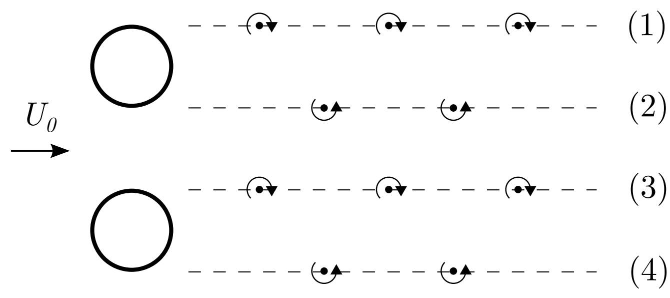

(b) In-phase

Figure 2.7: Two possible modes of coupled vortex streets: (a) out-of-phase and (b) in-phase. Based on the results of [37].

$0° < \beta < 45°$, the length of the separated shear layer on each side is notably different. The length of the shear layer from the upstream cylinder is larger. This shear layer is more unstable and usually develops Kelvin-Helmholtz instabilities [38]. As the angle is increased to $45° < \beta < 90°$, the difference between the two shear layers is minimal and instabilities observed (if any) appear in both shear layers. The small gap flow between the cylinders penetrates the near-wake region which leads to an increase in the vortex formation length, in comparison to the case when the two cylinders are in contact (i.e., no gap flow). Also, this gap flow typically results in a wider near-wake region behind the two cylinders [38].

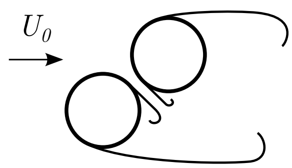

(a) Single vortex street

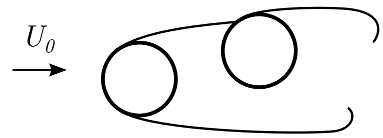

(b) Shear layer reattachment

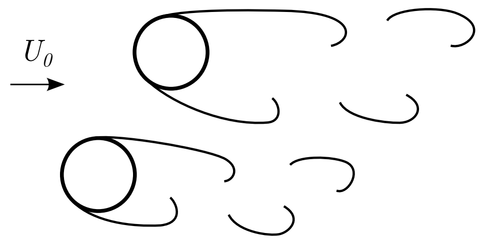

(c) Synchronized streets

Figure 2.8: Typical flow patterns for staggered cylinders. Adapted from [38].

Shear layer reattachment

For $1.1 < P/D < 4$ and $0° < \beta < 20°$, shear layer reattachment is present along with a single vortex street behind the two cylinders [38], as seen in Figure 2.8b. There is no shedding directly behind the upstream cylinder. The inner shear layers from the upstream cylinder reattach onto the downstream cylinder surface. Behind the two cylinders, only a single vortex street is present. Gu & Sun [39] also observed shear layer reattachment on the downstream cylinder surface at high Reynolds numbers ($\sim 10^5$). The reattachment of the shear layer causes the surface pressure at the reattachment point on the downstream cylinder to increase. Similar to the previous flow regime, the two separated shear layers forming the single street behind the two cylinders still have different lengths. The longer shear layer is more unstable and has a tendency to develop Kelvin-Helmholtz instabilities.

Synchronized vortex shedding

For $1.5 < P/D < 5$ and $15° < \beta < 90°$, the two wakes behind both cylinders are synchronized in frequency and phase [38]. The deflection in the gap flow forms two different sized near-wake regions behind the two cylinders. The gap vortices on either side pair up and are synchronized in their shedding process. The flow behavior is similar to that of two coupled streets for a pair of side-by-side cylinders (Figure 2.7); however, only the out-of-phase mode is seen for the case of two cylinders in a staggered configuration, as illustrated in Figure 2.8c.

2.3 Flow through triangular cluster of three cylinders

The geometry definition for a triangular cluster of three cylinders is shown in Figure 1.1. Flow development over this geometry depends on Reynolds number, the spacing ratios, P/D, S/D, and T/D, and cluster orientation relative to the free-stream flow direction, α.

2.3.1 Effect of spacing ratios

Zdravkovich [9] studied the effect of longitudinal and transverse spacing ratios using smoke visualization for $5 \leq S/D \leq 21$, $2 \leq T/D \leq 10$, and $0° \leq \alpha \leq 60°$ at low Reynolds numbers ($60 < Re_D < 300$). He identified two distinct flow interference patterns at $\alpha = 0°$: (i) a single vortex street forms behind the cluster for $2 \leq T/D \leq 6$ and (ii) three individual streets form for $T/D > 6$, as seen in Figure 2.9. For case (i), the length of the formation region where initial roll up of the shear layers occurs varies with the transverse spacing. The length of this region decreases as the spacing between the downstream cylinders decreases. Also, the single vortex street downstream of the cluster shows significant expansion (i.e., the vortex rows on either side diverge from the wake axis at a considerable angle). Zdravkovich [9] compares this expansion in the vortex street to the wake of a single vibrating cylinder [40, 41]. He suggested that the expansion in the wake of the three cylinder cluster for $2 \leq T/D \leq 6$ is a consequence of oscillations in the flow approaching the two downstream cylinders produced by the upstream cylinder. For case (ii) ($T/D > 6$), there is minimal interaction between the three vortex streets immediately downstream of the cluster; however, vortex interactions between the three vortex streets further downstream trigger considerable variation in the spatial arrangement of the middle vortex street. The opposite sense vortices on each side of the middle street gradually cross the center line of the wake, briefly forming a single row of vortices, and then continuing to the opposite side of the wake axis.

Different flow patterns were also observed by Zdravkovich [9] for various S/D values at $\alpha = 0°$. A traditional von Kármán vortex street exists behind the upstream cylinder for S/D exceeding some critical value, which depends on the Reynolds number [9]. For S/D larger than this critical value, interaction between the upstream vortex street and the two downstream cylinders occurs. As S/D decreases below the critical value, no vortex street is visible behind the upstream cylinder and the cluster behaves like a single bluff body.

Sayers [10] and Price & Paidoussis [11] measured the forces exerted on the three cylinders in a triangular cluster at $Re_D = 3.18 \times 10^4$ and $Re_D = 5.1 \times 10^4$, respectively.

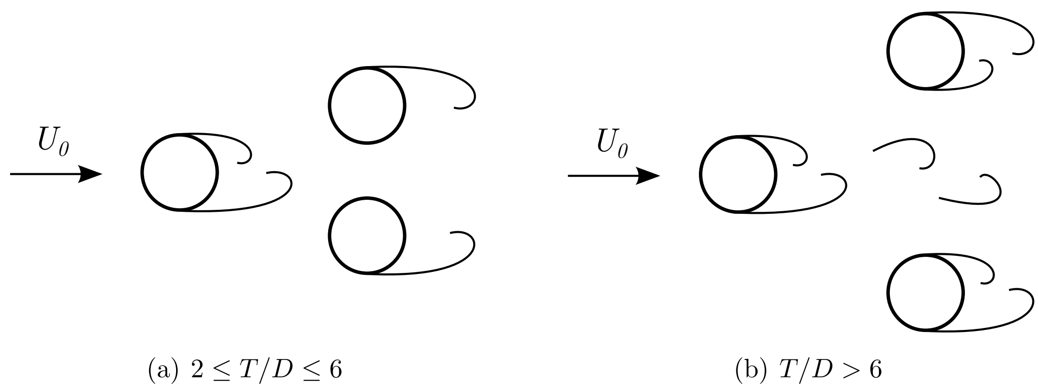

Figure 2.9: Flow development for various T/D at $\alpha = 0°$. Based on the results of [42].

Sayers [10] found that the drag coefficient on the cylinders is equal to that of a single isolated cylinder for $P/D > 4$. For $P/D > 4$, there is minimal interaction between the three cylinders in the cluster. For a particular case of $P/D < 4$ and $\alpha = 0°$, the drag coefficient on the upstream cylinder decreases with decreasing P/D due to the interaction between the wake of the upstream cylinder and the two downstream cylinders. Price & Paidoussis [11] noticed the drag coefficient on the cylinders for all cluster orientations is equal to that of a single cylinder for $P/D > 5$. The difference in the reported lower bound for P/D by [10] and [11], for which all three cylinders in the cluster behave similar to an isolated single cylinder, may be due to difference in the operating Reynolds number in both experiments.

2.3.2 Effect of cluster orientation

The cluster orientation angle, α, is another parameter which influences the flow for this geometry. Lam & Cheung [12] investigated the effects of orientation angle for an equilateral

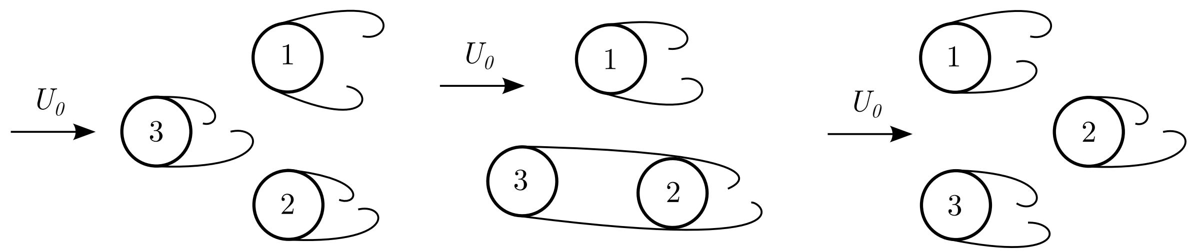

(a) $\alpha = 0°$ (b) $\alpha = \alpha_s$ (c) $\alpha = 60°$

Figure 2.10: Flow development for various orientations between $1.27 \leq P/D \leq 2.29$. Based on the results of [12].

triangular cluster for $1.27 \leq P/D \leq 5.43$ at $Re_D = 2100$ and 3.5×10^3. Figure 2.10 shows the typical flow development observed in [12]. For $\alpha = 0°$, a bistable wake exists, as shown in Figure 2.10a. For a range of orientation angles ($0 < \alpha_s < 30$), the downstream cylinder is fully shielded by the separated shear layers from the upstream cylinder (Figure 2.10b) [12]. Figure 2.10c shows a symmetric wake development for $\alpha = 60°$.

For $\alpha = 0°$ and $1.27 \leq P/D \leq 2.29$, flow patterns behind the cluster are similar to the bistable case observed in flow past two cylinders in a side-by-side arrangement [23]. A narrow and a wide wake exist behind the downstream cylinders, as seen in Figure 2.10a. Lam & Cheung [12] have characterized this flow regime as bistable. The gap or jet flow (i.e., flow exiting between the two downstream cylinders) is biased towards either side of the two downstream cylinders. The biased direction of the jet flow is dependent on the initial conditions. Lam & Cheung [12] did not notice any intermittent switching during experimentation, as observed for the two cylinder in a side-by-side arrangement case [23]. The shedding frequency for the narrow wake is larger than for the wide wake. For the upstream cylinder, the Strouhal number can vary between 0.4 to 0.6. Lam & Cheung [12] suggested that such high St_D values for the upstream cylinder are due to the "compression" of the separated shear layers emanating from the upstream cylinder in the gap between the two downstream cylinders. This effect leads to an increase in vortex shedding frequency. As the spacing ratio increases to $2.29 < P/D < 4.65$, the bistable phenomenon does not occur. Also, the Strouhal number for the upstream cylinder decreases with increasing P/D.

For $P/D \leq 4.65$, vortex shedding from the upstream cylinder is suppressed at some angle below 30°. This angle is defined by Lam & Cheung [12] as the angle of fully shielded flow, α_s. At $\alpha = \alpha_s$, the downstream cylinder is fully shielded by the separated shear layers from the upstream cylinder, as seen in Figure 2.10b. The angle of fully shielded flow increases as P/D increases, reaching $\alpha_s = 30°$ at $P/D = 4.65$. For $\alpha = 20°$, no shedding occurs behind the upstream cylinder for the range $2.29 < P/D < 3.00$. As α increases from α_s to 60°, the St_D values for cylinder 1 approach the values of cylinder 3 and no significant changes are seen in the St_D values for cylinder 2.

At $\alpha = 60°$, for $1.27 \leq P/D \leq 5.43$, the bistable flow behavior disappears completely even though the two upstream cylinders are in a side-by-side arrangement [12]. The presence of the downstream cylinder prevents the formation of wide and narrow wakes, producing two symmetric wakes behind the upstream cylinders, as shown in Figure 2.10c.

For $1.27 \leq P/D \leq 2.29$, the flow patterns are similar far downstream at all orientation angles. Entrainment, and subsequent merging, of the vortices shed in the narrow wake(s) leads to the formation of larger vortices 5 to 6 diameters downstream of the cluster [12]. The Strouhal number, based on the height of the projected area of the cluster, D_h, in this region is approximately equal to that of a single isolated cylinder with equivalent diameter, suggesting that the cluster behaves like a single bluff body in terms of the large scale shedding characteristics. Also, for all orientations, the St_D values behind each cylinder is approximately equal to the single cylinder case for $P/D \gtrsim 5$.

In addition to the differences in the Strouhal number with varying α, variations in the drag coefficient for each cylinder are observed at different values of α [10]. The drag on each cylinder is dependent on the cylinder position in the cluster. For example, for $1.25 \leq P/D \leq 5$ at $Re_D = 3.18 \times 10^4$, the minimum drag at $\alpha = 30°$ occurs for the most downstream cylinder (cylinder 2) [10]. This configuration consists of the downstream cylinder positioned directly inline with the upstream cylinder. However, the drag coefficient of the downstream cylinder is still higher than compared to that for the two cylinder tandem arrangement [11].

Chapter 3

Experimental methodology

3.1 Experimental facility

Figure 3.1 shows an illustration of the re-circulating water flume facility in the Fluid Mechanics Research Laboratory at the University of Waterloo. As shown in Figure 3.1, flow exiting the settling chamber is conditioned via one honeycomb structure and five screens, resulting in a free-stream turbulence intensity of less than 1% and flow uniformity within 3%. A gate valve is implemented to make adjustments to the flow rate in the test section. The test section walls are made from 19 mm thick glass for optical access. The test section is 2.4 m long with a cross-sectional area of 1.2 m by 1.2 m. The water level is maintained at 0.8 m from the bottom of the channel with the assistance of a perforated plate placed downstream of the test section.

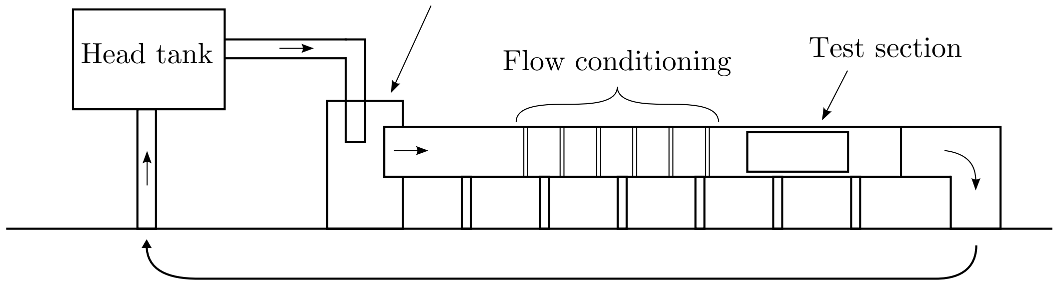

Figure 3.1: University of Waterloo water flume facility.

3.2 Model specifications

The triangular cluster of three cylinders was mounted at the midspan of the test section of the water flume. Figure 3.2 shows the cluster geometry mounted at the base of the test section. The cluster consisted of three equally spaced circular cylinders, 25.4 mm in diameter, D. Each cylinder was made from two aluminum rods with fluorinated ethylene propylene (FEP) inserts filled with water at the midspan (Figure 3.2). FEP was selected for the inserts because its index of refraction of 1.344 is approximately equal to that of water (1.333). This allowed to virtually eliminate refraction of the laser sheet passing through the inserts during the experiments. The three cylinders, each approximately $16D$ long, were equally spaced with a spacing ratio of $P/D = 1.35$ and mounted between two endplates. The FEP inserts were $2D$ long with a wall thickness of $D/32$. The aluminum rods were polished using 500 grit sandpaper and painted black to minimize laser light reflections. The cluster was mounted on a cylindrical base via a precision drive shaft and sleeve bearing. The tolerance for the shaft diameter was ±0.001", which resulted in a

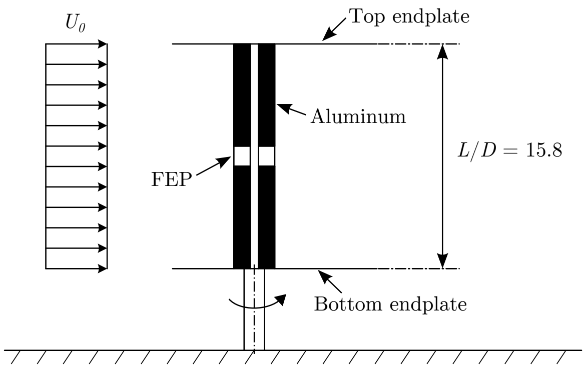

(a) Front view

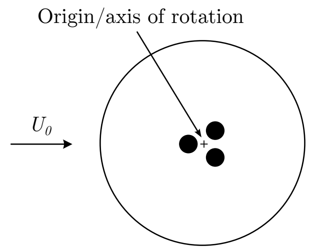

(b) Top view

Figure 3.2: Experimental arrangement of triangular cluster at $\alpha = 0°$.

sliding fit connection and allowed the cluster to rotate about the origin (Figure 3.2b).

Figure 3.3 shows the two circular acrylic endplates which were mounted at the ends of the three cylinders. A digital level was used to ensure the horizontal alignment of both end plates to $\pm 0.1°$. The endplates had an outer diameter of $14D$, following the recommendations of Fox and West [43]. On both endplates, the outer edges were chamfered at an angle of 60°. The thickness of each endplate was $D/8$. On the top endplate, a section of the chamfered edge was not implemented, as seen in Figure 3.3a. This minimized optical distortions in the images captured from above the cluster during experiments. The chamfered edge was removed within a sector (Figure 3.4), such that it was not visible at all cluster orientations of interest. To rotate the cluster, a scotch yoke mechanism was constructed and attached to the top endplate (Figure 3.4). The yoke, controlled by a stepper motor (not shown in Figure 3.4), moved on a linear guide rail. A stud mounted on the top endplate, and placed in the slot of the yoke, moved inside the slot, causing the

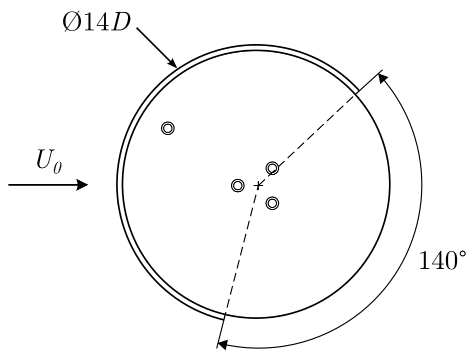

(a) Top endplate

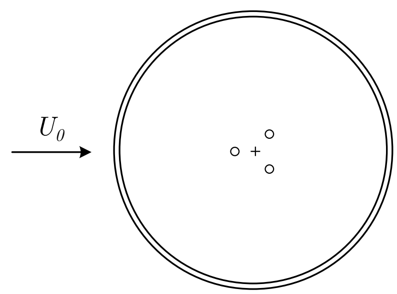

(b) Bottom endplate

Figure 3.3: Top view of top and bottom endplates at $\alpha = 0°$.

cluster to rotate about the origin (Figure 3.4).

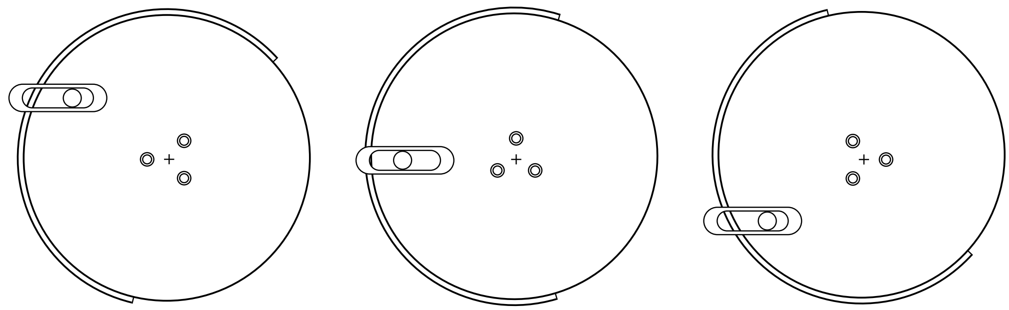

(a) $\alpha = 0°$ (b) $\alpha = 30°$ (c) $\alpha = 60°$

Figure 3.4: Illustration of scotch yoke rotating mechanism.

3.3 Hydrogen bubble flow visualization

A hydrogen bubble technique was used to visualize the wake of the cluster. Werlé and Gallon [44] were one of the first to use this method for flow visualization. Figure 3.5 shows the hydrogen bubble experimental setup in the water flume. The cathode was a $0.004D$ thin stainless steel wire positioned horizontally, approximately $1.35D$ upstream and at the midspan of the cluster. The Reynolds number based on the wire diameter was approximately eight, so that no vortex shedding occurred behind the wire [6]. A Nd:YLF laser (not shown in Figure 3.5) was used to illuminate the horizontal sheet of hydrogen bubbles in the image plane. A high-speed 1024x1024 pixels Photron SA4 camera equipped with a 50 mm focal length Nikon lens was used to capture images of the cluster wake at an acquisition rate of 100 Hz. The size of the hydrogen bubbles is directly related to the amount of voltage applied [45]. As the applied voltage increases, the size of hydrogen bubbles also increases which provides greater visibility; however, this increases buoyancy of the bubbles [46]. Preliminary tests showed that hydrogen bubbles have a negligible raising

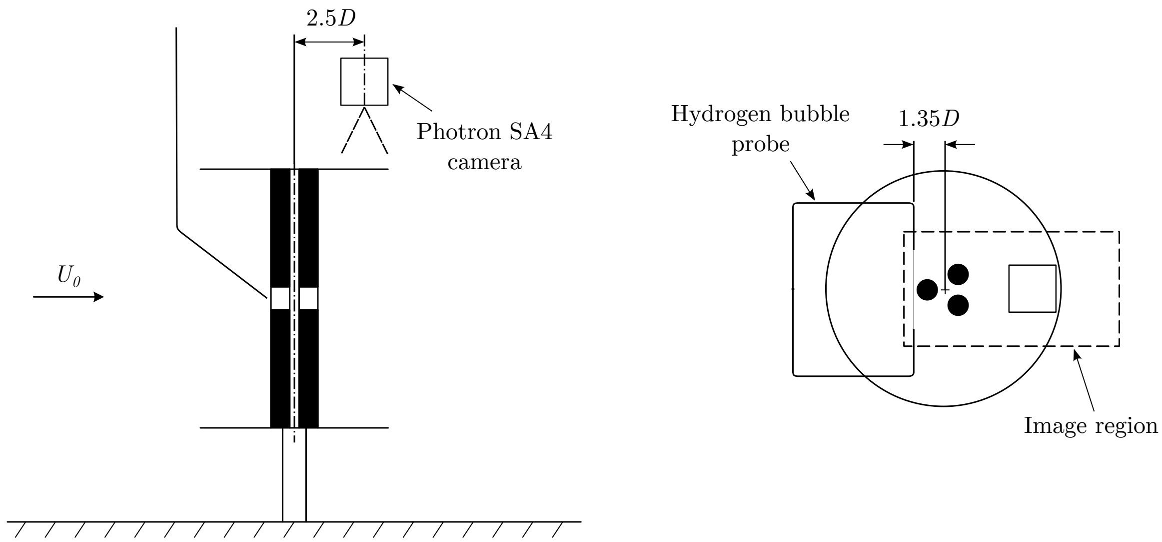

(a) Front view (b) Top view

Figure 3.5: Front and top view of hydrogen bubble experimental setup.

velocity for 40 VDC or less. The applied voltage during operation was 15 VDC, which resulted in a clearly visible bubble sheet, with negligible buoyancy effects within the flow region of interest.

3.4 Velocity measurements

Two-component, time-resolved particle image velocimetry (TR-PIV) was used to measure wake velocity fields. A detailed explanation of working principles of TR-PIV can be found in Raffel et al. [47], Mayinger & Feldmann [48], Adrian [49], and Westerweel [50]. Figure 3.6 shows the setup of PIV experiments in the water flume. The flow was seeded with with small neutrally buoyant hollow glass sphere particles with an average diameter of

$10\,\mu$m. To capture particle images within a large field of view (FOV) and at a high spatial resolution, two high-speed 1024x1024 pixels Photron SA4 cameras with 50 mm focal length Nikon lenses were installed above the cluster. One was centered at the origin to allow velocity measurements between the cylinders, and the other was positioned further downstream such that there was approximately 20% overlap between the two FOVs (Figure 3.6). The resulting joined FOV is approximately $13D$ in streamwise and $7D$ in transverse directions. The glass particles were illuminated with a Nd:YLF laser at the midspan of the cluster. The thickness of the sheet within the FOV was approximately 2 mm ($0.08D$). During the experiments, sets of 5457 single frame images were acquired at an acquisition rate of 100 Hz (approximately 50 times larger than the largest frequency of interest). Synchronization of the laser pulses and image acquisition was carried out using LaVision DaVis 8 software. The acquired data sets were also processed in LaVision DaVis 8 software. An iterative, multi-grid, multi-pass correlation scheme was used to compute the velocity fields. The final window size was 16x16 pixels, with 75% overlap, resulting in a vector pitch of approximately 32 velocity vectors per cylinder diameter. For joining the two velocity fields from the two cameras, a cross-correlation algorithm was applied within the overlapping region between the FOV of the two cameras. The resultant vectors in the overlapping region were calculated using a weighted average with a linear blending factor between the two sets of velocity vectors (one from each camera).

One component laser Doppler velocimetry (LDV) was used to obtain local velocity measurements in the cluster wake. For the present study, a Measurement Science Equipment (MSE) miniLDV system (a dual-beam configuration) was used to perform LDV measurements of the streamwise velocity component in the cluster wake (Figure 3.7). The miniLDV

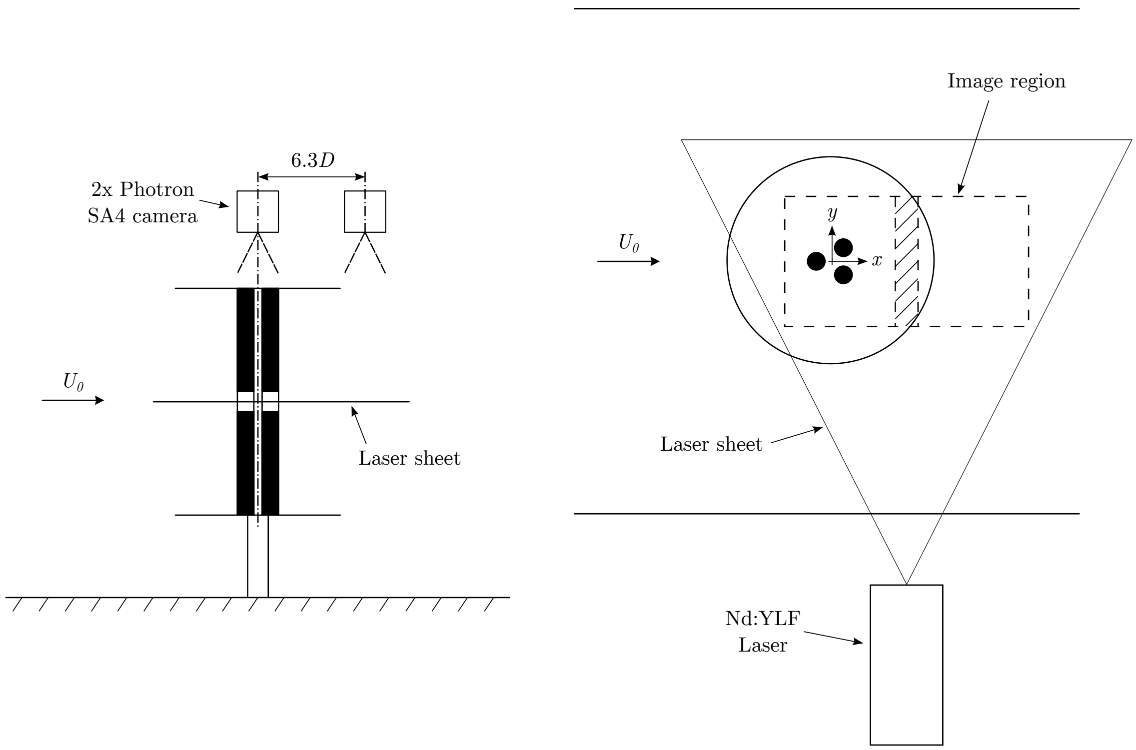

(a) Front view (b) Top view

Figure 3.6: Front and top view of the PIV experimental setup. The hatched window in (b) indicates the overlap region between the two field of views at the midspan of the cluster. Note, the two cameras are not shown in (b) for clarity.

system consists of a 140 mW Argon-Ion laser (628 nm wavelength), Bragg cells, and detection system. The size of the probe volume is $x = 0.15$ mm, $y = 1.24$ mm, and $z = 0.15$ mm ($x/D = 0.006$, $y/D = 0.050$, and $z/D = 0.006$), as illustrated in Figure 3.7. The probe volume distance from the sensor was 600 mm. The streamwise velocity component was measured at $x/D = 12.8$ and $y/D = -1.5$. The accuracy of the probe position was ± 1 mm ($\pm 0.04D$) in both transverse and streamwise directions. The flow was seeded with the

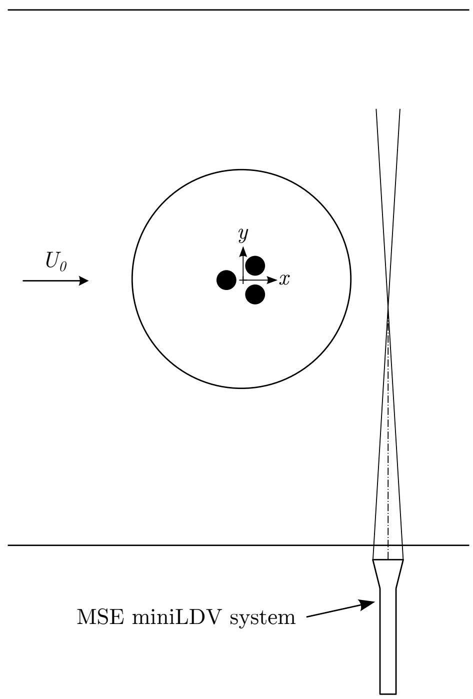

Figure 3.7: LDV experimental setup. Probe located at the midspan in the cluster wake.

same seed particles used for PIV experiments. The average acquisition rate for all cases was greater than 30 Hz. The number of samples for each case was 2^{14}. To facilitate spectral analysis, the velocity signals were re-sampled at 15 Hz (approximately 8 times greater than the largest frequency of interest) using a sample-and-hold technique described by Adrian & Yao [51].

3.4.1 Data analysis

After re-sampling LDV results, each signal was partitioned into 16 segments, each consisting of 1024 data points with 0% overlap. The fast Fourier transform (FFT) was computed for each individual segment and then averaged. The frequency bandwidth resolution for the spectra was $\pm 0.002 fD/U_0$.

Experimental uncertainty for both PIV and LDV experiments is discussed in Appendix D. For PIV experiments, the random error was estimated to be ± 1.5 mm/s ($\pm 0.017U_0$). Appendix D.2 also discusses measures which were taken during the experiments to minimize errors in computing particle displacements. For LDV, the bias error was estimated to be ± 1.6 mm/s ($\pm 0.019U_0$). The MSE miniLDV system has a repeatability uncertainty of 0.1% and an accuracy of 99.7% according to the manufactures specifications [52].

Lumley [53] introduced the method of proper orthogonal decomposition (POD), initially to assist in defining coherent structures in turbulent flows. POD is a transformation of velocity fluctuations in the flow field characterizing the most apparent realizations (i.e., energy content) [54]. POD was performed on the PIV results to investigate the formation and evolution of the most energetic structures in the cluster wake. POD allowed filtering of low energy modes in the wake. The procedure solves the integral eigenvalue problem (i.e., Fredholm equation [55]) and decomposes the fluctuating component of the velocity to

$$\vec{v}'(x, y, t) = \sum_{n=1}^{N} a_n(t)\vec{\phi}_n(x, y) \tag{3.1}$$

where a_n and ϕ_n are temporal and spatial modes, respectively. The solved eigen values are sorted in decreasing order with mode 1 corresponding to the largest eigen value (i.e., the mode with the largest energy content). A reduced-order model of the flow field can be formulated comprising of the first several modes to remove smaller scale turbulent fluctuations. For further reading on the methodology, the reader is referred to the works of

Holmes et al. [56], Berkooz et al. [57], Chatterjee [58], Oudheusden et al. [59], and Druault et. al [60]. In the present work, a reduced-order model comprising of the first 40 modes, which contain, 75% to 90% (depending on α) of the total wake energy (i.e., energy of the velocity fluctuations in the wake) (Figure 5.23a) was simulated to study the formation, evolution, and interaction of vortex structures shed from narrow and wide wakes.

Chapter 4

Numerical model

Flow through the equispaced triangular cluster was modeled numerically using ANSYS CFX 13.0. The simulations were performed for two different flow conditions: (a) $Re_D = 100$ and (b) $Re_D = 2100$. The cases of $Re_D = 100$ and $Re_D = 2100$ correspond to two different vortex shedding regimes. Figure 4.1 shows the computational domain used for simulations. The domain size for the present geometry is selected based on prior results for a single cylinder case (Table 4.1). To facilitate an adequate comparison between the two geometries, a cluster diameter, D_c, is defined as the diameter of a circumscribed circle that is tangent to the three cylinders ($D_c \approx 2.6D$). Using this parameter, the domain size, relative to the cluster origin, is set at approximately $17D_c$ for the upstream distance, $23D_c$ for the downstream distance, and $14D_c$ for the transverse distance. For the selected domain size, the maximum solid blockage is approximately 2.8%. Figure 4.1 shows the domain size in terms of D_c and the diameter of one cylinder in the cluster (i.e., D). The dimensions shown in terms of D_c (Figure 4.1) are larger than the values listed in Table 4.1.

Table 4.1: Domain size recommendations for numerically modeling a single circular cylinder for laminar and turbulent flow regimes.

Direction	Distance from origin
Upstream	$8D$ [61], $9D$ [62], $10D$ [63]
Downstream	$14.5D$ [64], $15D$ [63], $17D$ [62], $22D$ [61]
Transverse	$6D$ [62], $8D$ [61, 65], $10D$ [63]

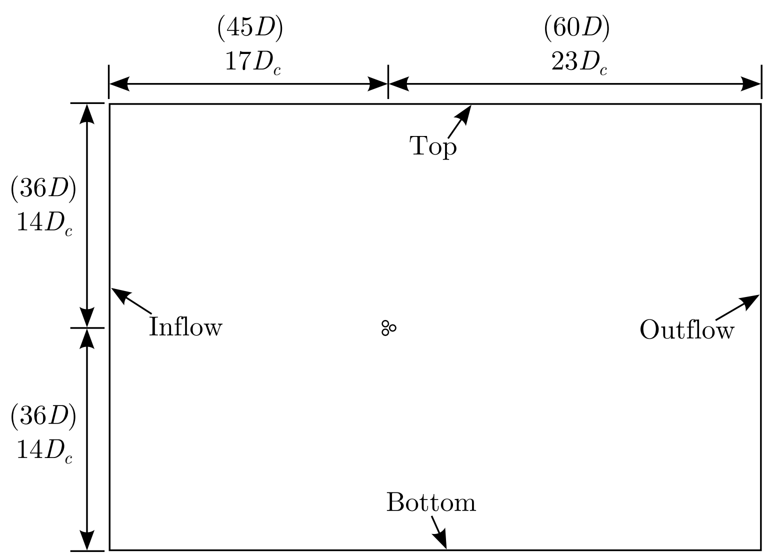

Figure 4.1: Computational domain.

4.1 Vortex shedding at $Re_D = 100$

A laminar model was used to simulate vortex shedding at $Re_D = 100$. From literature, it is well known that transition to mode A shedding for a single cylinder occurs at $Re_D \approx 200$ [5].

For the present cluster geometry, $Re_D = 100$ corresponds to a Reynolds number,$Re_{D_h} = 235$, based on the maximum height of the projected area of the cluster on the plane perpendicular to the incoming flow. This is slightly larger than the transition Reynolds number for a single cylinder. However, previous studies have shown that the error in the main performance parameters introduced by the two-dimensional model for a single cylinder at $Re_D = 235$ is less than 2% for St_D [5, 66, 67], 1% for C_D [67], and 6% for C'_L [66, 67]. Therefore, for the purpose of this study, vortex shedding at $Re_D = 100$ is modeled as two-dimensional. Figure 4.2 shows the structured 2D mesh used for the laminar model. First, a mesh refinement was carried out. Table 4.2 shows the results for four different mesh cases using data pertaining to $\alpha = 60°$ at $Re_D = 100$. The error in the drag coefficient, lift RMS, and Strouhal number between case C and D for each cylinder was less then 1%. Therefore, mesh case C was selected. For the selected mesh, the face sizing in the square section near the cluster (Figure 4.2b) was $0.02D$, which resulted in a spatial resolution of approximately 160 elements on the surface of each cylinder in the cluster. Near the surface of each cylinder, 12 inflation layers were inserted with a growth rate of 1.25 such that at least 10 elements resolved the boundary layer. Using mesh case C, computations were performed on a single cylinder for validation. Table 4.3 shows the comparison between mesh case C results and experimental data. The drag coefficient, lift RMS, and Strouhal number all fall within the expected range reported in experiments.

The following boundary conditions were applied at each domain surface. For the top and bottom surfaces, a free-slip wall boundary condition was applied (i.e., $v = 0$, $\frac{\partial u}{\partial n} = 0$, and $\frac{\partial P}{\partial n} = 0$). At the inlet, a uniform inlet velocity, U_0, was prescribed. At the outlet, the relative static pressure was set to zero and $\frac{\partial u}{\partial n} = \frac{\partial v}{\partial n} = 0$. At each cylinder surface, a no

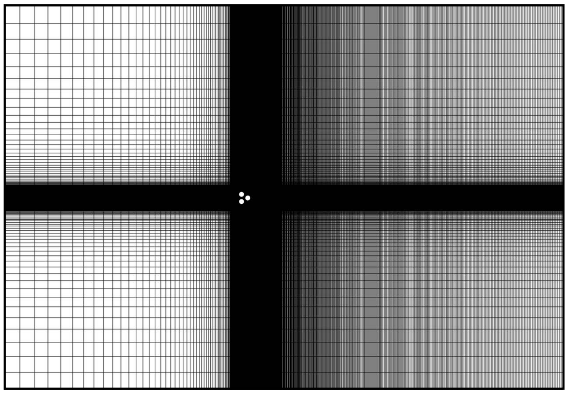

(a) Full domain

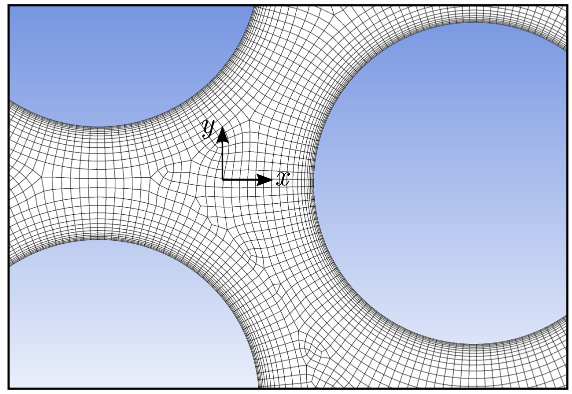

(b) Near the cluster

Figure 4.2: Laminar model computational mesh.

Table 4.2: Mesh refinement study for $\alpha = 60°$ at $Re_D = 100$.

Case	Nodes	C_{D_1}	C_{D_2}	C_{D_3}	C'_{L1}	C'_{L2}	C'_{L3}	St_{D_h}
A	40386	1.55	0.36	1.56	0.062	0.184	0.063	0.191
B	87364	1.58	0.36	1.57	0.063	0.192	0.063	0.191
C	149748	1.58	0.36	1.57	0.060	0.198	0.061	0.191
D	267910	1.58	0.36	1.57	0.060	0.199	0.061	0.191

slip boundary condition was applied (i.e., $u = v = 0$ and $\frac{\partial P}{\partial n} = 0$).

The time step was selected such that the Courant-Friedrichs-Lewy (CFL) number was less than one. A high resolution scheme was used for the advection term in the Navier-Stokes equations. For the transient term, a second order backward Euler scheme was applied. The convergence criteria was set to a RMS residual target of 10^{-4}. The computations were initialized with $u = 0$, $v = 0$, and $P = 0$ at $t = 0$. It is common to apply a perturbation to decrease computation time required to initiate vortex shedding

Table 4.3: Numerical and experimental comparison using mesh case C on a single cylinder at $Re_D = 100$.

	C_D	C'_L	St_D
Numerical	1.32	0.22	0.168
Experimental	1.26-1.35 [1, 62]	0.18-0.24 [66, 68]	0.165-0.170 [5, 69]

process [70, 71]. For the present model, the simulation was first performed on a coarse mesh (13700 nodes) to allow numerical errors to initiate the global instability in the near wake. Once the shedding process was established, the simulation was stopped, and the results were used as initial conditions for the selected refined mesh (i.e., mesh case C). All of the data was sampled after the shedding process was quasi-steady. The sample time was set to 40 vortex shedding cycles. The frequency resolution for the velocity spectra was $\pm 0.009 fD/U_0$.

4.2 Simulations at $Re_D = 2100$

Reynolds-Averaged Navier-Stokes (RANS) equations were used to model the turbulent shedding regime. RANS is commonly used in industry for modeling flows in various types of engineering applications to obtain steady state solutions. It is of interest to evaluate the performance of different turbulence models commonly used in RANS for the present geometry. For the turbulent shedding case, the same computational domain size as that used for the laminar model (Figure 4.1) was employed. The turbulence models evaluated in this study are $k - \epsilon$ [72], $k - \omega$ [73], Shear Stress Transport (SST) [74], and LRR-IP Reynolds stress models [75]. The $k - \epsilon$ model is one of the most popular models used in industry due to its fast convergence rate (i.e., low computational costs) [72]. The $k-\omega$ model is more accurate than $k-\epsilon$ when modeling separated flows; however, it requires more computational resources than the $k-\epsilon$ model [72, 73]. The SST model is a hybrid of $k-\epsilon$ and $k-\omega$ and is more accurate than both $k-\epsilon$ and $k-\omega$ [76]. The LRR-IP model requires the most computational resources out of these four models and is used to solve flows with high strain rates [75]. Direct comparisons with experimental results is performed to evaluate the accuracy of each of these turbulence models.

A mesh refinement study, similar to that in Section 4.1, was conducted using the SST model. Table 4.4 shows the results from various mesh cases. Acceptable convergence is achieved for mesh case F with the difference in the drag coefficient for each cylinder between mesh cases M and N being less than 1%, as shown in Table 4.4 and Figure 4.3. The structured mesh for case M is shown in Figure 4.4. The face sizing in the square region near the cluster was $0.012D$, resulting in approximately 260 elements on the surface of each cylinder in the cluster. Near the surface of each cylinder, 20 inflation layers with a growth rate of 1.15 were inserted. The same boundary conditions were applied to each of the surfaces in the domain as those described in Section 4.1 (Figure 4.1). For the advection term, a high resolution scheme was applied. The equations from the turbulence models are discretized using a first order upwind advection scheme. The convergence criteria was set to an RMS residual target of 10^{-4}. For all turbulence models, default values for the model coefficients set in ANSYS CFX 13.0 were used.

Mesh case M was tested by performing computations on a single cylinder for all the turbulence models investigated. Table 4.5 shows the comparison between the numerical results and experimental data. The drag results from SST and $k-\omega$ model agree well

Table 4.4: Mesh refinement study for $\alpha = 60°$ at $Re_D = 2100$ using the SST model.

Case	Nodes	C_{D_1}	C_{D_2}	C_{D_3}
A	251314	0.901	0.317	0.887
B	317482	0.909	0.331	0.904
C	384094	0.930	0.341	0.909
D	467006	0.967	0.346	0.943
E	541560	0.950	0.362	0.953
F	630526	0.992	0.372	0.991
G	686294	0.983	0.380	0.993
H	742966	0.972	0.380	0.989
I	789600	0.964	0.375	0.966
J	824626	0.944	0.385	0.960
K	869568	0.950	0.382	0.951
L	905140	0.940	0.386	0.951
M	938586	0.950	0.387	0.953
N	978794	0.946	0.384	0.949

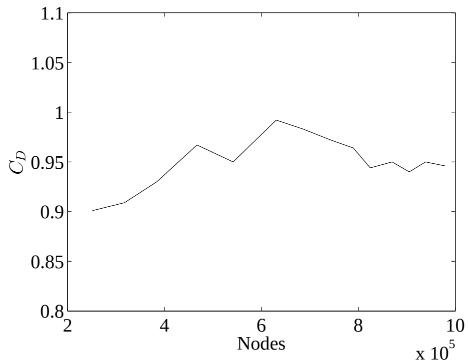

(a) Cylinder 1

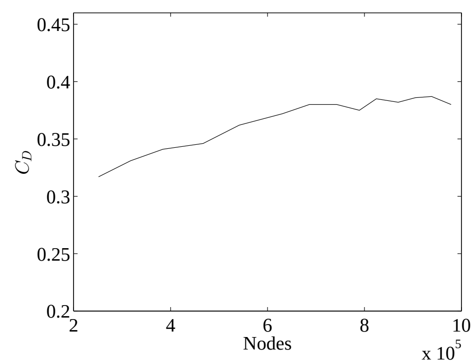

(b) Cylinder 2

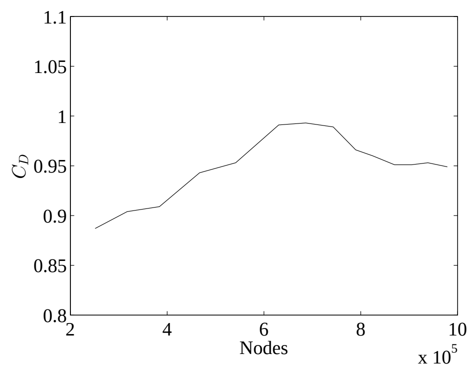

(c) Cylinder 3

Figure 4.3: Mesh convergence for each cylinder for $\alpha = 60°$.

(within 3%) with experimental data. The errors for the $k - \epsilon$ and LRR-IP models are approximately 10%. Despite the errors with the $k - \epsilon$ and LRR-IP models, it is of interest to evaluate the performance of all four turbulence models for the present study.

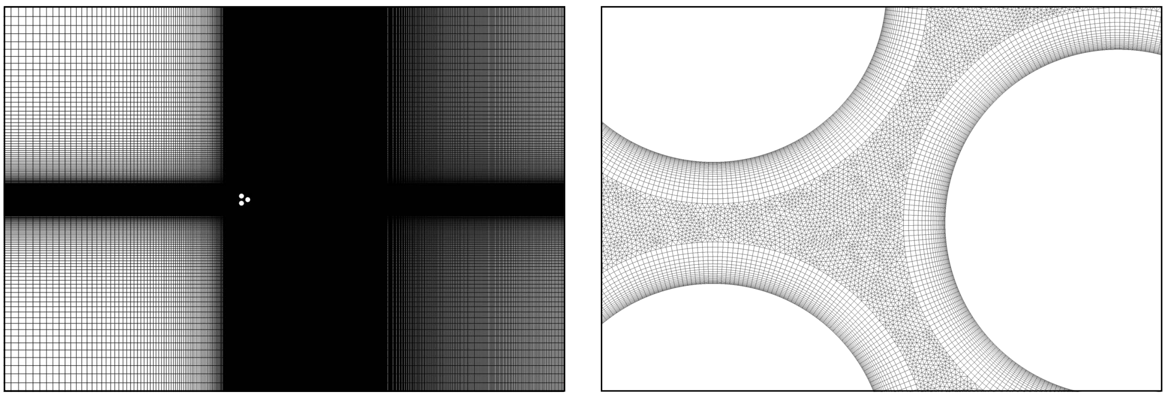

(a) Full domain

(b) Near the cluster

Figure 4.4: RANS model computational mesh.

Table 4.5: Validation of turbulence models on a single cylinder case.

	SST	$k-\epsilon$	$k-\omega$	LRR-IP	Experimental [77]
C_D	0.90	0.85	0.94	1.01	0.92
Error [%]	1.2	7.6	2.5	10.2	-

Chapter 5

Experimental results

In this chapter, the results of flow visualization experiments and quantitative velocity measurements are analyzed and discussed. All experiments were performed at $Re_D = 2100$, $P/D = 1.35$, and for $0° \leq \alpha \leq 60°$. First, an overview of flow development from qualitative flow visualization is provided in Section 5.1. Section 5.2 illustrates the mean flow characteristics and Root-Mean-Square (RMS) contours of the streamwise and transverse velocity component for all orientations investigated. Vortex shedding in the cluster wake is visualized using time sequences of vorticity contours in Section 5.3. Also, Section 5.3 studies shedding frequency of vortex structures in the wake of the cluster using LDV measurements. For further insight, wake regions corresponding to such frequency-centered activities are investigated using spectral energy maps from PIV measurements for various band-pass filtered frequencies. Lastly, POD analysis is performed in Section 5.4 to analyze energy content of periodic structures in the wake and visualize near-wake development.

5.1 Flow visualization

Figures 5.1 to 5.8 depict flow visualization image sequences of the cluster wake development for a full shedding cycle of the large scale structures for each cluster orientation. The image sequences show large scale vortex shedding beyond $x/D \approx 5$ for all orientation angles. Behind the two most downstream cylinders, two asymmetric wakes are present for all α, except for $\alpha = 60°$. The gap flow exiting the cluster (i.e., flow exiting from between the two most downstream cylinders) is deflected towards one side of the wake axis, resulting in a narrow and wide wake behind the cluster. In the vicinity of the cluster, notable differences in the flow development occur for each cluster orientation.

At $\alpha = 0°$, the most evident observation is the presence of a bistable wake development behind the two downstream cylinders (labeled as cylinders 1 and 2 in Figures 5.1a and 5.2a). Specifically, two quasi-steady wake configurations exist, each consisting of two different sized wakes behind the cluster. Figures 5.1 and 5.2 show both of these configurations, with the gap flow (or jet flow) being directed towards the wake of either of the two downstream cylinders. In Figure 5.1, the gap flow is directed towards the wake of cylinder 2, resulting in a wide wake behind cylinder 1 and a narrow wake behind cylinder 2. The opposite behavior is observed for the other configuration (Figure 5.2). This bistable wake behavior was also reported by Lam & Cheung [12], who studied flow over equispaced triangular cluster of three cylinder using flow visualization via dye injection. It should be noted that during experiments, no intermittent switching between the two bistable wake configurations occurred. Both bistable cases for $\alpha = 0°$ were achieved in two different ways. The first approach involved starting and shutting down the water supply. The initial conditions of the setup deflect the gap flow to one side of the wake axis, resulting in one of the bistable wake configurations. Multiple iterations of this approach showed presence of both bistable wake configurations at $\alpha = 0°$. The second method involved rotating the cluster, with the water supply on, from $\alpha = \pm 10°$ to $\alpha = 0°$. For example, if the cluster is rotated from $\alpha = 10°$ to $0°$, the narrow and wide wakes would form behind cylinder 1 and cylinder 2, respectively, for $\alpha = 0°$, similar to $\alpha = 10°$ (Figure 5.3). The origin of this bistable phenomenon is still unknown. Lam & Cheung [12] suggested that the onset of this instability is strongly dependent on the small deflection or disturbance in the gap flow caused by the initial conditions of the experiment. A small deflection disrupts the balance of vorticity between the inner shear layers of cylinders 1 and 2, resulting in an increase of vorticity towards one side. The presence of a narrow and wide wake results in different wake vortex dynamics on either side of the wake axis ($y = 0$). For example, in Figure 5.1, large and small scale structures are present on either side of the wake axis. The leftmost separated shear layer rolls up into a vortex at $x/D \approx 5$ & $y/D \approx 1$, which is then shed downstream, as shown in the image sequence in Figure 5.1. On the opposite side of the wake, formation of smaller scale vortices occur at $x/D \approx 2$ & $y/D \approx -1$, which result in complex vortex interactions at the interface between the narrow and wide wakes. The narrow wake produces vortex structures ($\approx 0.5D$ in diameter) which are smaller in size and shed at a higher frequency compared to the larger structures on the opposite side of the cluster wake. However, on both sides of the cluster wake, vortices form from the outer shear layers of cylinders 1 and 2 within $2 < x/D < 5$ and show oscillatory wake behavior reminiscent of a bluff body shedding at and beyond $x/D \approx 5$.

As the orientation angle is increased to $\alpha = 10°$, the bistable wake phenomenon is no longer present (Figure 5.3). The asymmetry in the cluster geometry directs the gap flow towards the wake of cylinder 1, producing a narrower wake behind cylinder 1 as compared to that behind cylinder 2 (Figure 5.3). The right shear layer bounding the wide wake (i.e., the rightmost shear layer) sheds large scale vortices which do not interact with the small scale structures forming on the opposite side of the wide wake. It should be noted that the shear layers bounding the wide wake originate from the surface of cylinder 3 (Figure 5.3). These shear layers do not reattach to the surface of cylinder 2. This configuration represents the fully shield case ($\alpha = \alpha_s$) [12], in which cylinder 2 is fully shielded by the separated shear layers of cylinder 3. This result agrees with the findings of Lam & Cheung [12], who found α_s to range from $8° - 10°$ for the present spacing ratio ($P/D = 1.35$) and Reynolds number ($Re_D = 2100$).

For $\alpha = 20°$ to $60°$, the asymmetry in the wake development about the wake axis (i.e., $y = 0$) decreases with increasing α (Figures 5.4 to 5.8). Specifically, the streamwise extent of the recirculation region behind cylinder 1 decreases with increasing α. For $\alpha = 60°$, the wake development is symmetric about $y = 0$ with two equally sized recirculation regions behind the two upstream cylinders.

In particular, for $\alpha = 30°$, the image sequences show Kelvin-Helmholtz vortices within the separated shear layers of cylinder 2 (Figures 5.5d and 5.5e). This shear layer instability occurs for the case of single circular cylinders in the shear layer transition flow regime ($1 \times 10^4 < Re_D < 2 \times 10^5$) [17,19]. Also, the flow visualization results show that the separated shear layers of cylinder 2 flap periodically (at the large scale shedding frequency) in the transverse direction. During the flapping cycle, the Kelvin-Helmholtz vortices are present when the separated shear layers are approximately parallel to the free-stream direction, as illustrated in the sequence of images in Figure 5.5. These Kelvin-Helmholtz vortices were only observed for the case of $\alpha = 30°$.

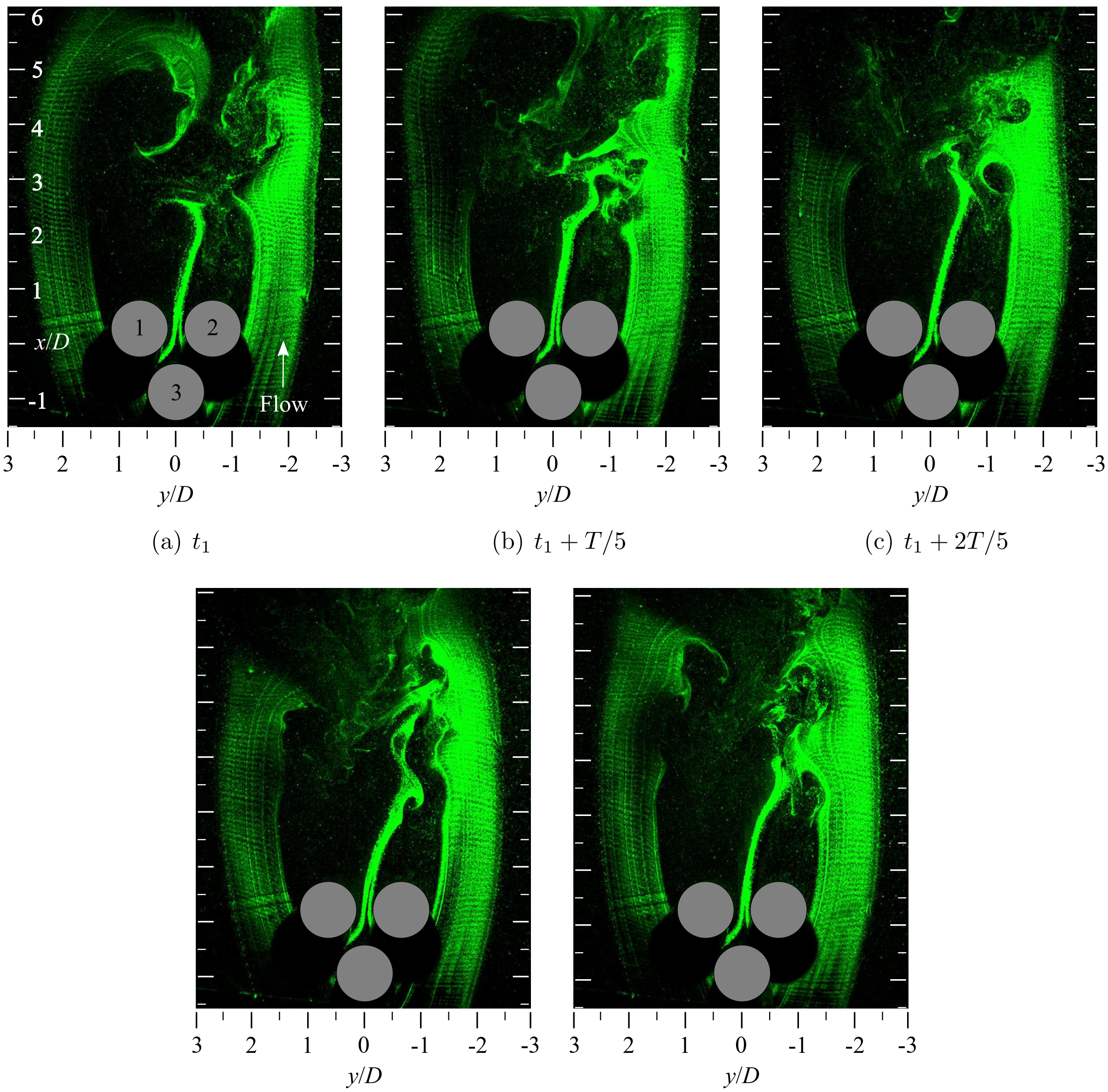

(a) t_1

(b) $t_1 + T/5$

(c) $t_1 + 2T/5$

(d) $t_1 + 3T/5$

(e) $t_1 + 4T/5$

Figure 5.1: Flow visualization of the cluster wake development at $\alpha = 0°$ with the gap flow directed towards the wake of cylinder 2. T is the shedding period of the large scale structures.

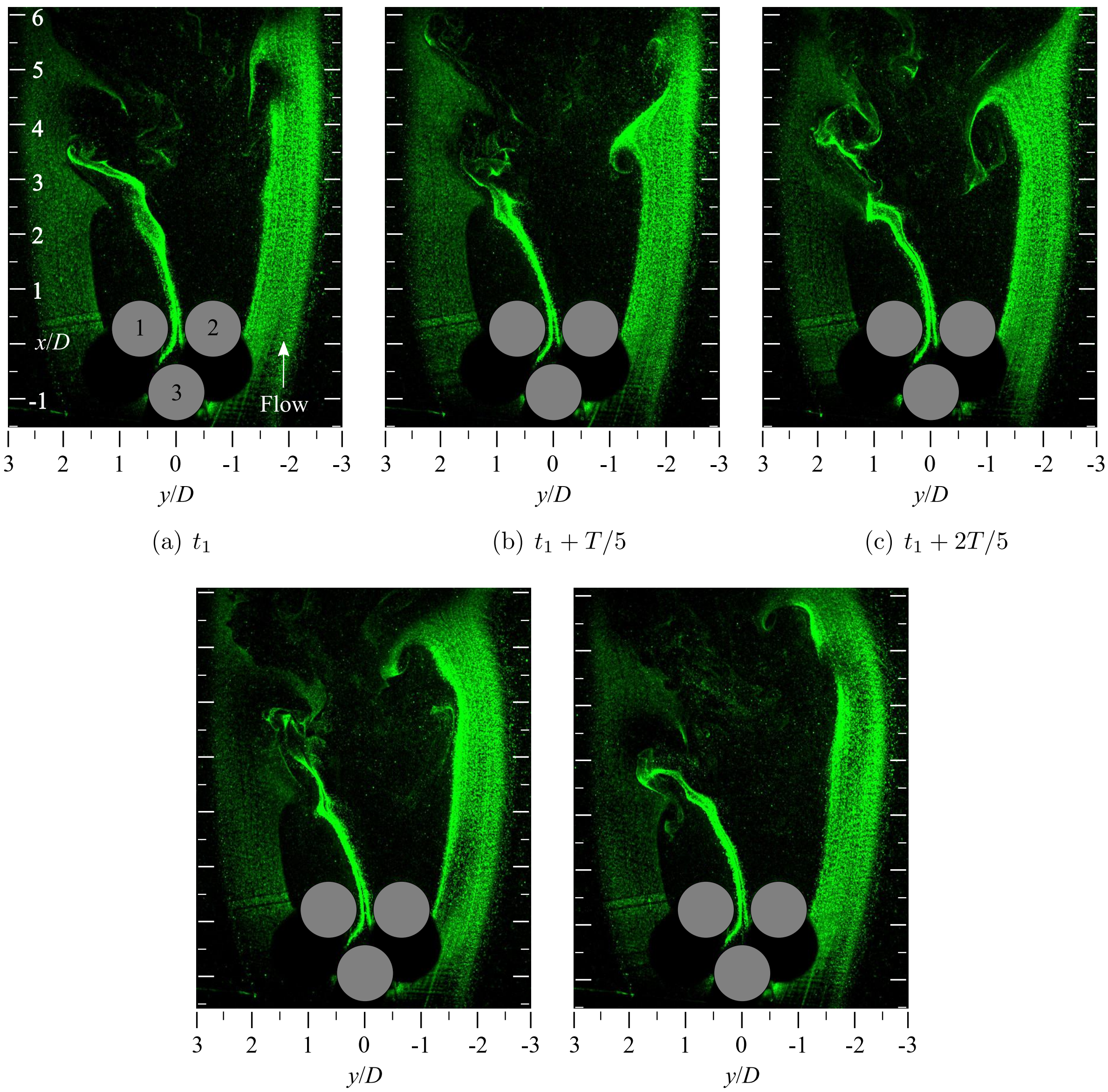

(a) t_1 (b) $t_1 + T/5$ (c) $t_1 + 2T/5$

(d) $t_1 + 3T/5$ (e) $t_1 + 4T/5$

Figure 5.2: Flow visualization of the cluster wake development at $\alpha = 0°$ with the gap flow directed towards the wake of cylinder 1.

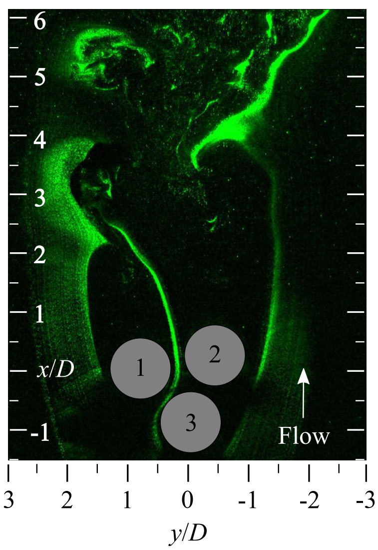

(a) t_1

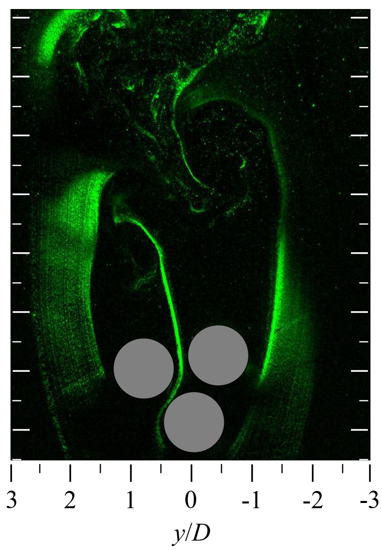

(b) $t_1 + T/5$

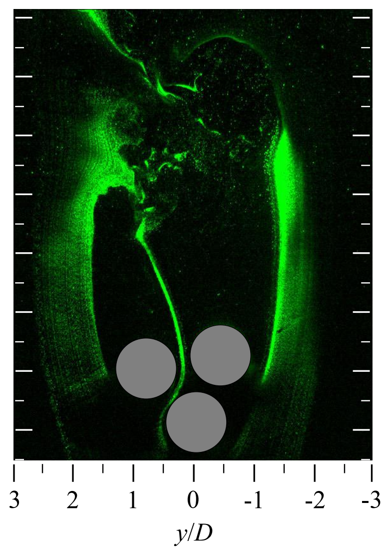

(c) $t_1 + 2T/5$

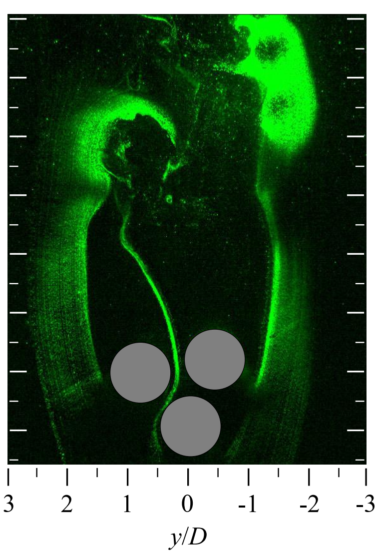

(d) $t_1 + 3T/5$

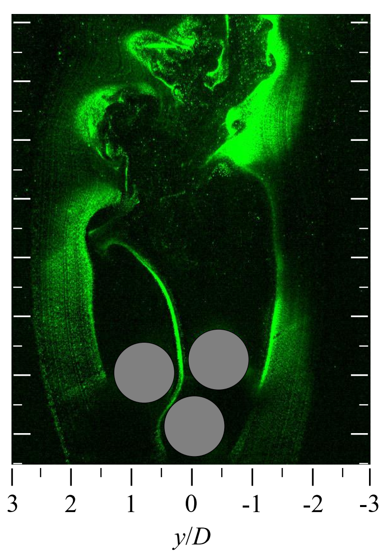

(e) $t_1 + 4T/5$

Figure 5.3: Flow visualization of the cluster wake development at $\alpha = 10°$.

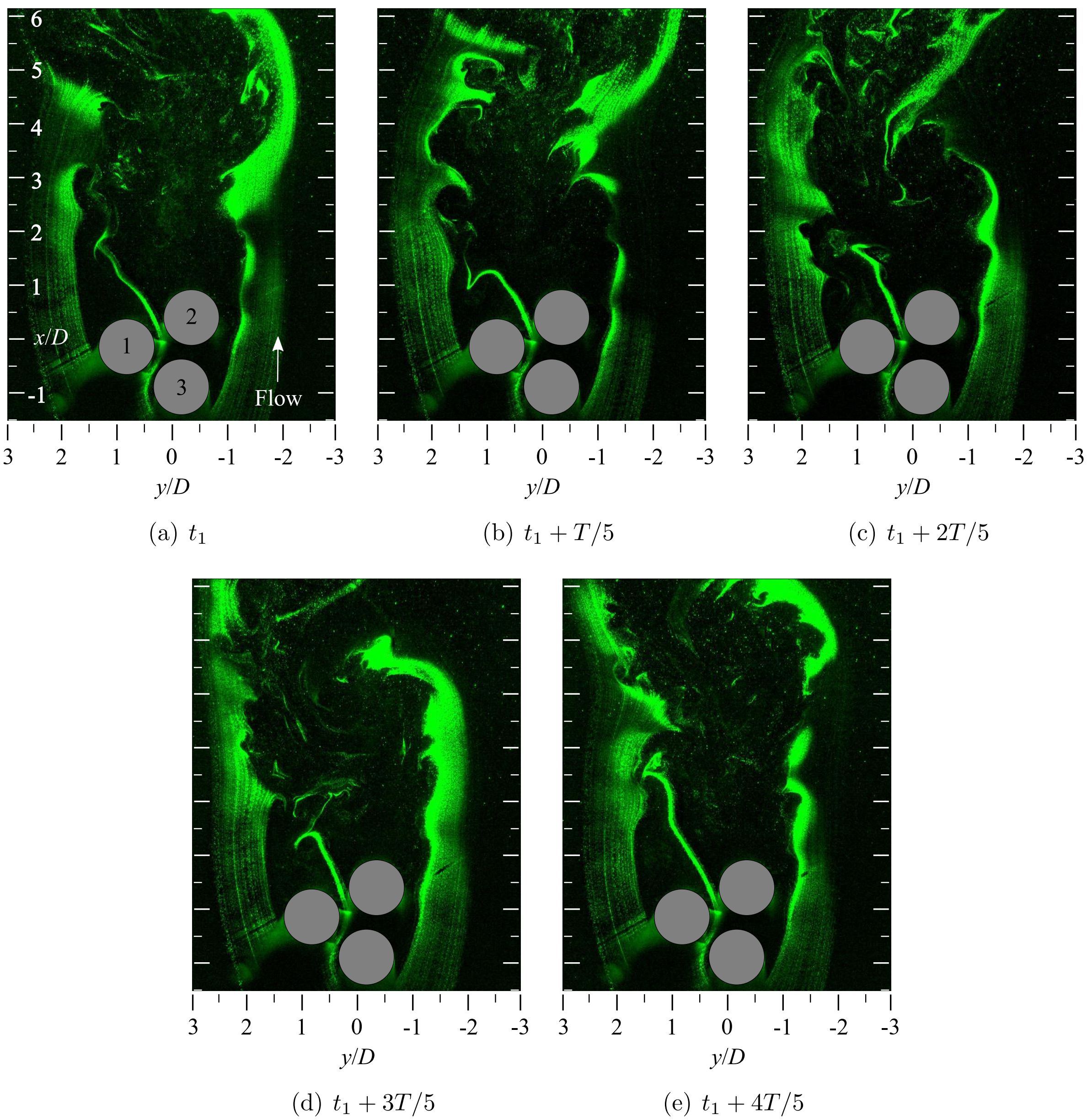

Figure 5.4: Flow visualization of the cluster wake development at $\alpha = 20°$.

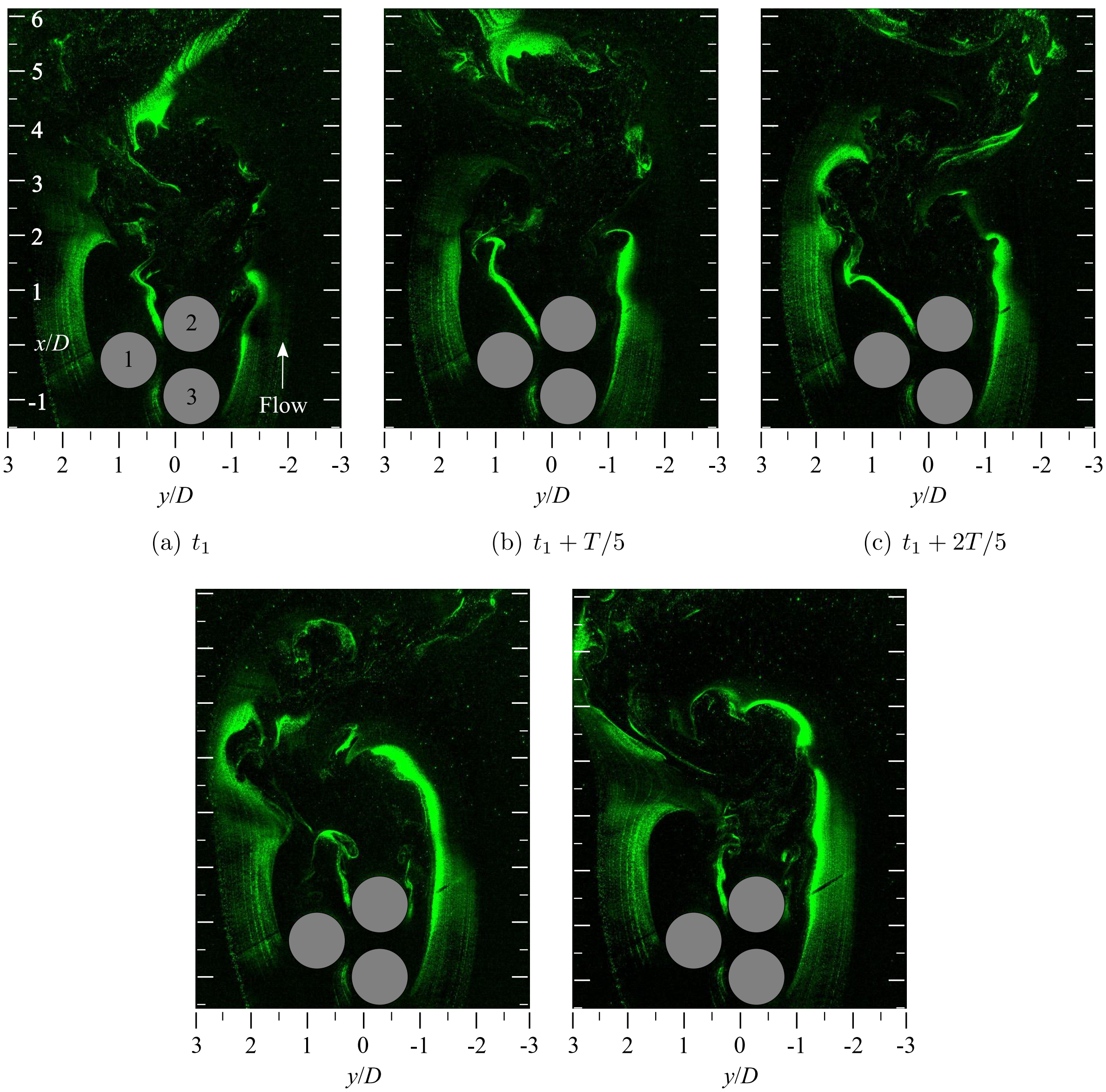

(a) t_1

(b) $t_1 + T/5$

(c) $t_1 + 2T/5$

(d) $t_1 + 3T/5$

(e) $t_1 + 4T/5$

Figure 5.5: Flow visualization of the cluster wake development at $\alpha = 30°$.

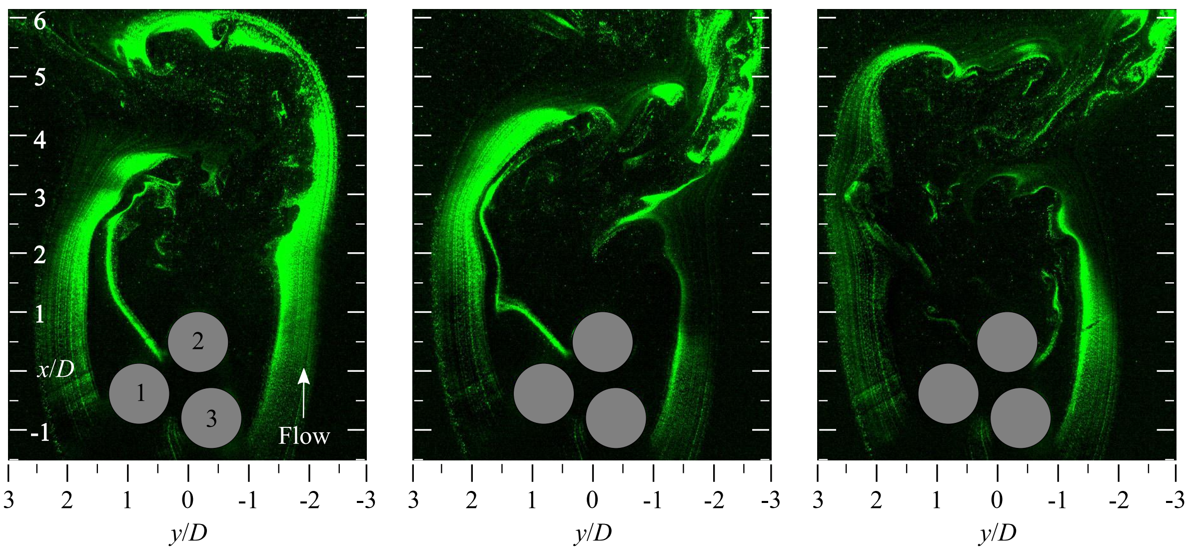

(a) t_1 (b) $t_1 + T/5$ (c) $t_1 + 2T/5$

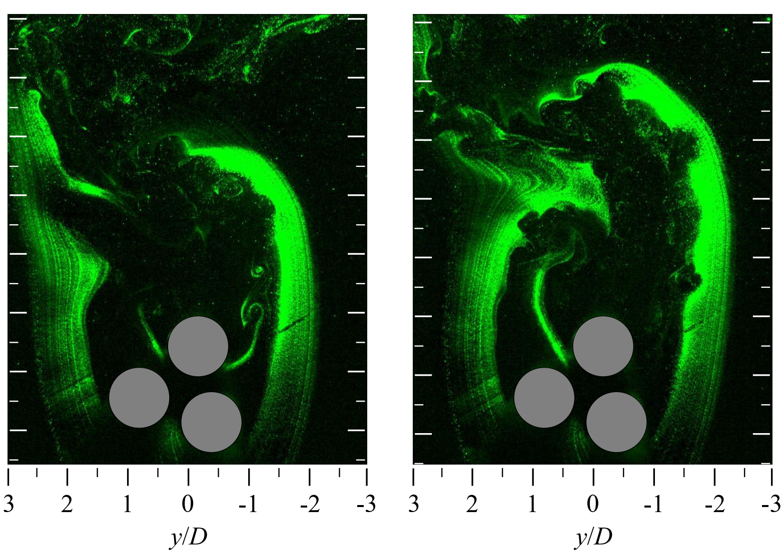

(d) $t_1 + 3T/5$ (e) $t_1 + 4T/5$

Figure 5.6: Flow visualization of the cluster wake development at $\alpha = 40°$.

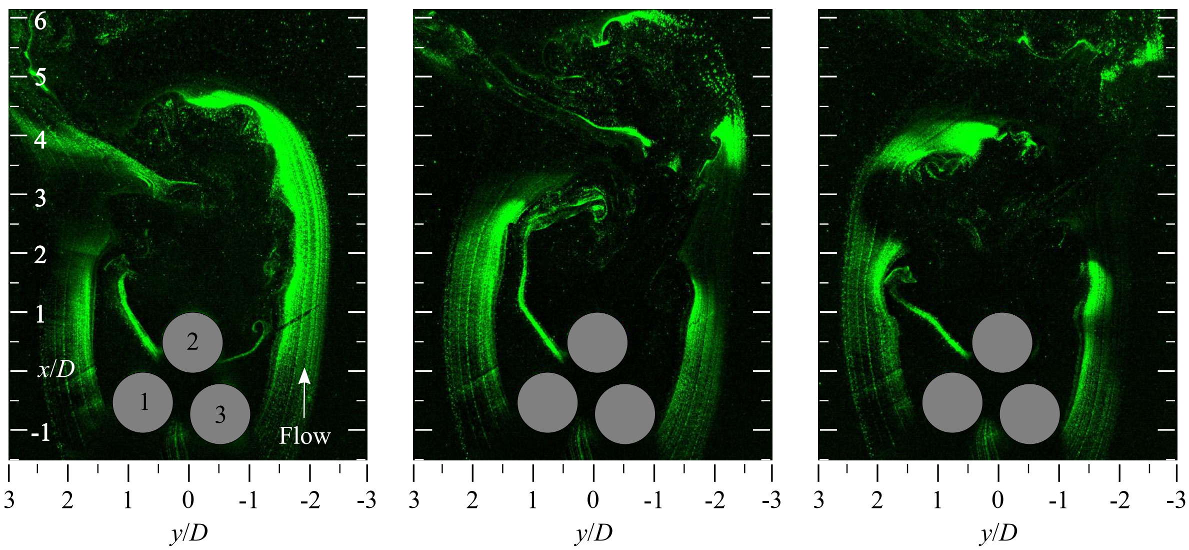

(a) t_1 (b) $t_1 + T/5$ (c) $t_1 + 2T/5$

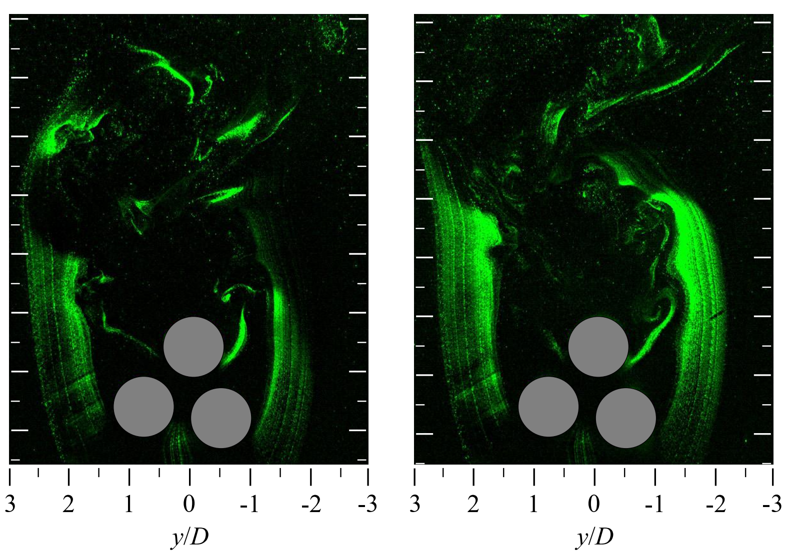

(d) $t_1 + 3T/5$ (e) $t_1 + 4T/5$

Figure 5.7: Flow visualization of the cluster wake development at $\alpha = 50°$.

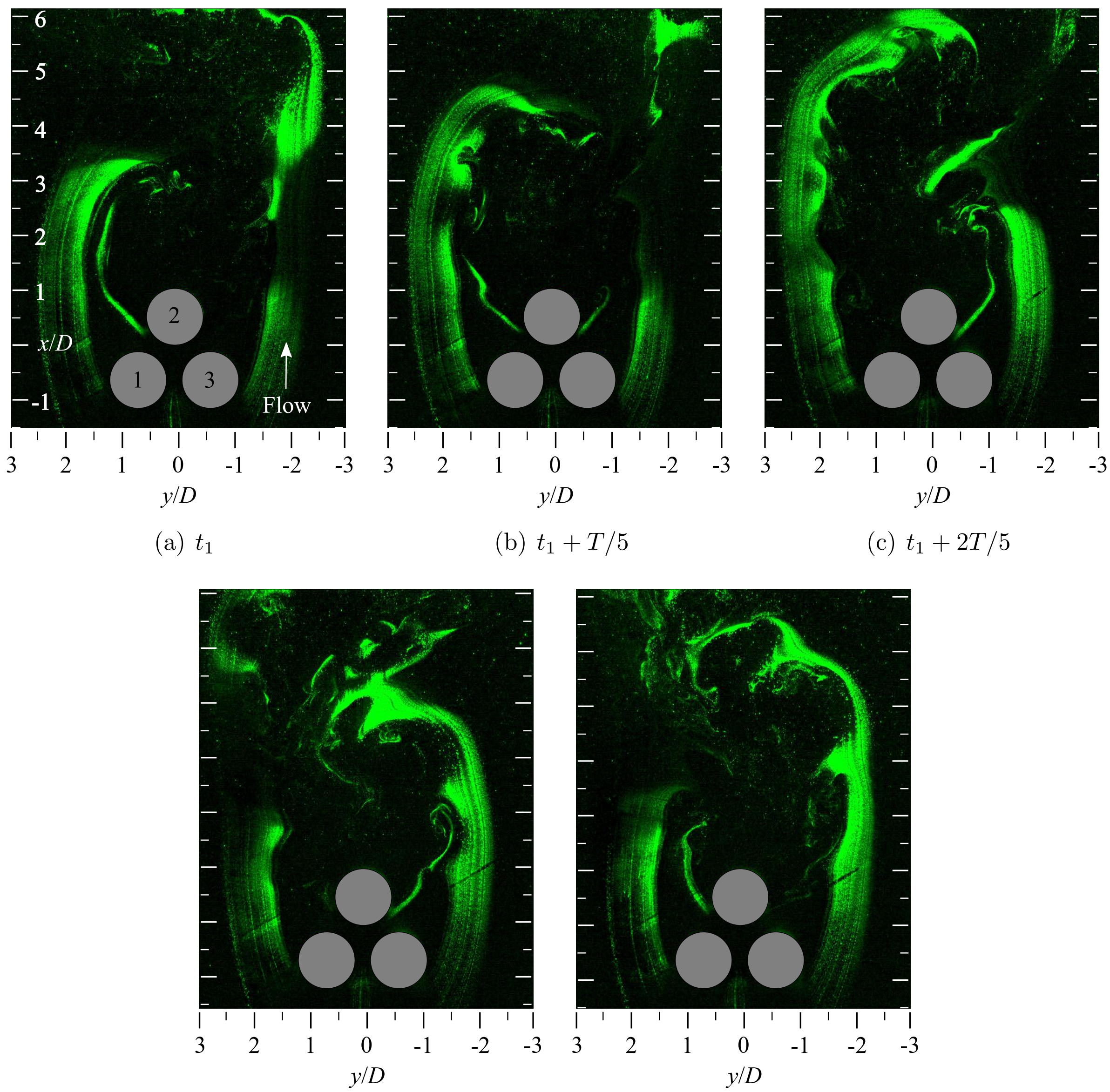

(a) t_1

(b) $t_1 + T/5$

(c) $t_1 + 2T/5$

(d) $t_1 + 3T/5$

(e) $t_1 + 4T/5$

Figure 5.8: Flow visualization of the cluster wake development at $\alpha = 60°$.

5.2 Mean flow statistics

Figure 5.9 shows the mean streamwise velocity contours for all cluster orientations. All cluster orientations investigated, except for $\alpha = 60°$, show an asymmetric wake development about $y = 0$. The degree of asymmetry in the wide and narrow wakes is correlated with the orientation of the high-speed jet relative to the free-stream direction. The results show that, with increasing α from $0°$ to $60°$, the streamwise extent of the recirculation region behind cylinder 1 decreases from $x/D \approx 2.5$ to $x/D \approx 1$ and the streamwise extent of the recirculation region behind cylinder 3 increases from $x/D \approx 0$ to $x/D \approx 1$, respectively. The two quasi-steady wake configurations for $\alpha = 0°$ are illustrated in Figures 5.9a and 5.9b. The results show the two bistable flow regimes observed at $\alpha = 0°$, with the high-speed jet directed towards either of the two downstream cylinders. For $\alpha = 30°$, cylinders 2 and 3 are in a tandem arrangement (relative to the flow direction). Previous studies (e.g., [13, 24, 27]) show that, for the case of two tandem cylinders in cross-flow under the present operating conditions (i.e., $P/D = 1.35$ and $Re_D = 2.1 \times 10^3$), cylinder 2 is bounded by the separated shear layers of cylinder 3. However, for the cluster of three cylinders at $\alpha = 0°$, cylinder 2 is not shielded by the shear layers of cylinder 3 (Figure 5.9e). For the three cylinder cluster, the shielded cases occurs at $\alpha = 10°$. The difference is attributed to the presence of cylinder 1, causing the formation of high-speed jet that displaces the recirculation region behind cylinder 3 towards the right side of the wake axis ($y = 0$).

Figure 5.10 shows the streamwise extent of the recirculation region of the wide and narrow wakes for all the cluster orientations investigated. The length of the recirculation region, L_f, is defined as the distance from the cluster origin to the furthest downstream location where zero mean velocity in the narrow and wide wakes occurs. For the narrow wake (i.e., the wake of cylinder 1), L_f decreases as the angle is increased from $\alpha = 10°$ to $60°$. For the wide wake (i.e., the wake of cylinder 2), L_f decreases as the angle is increased from $\alpha = 10°$ to $40°$ and then increases again from $\alpha = 40°$ to $60°$. In both cases, L_f decreases from $\alpha = 10°$ to $0°$. For the narrow wake, the observed trend can be explained by the change in the trajectory of the jet exiting between cylinders 1 and 2 with increasing α. As α increases from $0°$ to $60°$, the angle between the jet and y-axis increases, which results in delayed separation of the inner shear layer of cylinder 1. This decreases the streamwise extent of the recirculation region of the narrow wake. For the wide wake, the changes in L_f can be explained by the change in the projected height of the cluster, D_h, and flow rate, Q, through the gap in the cluster, $D_g = P - D$, with increasing α. Figure 5.11 shows the variation in D_h and Q with α. On one hand, the streamwise extent of the recirculation region is proportional to the solid blockage of the cluster, D_h, similar to bluff body flows for $350 < Re_D < 3.2 \times 10^3$ [17]. On the other hand, similar to flow over porous bodies with bleed flow [78–80], the streamwise extent of the recirculation region is expected to be inversely proportional to the flow rate through the cluster. For α increasing from $10°$ to $30°$, D_h decreases and Q increases (Figure 5.11), so that the length of the recirculation region for the wide wake decreases, as expected. For α increasing from $30°$ to $60°$, both D_h and Q increase (Figure 5.11), producing two competing effects on L_f. While D_h is minimum at $\alpha = 30°$, the presence of the bleed flow through the cluster shifts the minimum L_f to $\alpha = 40°$. The variation of flow rate through the cluster also explains the change in L_f between $10°$ to $0°$ (Figure 5.10). Compared to $\alpha = 10°$, there is increased flow rate through the cluster at $\alpha = 0°$ (Figure 5.11), causing a decrease in L_f observed in

Figure 5.10.

The comparison of the wake width with respect to the downstream distance and the cluster orientation is presented in Figure 5.12. The parameter used to quantify the width of wake is the half wake width, b. The half wake width is defined as the transverse distance between two points on the velocity profile where the streamwise velocity deficit is equal to 50% of the maximum local velocity deficit [81]. Figure 5.12a shows that the wake width increases with x/D and scales approximately with $\sqrt{x}$, similar to the trend expected for far wakes of bluff bodies [81]. Figure 5.12b illustrates the variation in b with increasing α at two different downstream locations. The width of the wake is proportional to D_h (i.e., the vertical extent of the cluster) (Figure 5.11). As the physical blockage of the cluster increases, the wake width also increases, and vice versa.

The contours of the RMS of the streamwise and transverse velocity components for all α are shown in Figures 5.13 and 5.14, respectively. For the streamwise component, several regions of high velocity fluctuations are present for all orientations within $1 < x/D < 3$ and further downstream ($x/D > 3$). For $x/D > 3$, two regions of high velocity fluctuations are present on both sides of the wake axis. These fluctuations are produced due to the formation and shedding of the large scale vortical structures, seen in qualitative and quantitative visualizations. On the average, the maximum magnitude of these velocity fluctuations increases with increasing α. Immediately downstream of the cluster, notable velocity fluctuations occur within the shear layers bounding the narrow wake and the inner shear layer of the wide wake. According to the flow visualization, these velocity fluctuations are associated with the shedding of small scale vortices. On the average, the maximum magnitude of the velocity fluctuations within the shear layers bounding the narrow wake of cylinder 3 increases with increasing α. For the transverse RMS component (Figure 5.14), high velocity fluctuations are present in the shear layers bounding the narrow wake ($1 < x/D < 3$) and further downstream ($x/D > 3$) along the wake center line. For $x/D > 3$, high transverse velocity fluctuations are induced by large scale shedding. For $1 < x/D < 3$, high transverse velocity fluctuations are produced due to small scale vortex shedding, seen in the flow visualization. Both the streamwise and transverse RMS figures for $\alpha = 60°$ and $x/D > 1.5$ are similar to that of a single cylinder [82].

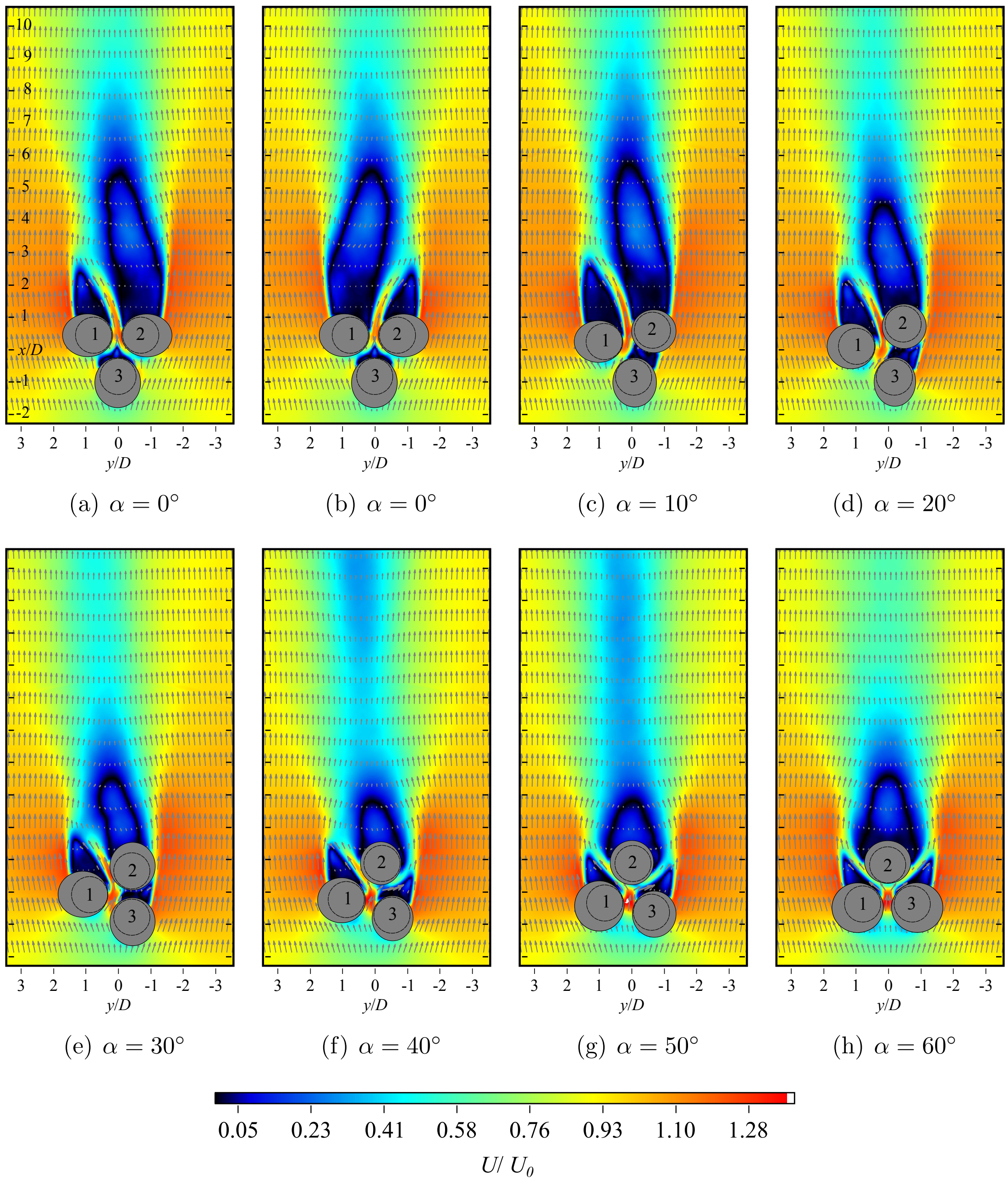

Figure 5.9: Mean streamwise velocity contours with velocity vectors. Masked region is shaded in gray and cylinder contours are outlined by dashed black lines.

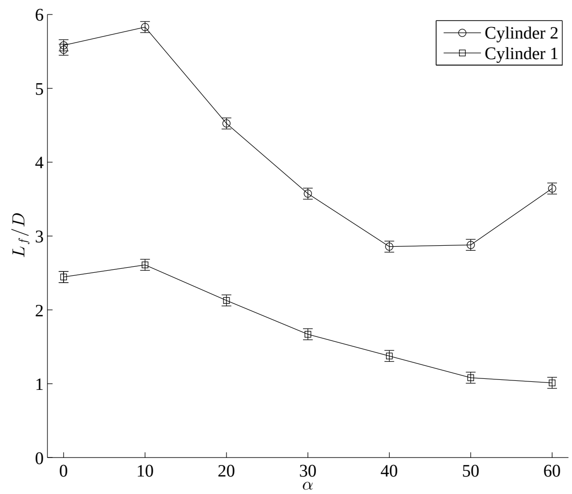

Figure 5.10: Length of the recirculation region of cylinder 1 and 2 wakes for all α. The length is defined as the streamwise distance from the cluster origin to the most downstream point of zero velocity.

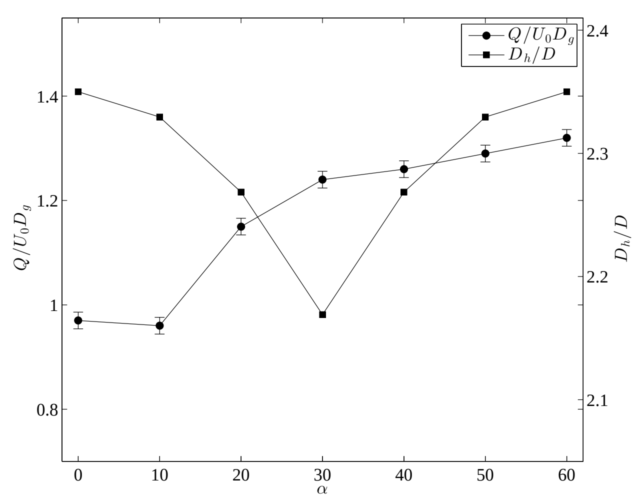

Figure 5.11: Variation of D_h and flow rate through the cluster, Q, with respect to α.

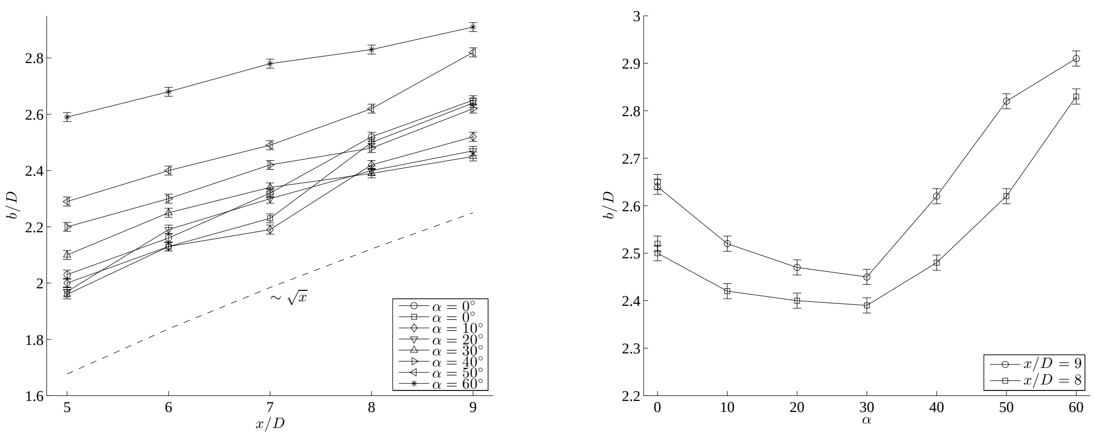

(a) (b)

Figure 5.12: Variation of half wake width with respect to (a) x/D and (b) α.

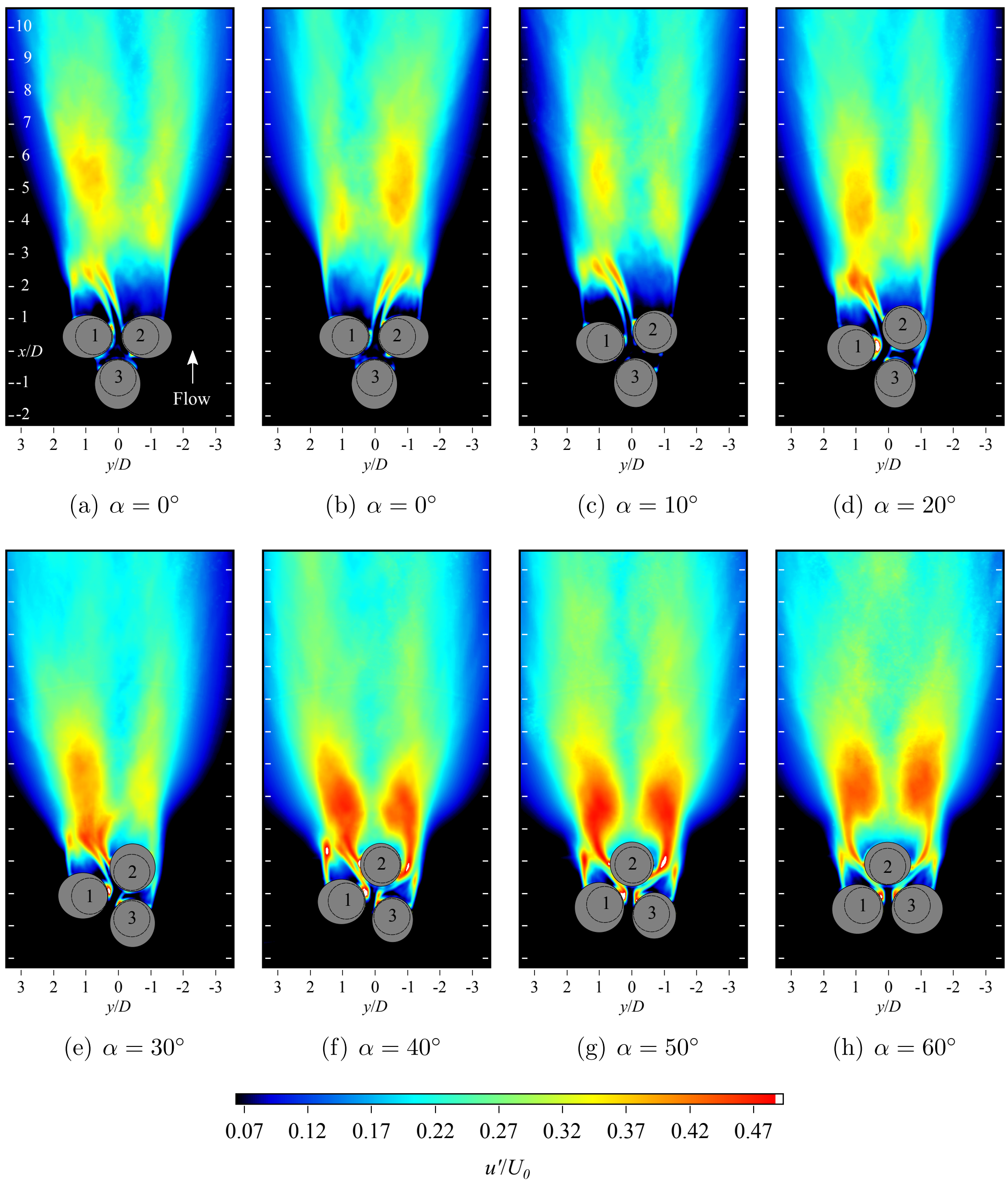

Figure 5.13: RMS contours of the streamwise velocity. Masked region is shaded in gray and cylinder contours in the measurements plane are outlined by dashed black lines.

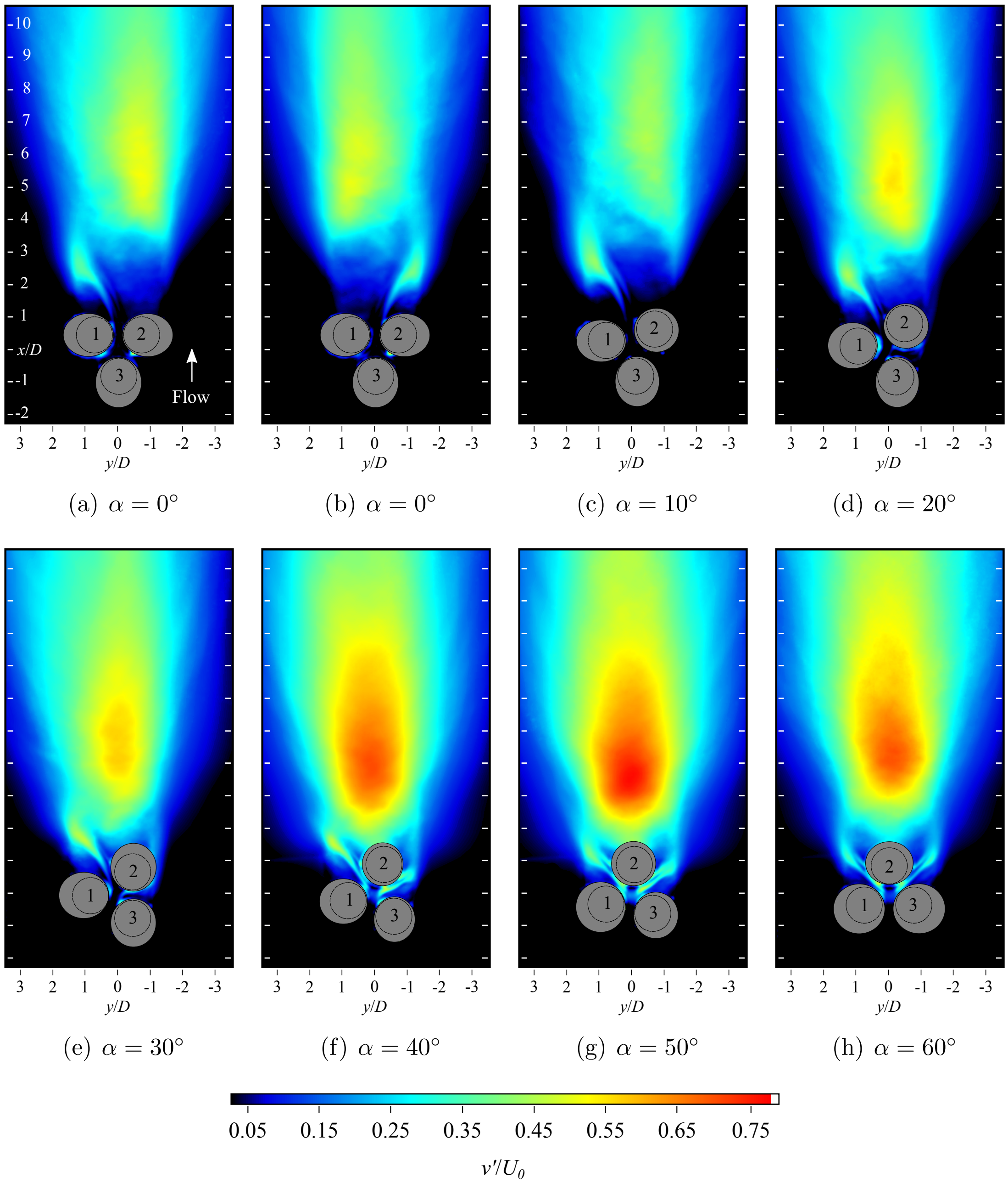

(a) $\alpha = 0°$ (b) $\alpha = 0°$ (c) $\alpha = 10°$ (d) $\alpha = 20°$

(e) $\alpha = 30°$ (f) $\alpha = 40°$ (g) $\alpha = 50°$ (h) $\alpha = 60°$

Figure 5.14: RMS contours of the transverse velocity.

5.3 Characteristics of coherent structures

Figures 5.15-5.17 and A.1-A.5 show a sequence of instantaneous vorticity fields for one large scale shedding cycle for all angles investigated. For all α, periodic large scale and smaller scale shedding occur in the cluster wake, similar to the qualitative visualizations discussed in Section 5.1. Large and smaller scale vortices are produced due to the roll up of the shear layers bounding the wide and narrow wakes, respectively. For all orientations, large scale shedding is observed at and beyond $x/D = 5$. In all asymmetric cases, more coherent large scale vortices are formed on the opposite side of the high-momentum jet direction. On the side of the jet direction, smaller scale vortices are produced due to the roll up of shear layers bounding the narrow wake. These smaller scale vortices merge with the shear layer of the wide wake of same vorticity sense, producing weaker large scale vortices, compared to the ones forming on the opposite side of the wake axis.

Instantaneous vorticity fields for the bistable configuration at $\alpha = 0°$ are shown in Figures 5.15 and 5.16. When the jet is directed towards cylinder 2 (Figure 5.15), the outer shear layer of the wide wake starts to roll up at approximately $x/D = 3$ (Figure 5.15b). The vortex grows to a size of approximately $1.5D$ just before it is shed, as seen in Figure 5.15d. The large scale structures on the opposite side of the wake are produced due to the roll up the inner shear layer of the wide wake and its interaction with smaller scale vortices shed from the narrow wake of cylinder 2. The small scale vortices grow to a size of approximately $0.3D$ and are shed at $x/D \approx 2.5$ (Figure 5.15c). The interaction between the inner shear layer of the wide wake and the small scale vortices is discussed in detail in Section 5.4. The large scale vortices on this side of the wake axis consists of smaller scale structures. These large scale structures are weaker than the ones formed on the opposite side of the wake axis. Both structures on either side of the wake axis are shed periodically at the same frequency. On the average, the size of the large scale structures forming from the outer shear layers of the wide wake decreases with increasing α until $\alpha = 30°$, and then increases with increasing α for $30° \leq \alpha \leq 60°$. For the smaller scale structures shed from the narrow wake, their size decreases with increasing α for $0° \leq \alpha \leq 60°$. This variation in the size of the large scale and smaller scale vortices correlates with the variation of the length of the formation region of the wide and narrow wakes with α (Figure 5.10). At $\alpha = 60°$ (Figure 5.17), both large scale structures on either side of the wake axis are symmetric and consist of smaller scale structures that are shed from the narrow wakes at $x/D \approx 1$.

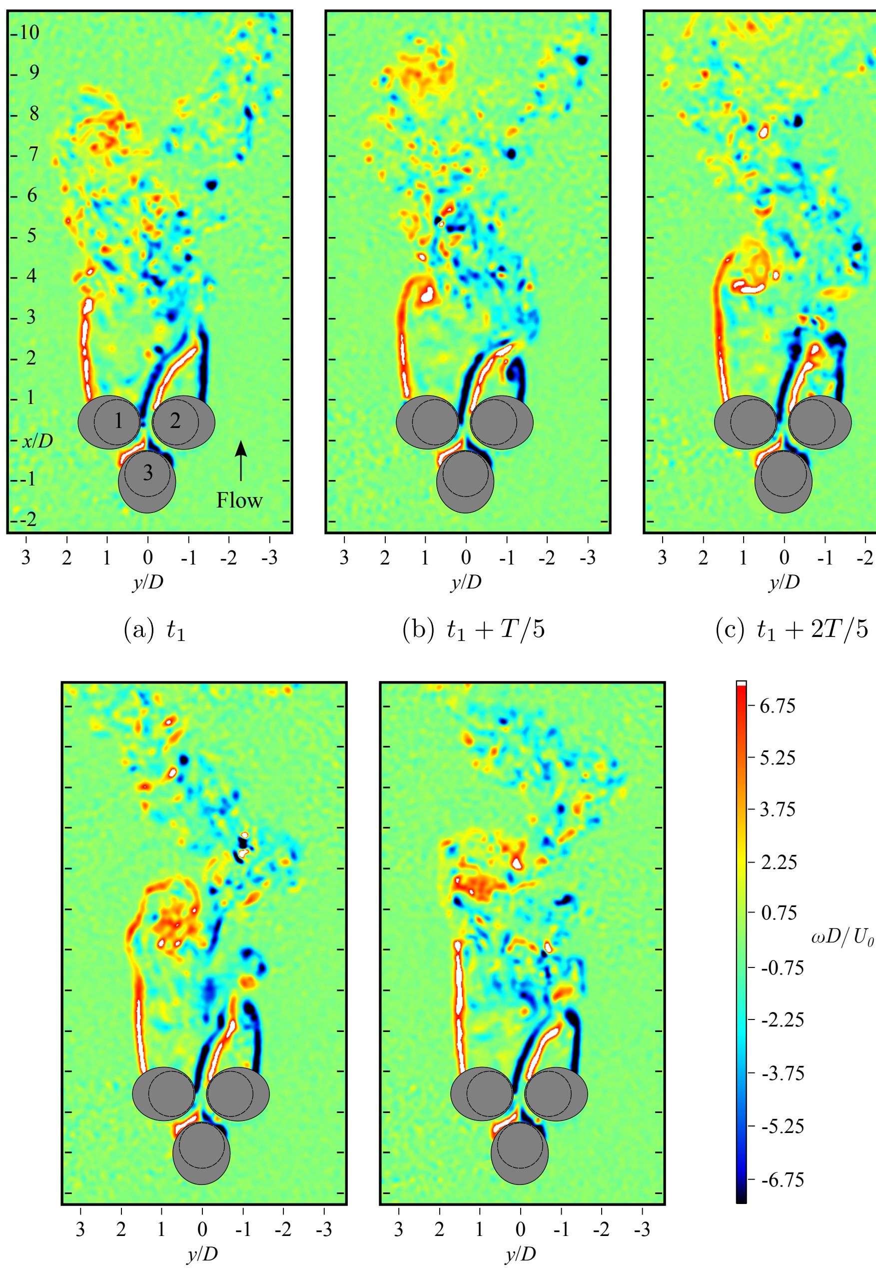

(a) t_1 (b) $t_1 + T/5$ (c) $t_1 + 2T/5$

(d) $t_1 + 3T/5$ (e) $t_1 + 4T/5$

Figure 5.15: Vorticity contours for $\alpha = 0°$ with the gap flow directed towards cylinder 2.

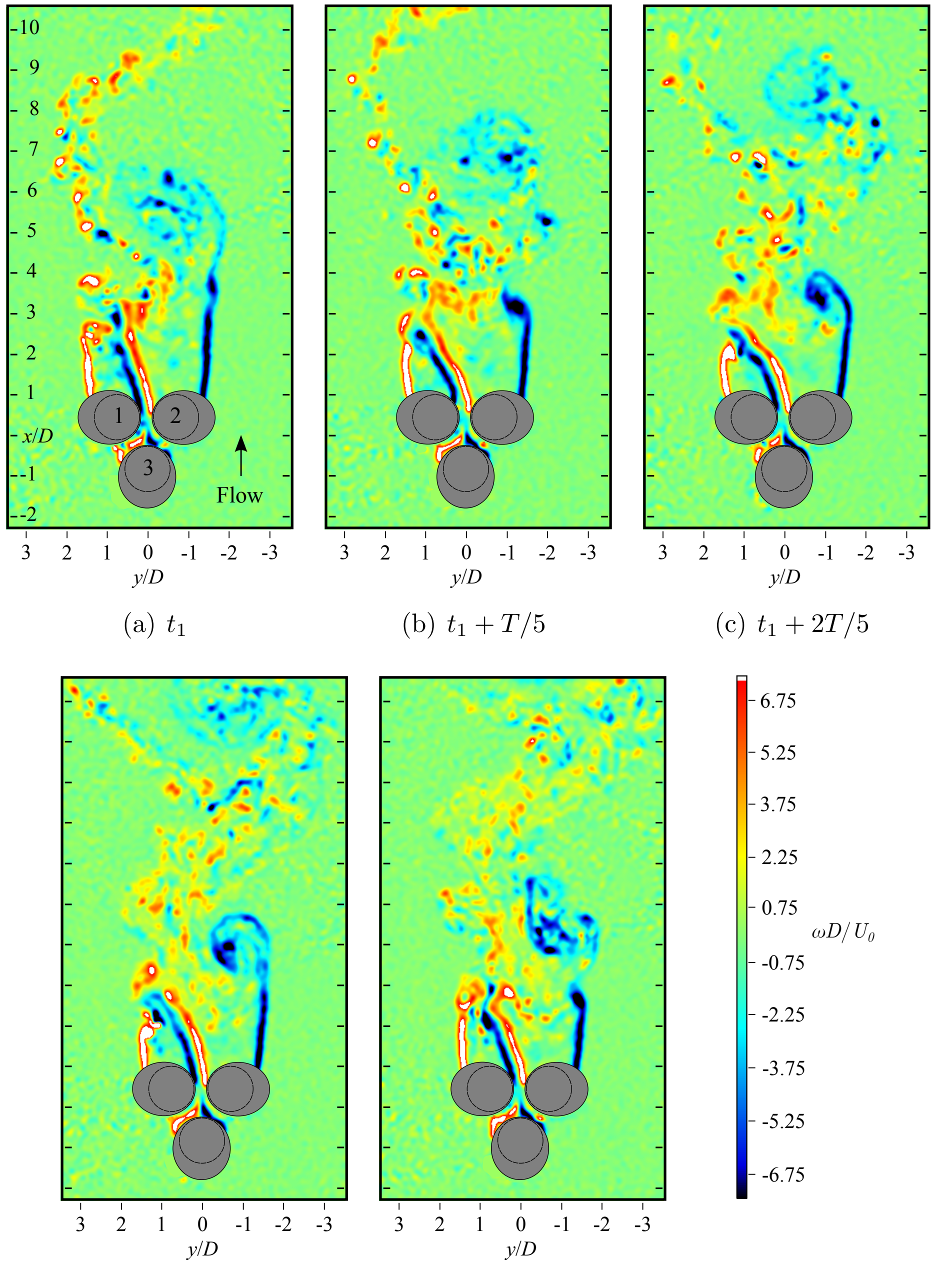

(a) t_1

(b) $t_1 + T/5$

(c) $t_1 + 2T/5$

(d) $t_1 + 3T/5$

(e) $t_1 + 4T/5$

Figure 5.16: Vorticity contours for $\alpha = 0°$ with the gap flow directed towards cylinder 1.

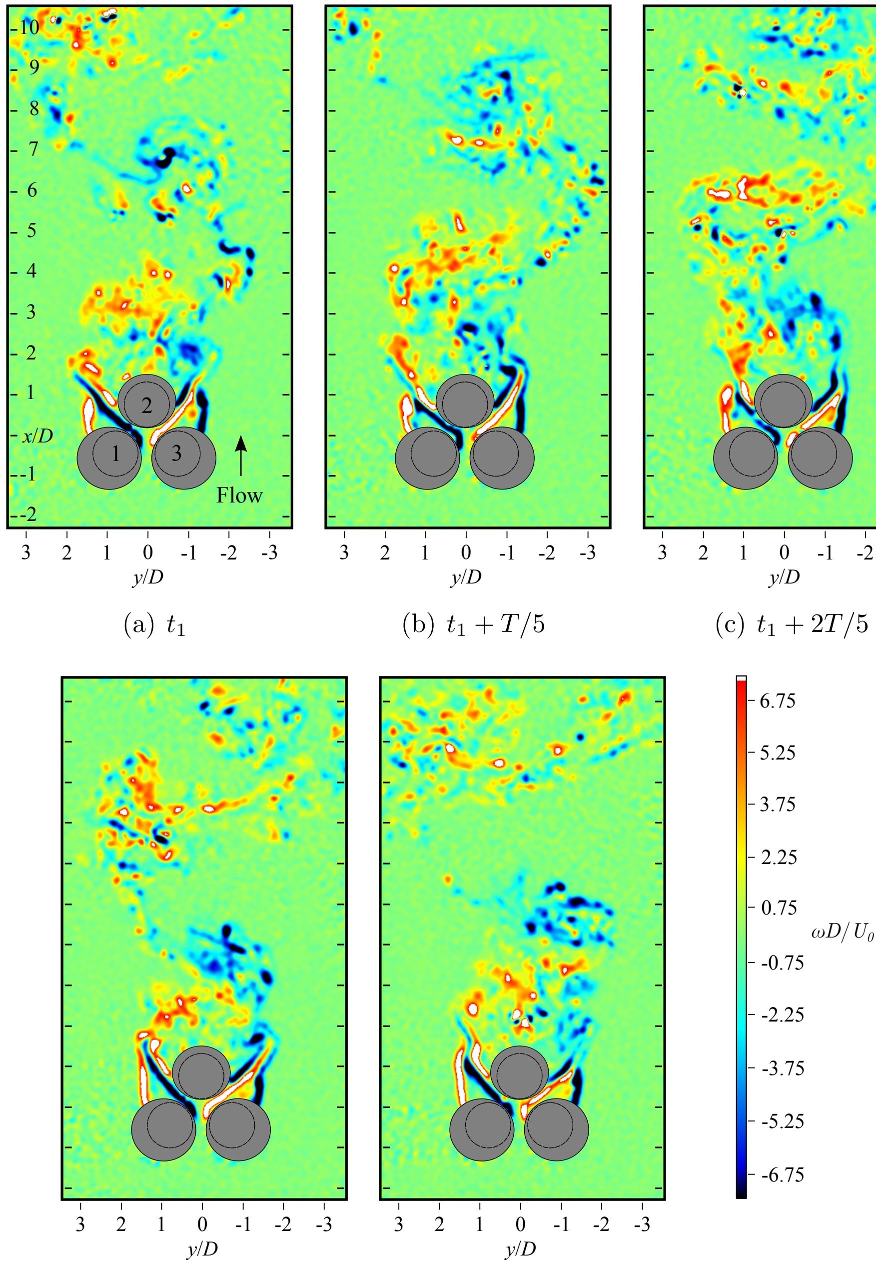

(a) t_1

(b) $t_1 + T/5$

(c) $t_1 + 2T/5$

(d) $t_1 + 3T/5$

(e) $t_1 + 4T/5$

Figure 5.17: Vorticity contours for $\alpha = 60°$.

The flow visualization and time-resolved PIV results suggest the presence of multiple frequency-centered activities in the wake of the cluster at all orientation angles investigated. Spectral analysis of the wake velocity fluctuations was performed to identify shedding frequencies of the large scale and smaller scale structures in cluster wake. The signals were acquired using an LDV system. For the large scale structures, the LDV probe was positioned at $x/D = 13$ and $y/D = 1.5$. The results presented thus far show that large scale shedding occurs beyond $x/D = 5$ for all orientations. Therefore, the probe was positioned at a downstream location where the large scale structures were fully formed and convected by the flow. Figure 5.18 shows the velocity spectra obtained for all cluster orientation angles investigated. In the figure, adjacent spectra are offset by one order of magnitude for clarity. In all spectra, clear dominant peaks exist and are attributed to the shedding of the large scale structures. The secondary peaks also appear for some orientations (e.g., $\alpha = 20°$) at the second harmonic of the large scale shedding frequency. The average St_{D_h} is presented by the dashed line in Figure 5.18. The results show that, when scaled with the height of the projected area of the cluster, D_h, non-dimensional frequency remains constant at $St_{D_h} \approx 0.21$. This Strouhal number value is approximately equal to that expected for a single cylinder with equivalent diameter [66]. Thus, the present geometry behaves similar to a single bluff body in terms of its large scale shedding characteristics, regardless of the orientation angle.

In the near-wake region of the cluster ($1.5 < x/D < 3.5$), smaller scale structures are formed in the narrow wake region, as seen in the qualitative and quantitative results. It is of interest to quantify their characteristic frequencies and the associated energy content. For this purpose, spectral analysis was performed in the near-wake region using PIV results.

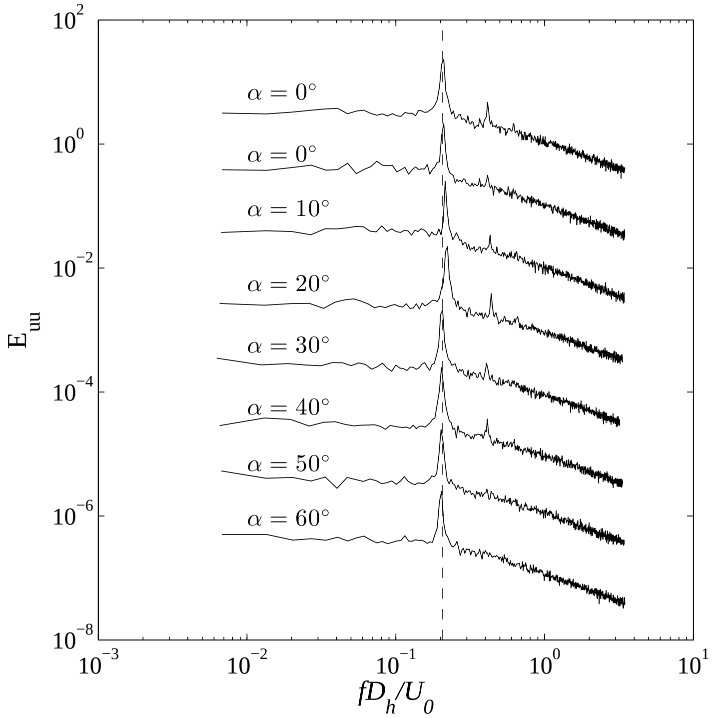

Figure 5.18: Velocity spectra of the streamwise velocity component at $x/D \approx 13$ and $y/D \approx 1.5$. The two spectra for $\alpha = 0°$ correspond to the bistable case. D_h is the height of the projected area of the cluster at each α. The dashed line shows the average St_{D_h}.

Representative spectra of the streamwise velocity component are shown in Figure 5.19. The measurement locations corresponding to the spectra for each α are shown in Table 5.1. These specific locations were selected based on the high velocity fluctuations observed in the near-wake region of cluster in Figure 5.13. The results show two peaks (indicated by markers in Figure 5.19), associated with significant energy content for all orientation cases. The lower frequency peaks are attributed to the velocity fluctuations induced by the large scale shedding. The higher frequency peaks are attributed to the smaller scale shedding in the narrow wake. The dashed line in Figure 5.19 shows the non-dimensional shedding frequency expected for a single cylinder at the same Reynolds number. For all orientations, the large and small scale Strouhal number are lower and higher, respectively, than that for a single cylinder. This difference in the Strouhal number between the cluster wakes and the wake of a single cylinder can be related to the differences in the length of the formation region. The length of the formation region scales inversely with the Strouhal number [5]. For $Re_D = 2100$, the length of the formation region for a single circular cylinder is approximately $2.3D$ [17]. Figure 5.10 shows that the length of the formation region is larger for the wide wake and smaller for the narrow wake than that for the single cylinder wake for all orientations. Therefore, it is expected that the Strouhal number for the large and small scale shedding be smaller and larger, respectively, than that for a single cylinder.

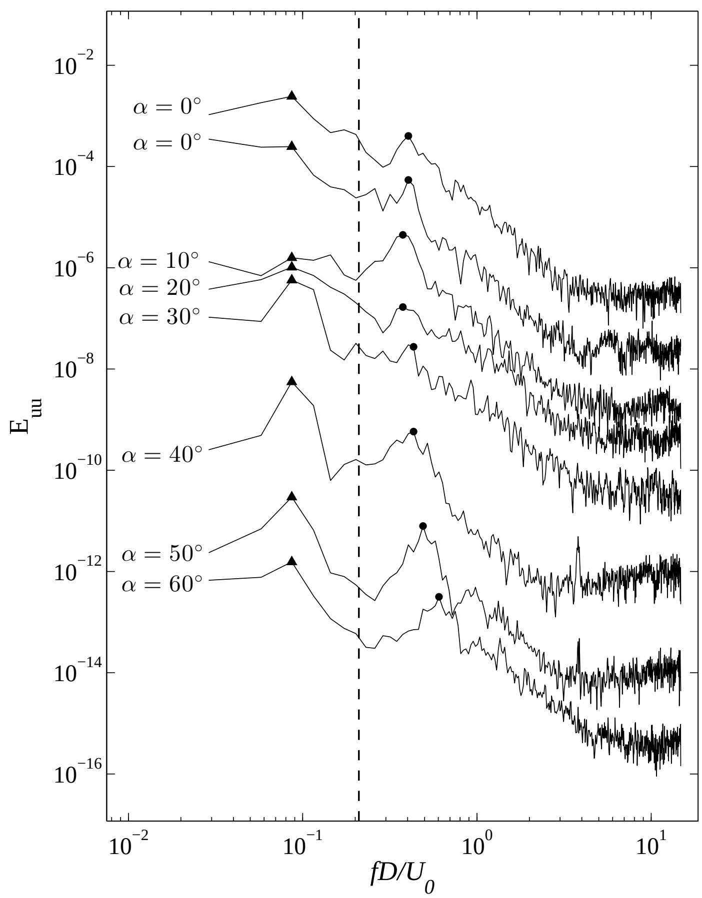

Figure 5.19: Velocity spectra of the streamwise velocity component measured in the near-wake region of the cluster. The triangle and circle filled markers locate the frequencies of the large scale and smaller scale shedding phenomenon, respectively, at each orientation angle. The dashed line represents the non-dimensional shedding frequency for a single cylinder at $Re_D = 2100$.

Table 5.1: Locations of the spectra measurments in the near-wake reigon of the cluster. For $\alpha = 0°$, both bistable cases are listed and indicated by the direction of the jet exicting the cluster relative to the wake axis.

α	x/D	y/D
0° (left)	3.57	0.95
0° (right)	3.40	-0.95
10°	2.91	1.80
20°	3.01	1.47
30°	2.95	1.51
40°	1.60	1.93
50°	1.44	1.93
60°	1.60	1.60

Figure 5.20 shows the relationship between the shedding frequency of the smaller scale structures and the cluster orientation angle. On the average, the results shows that the Strouhal number decreases with increasing α for $0° \leq \alpha \leq 10°$, and increases with increasing α for $10° \leq \alpha \leq 60°$. The variation in Strouhal number is inversely proportional to the variation in the streamwise extent of the formation region of the narrow wake (Figure 5.10) with α. The values agree reasonably well with the results of Lam & Cheung [12] who estimated shedding frequencies in the near-wake region of the cluster at the same spacing ratio and Reynolds number using flow visualization images.

Spectral analysis of band-pass filtered velocity signals was performed to identify regions in the cluster wake associated with the large scale and smaller scale frequency-centered activities. First, the spectra of the streamwise velocity component at each vector location

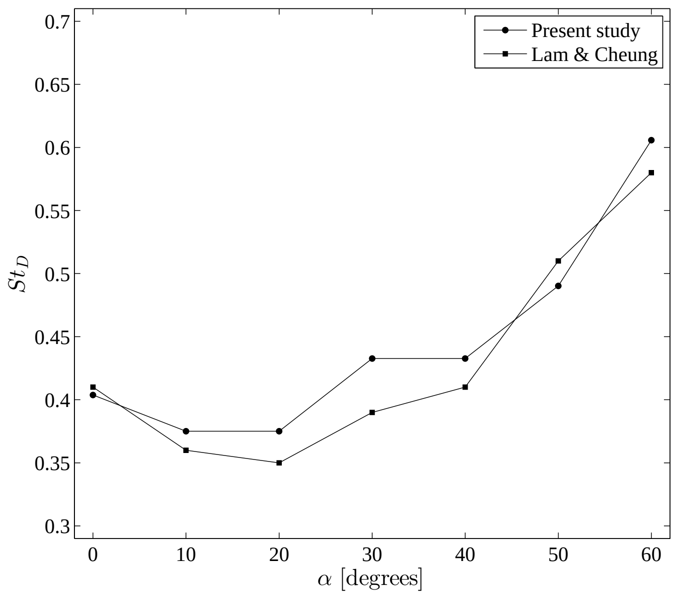

Figure 5.20: Strouhal number relationship with the cluster orientation. Results from Lam & Cheung [12] are presented for a triangular cluster with $P/D = 1.35$ and $Re_D = 2100$.

in the flow field was computed using PIV results. Then, an average energy content with a frequency band of width $\pm 0.015 St_D$ centered at the corresponding shedding frequency was computed. Figures 5.21 and 5.22 show energy maps corresponding to large and small scale shedding frequencies, respectively. In Figure 5.21, notable velocity fluctuations at the large scale shedding frequency occur in the shear layers bounding the narrow and wide wakes, as well as two regions downstream of $x/D > 3$ on each side of the wake axis. For $x/D > 3$, the high velocity fluctuations for each orientation correspond to the formation of large scale vortices, as seen in the flow visualization. Figure 5.21 shows that there is significant energy content within the shear layers bounding the narrow wake at the large scale shedding frequency. Similar to Figure 5.13, the maximum u'_f occurs on the same side of the wake as the direction of the high speed jet. On the average, as α increases from 0° to 60°, the maximum u'_f increases.

Figure 5.22 shows contours of the energy content associated with the small scale shedding frequency. For all orientations, high velocity fluctuations at the small scale shedding frequency take place primarily at the downstream end of the narrow wake ($x/D \approx 2$). This is associated with the shedding of the small scale vortices, seen in qualitative and quantitative results presented thus far. Relative to Figure 5.21, the energy content within the shear layers bounding the narrow wake is low. Also, the results in Figure 5.22 show that significant energy content associated with the small scale shedding frequency persists into the formation region of the large scale structures. Thus, there are interactions between the large and small scale structures within the formation region of the large scale structures, which agrees with previous observations from the sequence of vorticity fields for all orientations.

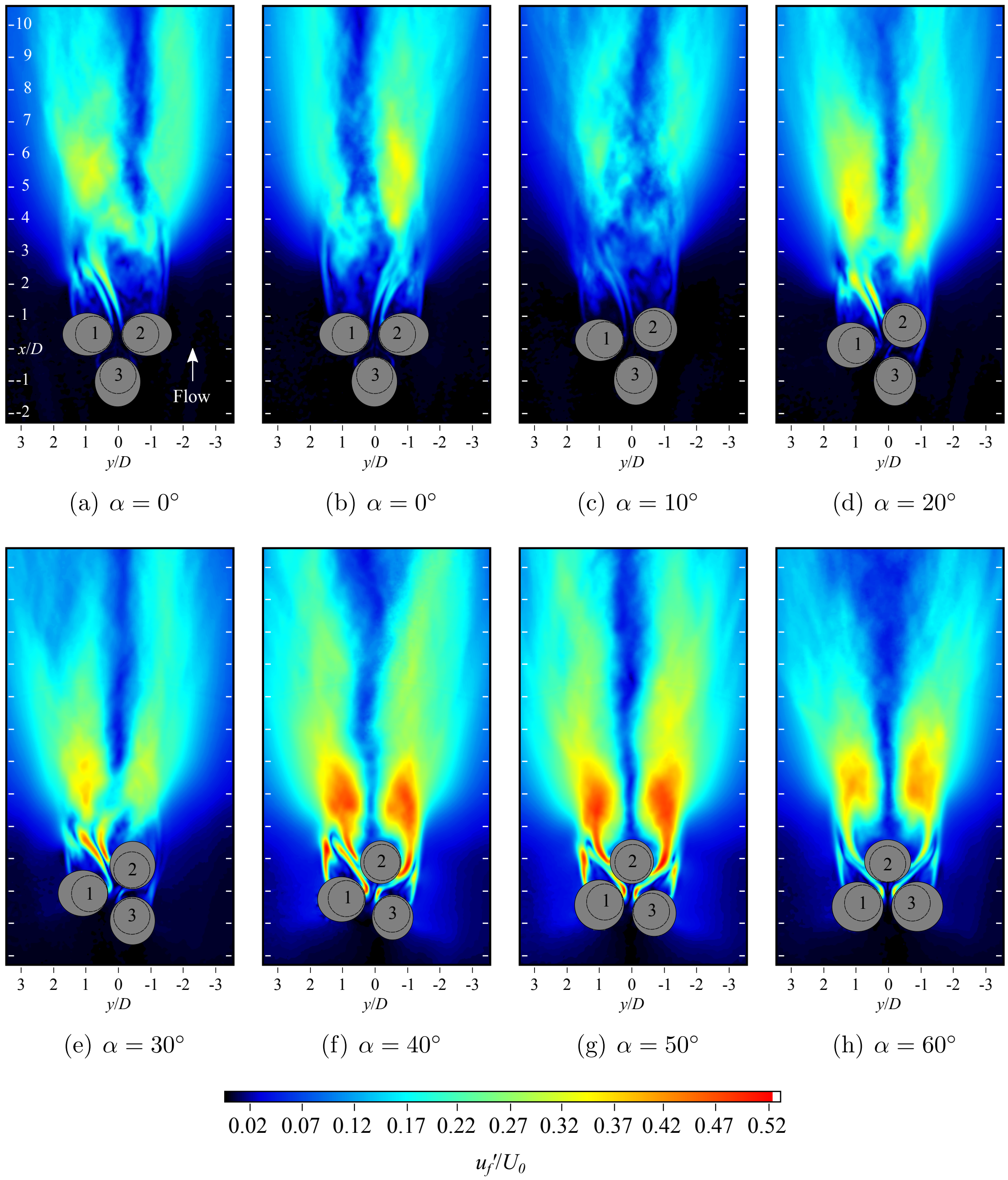

Figure 5.21: Spectral energy map using a band-pass filter of width $\pm 0.015 St_D$ at the large scale shedding frequency for all cluster orientations.

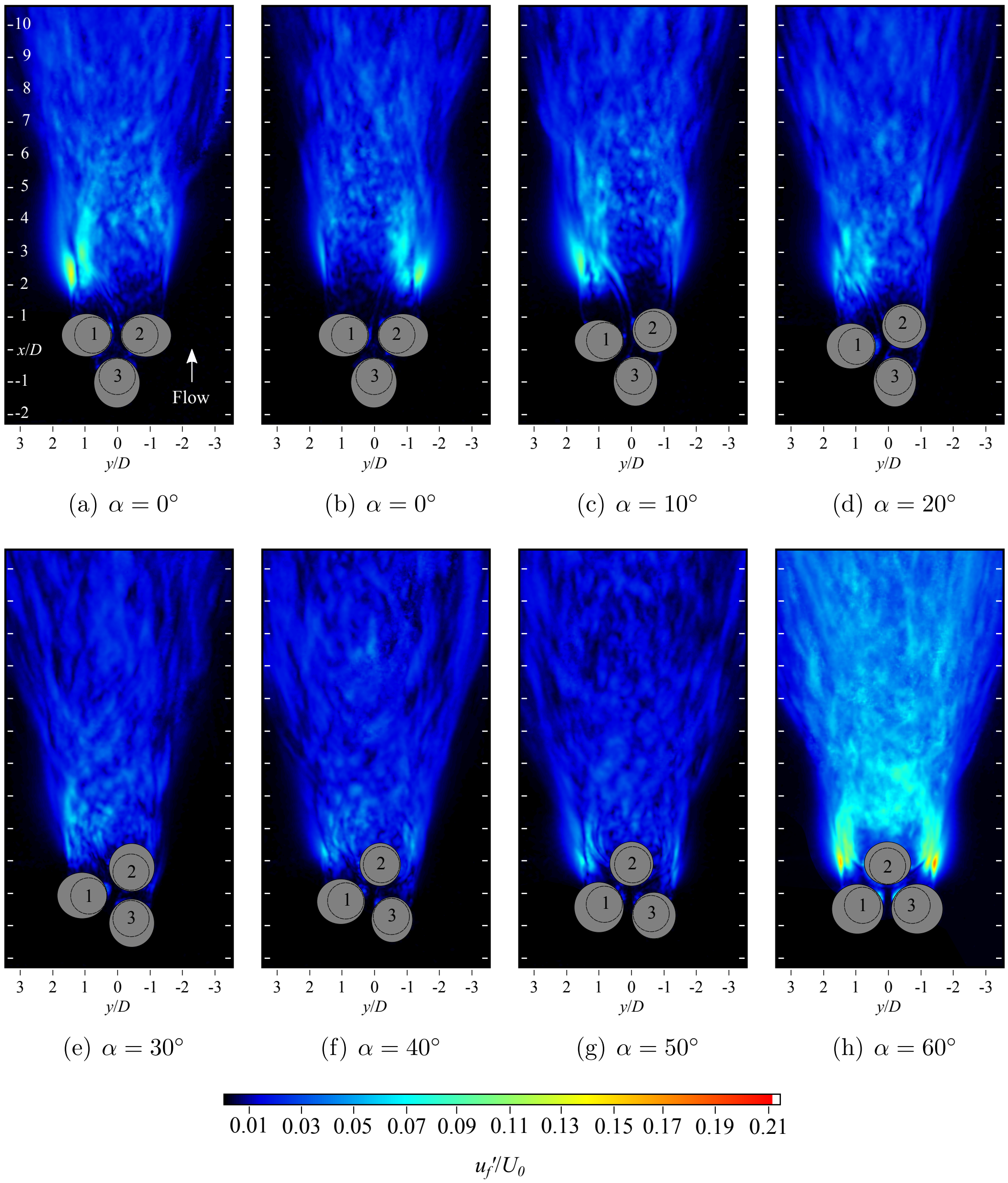

Figure 5.22: Spectral energy map using a band-pass filter of width $\pm 0.015 St_D$ at the small scale shedding frequency for all cluster orientations.

5.4 POD analysis

For all orientations, POD was performed to analyze the development of large and small scale structures in the cluster wake and their interactions using reduced-order models. Figure 5.23 shows the cumulative mode energy and mode energy distribution for the first 500 modes and all orientation angles investigated. Figure 5.23a demonstrates that the first 500 modes capture approximately 98% of the total energy content. The energy content of the first two modes is approximately 45% to 70%, depending on α. This mode pair is expected to capture the characteristics of the large scale shedding for bluff body flows [59,83,84]. On the average, the cumulative mode energy for the first two modes increases with increasing α. Figures 5.24 to 5.29 show the first two temporal coefficients and spatial modes for $\alpha = 0°$ and 60°. Appendix B presents similar plots for $10° \leq \alpha \leq 50°$. The first two temporal coefficients display strong periodic signals with a phase offset of 90°. The frequency of the signals matches the large scale shedding frequency (Figure 5.18). The combined first two spatial modes along with their temporal coefficients illustrate the evolution of the large scale structures, similar to the case of a circular cylinder [83–85].

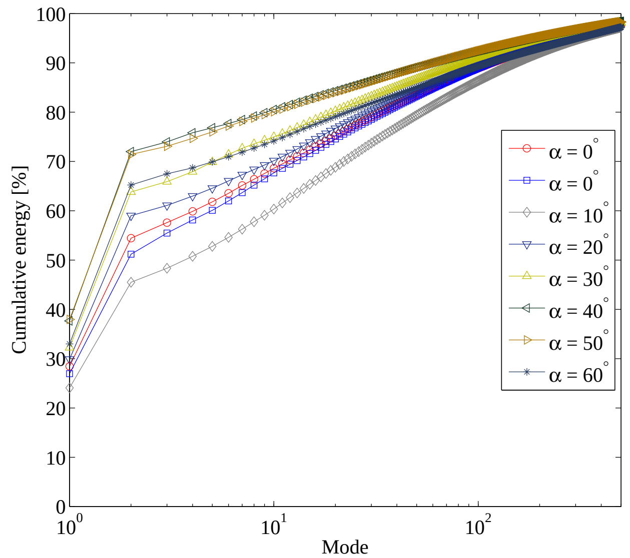

(a) Cumulative energy

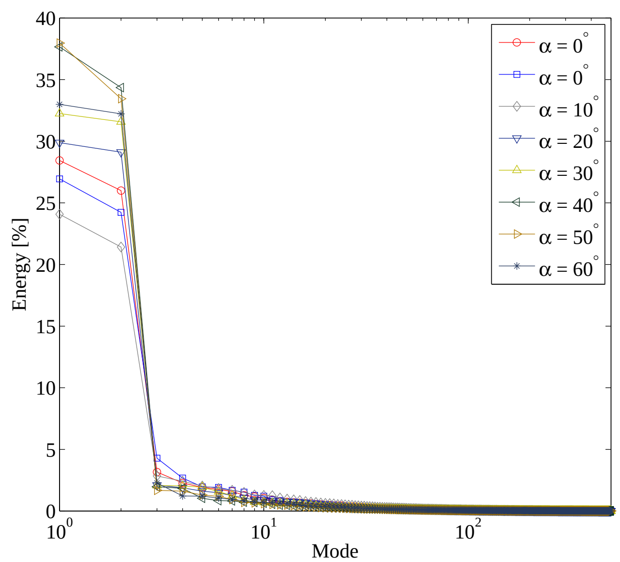

(b) Energy

Figure 5.23: Mode energy distribution for all cluster orientations.

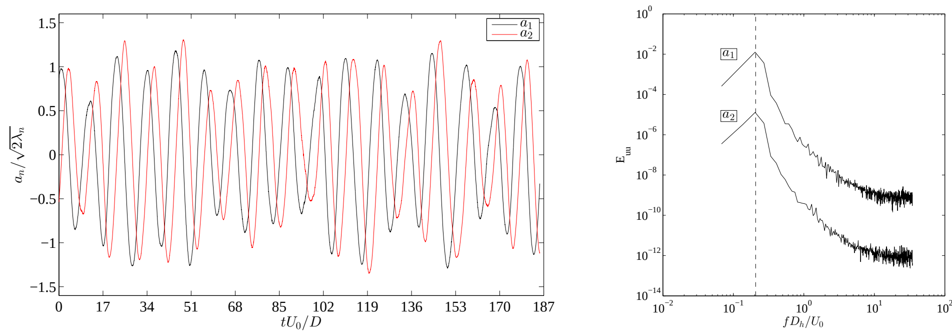

(a) (b)

Figure 5.24: Temporal coefficient (a) signal and (b) spectra for the first two modes corresponding to large scale shedding for the bistable case (i.e., $\alpha = 0°$).

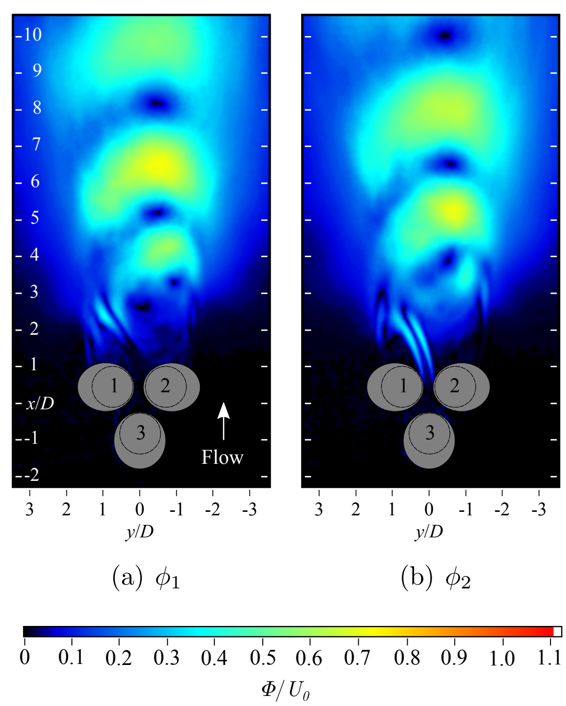

(a) ϕ_1 (b) ϕ_2

Figure 5.25: First and second spatial modes corresponding to large scale shedding for the bistable case (i.e., $\alpha = 0°$), in which the jet is directed to cylinder 1.

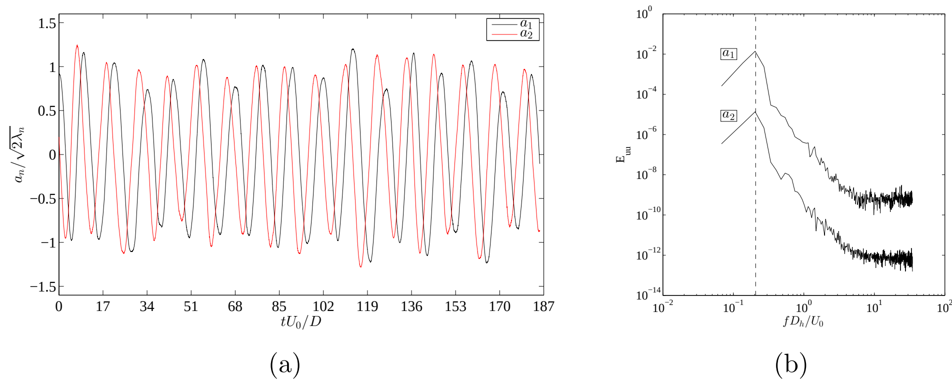

Figure 5.26: Temporal coefficient (a) signal and (b) spectra for the first two modes corresponding to large scale shedding for the bistable case (i.e., $\alpha = 0°$).

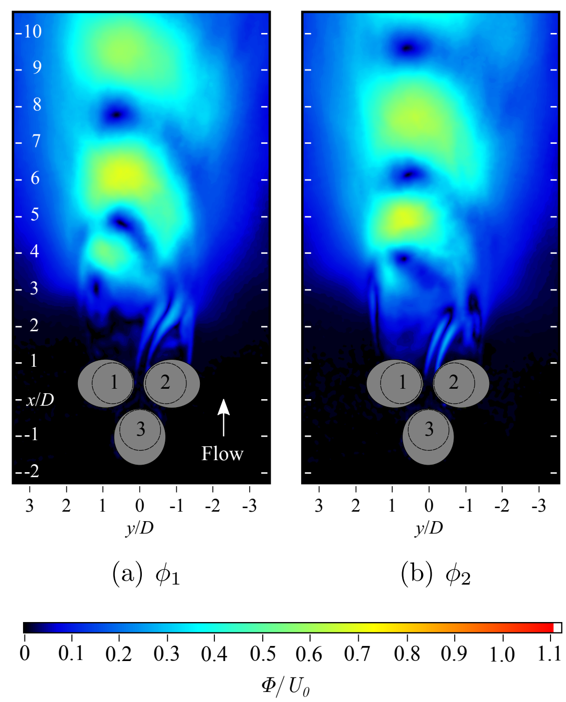

Figure 5.27: First and second spatial modes corresponding to large scale shedding for the bistable case (i.e., $\alpha = 0°$), in which the jet is directed to cylinder 2.

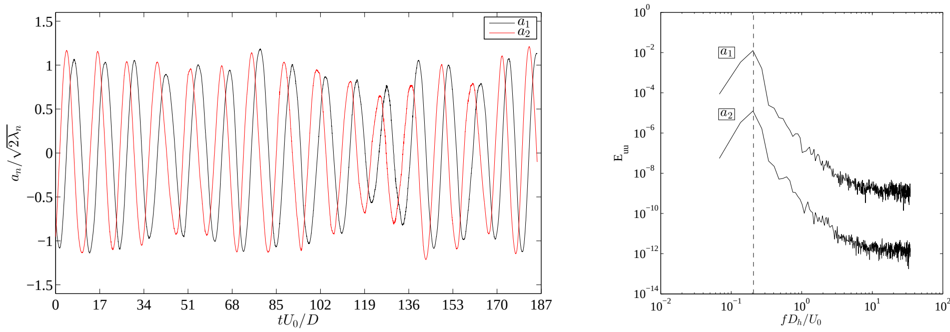

(a) (b)

Figure 5.28: Temporal coefficient (a) signal and (b) spectra for the first two modes corresponding to large scale shedding for $\alpha = 60°$.

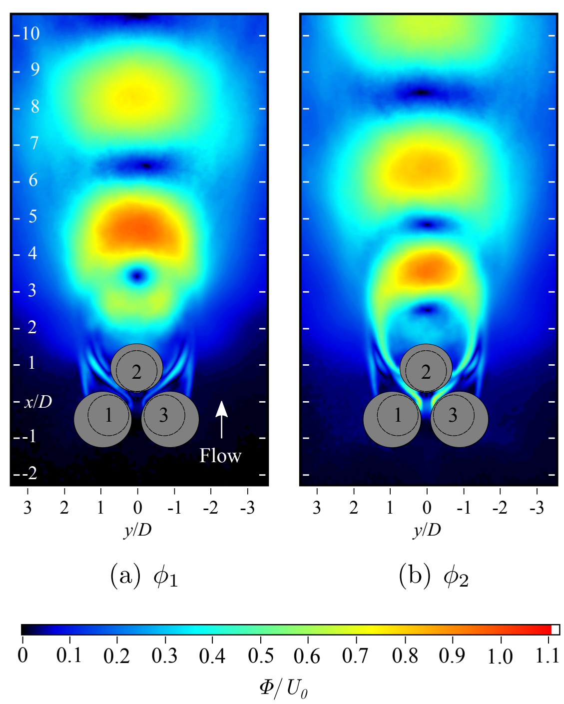

(a) ϕ_1 (b) ϕ_2

Figure 5.29: First and second spatial modes corresponding to large scale shedding for $\alpha = 60°$.

To identify modes associated with the small scale shedding observed in the narrow wake of the cluster in previously discussed results, spectral analysis of the temporal coefficients was performed. Modes associated with the small scale shedding were identified as those for which a peak in the spectra at the small scale shedding frequency was detected, excluding modes with less than 1% of the total wake energy content. The identified modes are shown in Figures 5.30 to 5.35 for $\alpha = 0°$ and 60° and the results for $10° \leq \alpha \leq 50°$ are shown in Appendix B. For $\alpha = 0°$ (Figure 5.30), the spectra of a_{14} and a_{15} show a single peak and the spectra of a_{16} and a_{17} show multiple peaks. For a_{14} and a_{15}, the peak is centered at the small scale shedding frequency; whereas, for a_{16} and a_{17}, peaks occur at the small scale shedding frequency and at the first harmonic of the large scale shedding frequency. Figure 5.31 shows the spatial modes for the corresponding temporal coefficients for $\alpha = 0°$. The spatial modes for the first mode pair (ϕ_{14} & ϕ_{15}) show similar features in the narrow wake as those seen in the spatial modes for the large scale shedding for the cluster (Figure 5.21b) and the wake of a single cylinder [83–85]. The spatial modes for the second mode pair (ϕ_{16} & ϕ_{17}) show features of small scale shedding in the narrow wake and first harmonic of the large scale shedding frequency. For $\alpha = 60°$, the modes associated with the small scale shedding are modes 33, 34, 36, and 37. The spectra of the corresponding temporal coefficients show clear peaks at the small scale shedding frequency for $\alpha = 60°$ (Figure 5.34). The spatial modes in Figure 5.35 display features of small scale shedding in the narrow wake, similar to $\alpha = 0°$, and other periodic activity in the wide wake. As α increases from 0° to 60°, the energy content associated with small scale shedding decreases from 4% to 1%. This effect is linked to the changes in the length of the formation region for the small scale vortices and their physical size. As α increases from 0°

to 60°, the length of the formation region and the size of the small scale vortices decreases, resulting in the reduction of the energy content associated with these structures. It should be noted that, for all orientations, the energy content of the small scale vortices is only 2% to 9%, depending on α, of that of the large scale vortices.

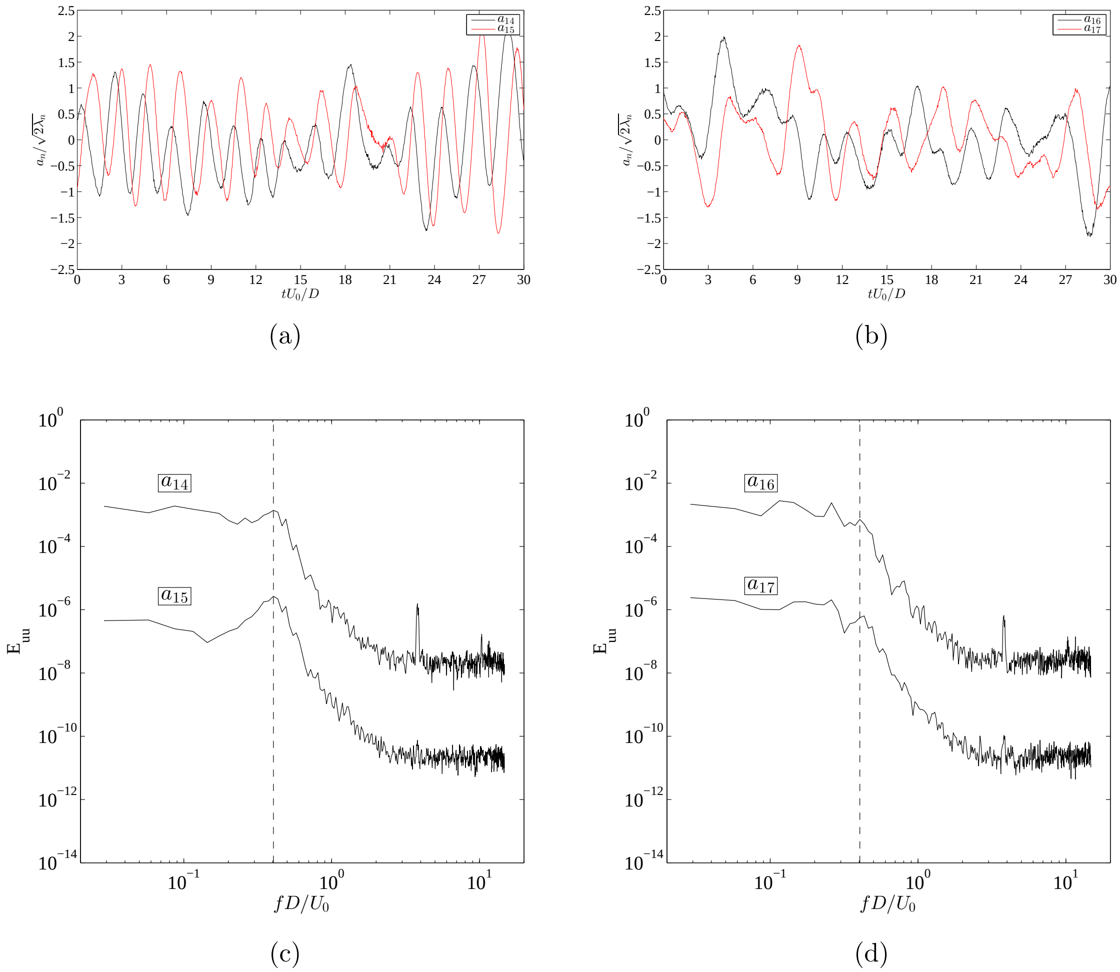

Figure 5.30: Temporal coefficient (a) & (b) signal and (c) & (d) spectra for modes corresponding to the small scale shedding for the bistable case (i.e., $\alpha = 0°$), in which the jet is directed to cylinder 2.

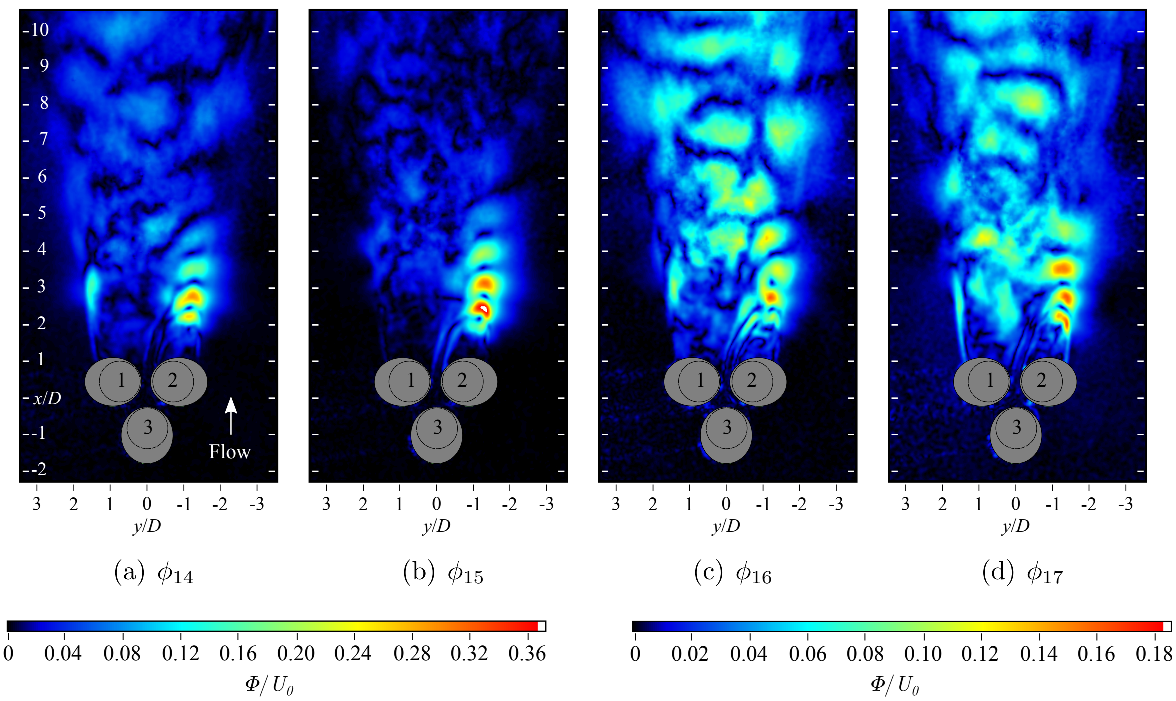

Figure 5.31: Spatial modes corresponding to the small scale shedding for the bistable case (i.e., $\alpha = 0°$), in which the jet is directed to cylinder 2.

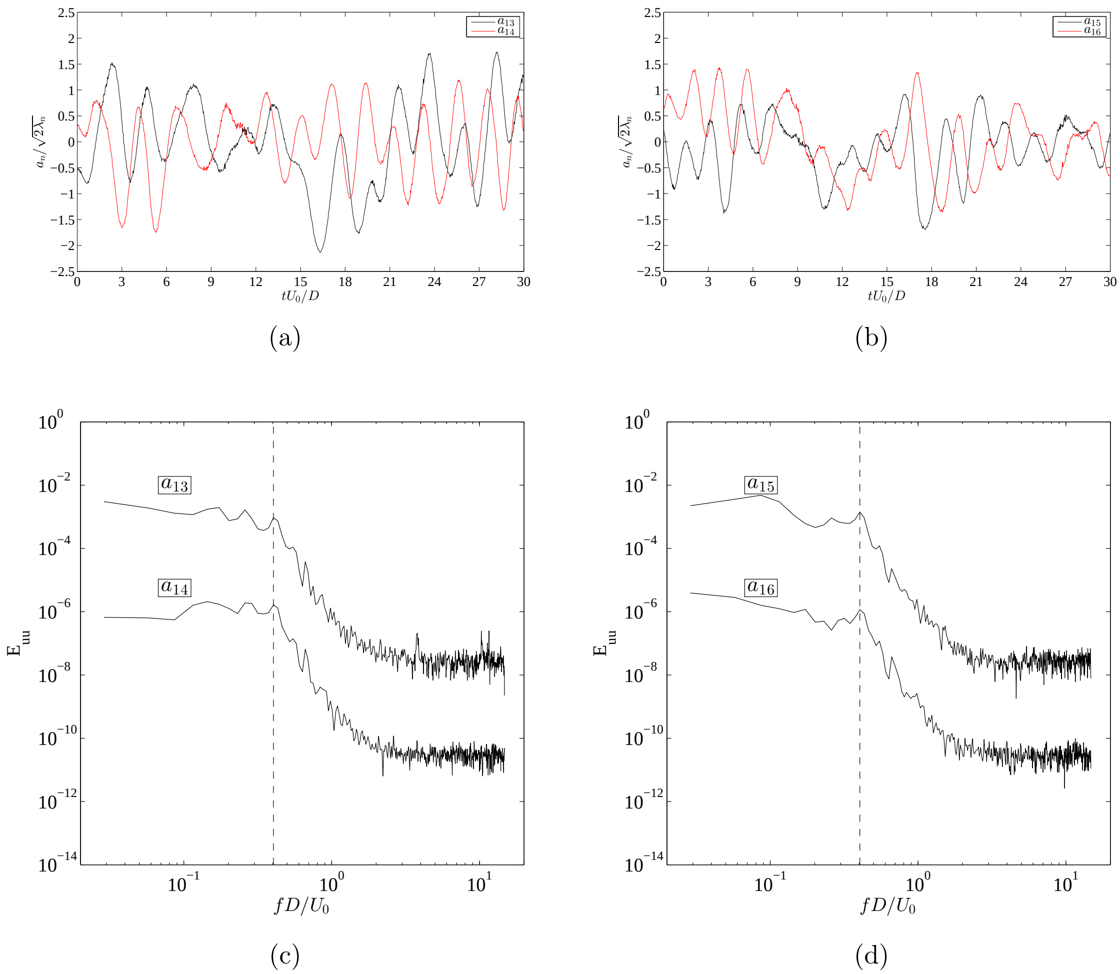

Figure 5.32: Temporal coefficient (a) & (b) signal and (c) & (d) spectra for modes corresponding to the small scale shedding for the bistable case (i.e., $\alpha = 0°$), in which the jet is directed to cylinder 1.

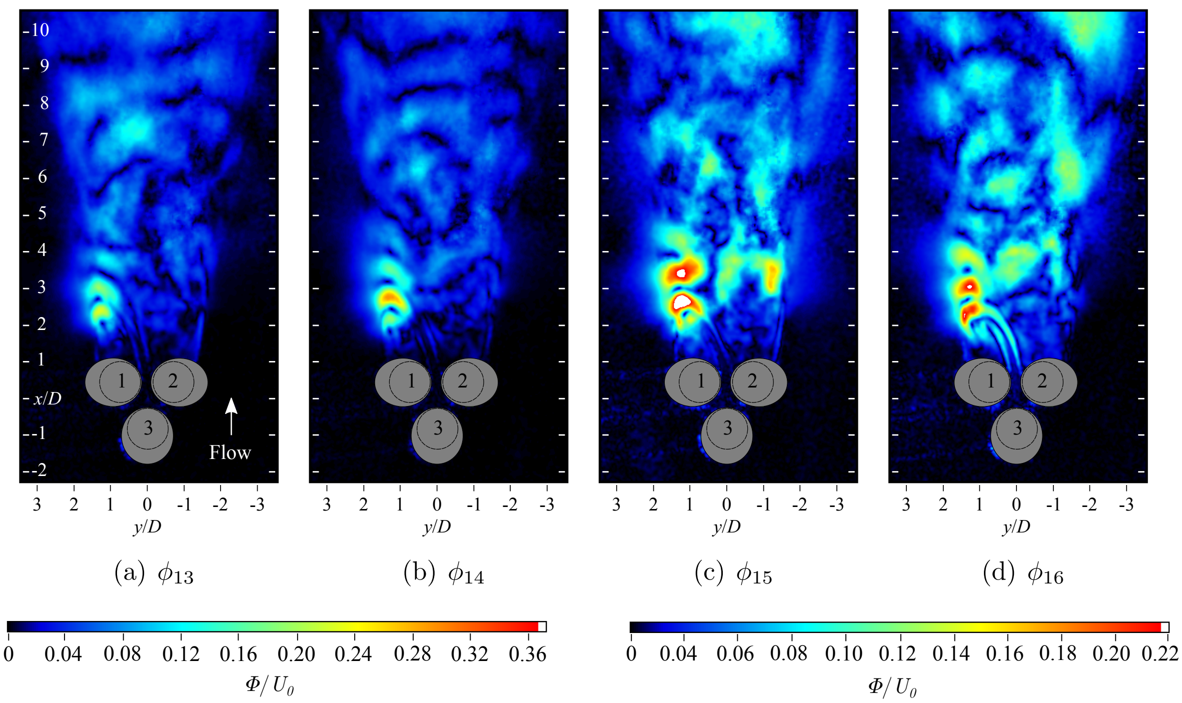

Figure 5.33: Spatial modes corresponding to the small scale shedding for $\alpha = 0°$.

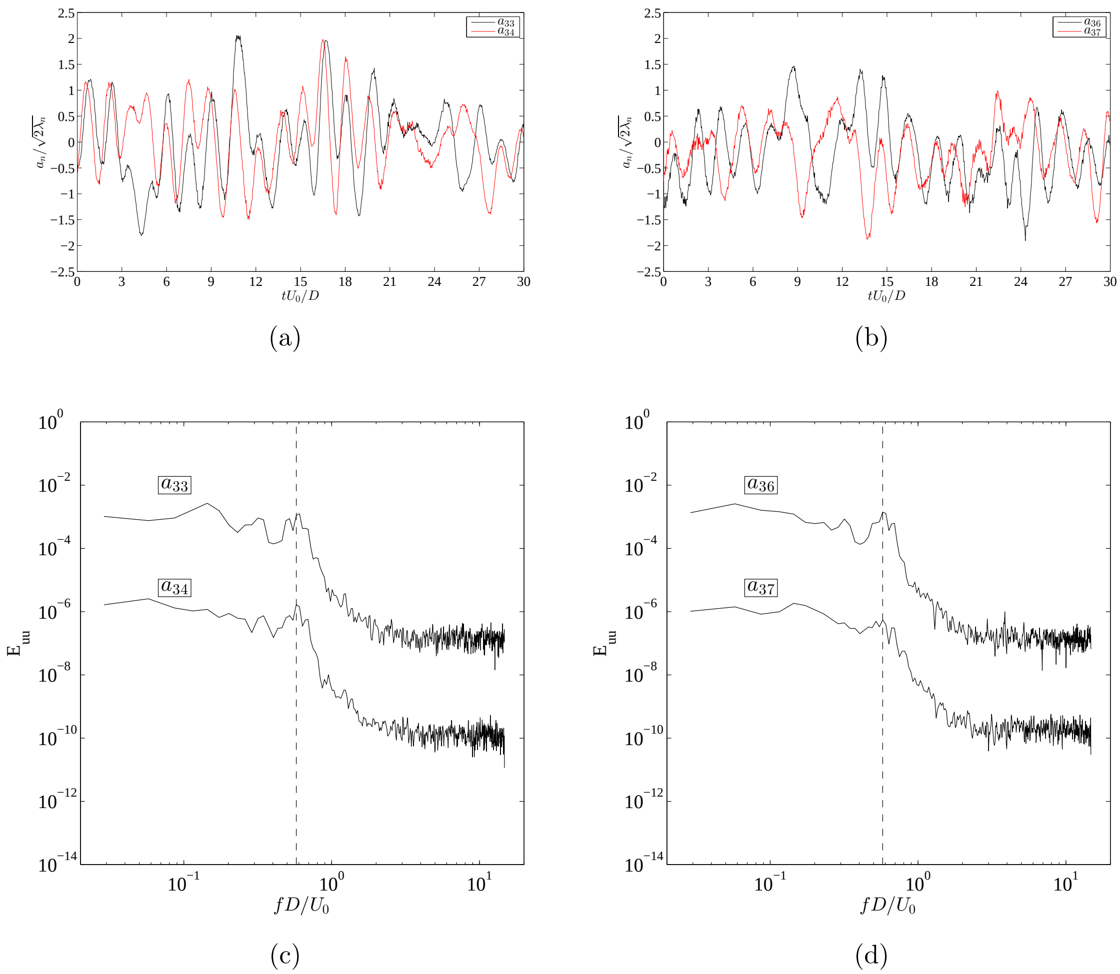

Figure 5.34: Temporal coefficient (a) & (b) signal and (c) & (d) spectra for modes corresponding to the small scale shedding for $\alpha = 60°$.

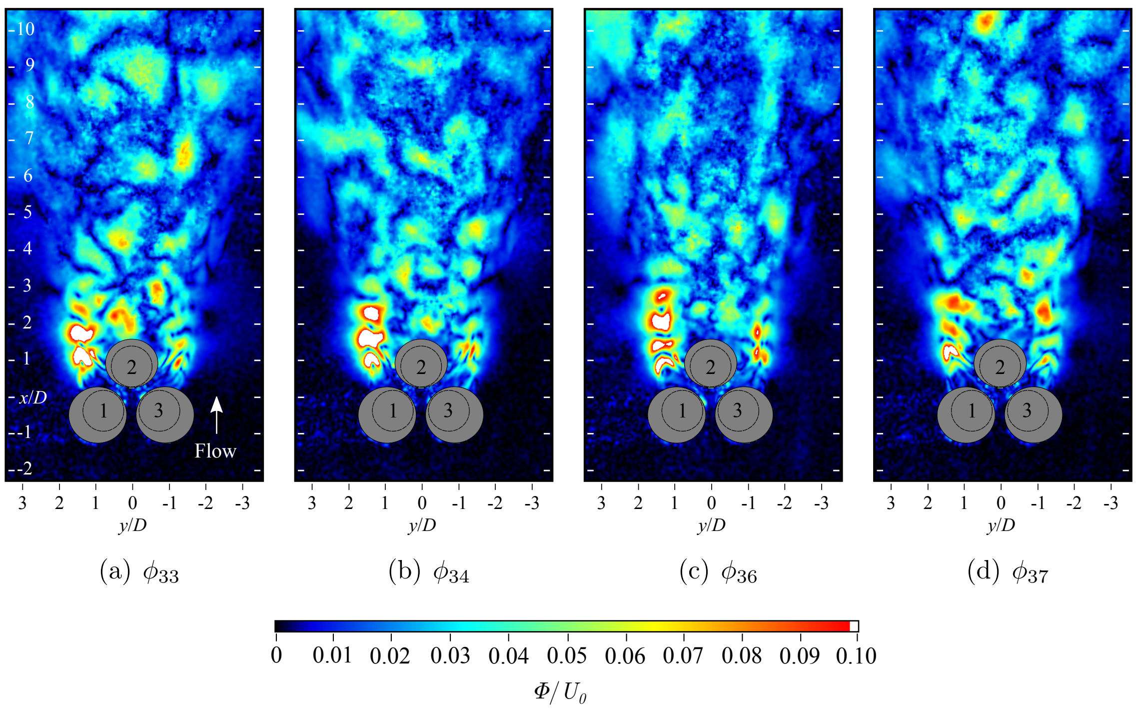

Figure 5.35: Spatial modes corresponding to the small scale shedding for $\alpha = 60°$.

The previous analysis showed that modes 1 and 2 capture large scale shedding, while the first 40 modes capture both large and small scale shedding for all orientations. Based on this, two different reduced-order models were produced. The first reduced-order model, consisting of the first two modes, was produced to analyze large scale shedding for all orientations. The second reduced-order model consists of the first 40 modes, capturing 75% to 90%, depending on α, of the total energy content of the wake. The purpose of this model is to analyze the interactions between the large and small scale structures. Figures 5.36 to 5.38 show the reconstructed flow using the first two modes for $\alpha = 0°$ and $60°$. The results for $10° \leq \alpha \leq 50°$ are shown in Appendix B. For $\alpha = 0°$ (Figure 5.36), the outer shear layer of cylinder 1 rolls up into a vortex within $3 < x/D < 5$. On the opposite side of the wake axis, the inner shear layer of cylinder 1 interacts with the outer shear layer of cylinder 2. Figures 5.36a-5.36b show the start of the roll up of the inner shear layer of cylinder 1. As this shear layer rolls up, it merges with the outer shear layer of cylinder 2, forming a large scale vortex, as seen in Figures 5.36b and 5.36c. The vortex is being shed and convects downstream in Figures 5.36d and 5.36e, while the outer shear layer of cylinder 1 forms into a new vortex on the opposite side of the wake centerline. The results show that vortices forming downstream of cylinder 2 are less coherent than those forming downstream of cylinder 1. For $\alpha = 60°$, shear layers of cylinder 2 merge with the outer shear layers of cylinders 1 and 3 as they roll up, similar to $\alpha = 0°$ case.

The results for the second reduced-order model consisting of the first 40 modes are illustrated in Figure 5.39 for $\alpha = 0°$. The results for other cases are presented in Appendix B. Figure 5.39 shows one half of the large scale shedding cycle. On the left hand side in Figure 5.39, large scale vortices shed due to the roll up of the outer shear layer of cylinder

1. Formation of another large scale vortex is expected on the right hand side, similar to the results from the previous reduced-order model (Figure 5.36). The results show complex interactions involved during the formation of the large scale structure on the right hand side of the wake axis (Figure 5.39). Specifically, the ratio between the small and large scale vortex shedding frequencies is approximately four, so that four small scale vortices are shed while one large scale vortex is rolling up. For example, the sequence in Figure 5.39 begins at the start of the roll up of the inner shear layer of cylinder 1. As this shear layer rolls up into a vortex within $2 < x/D < 3$, it merges with the small scale vortex of same vorticity sense forming due to the roll up of the outer shear layer of cylinder 2, as seen in Figures 5.39a-5.39h. While this merging process occurs, the inner shear layer of cylinder 2 rolls up into a small scale vortex of opposite sense, relative to the inner shear layer of the wide wake, within $1.5 < x/D < 2$ (Figures 5.39a-5.39c). This opposite sense vortex cuts further supply of circulation from the outer shear layer of cylinder 2 and is then shed into the formation region of the large scale vortex, as seen in Figures 5.39d-5.39h. The process during one small scale shedding cycle is repeated in Figures 5.39h-5.39o, and four of these events occur during the formation of the large scale vortex. The fully formed large scale vortex on the right hand side of the wake in Figure 5.39 encompasses four smaller scale vortices with opposite vorticity sense. Thus, the large scale vortices on the right hand side of the wake axis are less coherent than those formed on the left hand side. Similar interactions between the inner shear layer of the wide wake and vortices shed from the narrow wake occur for all orientations.

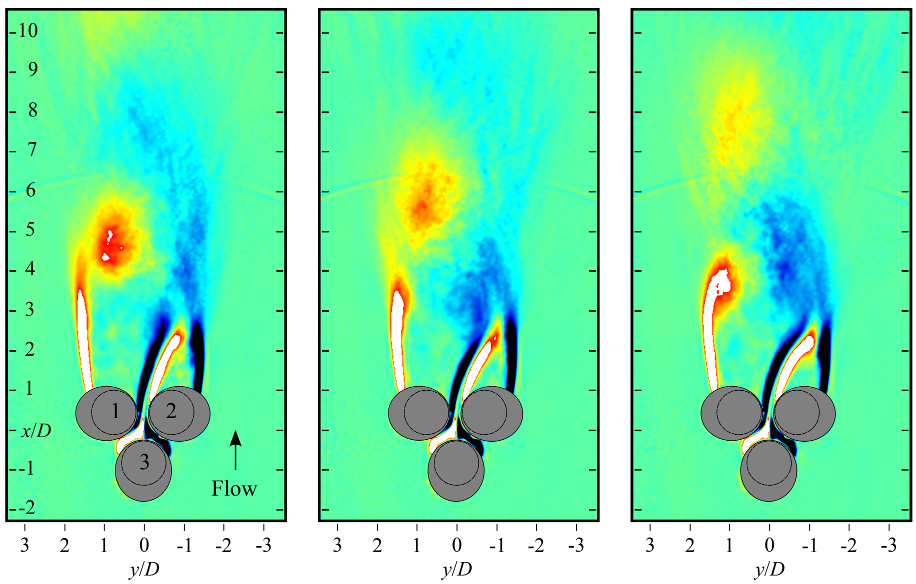

(a) t_1 (b) $t_1 + T/5$ (c) $t_1 + 2T/5$

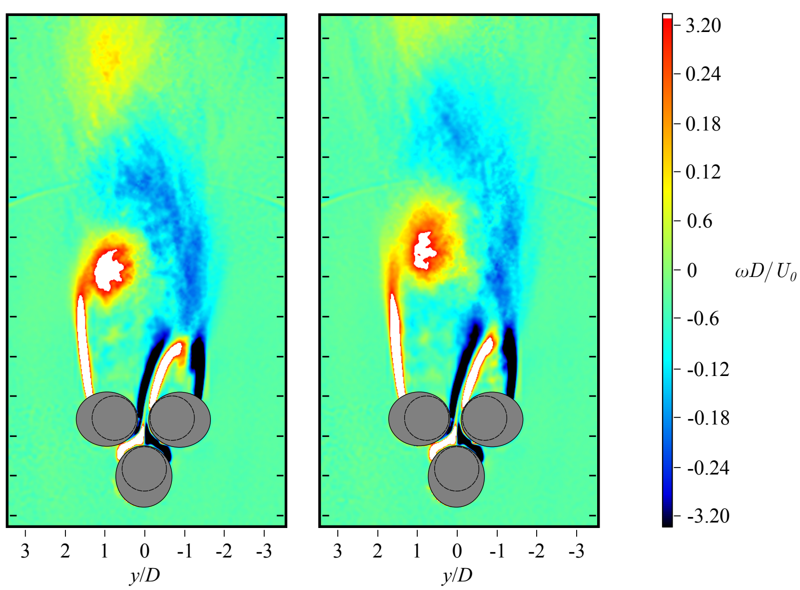

(d) $t_1 + 3T/5$ (e) $t_1 + 4T/5$

Figure 5.36: Vorticity contours of the reduced-order model consisting of the first two modes for $\alpha = 0°$ (gap flow directed towards cylinder 2).

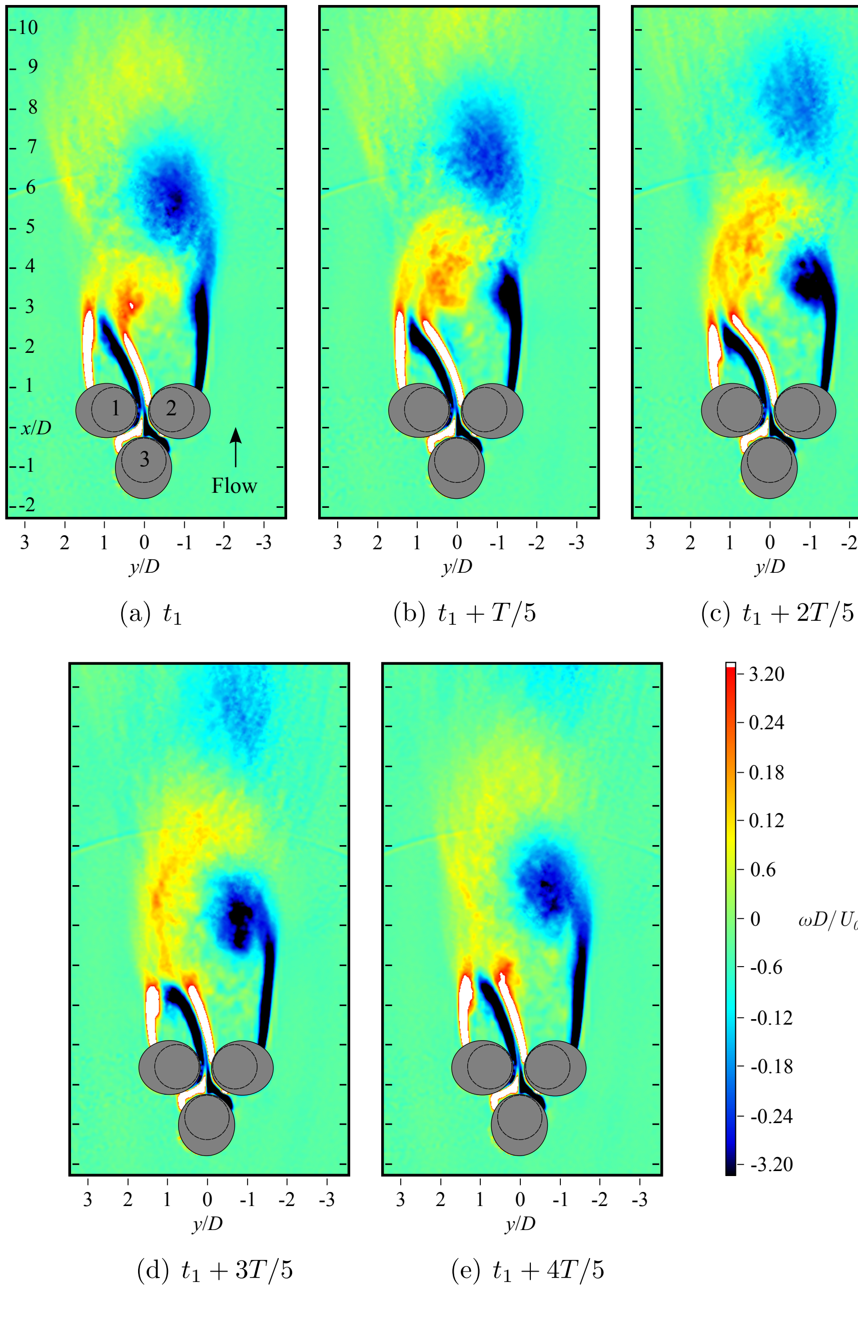

(a) t_1 (b) $t_1 + T/5$ (c) $t_1 + 2T/5$

(d) $t_1 + 3T/5$ (e) $t_1 + 4T/5$

Figure 5.37: Vorticity contours of the reduced-order model consisting of the first two modes for $\alpha = 0°$ (gap flow directed towards cylinder 1).

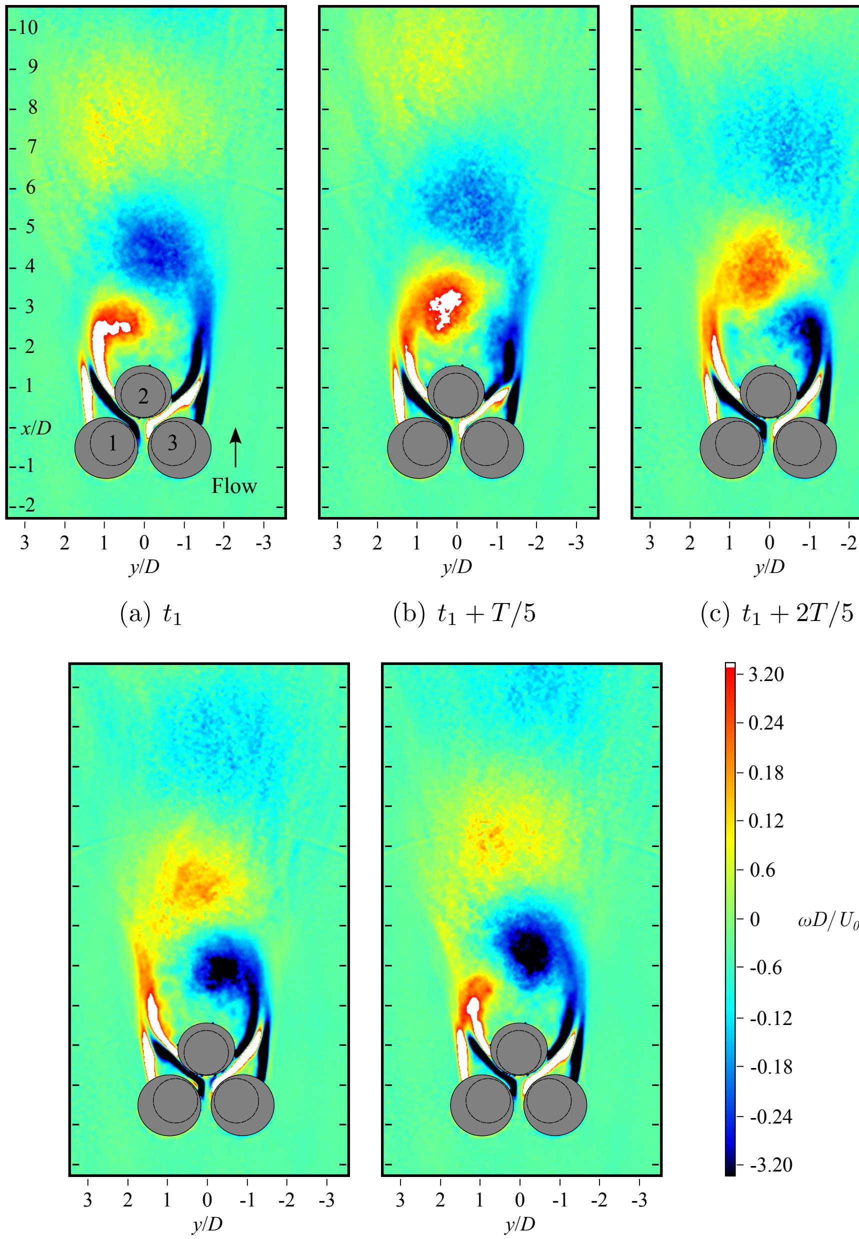

(a) t_1 (b) $t_1 + T/5$ (c) $t_1 + 2T/5$

(d) $t_1 + 3T/5$ (e) $t_1 + 4T/5$

Figure 5.38: Vorticity contours of the reduced-order model consisting of the first two modes for $\alpha = 60°$.

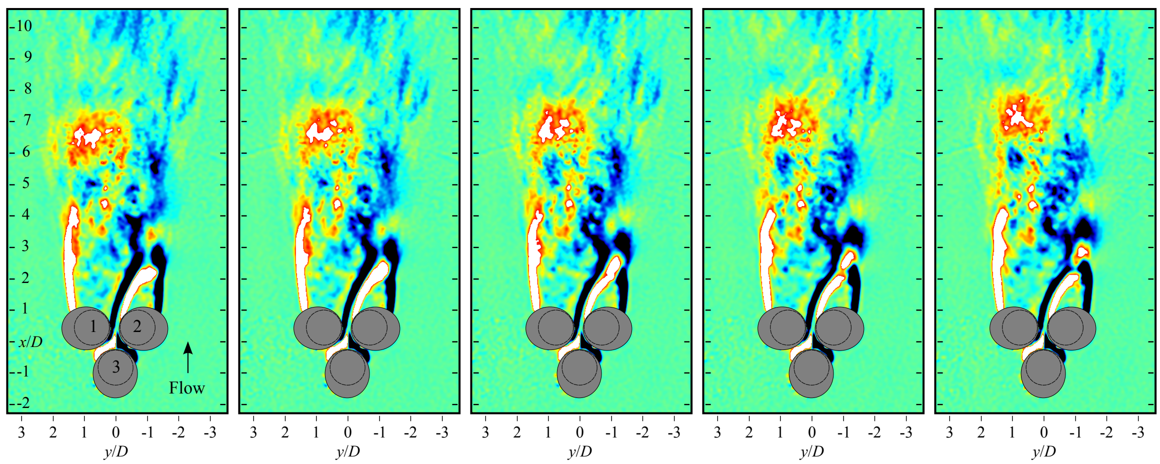

(a) t_1 (b) $t_1 + T/30$ (c) $t_1 + 2T/30$ (d) $t_1 + 3T/30$ (e) $t_1 + 4T/30$

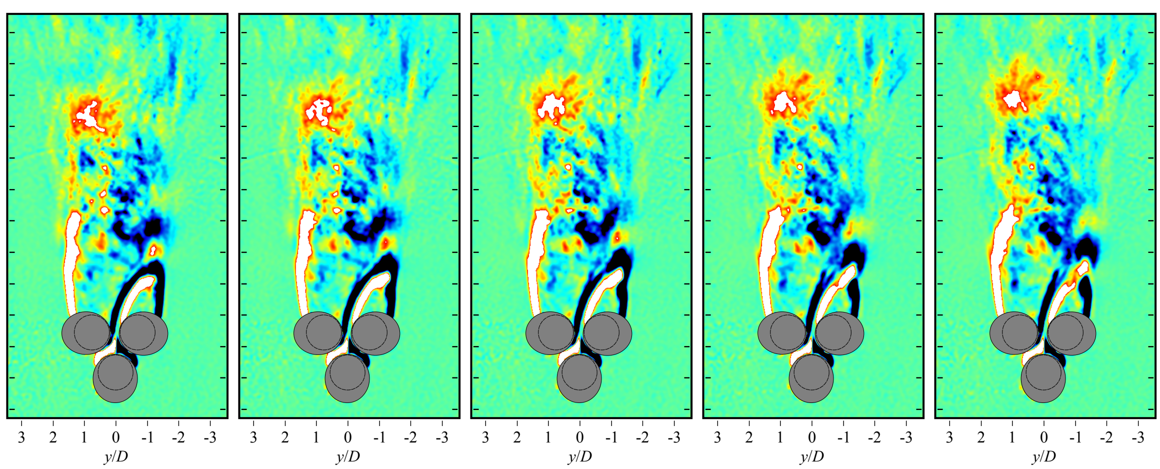

(f) $t_1 + 5T/30$ (g) $t_1 + 6T/30$ (h) $t_1 + 7T/30$ (i) $t_1 + 8T/30$ (j) $t_1 + 9T/30$

Figure 5.39: (See next page for figure caption)

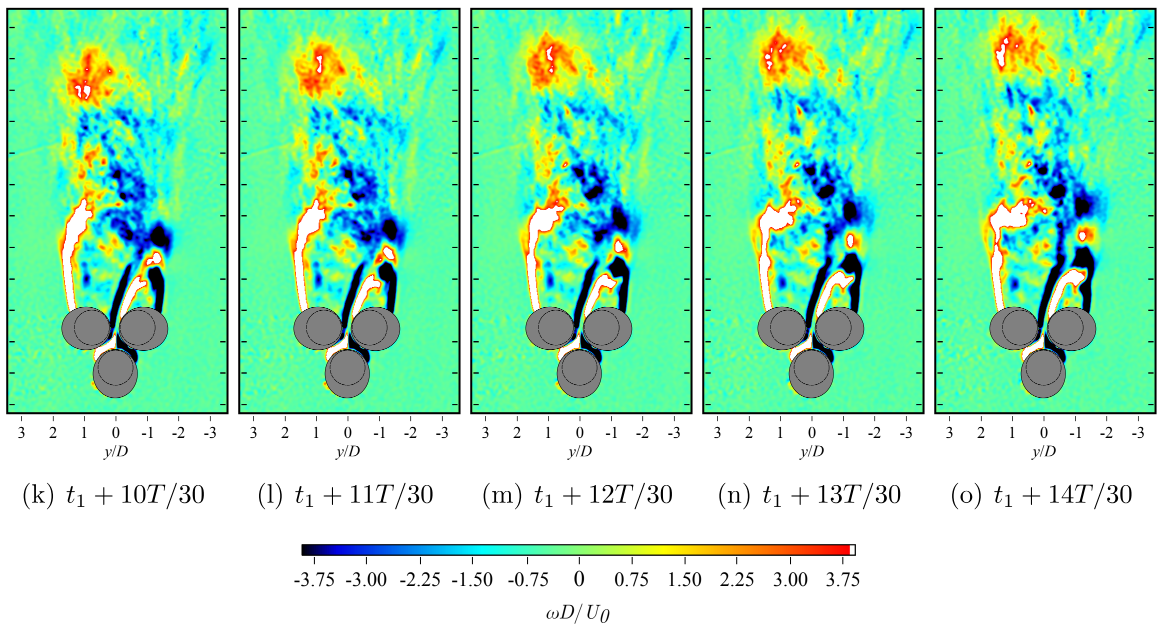

(k) $t_1 + 10T/30$ (l) $t_1 + 11T/30$ (m) $t_1 + 12T/30$ (n) $t_1 + 13T/30$ (o) $t_1 + 14T/30$

Figure 5.39: Vorticity contours of the reduced-order model consisting of the first forty modes for one half of the large scale shedding cycle for $\alpha = 0°$ (gap flow directed towards cylinder 2).

Chapter 6

Numerical results

In this chapter, the laminar and RANS simulation results for flow over the equispaced triangular cluster are analyzed and discussed. Section 6.1 shows the laminar simulation results. Similar to the experimental results, first an overview of the flow development for the vortex shedding regime at $Re_D = 100$ is provided. The mean and RMS fields of the streamwise and transverse velocity components are discussed, followed by frequency and force analyses. Section 6.2 presents results from the RANS simulations. In this section, results from four turbulence models are compared: (i) SST, (ii) $k - \epsilon$, (iii) $k - \omega$, and (iv) LRR-IP. The mean flow field is analyzed and compared between all turbulence models investigated and the experimental results. Also, mean pressure contours and aerodynamic forces for all turbulence models are computed and discussed.

6.1 Simulations at $Re_D = 100$

6.1.1 Overview of flow development

Figures 6.1 and 6.2 show the flow development at $Re_D = 100$ for the triangular cluster at $\alpha = 0°$ and $60°$, respectively. For both orientations, the wake development is symmetric about $y = 0$ and is dominated by the shedding of large scale structures. Large scale vortex shedding is present beyond $x/D \approx 4$ for both orientations, similar to that for a single cylinder [6]. For $\alpha = 0°$ (Figure 6.1), the shear layers emanating from cylinder 3 impinge on the surfaces of cylinders 1 & 2 and merge with the boundary layers of same vorticity sense. The outer shear layers of cylinders 1 and 2 roll up into vortices at approximately $x/D = 2.5D$. The jet between cylinders 1 and 2 fluctuates periodically in the transverse direction due to the large scale vortex shedding. Specifically, the jet is directed towards the side of the wake where the vortex is being formed (i.e., the side of the wake axis with larger circulation within the formation region). Unlike the case of $Re_D = 2100$, there is no bistable wake development at $\alpha = 0°$ for $Re_D = 100$. Due to the absence of the bistable phenomenon, no smaller scale shedding is present in addition to the shedding of the main vortices.

For $\alpha = 60°$ (Figure 6.2), the flow development behind the cluster is similar to $\alpha = 0°$ case. The outer shear layers of cylinders 1 and 3 merge with the same sense shear layers of cylinder 2, producing large scale vortices at approximately $x/D = 3$. The size of these vortices is larger than that for $\alpha = 0°$. The jets exiting the cluster between cylinders 1 & 2 and 3 & 2 do not fluctuate appreciably with the shedding frequency, contrary to the case of $\alpha = 0°$. Compared to $Re_D = 2100$, the inner shear layers of cylinders 1 and 3 do not roll up into smaller scale vortices for $Re_D = 100$.

Multiple tests were performed to ensure there is no bistable wake development for $\alpha = 0°$ at $Re_D = 100$. Previous studies (e.g., [19]) show that a bistable wake configuration occurs behind two cylinders in a side-by-side arrangement at a Reynolds number as low as 55. Hence, the model was tested for a two cylinder setup in a side-by-side arrangement (i.e., $\alpha = 0°$) under the present conditions to verify that a bistable wake is achieved. The streamwise mean velocity fields for the two cylinder setup, presented in Appendix C.1, show a bistable wake development. For the triangular cluster, a finite transverse velocity component in both directions was applied to the initial velocity field to force the narrow wake behind either of the two downstream cylinders. Also, tests with small cluster orientations (i.e., $-3° \leq \alpha \leq 3°$) were performed to force the bistable wake development. The results for some of the tests are shown in Appendix C.1. Streamwise mean velocity fields for all tests showed no bistable wake. Thus, it is concluded that there is no bistable wake development for a triangular cluster at the present spacing ratio for $\alpha = 0°$ and $Re_D = 100$.

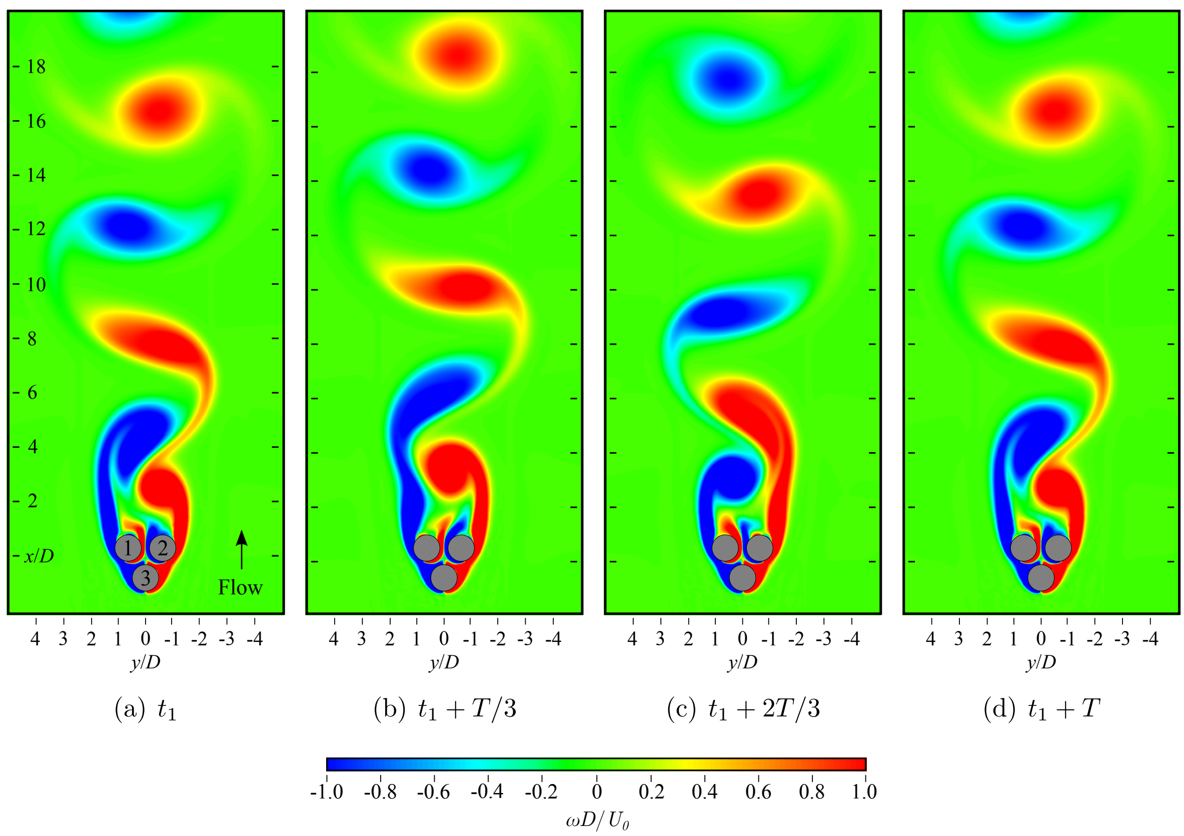

Figure 6.1: Vorticity contours for one large scale shedding cycle for $\alpha = 0°$ at $Re_D = 100$.

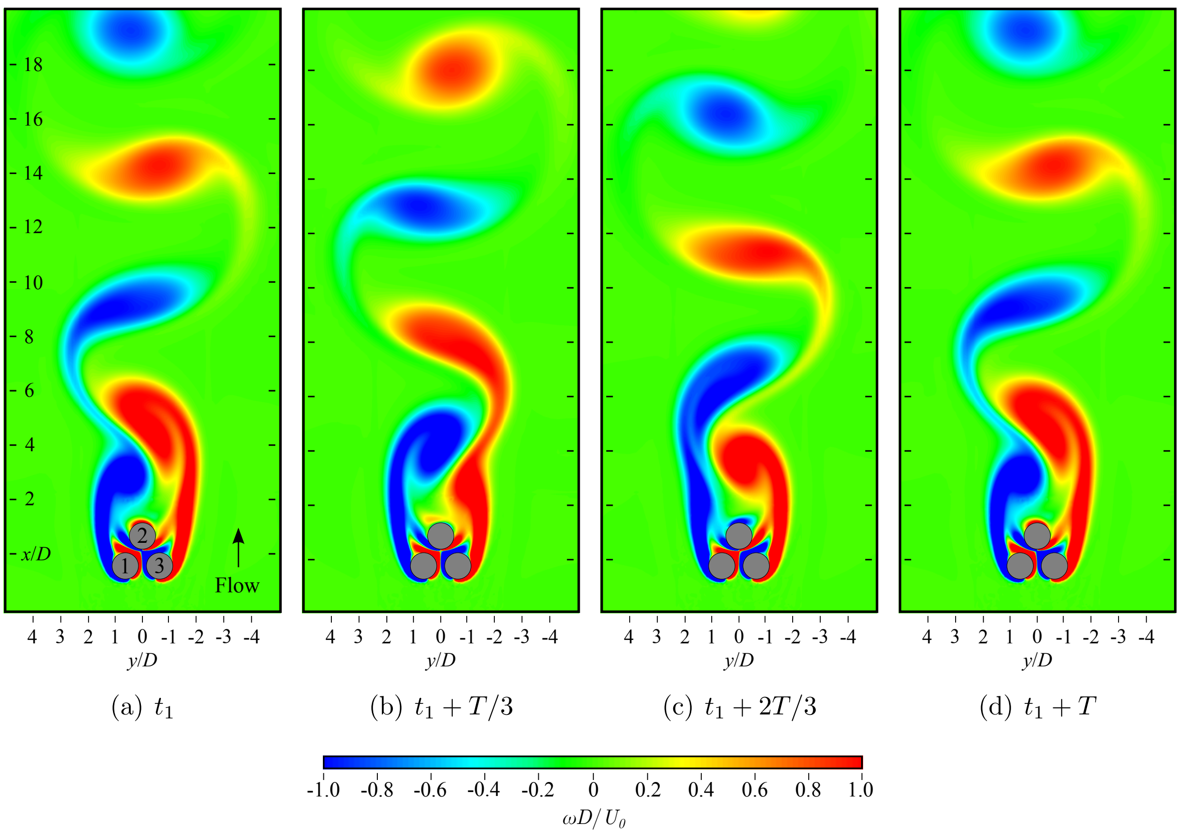

(a) t_1 (b) $t_1 + T/3$ (c) $t_1 + 2T/3$ (d) $t_1 + T$

Figure 6.2: Vorticity contours for one large scale shedding cycle for $\alpha = 60°$ at $Re_D = 100$.

6.1.2 Mean statistics

The mean velocity fields for $\alpha = 0°$ and $60°$ are presented in Figure 6.3. The results show a symmetric wake development about $y/D = 0$ for both orientations. For $\alpha = 0°$, one large recirculation region is present behind the two downstream cylinders. The streamwise velocity of the jet between cylinders 1 and 2 decreases rapidly with increasing x/D due to the reverse flow in the recirculation region. For $\alpha = 60°$ (Figure 6.3b), symmetric narrow wakes are produced behind cylinders 1 & 3 and a wide wake forms behind cylinder 2, similar to the experimental results at $Re_D = 2100$.

Table 6.1 shows the downstream extent of the recirculation region, L_f, defined as the distance from the origin of the cluster to the point of zero velocity along the wake axis, for $\alpha = 0°$ and $60°$. The results show that L_f for $\alpha = 0°$ is approximately 10% smaller than that for $\alpha = 60°$. This decrease in L_f is attributed to the high speed jet exiting the cluster (Figure 6.3). For the case of $\alpha = 0°$, there is increased flow rate from the jet between cylinders 1 and 2 into the recirculation region (Figure 6.3). As discussed in Chapter 5, the length of the recirculation region is inversely proportional to the amount of bleed flow added to the recirculation region. Therefore, for the cluster, it is expected that L_f should be smaller for the case of $\alpha = 0°$ than that for $\alpha = 60°$ (Figure 6.3). Table 6.1 also shows the comparison of L_f with Reynolds number for both cluster orientations. For both orientations, L_f increases with Re_D. However, the increase in L_f is greater for $\alpha = 0°$ than that for $\alpha = 60°$. In comparison to $\alpha = 0°$ at $Re_D = 2100$ (Figure 5.9), the bleed flow entering the recirculation region is greater for $Re_D = 100$ because the jet is directed towards either of the downstream cylinders for $Re_D = 2100$.

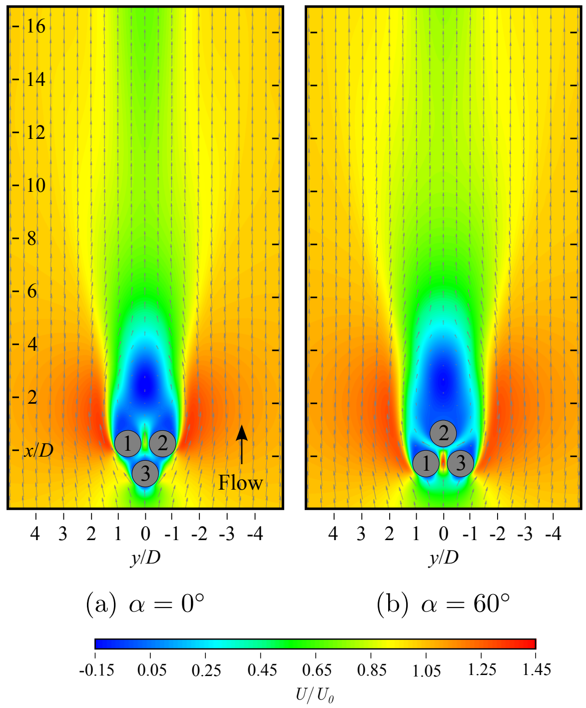

Figure 6.3: Mean streamwise velocity contours for $\alpha = 0°$ and $60°$ at $Re_D = 100$.

The RMS fields for the streamwise and transverse velocity component are presented in Figure 6.4. The results for the streamwise component show two symmetric regions of relatively high velocity fluctuations located approximately within $2 < x/D < 5$ for both orientations. These fluctuations are associated with the wake vortex shedding. For $\alpha = 0°$, the maximum u' occurs at $x/D \approx 3$ and $y/D \approx \pm 1$, which is associated with location of vortex formation. The inner shear layers of cylinders 1 & 2 have higher velocity fluctuations than the outer ones. This is due to the flapping of the inner shear layers seen previously in the sequence of vorticity fields (Figure 6.1). For $\alpha = 60°$, the maximum u' occurs at $x/D \approx 3.5$ and $y/D \approx \pm 1$, which is also associated with location of vortex formation. The

Table 6.1: Length of the recirculation region for $\alpha = 0°$ and $60°$ at $Re_D = 100$ and $Re_D = 2100$.

α	$L_f/D\,(Re_D = 100)$	$L_f/D\,(Re_D = 2100)$
$0°$	2.62	5.56
$60°$	2.91	3.69

transverse RMS field for both orientations (Figure 6.4c and 6.4d) shows a single region along the centerline of high velocity fluctuations induced by the shedding. The transverse RMS fields for both orientations shows similar features; however, the magnitude of the maximum fluctuation for $\alpha = 60°$ is lower. For both orientations, the streamwise and transverse RMS fields show similar features to those for the wake of a single cylinder [82, 86].

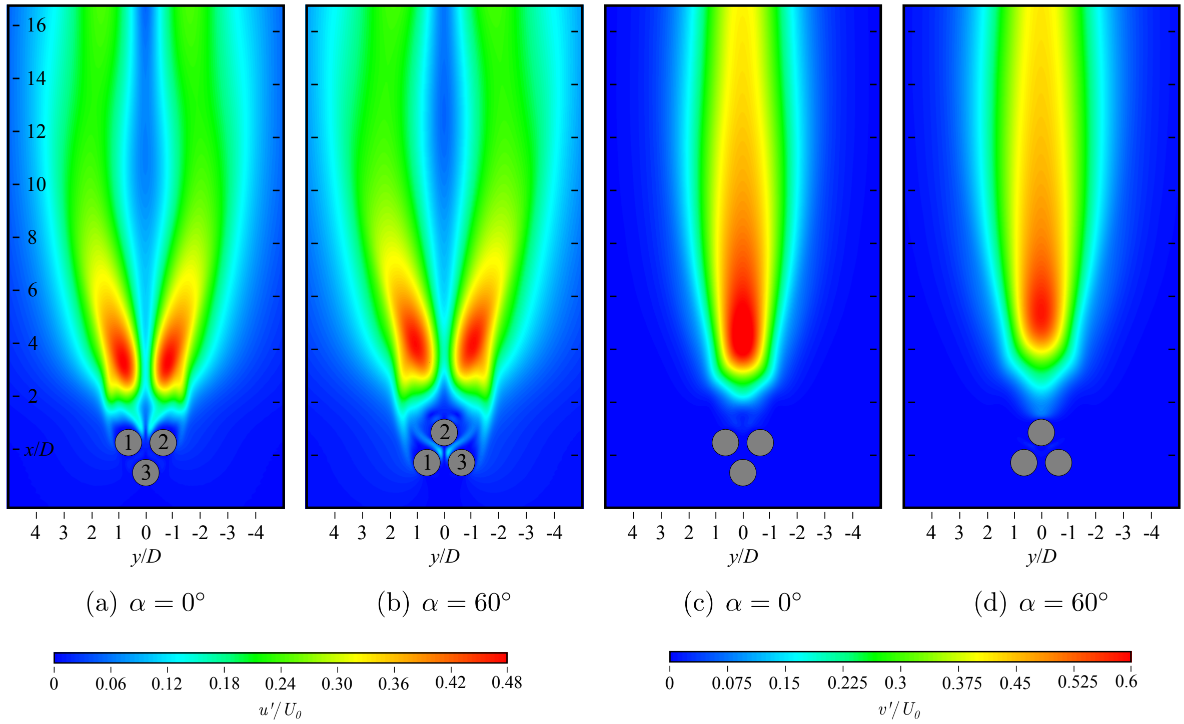

(a) $\alpha = 0°$ (b) $\alpha = 60°$ (c) $\alpha = 0°$ (d) $\alpha = 60°$

Figure 6.4: Contours of the RMS of the streamwise and transverse velocity component for $\alpha = 0°$ and $60°$ at $Re_D = 100$.

6.1.3 Frequency analysis

Figure 6.5 shows the velocity spectra of the streamwise velocity component measured downstream of the vortex formation region for $\alpha = 0°$ and $60°$. Both spectra show a dominant peak associated with the vortex shedding at $St_{D_h} \approx 0.2$. Other spectral peaks with lower energy content are associated with the harmonics of this shedding frequency. Table 6.2 compares the Strouhal number (normalized by the projected height of the cluster, D_h) for $Re_D = 100$ ($Re_{D_h} = 235$) and $Re_D = 2100$ ($Re_{D_h} = 4.9 \times 10^3$). The results show that the Strouhal number for the large scale shedding is approximately equal to that for

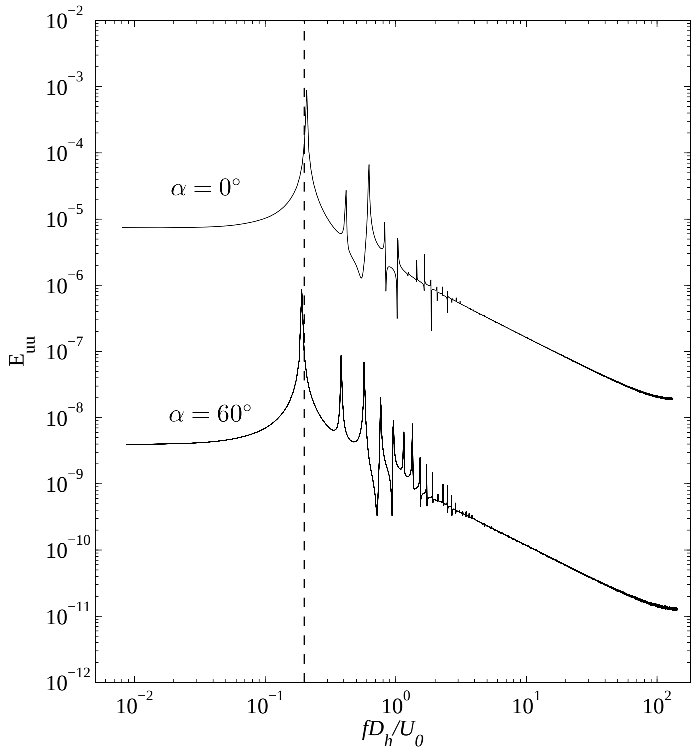

Figure 6.5: Velocity spectra of the streamwise velocity component at $x/D = 13$ and $y/D = -1.5$ for $\alpha = 0^\circ$ and 60° at $Re_D = 100$.

a single cylinder at the same Reynolds number for both orientations, suggesting that the cluster behaves like a single bluff body in terms of shedding frequency characteristics, regardless of the cluster orientation. Also, as the Reynolds number increases from $Re_{D_h} = 235$ to 4.9×10^3, St_{D_h} increases by approximately 5%, similar to the increase expected for a single cylinder.

Table 6.2: Strouhal number comparison when normalized by the projected height of the cluster.

Case	$St_{D_h}(Re_{D_h} = 235)$	$St_{D_h}(Re_{D_h} = 4.9 \times 10^3)$
$\alpha = 0°$	0.20 ± 0.005	0.21 ± 0.005
$\alpha = 60°$	0.20 ± 0.005	0.21 ± 0.005
Single cylinder [66]	0.20	0.21

6.1.4 Aerodynamic forces

Figures 6.6, 6.9 and 6.10 show the mean drag coefficient, mean lift coefficient, and RMS lift, respectively, for each cylinder in the cluster for $\alpha = 0°$ and $60°$ at $Re_D = 100$. In Figures 6.6 and 6.10, a dashed line represents the corresponding results expected for a single cylinder in uniform cross-flow at $Re_D = 100$. For the drag coefficient (Figure 6.6), both the maximum and minimum drag occur on individual cylinders within the cluster at $\alpha = 60°$. The maximum drag occurs on cylinders 1 & 3, and the minimum drag occurs on cylinder 2. Also, the drag on cylinders 1 & 3 for $\alpha = 60°$ is approximately 10% larger than that for a single cylinder. For $\alpha = 0°$, the drag on any of the cylinders is lower by at least 25% than the drag on a single cylinder. The mean pressure contours for $\alpha = 0°$ and $60°$ are shown in Figure 6.7. For $\alpha = 0°$, there is a relatively high base pressure ($C_{Pb} \approx 0$) on cylinder 3. This is higher than $C_{Pb} = -0.7$ expected for a single cylinder [5]. The higher base pressure is due to the presence of the two downstream cylinders, and leads to a reduction in drag on cylinder 3 compared to that for a single cylinder. For the two downstream cylinders, the highest pressure at the front of the cylinders is $C_P \approx 0.5$ and the base pressure is $C_{Pb} \approx -0.7$. The reduced pressure at the front of the cylinders is due

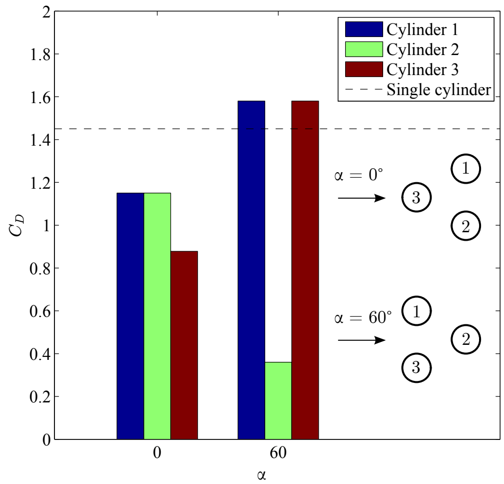

Figure 6.6: Mean drag coefficient of each cylinder for $\alpha = 0°$ and $60°$ at $Re_D = 100$. Dashed line represents result for the single cylinder case [77].

to the presence of the blockage from the upstream cylinder. This results in a lower drag coefficient for both downstream cylinders than that for a single cylinder. For $\alpha = 60°$, the stagnation pressure ($C_P \approx 1$) and base pressure ($C_{Pb} \approx -0.7$) on the two upstream cylinders are the same as those expected for a single cylinder. However, the extent of the low pressure region in the aft portion of the two upstream cylinders is larger (Figure 6.7b) due to earlier separation of the outer boundary layer ($\approx 80°$) compared to that expected for a single cylinder at the same Re_D ($\approx 115°$ [70]). This produces a larger drag on the upstream cylinders in the cluster compared to a single cylinder. The stagnation pressure on cylinder 2 is $C_P \approx 0$ and the base pressure is $C_{Pb} \approx -0.7$. Similar to $\alpha = 0°$, the relatively low stagnation pressure is due to the blockage from the two upstream cylinders. Therefore, the drag coefficient for cylinder 2 is lower than that for a single cylinder.

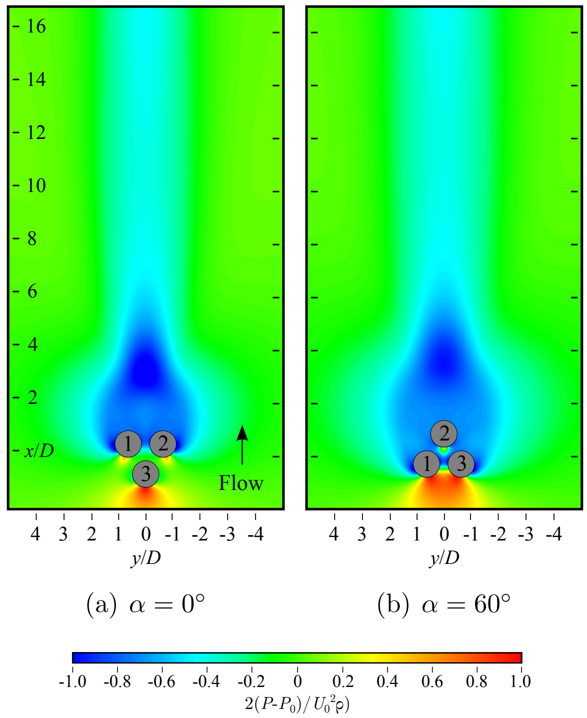

Figure 6.7: Contours of the mean pressure for $\alpha = 0°$ and $60°$ at $Re_D = 100$.

The total mean drag coefficient, based on the projected height of the cluster, is shown in Figure 6.8 for both orientations. The results show that the total drag coefficient on the cluster is approximately 13% higher for $\alpha = 60°$ than that for $\alpha = 0°$. Also, the total drag coefficient for $\alpha = 0°$ and $60°$ is approximately 6% lower and 8% higher, respectively, than that for a single cylinder at the same Reynolds number ($Re_{D_h} = 235$).

Figure 6.9 shows the mean lift coefficient for each cylinder in the cluster. As expected from the symmetry of the geometry about $y = 0$, there is no mean lift on cylinder 3 for $\alpha = 0°$ and cylinder 2 for $\alpha = 60°$. However, for all the other cylinders in the cluster, a mean lift force is produced due to the asymmetric pressure distribution on the cylinders

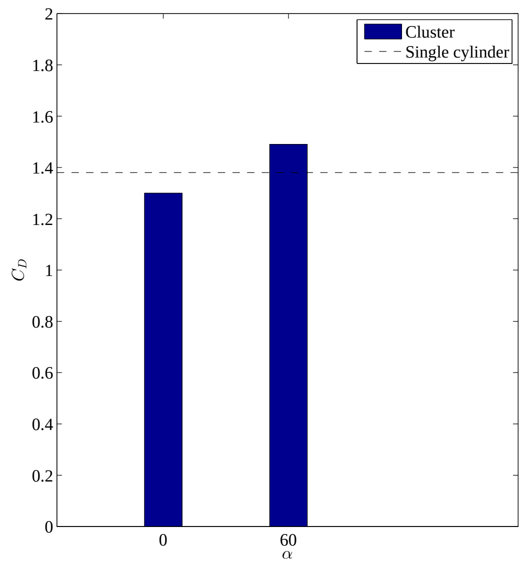

Figure 6.8: Total mean drag coefficient of the cluster for $\alpha = 0°$ and $60°$ at $Re_{D_h} = 235$. Dashed line represents result for the single cylinder case [77].

(Figure 6.7). For $\alpha = 0°$, the outer boundary layer of the two downstream cylinders separate earlier than the inner boundary layer, producing a lower pressure region on the outer sides of the downstream cylinders. This results in positive and negative mean lift forces on cylinders 1 and 2, respectively. For $\alpha = 60°$, the flow in the gap stagnates due to the presence of the downstream cylinder, producing a higher pressure region in the gap between cylinders 1 and 3. Thus, there is a mean lift force produced on the two upstream cylinders. However, for both $\alpha = 0°$ and $60°$, the total mean lift force on the cluster is zero due to symmetry of the flow about $y = 0$.

Figure 6.10 shows the RMS of the fluctuating lift coefficient for each cylinder. The maximum RMS lift occurs on cylinder 2 for $\alpha = 60°$ and is approximately 35% higher than

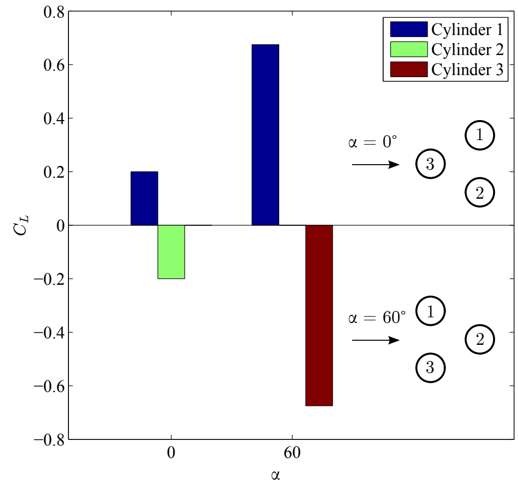

Figure 6.9: Mean lift coefficient of each cylinder for $\alpha = 0°$ and $60°$ at $Re_D = 100$.

that expected for a single cylinder. All other RMS lift forces are at least 45% lower than that for a single cylinder. The RMS lift is due to fluctuations in the pressure field induced by vortex shedding. The magnitude of the corresponding fluctuations is expected to be related to the length of the formation region and the strength of the vortices. For both orientations, cylinders positioned closer to the vortex formation region (i.e., cylinders 1 & 2 for $\alpha = 0°$ and cylinder 2 for $\alpha = 60°$) have higher RMS lifts than those for the upstream cylinder(s). Cylinders 1 & 2 for $\alpha = 0°$ have smaller RMS lift than cylinder 2 for $\alpha = 60°$ because cylinder 2 experiences high pressure fluctuations on both sides (Figure 6.12b); whereas, high pressure fluctuations on cylinders 1 & 2 for $\alpha = 0°$ occur only on the outer sides (Figure 6.12a). Also, the RMS lift on cylinder 2 at $\alpha = 60°$ exceeds the value of that expected for a single cylinder. The distance between cylinder 2 and the vortex formation region is approximately the same as that compared to a single cylinder [87]; however, the

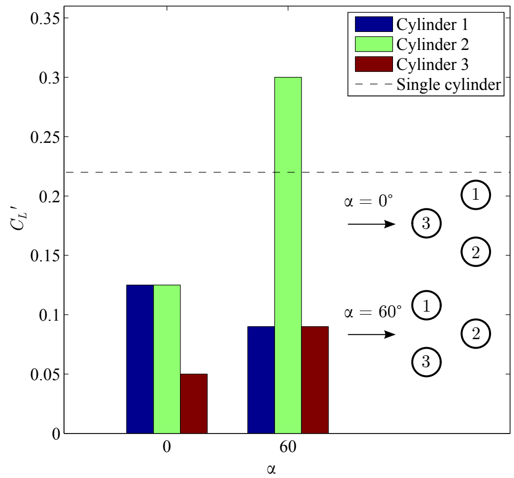

Figure 6.10: RMS of fluctuating lift coefficient of each cylinder for $\alpha = 0°$ and $60°$ at $Re_D = 100$. Dashed line represents result for the single cylinder case [66].

size of vortices forming behind the cluster are larger than those expected for the single cylinder case because they scale with the projected height of the cluster ($D_h = 2.35D$). Therefore, the RMS lift on cylinder 2 at $\alpha = 60°$ is larger than that expected for a single cylinder.

The total RMS lift coefficient, based on the projected height of the cluster, is shown in Figure 6.11 for both orientations. The results show that the total RMS coefficient on the cluster is approximately 70% higher for $\alpha = 60°$ than that for $\alpha = 0°$. Also, the total RMS coefficient for $\alpha = 0°$ and $60°$ is approximately 30% lower and 20% higher, respectively, than that for a single cylinder at the same Reynolds number ($Re_{D_h} = 235$).

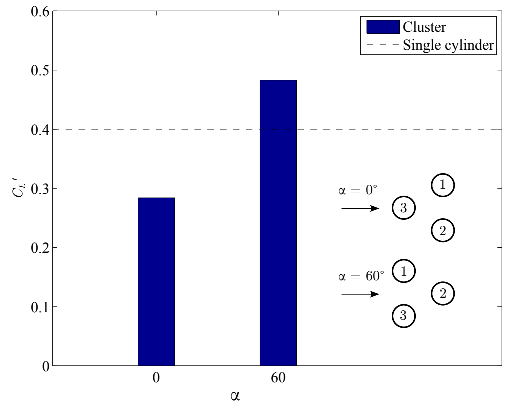

Figure 6.11: Total RMS of fluctuating lift coefficient of the cluster for $\alpha = 0°$ and $60°$ at $Re_D = 235$. Dashed line represents result for the single cylinder case [66].

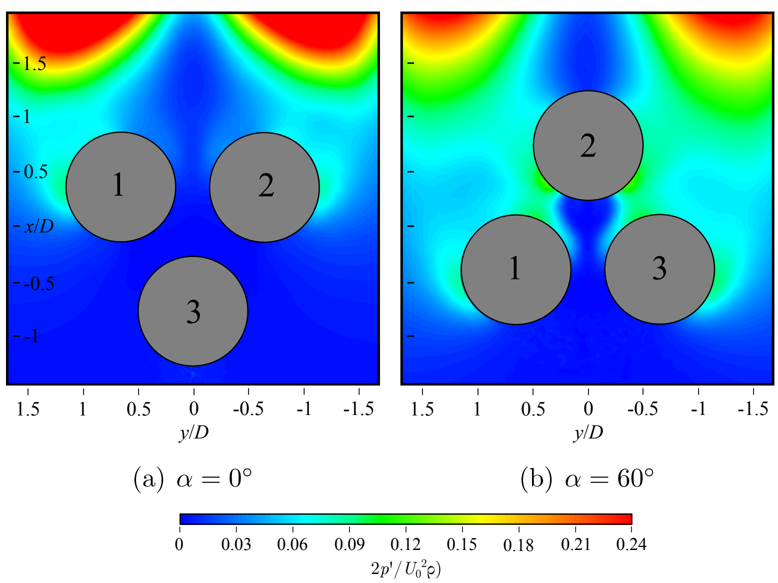

Figure 6.12: RMS of fluctuating pressure surrounding the cylinders of the cluster for $\alpha = 0°$ and $60°$ at $Re_D = 100$.

6.2 RANS simulations at $Re_D = 2100$

Four turbulence models were investigated for the present geometry: (i) SST, (ii) $k-\epsilon$, (iii) $k-\omega$, and (iv) LRR-IP. Figures 6.13, 6.14, and 6.15 show the mean streamwise velocity contours for $\alpha = 0°$ and $60°$ for each turbulence model. At $\alpha = 0°$, the bistable case was induced by prescribing $u = 0.1U_0$ and $v = \pm 0.1U_0$ as initial conditions. Only the SST and $k-\omega$ models show a bistable wake, in which the jet is directed towards either one of the two downstream cylinders. The $k-\epsilon$ and LRR-IP models show a symmetric wake development about the wake axis. From the experimental results at the same setup conditions, a bistable wake development was observed for $\alpha = 0°$ (Figures 5.1 and 5.2). For $\alpha = 60°$ (Figure 6.15), all the models predict a symmetric wake development, as expected from experimental results. However, the size of the recirculation regions behind each of the cylinders varies for each model. For both $\alpha = 0°$ and $60°$, the streamwise extent of the recirculation region behind each of the cylinders is smaller for $k-\epsilon$ & LRR-IP and larger for SST & $k-\omega$ when compared to the experimental results (Figure 5.9).

For a direct comparison between the results from the turbulence models and experimental results, mean streamwise velocity profiles were extracted. Figures 6.16, 6.17, and 6.18 shows the comparison at $x/D = 2$, 4, 6, and 8 for $\alpha = 0°$ and $60°$. For $\alpha = 0°$, the profiles at $x/D = 2$ and 4 from the SST and $k-\omega$ results agree well with the experimental data. Beyond $x/D = 4$, the SST and $k-\omega$ under-predict the mean streamwise velocity. This is also seen in the mean streamwise velocity contours for the SST and $k-\omega$ models (Figures 6.13 and 6.14), in which the streamwise extent of the recirculation region is approximately 2 times larger than the experimental results (Figure 5.9). Also, beyond $x/D = 4$, the

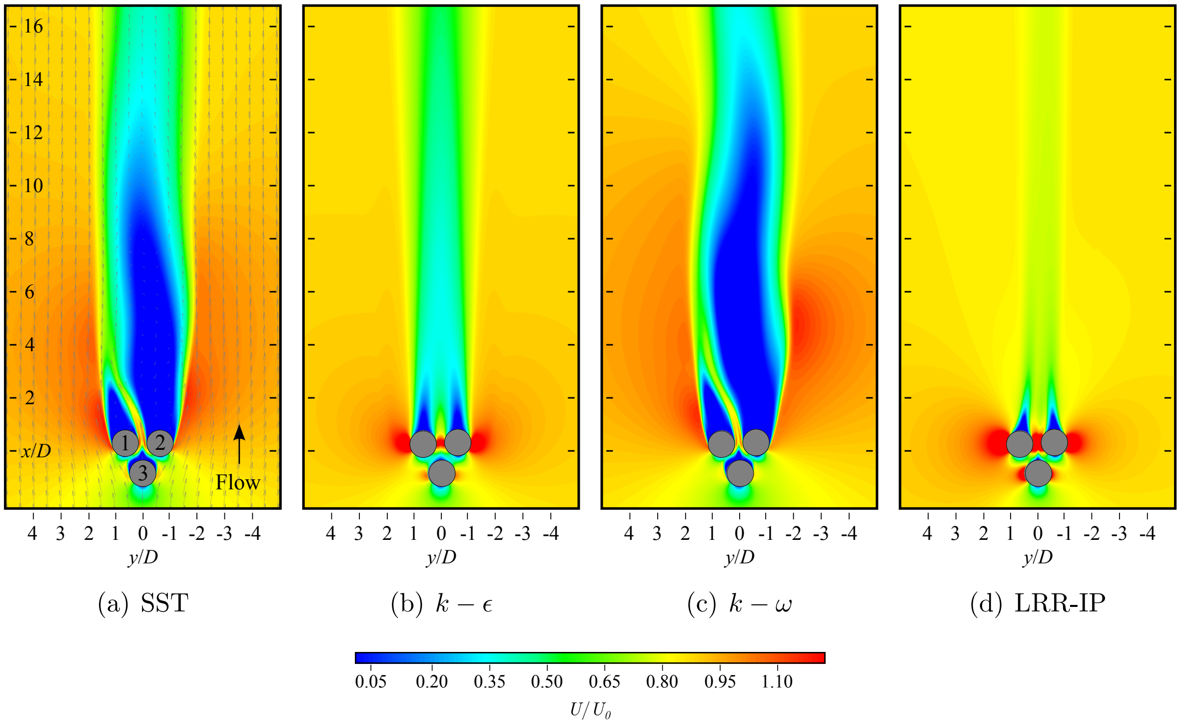

(a) SST (b) $k-\epsilon$ (c) $k-\omega$ (d) LRR-IP

Figure 6.13: Mean streamwise velocity contours for $\alpha = 0°$ with the jet deflected towards cylinder 1 at $Re_D = 2100$ for each turbulence model.

results from the $k-\epsilon$ model agree well with the experimental results. The LRR-IP model over-predicts the velocity at each location. For $\alpha = 60°$ (Figure 6.18), all the models fail to accurately reproduce the mean streamwise velocity at the near wake of the cluster (i.e., $x/D = 2$).

The mean drag and lift coefficients for each cylinder and turbulence model are shown in Figures 6.19, 6.20, and 6.21. Experimental results of sectional lift and drag coefficients for an equispaced cluster with $P/D = 1.25$ for $Re_D = 3 \times 10^4$ [10] and $P/D = 1.39$ for $Re_D = 6.2 \times 10^4$ [88] are shown for comparison in these figures. It should be noted that the

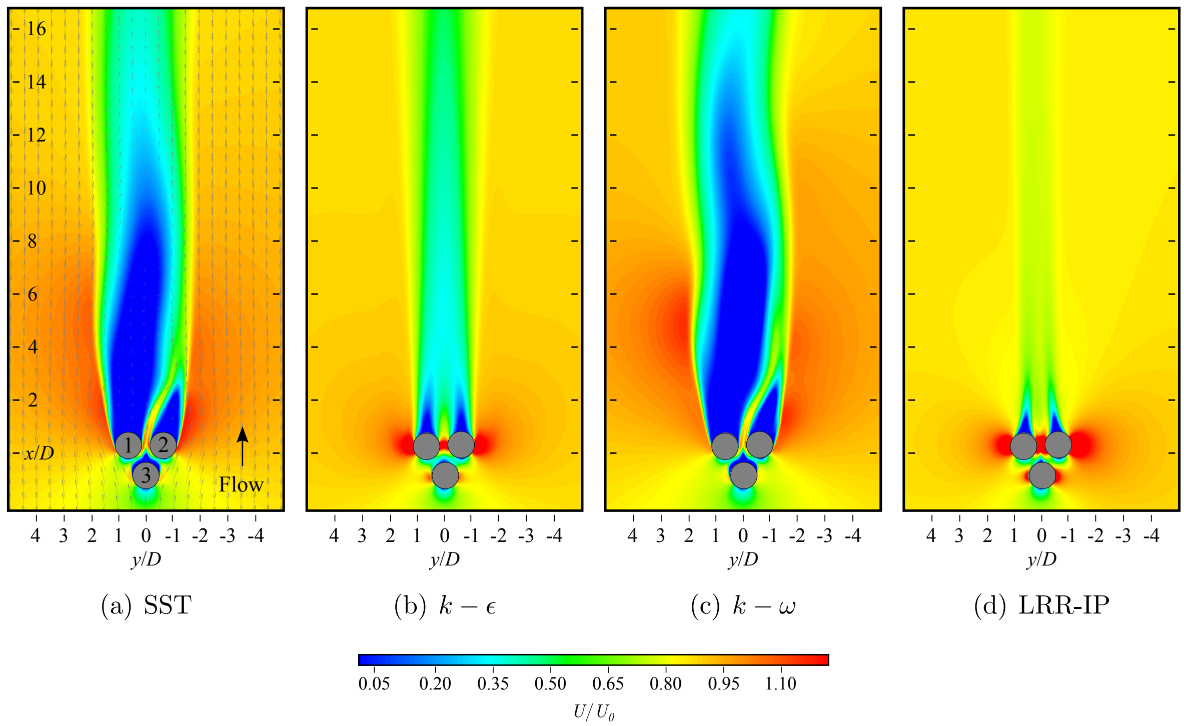

Figure 6.14: Mean streamwise velocity contours for $\alpha = 0°$ with the jet deflected towards cylinder 2 at $Re_D = 2100$ for each turbulence model.

purpose of these results is not a direct comparison; instead, they are presented to compare general trends. Also, a dashed line representing the results for a single cylinder case is shown in these figures for comparison purposes. In both orientations, the variation of the aerodynamic loads on each cylinder in the cluster follow the general trend in experimental data for the results from SST and $k-\omega$. For the other two models, the results do not follow the general trends of the experimental data. The evaluation of the four turbulence models thus far suggests that overall the results of SST and $k-\omega$ model show better agreement (within $\approx 25\%$) with experimental data. Thus, for clarity, the following discussion of forces

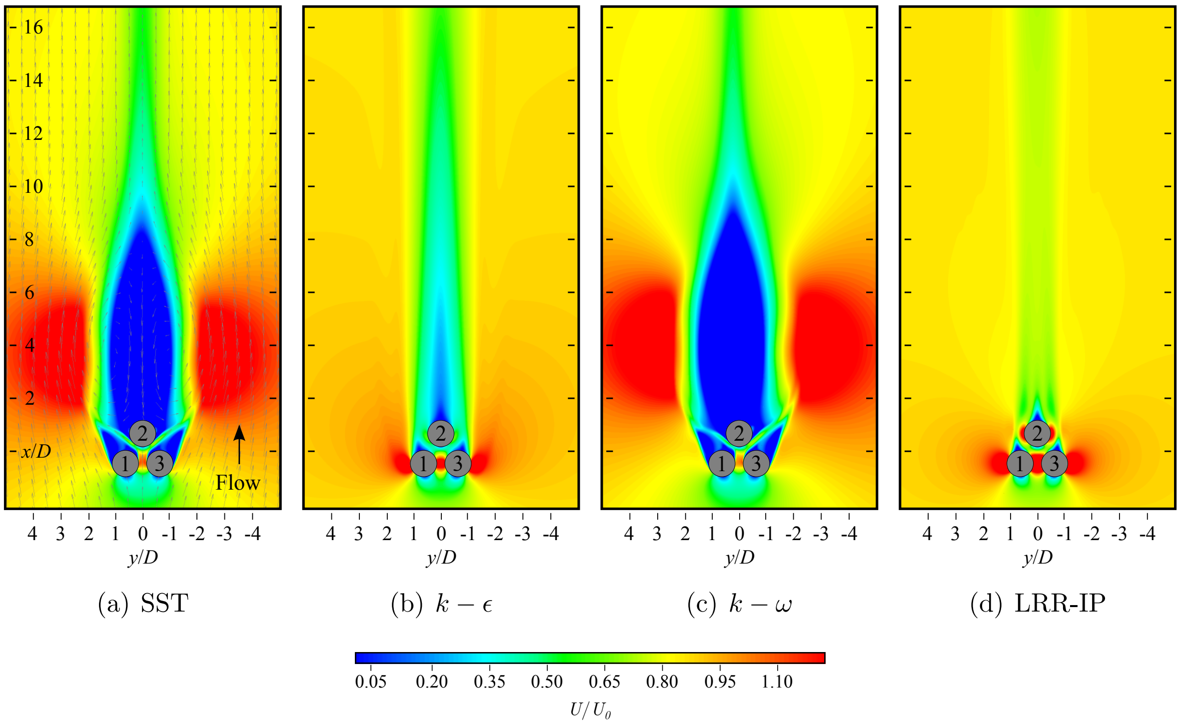

(a) SST (b) $k - \epsilon$ (c) $k - \omega$ (d) LRR-IP

Figure 6.15: Mean streamwise velocity contours for $\alpha = 60°$ at $Re_D = 2100$ for each turbulence model.

will be based on the results from the SST model.

Figure 6.22 shows the mean pressure contours near the cylinders in the cluster. For $\alpha = 0°$, the maximum drag occurs on the cylinder that produces the narrow wake (i.e., cylinder 1 in Figure 6.19 and cylinder 2 in Figure 6.20). For the case when the narrow wake is behind cylinder 1 (Figure 6.19), the base pressure on cylinder 1 ($C_{Pb} \approx -0.7$) is lower than that of cylinder 2 ($C_{Pb} \approx -0.4$), leading to a higher drag on cylinder 1. The drag on cylinder 3 is approximately the same as that on the cylinder producing the wide wake (i.e., cylinder 2 in Figure 6.19 and cylinder 1 in Figure 6.20). This is due to the stagnation and

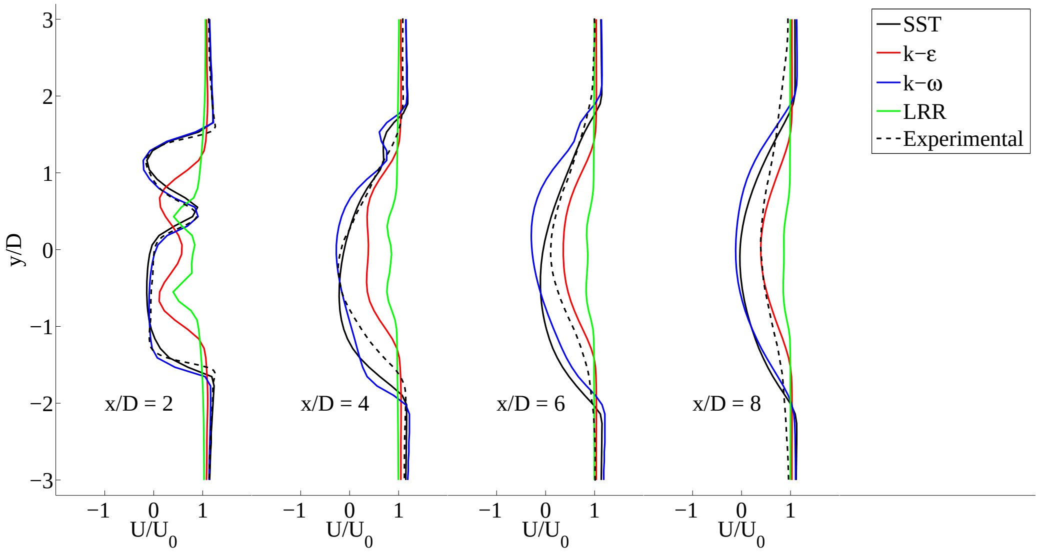

Figure 6.16: Profiles of the mean streamwise velocity component for all turbulence models at four downstream locations for $\alpha = 0°$ with the jet deflected towards cylinder 1.

base pressure of cylinder 3 are both being higher by the same ΔC_P than the stagnation and base pressure of the cylinder producing the wide wake. Also, for $Re_D = 2100$, the drag coefficient of all cylinders for this orientation is at least 20% smaller than that expected for a single cylinder [77]. This is similar to $Re_D = 100$; however, there are differences between the results for $Re_D = 100$ and $Re_D = 2100$ attributed to the absence of the bistable regime at the lower Re_D. Specifically, the drag on both downstream cylinders is not equal for $Re_D = 2100$; instead, the drag on the downstream cylinder producing the wide wake is approximately the same as that on the upstream cylinder.

For $\alpha = 60°$, the trends in drag of the three cylinders in the cluster at $Re_D = 2100$ are the same as those observed for $Re_D = 100$. The maximum drag in the cluster occurs on cylinders 1 and 3. Figure 6.22 shows that the base pressure on the upstream cylinders is

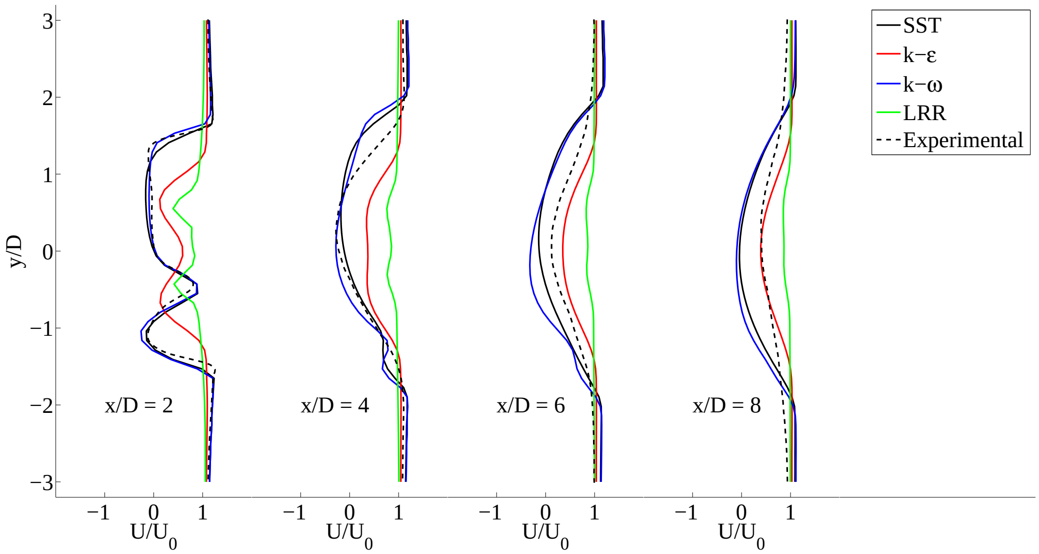

Figure 6.17: Profiles of the mean streamwise velocity component for all turbulence models at four downstream locations for $\alpha = 0°$ with the jet deflected towards cylinder 2.

smaller by $C_{Pb} \approx 0.3$ than that on the downstream cylinder. Also, the stagnation pressure is greater on the upstream cylinders. Therefore, the drag on the upstream cylinders is greater than that on cylinder 2. The stagnation pressure on the upstream cylinders is the same as that for a single cylinder case; however, due to the presence of the downstream cylinder, the base pressure on the upstream cylinders is greater than that on a single cylinder [5]. This produces a smaller drag on the upstream cylinders than that on a single cylinder. The drag on the downstream cylinder is smaller than that on a single cylinder because of the higher base pressure ($C_{Pb} \approx 0$) on the downstream cylinder.

Similar to $Re_D = 100$, mean lift forces are produced on the two downstream cylinders for $\alpha = 0°$ and the two upstream cylinders for $\alpha = 60°$ for $Re_D = 2100$ (Figure 6.21). The lift on cylinder 3 and 2 for $\alpha = 0°$ and $60°$, respectively, is zero due to the flow symmetry

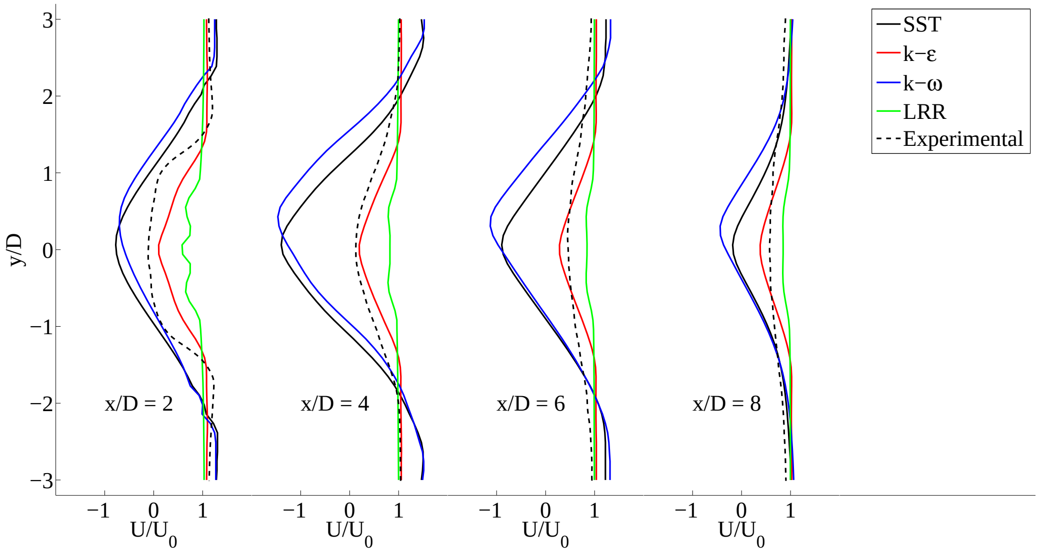

Figure 6.18: Profiles of the mean streamwise velocity component for all turbulence models at four downstream locations for $\alpha = 60°$.

about $y = 0$. Unlike $Re_D = 100$, the bistable nature of the flow leads to non-symmetric lift forces produced on the two downstream cylinders for $\alpha = 0°$. The direction of the forces also differs from that in the case of $Re_D = 100$. Specifically, the stagnation point is shifted towards the outer sides of cylinders 1 and 2, which leads to lift forces being directed towards $y = 0$. For $\alpha = 60°$, lift forces on cylinders 1 and 3 are equal and opposite in direction, similar to $Re_D = 100$. However, the magnitude of the lift coefficient for $Re_D = 2100$ is approximately 70% lower. This is due to the lower base pressure on the upstream cylinders for $Re_D = 100$.

The total drag for the cluster for $\alpha = 0°$ and $60°$ is shown in Figure 6.23. The total drag is approximately the same for both orientations and is approximately 15% smaller than that for a single cylinder at an equivalent Reynolds number ($Re_{D_h} = 4.9 \times 10^3$).

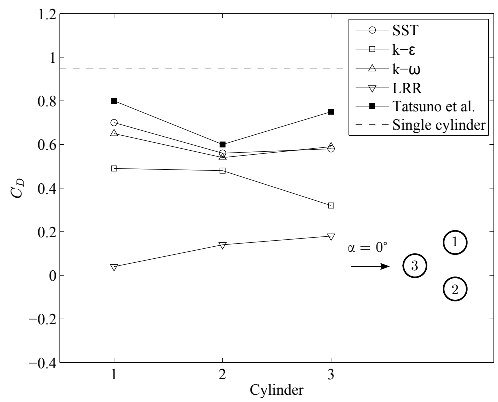

(a) C_D

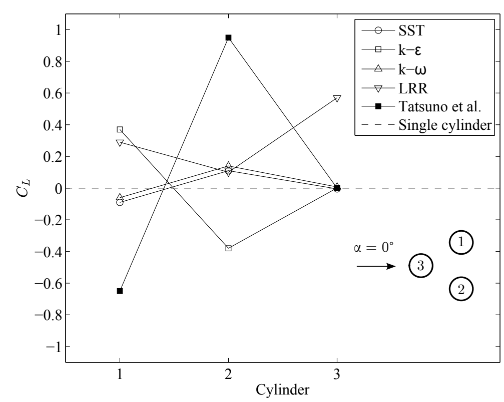

(b) C_L

Figure 6.19: Mean drag and lift coefficients for each cylinder in the cluster for $\alpha = 0°$ with the jet deflected towards cylinder 1. The filled-square markers show data for an equilateral cluster with $P/D = 1.39$ at $Re_D = 6.2 \times 10^4$ [88]. The dashed line represents the results for a single cylinder case at the same Reynolds number ($Re_D = 2100$) [77].

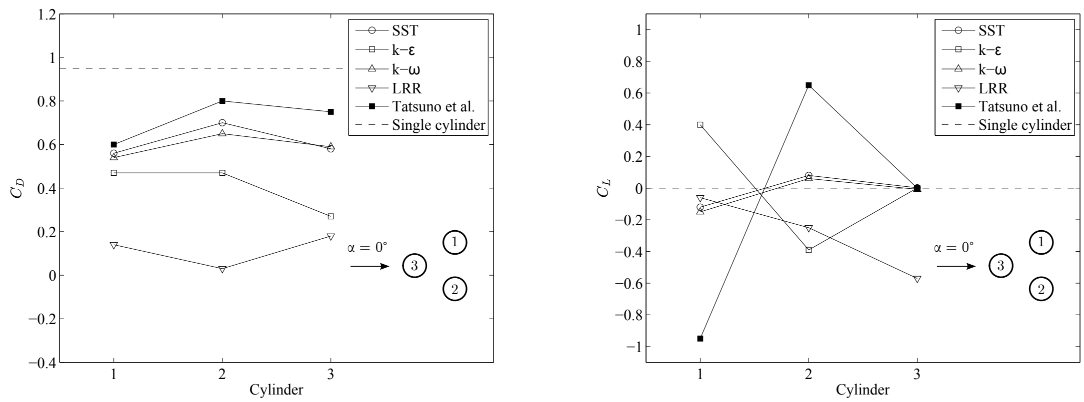

(a) C_D

(b) C_L

Figure 6.20: Mean drag and lift coefficients for each cylinder in the cluster for $\alpha = 0°$ with the jet deflected towards cylinder 2. The filled-square markers show data for an equilateral cluster with $P/D = 1.39$ at $Re_D = 6.2 \times 10^4$ [88]. The dashed line represents the results for a single cylinder case at the same Reynolds number ($Re_D = 2100$) [77].

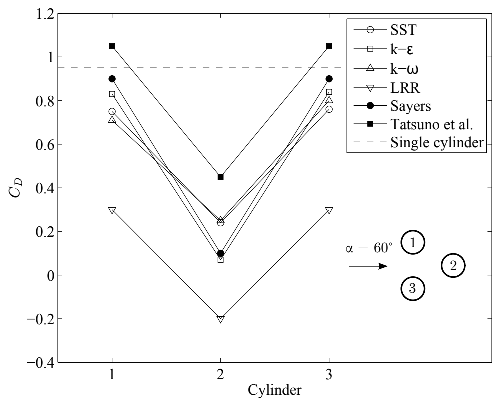

(a) C_D

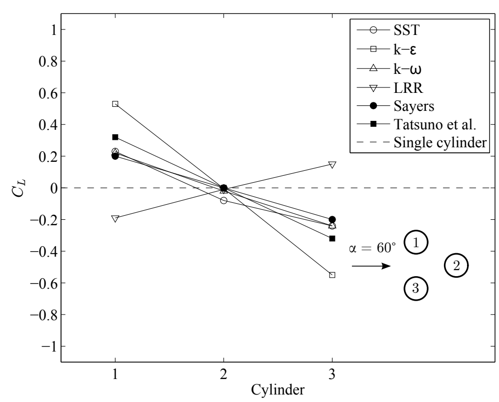

(b) C_L

Figure 6.21: Mean drag and lift coefficients for each cylinder in the cluster for $\alpha = 60°$. The filled-square markers show data for an equilateral cluster with $P/D = 1.39$ at $Re_D = 6.2\times10^4$ [88]. The filled-circle markers show data for an equilateral cluster with $P/D = 1.25$ at $Re_D = 3 \times 10^4$ [10]. The dashed line represents the results for a single cylinder case at the same Reynolds number ($Re_D = 2100$) [77].

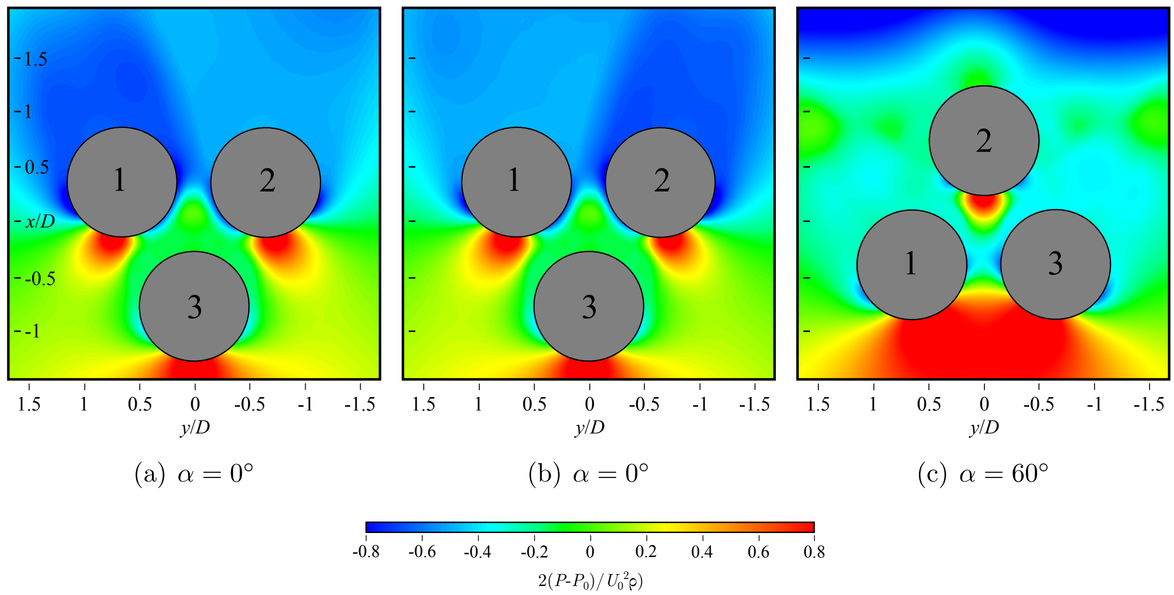

Figure 6.22: Mean pressure contours near the cylinders for $\alpha = 0°$ and $60°$.

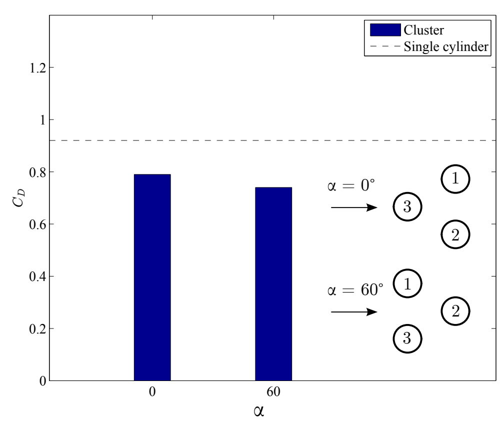

Figure 6.23: Total mean drag coefficient of the cluster for $\alpha = 0°$ and $60°$ at $Re_{D_h} = 4.9 \times 10^3$. Dashed line represents result for the single cylinder case [77].

Chapter 7

Conclusions

Flow development through a cluster of three equally spaced cylinders was investigated experimentally and numerically at $P/D = 1.35$. The main objective was to investigate the effects of cluster orientation on flow characteristics. Experiments were performed for $0° \leq \alpha \leq 60°$ at $Re_D = 2100$ using hydrogen bubble flow visualization, particle image velocimetry, and laser Doppler velocimetry. The flow was numerically modeled for $\alpha = 0°$ and $60°$ using laminar and RANS simulations at $Re_D = 100$ and $Re_D = 2100$, respectively. For $Re_D = 2100$, the SST, $k - \omega$, $k - \epsilon$, and LRR-IP turbulence models were evaluated by comparing to experimental results.

The experimental results for $Re_D = 2100$ show periodic large scale vortex shedding beyond $x/D \approx 5$ in the cluster wake for all orientations. The Strouhal number, based on the projected height of the cluster, is $St_D \approx 0.2$ for all orientations and to that expected for a single cylinder at the same Reynolds number. Experiments at $\alpha = 0°$ showed a bistable wake development behind the cluster. The jet exiting the cluster can orient towards either of the two downstream cylinders, producing a narrow and a wide wake behind the cluster, with no intermittent switching. Small scale vortices shed from the narrow wake interact with the inner shear layers of the wide wake, producing less coherent large scale structures as compared to the vortices forming on the opposite side of the wake. As α increases from $0°$ to $60°$, the asymmetry in the wake development about $y = 0$ decreases. For $\alpha = 60°$, a symmetric wake development is achieved, with two narrow wakes forming behind the upstream cylinders and a wide wake behind the downstream cylinder. The length of the recirculation region of the narrow and wide wakes both vary with the cluster orientation. For the narrow wake, the streamwise extent of the recirculation region is related to the trajectory of the jet exiting between cylinders 1 and 2. For the wide wake, it is proportional to the projected height of the cluster, D_h, and inversely proportional to the flow rate through the cluster. Also, the half wake width downstream of the recirculation region is proportional to D_h.

POD analysis showed that the first two modes are associated with large scale shedding for all orientations. Depending on α, the first two modes capture 45% to 75% of the total energy content in the wake. Modes associated with small scale shedding comprise of only 1% to 4%, depending on α, of the total energy content. The reduced-order model consisting of the first 40 modes illustrates the iteration between the large and small scale structures. During one small scale shedding cycle, three features were identified: (i) merging of the outer shear layer of the narrow wake and the inner shear layer of the wide wake, (ii) cancellation of supply of circulation from the outer shear layer of the narrow wake due to vortices forming from the inner shear layer of the narrow wake, and (iii) convection of vortices shed from the inner shear layer of the narrow wake into the formation region of the large scale structures. Depending on the ratio between the small and large scale shedding frequencies, approximately four to six interactions from (i) to (iii) occur for one large scale shedding cycle. This process results in the formation of a large scale structure encompassing smaller scale vortices with opposite sense, which reduces its coherence relative to the large scale vortices forming on the opposite side of the wake.

Numerical results for $Re_D = 100$ show a symmetric wake development for both $\alpha = 0°$ and $60°$. No bistable wake is present for $\alpha = 0°$ at $Re_D = 100$. For both orientations, there is no small scale shedding present, as compared to that for $Re_D = 2100$. The Strouhal number, based on the projected height of the cluster, is approximately the same ($St_D \approx 0.2$) for both orientations and as that expected for a single cylinder at the same Reynolds number. The length of the recirculation region for $\alpha = 0°$ is smaller than that for $\alpha = 60°$ due to the increased flow rate into the recirculation region from the jet between cylinders 1 and 2 for $\alpha = 0°$.

The force analysis for $Re_D = 100$ shows that the drag on all cylinders for $\alpha = 0°$ is at least 25% lower than that on a single cylinder. For $\alpha = 60°$, the drag on the two upstream cylinders is approximately 10% larger than that on a single cylinder. The total drag on the cluster for $\alpha = 0°$ and $60°$ is $C_P \approx 1.35$ and $C_P \approx 1.5$, respectively. The total drag on the cluster is approximately 6% smaller and 8% higher for $\alpha = 0°$ and $60°$, respectively, than that expected for a single cylinder. Mean lift forces are generated on the two downstream cylinders for $\alpha = 0°$ and the two upstream cylinders for $\alpha = 60°$. However, the total mean lift for the cluster is zero for both orientations. The total RMS for the cluster for $\alpha = 0°$ and $60°$ is ${C_L}' \approx 0.3$ and ${C_L}' \approx 0.5$, respectively. The maximum RMS lift is produced on the downstream cylinder for $\alpha = 60°$ and is approximately 35% larger than that for a single cylinder. The RMS lift forces for all other cylinders is at least 45% smaller than that for a single cylinder.

RANS simulations at $Re_D = 2100$ show that, overall, the results from the SST and $k-\omega$ models have better agreement (within $\approx 25\%$) with the experimental data and at the two model that predict the bistable wake development. The $k-\epsilon$ and LRR-IP model predict a symmetric wake development for $\alpha = 0°$ and under predicts the streamwise extent of the recirculation region for both orientations.

For clarity, the force analysis focused on the results from the SST model. For $\alpha = 0°$, the maximum drag occurs on the cylinder producing the narrow wake. Differences between the results for $Re_D = 2100$ and $Re_D = 100$ are attributed to the absence of the bistable phenomenon at $Re_D = 100$. For $\alpha = 60°$, the maximum drag occurs on the two upstream cylinders. The relative trends in the aerodynamic loads on each cylinder in the cluster are similar for both $Re_D = 2100$ and $Re_D = 100$. The drag coefficient for all cylinders in both orientations is at least 20% lower than that expected on a single cylinder. For both orientations, the total drag coefficient for the cluster is approximately 15% smaller than that for the single cylinder case. Mean lift forces are produced only on the two upstream cylinders for $\alpha = 60°$ and the two downstream cylinders for $\alpha = 0°$.

Chapter 8

Recommendations

While accomplishing the main objectives of this investigation, current work has encountered some unsolved questions. The following recommendations are provided for further research to address these questions:

1. It is of interest to investigate the bistable flow regime, which occurs for $\alpha = 0°$ at $Re_D = 2100$. The bistable wake development consists of two asymmetric wakes behind the cluster, resulting in complex vortex dynamics in the cluster near wake and different loading on the two downstream cylinders. The results showed that the bistable regime occurred at $Re_D = 2100$, but not at $Re_D = 100$. It is important to identify the onset of this instability for this geometry. One possible way to achieve this would be to perform numerical simulations for $100 < Re_D < 2100$.

2. The effects of cluster orientation on spanwise flow characteristics should be investigated. The present investigation was strictly focused on two-dimensional results. It

is recommended to perform flow visualization and quantitative measurements in the $x - z$ plane.

3. For further evaluation of the turbulence models, URANS should be performed. For improved accuracy, the domain should be modeled as three-dimensional and it is of interest to evaluate the same turbulence models based on the unsteady flow characteristics.

4. It is of interest to conduct a parametric study based on the spacing ratio, Reynolds number, and cluster orientation using qualitative and quantitative measurements. This will provide a more detailed map of various flow regimes for different combinations of flow and geometric parameters.

5. Qualitative and quantitative measurements should be performed with the yawed cluster. Industry applications of triangular clusters comprise of free-stream flow with both axial and cross-flow velocity components. It is of interest to understand the effects of the yaw angle on the flow characteristics.

Bibliography

[1] D. J. Tritton, "Experiments on the flow past a circular cylinder at low Reynolds numbers," *Journal of Fluid Mechanics*, vol. 6, pp. 547–567, 1959.

[2] A. Roshko, "Experiments on the flow past a circular cylinder at very high Reynolds number," *Journal of Fluid Mechanics*, vol. 10, pp. 345–356, 1961.

[3] J. H. Gerrard, "The mechanics of the formation region of vortices behind bluff bodies," *Journal of Fluid Mechanics*, vol. 25, pp. 401–413, Mar. 1966.

[4] J. H. Gerrard, "The wakes of cylindrical bluff bodies at low Reynolds number," *Philosophical Transactions of the Royal Society of London Series A, Mathematical and Physical Sciences*, vol. 288, pp. 351–382, 1978.

[5] C. H. K. Williamson, "Vortex dynamics in the cylinder wake," *Annual Reviews Fluid Mechanics*, pp. 477–539, 1996.

[6] M. M. Zdravkovich, *Flow Around Circular Cylinders, Vol 1: Fundamentals.* New York: Oxford University Press, 1997.

[7] M. Kiya, Y. Suzuki, M. Arie, and M. Hagino, "A contribution to the free-stream turbulence effect on the flow past a circular cylinder," *Journal of Fluid Mechanics*, vol. 115, pp. 151–164, 1982.

[8] A. Fage and J. H. Warsap, "Effects of turbulence and surface roughness on drag of circular cylinders," tech. rep., Aeronautical Research Council, 1930.

[9] M. M. Zdravkovich, "Smoke observations of the wake of a group of three cylinders at low Reynolds number," *Journal of Fluid Mechanics*, vol. 32, pp. 339–351, Mar. 1968.

[10] A. T. Sayers, "Flow interference between three equispaced cylinders when subjected to a cross flow," *Journal of Wind Engineering and Industrial Aerodynamics*, vol. 26, pp. 1–19, Jan. 1987.

[11] S. Price and M. Paidoussis, "The aerodynamic forces acting on groups of two and three circular cylinders when subject to a cross-flow," *Journal of Wind Engineering and Industrial Aerodynamics*, vol. 17, pp. 329–347, Sept. 1984.

[12] K. Lam and W. C. Cheung, "Phenomena of vortex shedding and flow interference of three cylinders in different equilateral arrangements," *Journal of Fluid Mechanics*, vol. 196, pp. 1–26, Apr. 1988.

[13] D. Biermann and W. Herrnstein Jr., "The interference between struts in various combinations," *National Advisory Committee for Aeronautics*, no. 468, 1933.

[14] S. Taneda, "Experimental investigation of the wakes behind cylinders and plates at low reynolds numbers," *Journal of the Physical Society of Japan*, vol. 11, 1956.

[15] W. Linke, "New measurements on aerodynamics of cylinders particularily their friction resistance," *Physikalische Zeitschrift*, vol. 32, pp. 900–914, 1931.

[16] O. M. Griffin and C. W. Votaw, "The vortex street in the wake of a vibrating cylinder," *Journal of Fluid Mechanics*, vol. 55, pp. 31–48, 1972.

[17] M. S. Bloor, "The transition to turbulence in the wake of a circular cylinder," *Journal of Fluid Mechanics*, vol. 19, no. 2, pp. 290–304, 1964.

[18] A. Prasad and C. H. K. Williamson, "The instability of the shear layer separating from a bluff body," *Journal of Fluid Mechanics*, vol. 333, pp. 375–402, Feb. 1997.

[19] C. H. K. Williamson, "Evolution of a single wake behind a pair of bluff bodies," *Journal of Fluid Mechanics*, vol. 159, pp. 1–18, Apr. 1985.

[20] D. G. Thomas and K. A. Kraus, "Interaction of vortex streets," *Journal of Applied Physics*, vol. 35, no. 12, 1964.

[21] P. W. Bearman and A. J. Wadcock, "The interaction between a pair of circular cylinders normal to a stream," *Journal of Fluid Mechanics*, vol. 61, no. 3, pp. 499–511, 1973.

[22] M. M. Zdravkovich, "Review of flow interference between two circular cylinders in various arrangements," *Journal of Fluids Engineering*, vol. 99, no. 4, pp. 618–633, 1977.

[23] M. M. Zdravkovich, "The effects of interference between circular cylinders in cross flow," *Journal of Fluids and Structures*, vol. 1, pp. 239–261, 1987.

[24] Z. G. Kostic and S. N. Oka, "Fluid flow and heat transfer with two cylinders in cross flow," *International Journal of Heat and Mass Transfer*, vol. 15, pp. 279–299, 1972.

[25] M. M. Zdravkovich and D. J. Stanhope, "Flow pattern in the gap between two cylinders in tandem," tech. rep., University of Salford, 1972.

[26] T. Igarashi, "Characteristics of the flow around two circular cylinders arranged in tandem (1st report)," *Bulletin of the JSME*, vol. 24, no. 188, pp. 323–331, 1981.

[27] M. M. Zdravkovich and D. L. Pridden, "Interference between two circular cylinders; Series of unexpected discontinuities," *Journal of Industrial Aerodynamics*, vol. 2, pp. 255–270, Nov. 1977.

[28] S. Ishigai, E. Nishikawa, K. Nishimura, and K. Cho, "Experimental study on structure of gas flow in tube banks with tube axes normal to flow: part 1, Karman vortex flow from two tubes at various spacings," *Bulletin of the JSME*, vol. 15, no. 86, pp. 949–956, 1972.

[29] A. Roshko, "On the wake and drag of bluff bodies," *Journal of the Aeronautical Sciences*, vol. 22, pp. 124–132, 1955.

[30] M. M. Zdravkovich, "Smoke observations of wakes of tandem cylinders at low Reynolds numbers," *Aeronautical Journal*, vol. 76, pp. 108–114, 1972.

[31] Y. Nakayama, *Flow, a Photographic Album.* Tokyo: JSME, 1984.

[32] M. M. Zdravkovich, “Discussion: Effect of vibrating upstream cylinder of two circular cylinders in tandem arrangement,” *Journal of Fluids Engineering*, vol. 108, pp. 383–385, 1986.

[33] H. M. Spivack, “Vortex frequency and flow pattern in the wake of two parallel cylinders at varied spacing normal to an air stream,” *Journal of the Aeronautical Sciences*, vol. 13, pp. 289–301, 1946.

[34] A. Okajima, K. Sugitani, and T. Mizota, “Flow around a pair of circular cylinders arranged side-by-side at high Reynolds numbers,” *Trans. JSME*, vol. 52, pp. 2844–2850, 1986.

[35] B. G. Newman, “The deflection of plane jets by adjacent boundaries - Coanda effect,” *Boundary layer and flow control*, vol. 1, pp. 232–264, 1961.

[36] M. M. Zdravkovich, “Interaction of bistable/metastable flows and stabilizing devices,” in *Proceedings of the 6th international conference on flow-induced vibrations*, pp. 431–439, 1995.

[37] L. Landweber, “Flow about a pair of adjacent, parallel cylinders normal to a stream,” tech. rep., 1942.

[38] D. Sumner, S. J. Price, and M. P. Païdoussis, “Flow-pattern identification for two staggered circular cylinders in cross-flow,” *Journal of Fluid Mechanics*, vol. 411, pp. 263–303, May 2000.

[39] Z. Gu and T. Sun, "On interference between two circular cylinders in staggered arrangement at high subcritical Reynolds numbers," *Journal of Wind Engineering and Industrial Aerodynamics*, vol. 80, pp. 287–309, Apr. 1999.

[40] S. Taneda, "Experimental investigation of vortex streets," *Journal of the Physical Society of Japan*, vol. 20, no. 9, pp. 1714–1721, 1965.

[41] G. H. Koopmann, "The vortex wakes of vibrating cylinders at low Reynolds numbers," *Journal of Fluid Mechanics*, vol. 28, pp. 501–512, Mar. 1967.

[42] M. M. Zdravkovich, *Flow Around Circular Cylinders, Vol 2: Applications.* Oxford University Press, 2003.

[43] T. A. Fox and G. S. West, "On the use of end plates with circular cylinders," *Experiments in Fluids*, vol. 9, no. 4, pp. 237–239, 1990.

[44] H. Werlé and M. Gallon, "The new hydrodynamic visualization laboratory of the aerodynamics division," *Recherche Aerospatiale*, vol. 5, pp. 289–311, 1982.

[45] W. Merzkirch, *Flow Visualization.* Orlando: Academic Press, 2nd ed., 1987.

[46] Q. Lian and T. Su, "The applications of the hydrogen bubble method in the investigations of complex flows," *Atlas of Visualization*, vol. 2, pp. 105–115, 1996.

[47] M. Raffel, C. E. Willert, and J. Kompenhans, *Particle Image Velocimetry, A Practical Guide.* Berlin: Springer, 1998.

[48] F. Mayinger and O. Feldmann, eds., *Optical Measurements.* Berlin: Springer, 2nd ed., 2001.

[49] R. Adrian, "Particle-imaging techniques for experimental fluid mechanics," *Annual Review of Fluid Mechanics*, vol. 23, pp. 261–304, Jan. 1991.

[50] J. Westerweel, "Fundamentals of digital particle image velocimetry," *Measurement Science and Technology*, vol. 8, pp. 1379–1392, 1997.

[51] R. J. Adrian and C. S. Yao, "Power spectra of fluid velocities measured by laser Doppler velocimetry," *Experiments in Fluids*, vol. 5, pp. 17–28, 1987.

[52] *Measurement Science Enterprise, Inc.* "miniLDV single-component laser Doppler velocimeter/anemometer": http://measurementsci.com/products_miniLDV.html.

[53] J. L. Lumley, "The structure of inhomogeneous turbulence," in *Atmospheric Turbulence and Wave Propagation*, pp. 166–178, 1967.

[54] A. Iollo, "Remarks on the approximation of the Euler equations by a low order model," tech. rep., 1997.

[55] C. W. Rowley, *Modeling, simulation and control of cavity flow oscillations.* Ph.d., California Institute of Technology, 2002.

[56] P. Holmes, J. L. Lumley, and G. Berkooz, *Turbulence, Coherent Structures, Dynamical Systems and Symmetry, Cambridge Monographs on Mechanics.* Cambridge: Cambridge University Press, 1996.

[57] G. Berkooz, P. Holmes, and J. L. Lumley, "The proper orthogonal decomposition in the analysis of turbulent flows," *Annual Review of Fluid Mechanics*, vol. 25, pp. 539–575, 1993.

[58] A. Chatterjee, "An introduction to the proper orthogonal decomposition," *Current Science*, vol. 78, no. 7, pp. 808–817, 2000.

[59] B. W. V. Oudheusden, F. Scarano, N. P. V. Hinsberg, and D. W. Watt, "Phase-resolved characterization of vortex shedding in the near wake of a square-section cylinder at incidence," *Experiments in Fluids*, vol. 39, pp. 86–98, May 2005.

[60] P. Druault, P. Guibert, and F. Alizon, "Use of proper orthogonal decomposition for time interpolation from PIV data," *Experiments in Fluids*, vol. 39, pp. 1009–1023, Sept. 2005.

[61] J. Shao and C. Zhang, "Numerical analysis of the flow around a circular cylinder using RANS and LES," *International Journal of Computational Fluid Dynamics*, vol. 20, no. 5, pp. 301–307, 2006.

[62] H. Persillon and M. Braza, "Physical analysis of the transition to turbulence in the wake of a circular cylinder by three-dimensional NavierStokes simulation," *Journal of Fluid Mechanics*, vol. 365, pp. 23–88, June 1998.

[63] J. Wissink and W. Rodi, "Numerical study of the near wake of a circular cylinder," *International Journal of Heat and Fluid Flow*, vol. 29, pp. 1060–1070, Aug. 2008.

[64] B. T. E. Tezduyar and R. Shin, "Numerical experiments on downstream boundary of flow past cylinder," *Journal of Engineering Mechanics*, vol. 117, no. 4, pp. 854–871, 1991.

[65] M. Behr, D. Hastreiter, S. Mittal, and T. Tezduyar, "Incompressible flow past a circular cylinder: dependence of the computed flow field on the location of the lat-

eral boundaries," *Computer Methods in Applied Mechanics and Engineering*, vol. 123, pp. 309–316, June 1995.

[66] C. Norberg, "Fluctuating lift on a circular cylinder: review and new measurements," *Journal of Fluids and Structures*, vol. 17, pp. 57–96, Jan. 2003.

[67] B. Rajani, A. Kandasamy, and S. Majumdar, "Numerical simulation of laminar flow past a circular cylinder," *Applied Mathematical Modelling*, vol. 33, pp. 1228–1247, Mar. 2009.

[68] H. Sakamoto and H. Haniu, "Optimum suppression of fluid forces acting on a circular cylinder," *Journal of Fluids Engineering*, vol. 116, pp. 221–227, 1994.

[69] A. Roshko, "On the development of turbulent wakes from vortex streets," *National Advisory Committee for Aeronautics*, 1954.

[70] M. Braza, P. Chassaing, and H. Ha Minh, "Numerical study and physical analysis of the pressure and velocity fields in the near wake of a circular cylinder," *Journal of Fluid Mechanics*, vol. 165, pp. 79–130, 1986.

[71] E. M. Saiki and S. Biringen, "Numerical simulation of a cylinder in uniform flow : application of a virtual boundary method," *Journal of Computational Physics*, vol. 123, pp. 450–465, 1996.

[72] B. E. Launder and D. B. Spalding, "The numerical computation of turbulent flows," *Computer Methods in Applied Mechanics and Engineering*, vol. 3, pp. 269–289, 1974.

[73] D. C. Wilcox, “Multiscale model for turbulent flows,” *AIAA Journal*, vol. 26, no. 11, pp. 1311–1320, 1988.

[74] F. R. Menter, “Two-equation eddy-viscosity turbulence models for engineering applications,” *AIAA Journal*, vol. 32, no. 8, pp. 1598–1605, 1994.

[75] B. E. Launder, G. J. Reece, and W. Rodi, “Progress in the development of a Reynolds-stress turbulence closure,” *Journal of Fluid Mechanics*, vol. 68, no. 3, pp. 537–566, 1975.

[76] J. E. Bardina, P. G. Huang, and T. J. Coakley, “Turbulence modeling validation, testing, and development,” Tech. Rep. April, National Aeronautics and Space Administration, 1997.

[77] C. Wieselsberger, “New data on the laws of fluid resistance,” *National Advisory Committee for Aeronautics*, 1922.

[78] L. G. Leal and A. Acrivos, “The effect of base bleed on the steady separated flow past bluff objects,” *Journal of Fluid Mechanics*, vol. 39, pp. 735–752, 1969.

[79] S. Bhattacharyya, S. Dhinakaran, and A. Khalili, “Fluid motion around and through a porous cylinder,” *Chemical Engineering Science*, vol. 61, pp. 4451–4461, July 2006.

[80] T.-C. Jue, “Numerical analysis of vortex shedding behind a porous square cylinder,” *International Journal of Numerical Methods for Heat & Fluid Flow*, vol. 14, no. 5, pp. 649–663, 2004.

[81] V. C. Patel and G. Scheuerer, “Calculation of two-dimensional near and far wakes,” *AIAA Journal*, vol. 20, no. 7, pp. 900–907, 1982.

[82] R. Perrin, C. Mockett, M. Braza, and E. Cid, *Joint numerical and experimental investigation of the flow around a circular cylinder at high Reynolds number*, vol. 244. Springer Berlin Heidelberg, 2008.

[83] R. Perrin, M. Braza, E. Cid, S. Cazin, A. Barthet, A. Sevrain, C. Mockett, and F. Thiele, “Phase averaged turbulence properties in the near wake of a circular cylinder at high Reynolds number using POD,” in *13th Int Symp on Applications of Laser Techniques to Fluid Mechanics*, (Lisbon, Portugal), pp. 26–29, 2006.

[84] X. Ma and G. E. Karniadakis, “A low-dimensional model for simulating three-dimensional cylinder flow,” *Journal of Fluid Mechanics*, vol. 458, pp. 181–190, May 2002.

[85] R. Perrin, M. Braza, E. Cid, S. Cazin, A. Barthet, A. Sevrain, C. Mockett, and F. Thiele, “Obtaining phase averaged turbulence properties in the near wake of a circular cylinder at high Reynolds number using POD,” *Experiments in Fluids*, vol. 43, pp. 341–355, Aug. 2007.

[86] S. Dong, G. E. Karniadakis, A. Ekmekci, and D. Rockwell, “A combined direct numerical simulationparticle image velocimetry study of the turbulent near wake,” *Journal of Fluid Mechanics*, vol. 569, pp. 185–207, Nov. 2006.

[87] J. H. Gerrard, "Numerical computation of the magnitude and frequency of the lift on a circular cylinder," *Philosophical Transactions of the Royal Society of London. Series A, Mathematical and Physical Sciences*, vol. 261, pp. 137–162, 1967.

[88] M. Tatsuno, H. Amamoto, and K. Ishi-i, "Effects of interference amoung three equidistantly arranged cylinders in a uniform flow," *Fluid Dynamics Research*, pp. 297–315, 1998.

[89] S. Tavoularis, *Measurement in Fluid Mechanics*. Cambridge University Press, 2005.

[90] D. K. McLaughlin and W. G. Tiederman, "Biasing correction for individual realization of laser anemometer measurements in turbulent flows," *Physics of Fluids*, vol. 16, pp. 2082–2088, 1973.

[91] R. J. Moffat, "Describing the uncertainties in experimental results," *Experimental Thermal and Fluid Science*, vol. 1, pp. 3–17, Jan. 1988.

[92] A. K. Prasad, R. J. Adrian, C. C. Landreth, and P. W. Offutt, "Effect of resolution on the speed and accuracy of particle image velocimetry interrogation," *Experiments in Fluids*, vol. 13, pp. 105–116, 1992.

[93] A. Boillot and A. K. Prasad, "Optimization procedure for pulse separation in cross-correlation PIV," *Experiments in Fluids*, vol. 21, pp. 87–93, 1996.

[94] R. D. Keane and R. J. Adrian, "Optimization of particle image velocimeters. part 1: double pulsed systems," *Measurement Science and Technology*, pp. 1202–1215, 1990.

[95] E. F. J. Overmars, N. G. W. Warncke, C. Poelma, and J. Westerweel, “Bias errors in PIV: the pixel locking effect revisited,” in *15th international symposium on applications of laser techniques to fluid mechanics*, (Lisbon), 2010.

Appendices

Appendix A

Vorticity contours

The following figures show the sequence of vorticity fields for one large scale shedding period for $10^\circ \leq \alpha \leq 50^\circ$. The discussion based on these figures is given in Chapter 5.

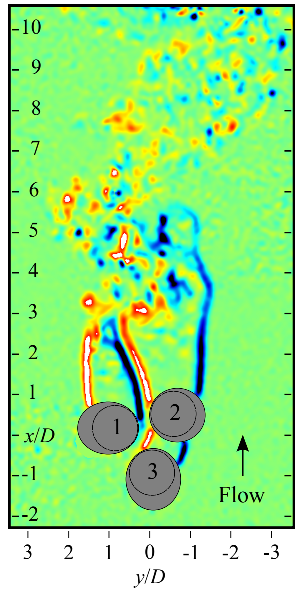

(a) t_1

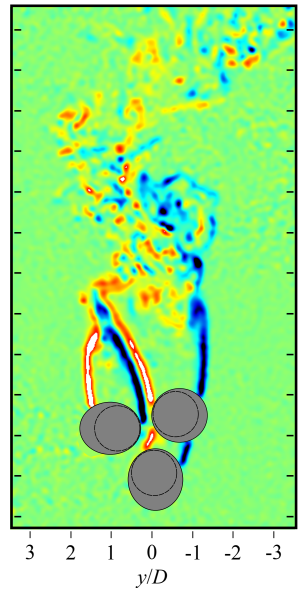

(b) $t_1 + T/5$

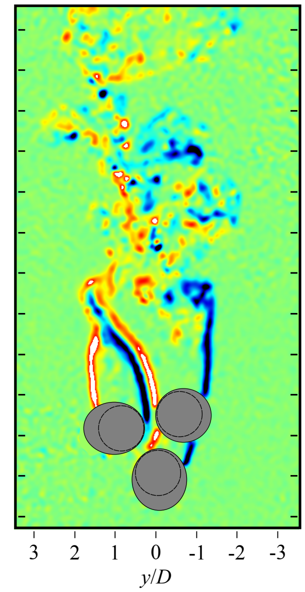

(c) $t_1 + 2T/5$

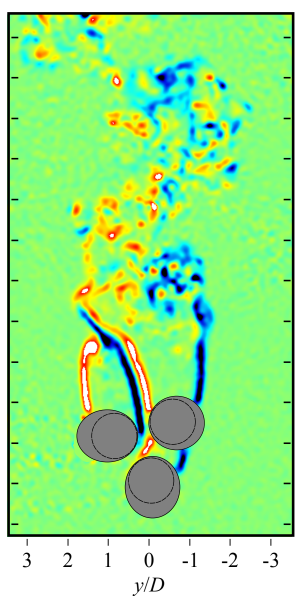

(d) $t_1 + 3T/5$

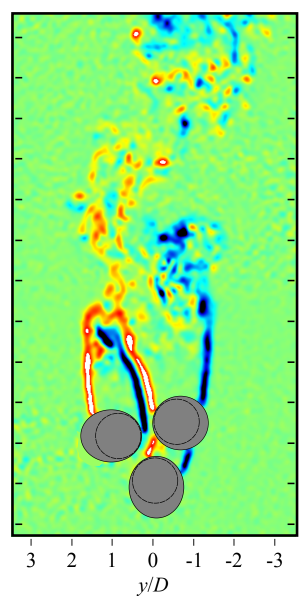

(e) $t_1 + 4T/5$

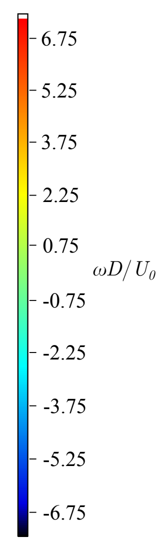

Figure A.1: Vorticity contours for $\alpha = 10°$.

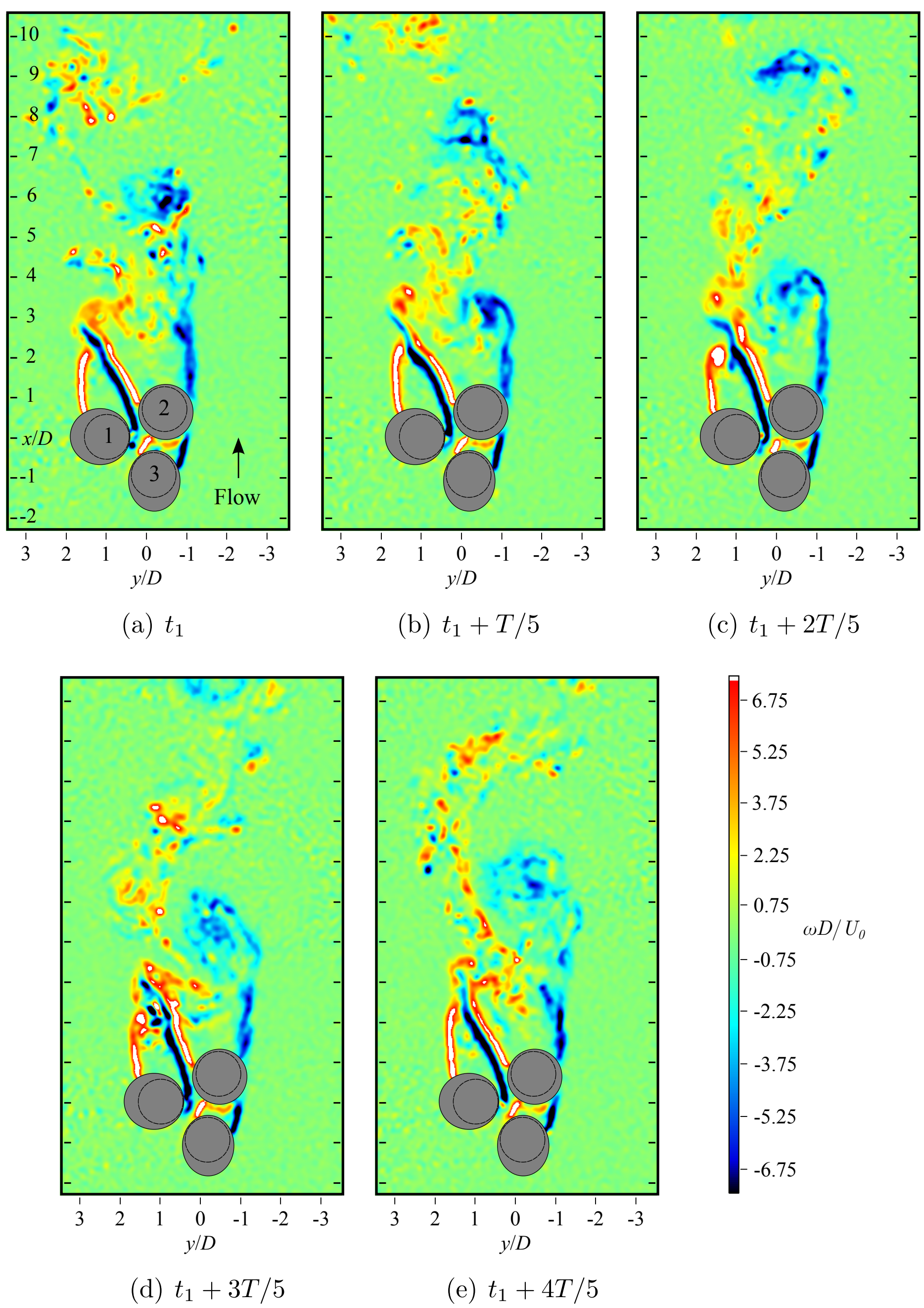

(a) t_1 (b) $t_1 + T/5$ (c) $t_1 + 2T/5$

(d) $t_1 + 3T/5$ (e) $t_1 + 4T/5$

Figure A.2: Vorticity contours for $\alpha = 20°$.

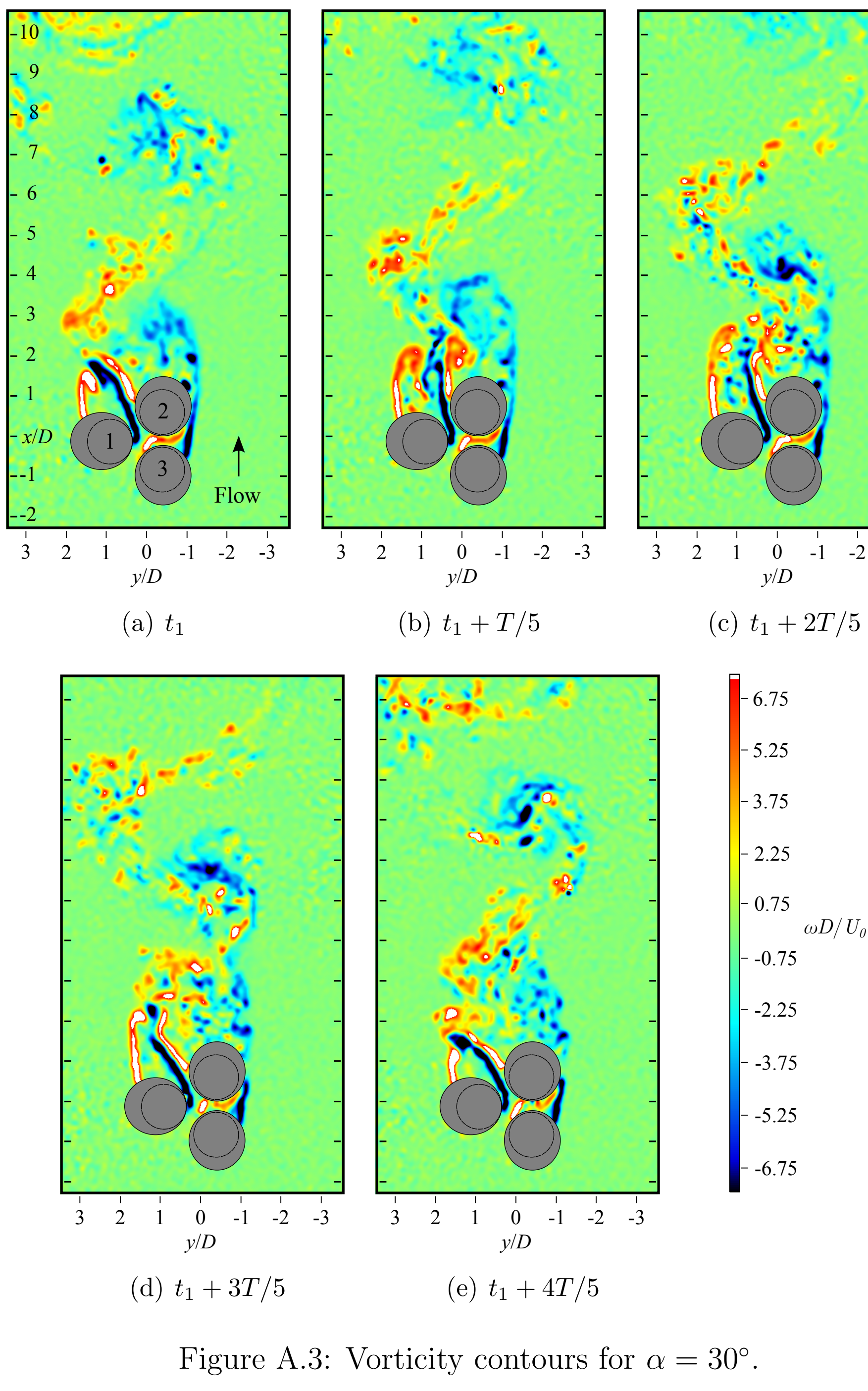

(a) t_1 (b) $t_1 + T/5$ (c) $t_1 + 2T/5$

(d) $t_1 + 3T/5$ (e) $t_1 + 4T/5$

Figure A.3: Vorticity contours for $\alpha = 30°$.

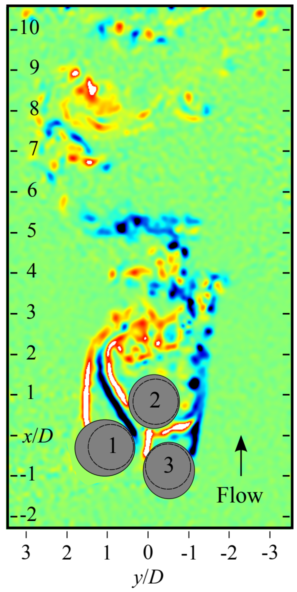

(a) t_1

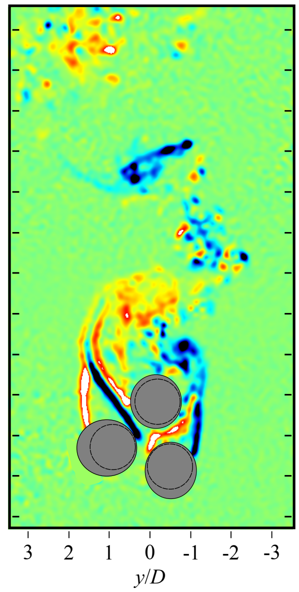

(b) $t_1 + T/5$

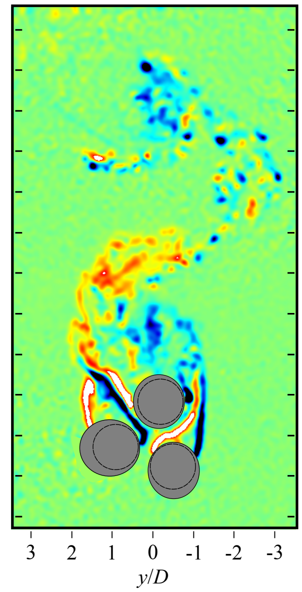

(c) $t_1 + 2T/5$

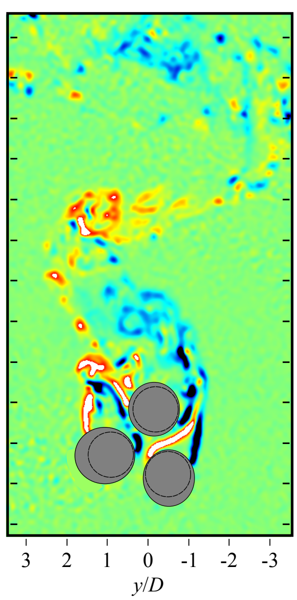

(d) $t_1 + 3T/5$

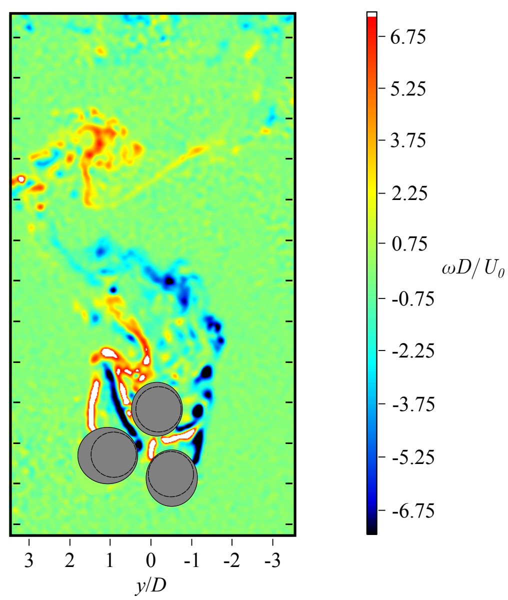

(e) $t_1 + 4T/5$

Figure A.4: Vorticity contours for $\alpha = 40°$.

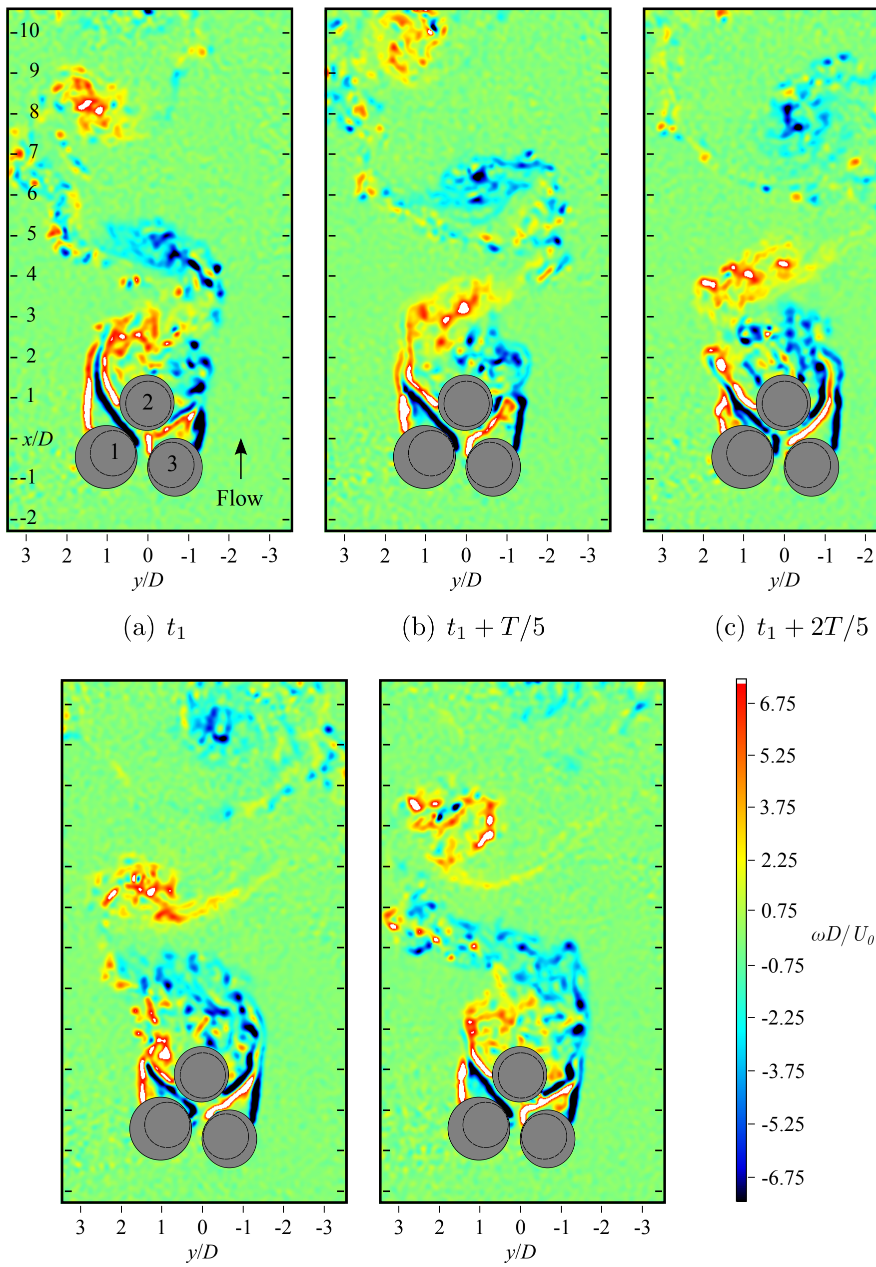

(a) t_1

(b) $t_1 + T/5$

(c) $t_1 + 2T/5$

(d) $t_1 + 3T/5$

(e) $t_1 + 4T/5$

Figure A.5: Vorticity contours for $\alpha = 50°$.

Appendix B

POD results

The following figures show the results from the POD analysis for $10^\circ \leq \alpha \leq 50^\circ$. The temporal and spatial modes corresponding to the large and small scale shedding, as well as the results from the reduced-order models for $10^\circ \leq \alpha \leq 50^\circ$ are shown in the following figures. The discussion based on all these figures is given in Chapter 5.

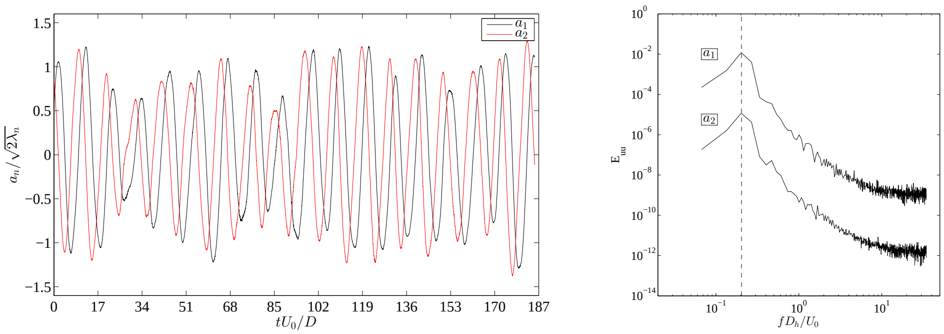

(a)

(b)

Figure B.1: Temporal coefficient (a) signal and (b) spectra for the first two modes corresponding to the large scale shedding for $\alpha = 10°$.

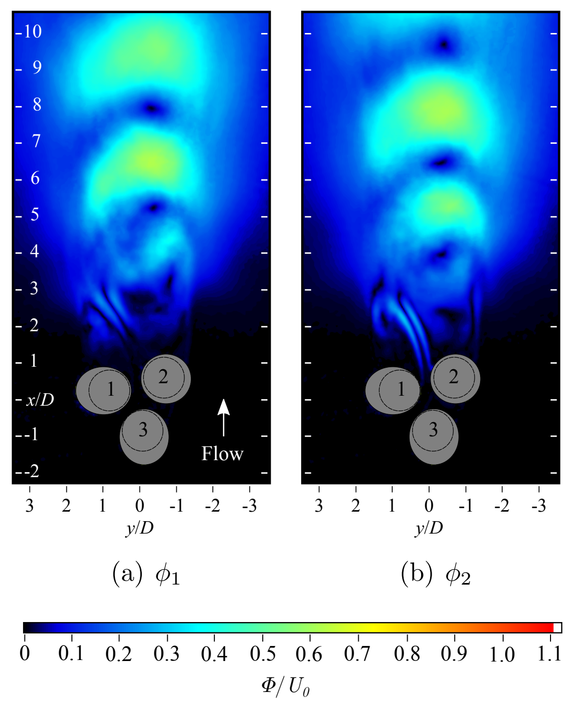

(a) ϕ_1

(b) ϕ_2

Figure B.2: First and second spatial modes corresponding to the large scale shedding for $\alpha = 10°$.

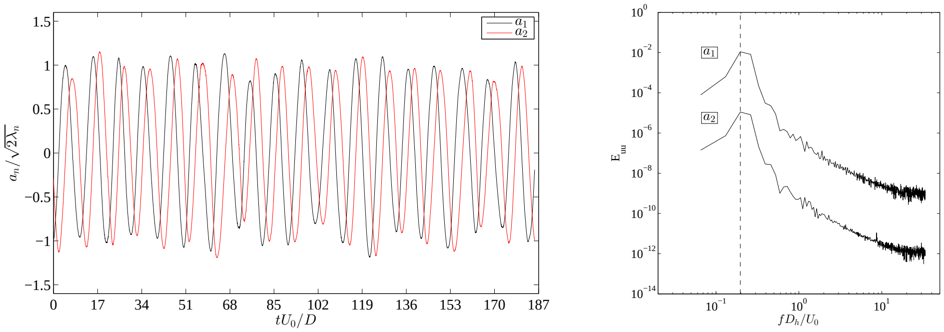

(a) (b)

Figure B.3: Temporal coefficient (a) signal and (b) spectra for the first two modes corresponding to the large scale shedding for $\alpha = 20°$.

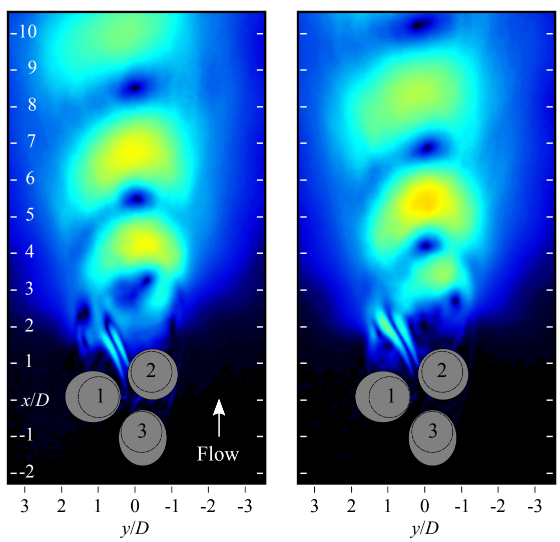

(a) ϕ_1 (b) ϕ_2

Figure B.4: First and second spatial modes corresponding to the large scale shedding for $\alpha = 20°$.

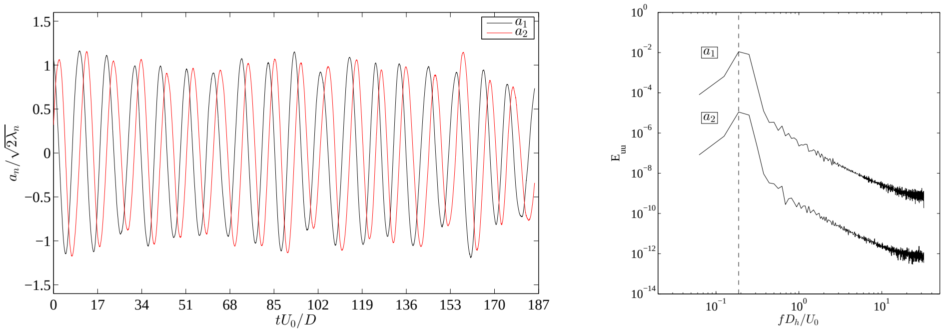

(a) (b)

Figure B.5: Temporal coefficient (a) signal and (b) spectra for the first two modes corresponding to the large scale shedding for $\alpha = 30°$.

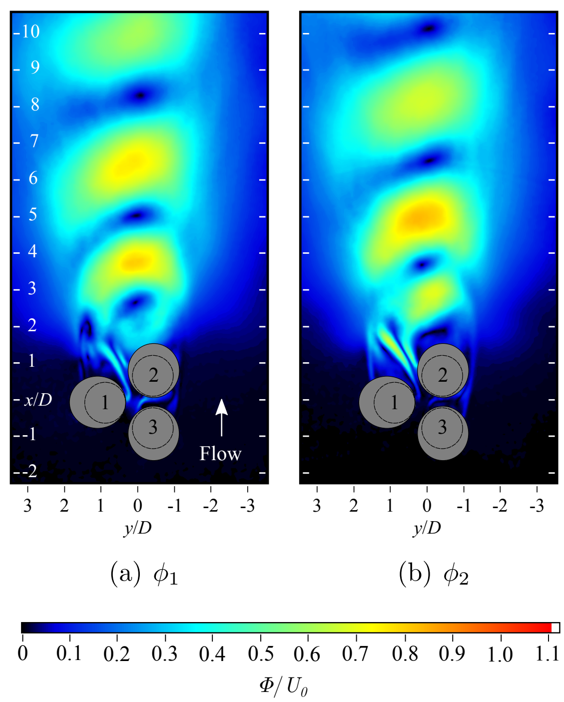

(a) ϕ_1 (b) ϕ_2

Figure B.6: First and second spatial modes corresponding to the large scale shedding for $\alpha = 30°$.

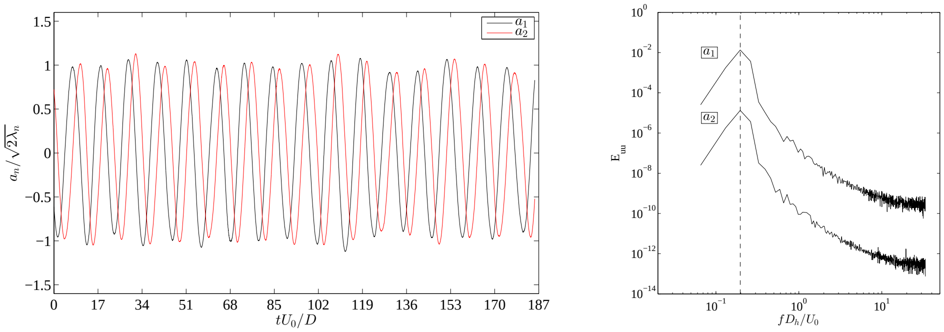

(a)

(b)

Figure B.7: Temporal coefficient (a) signal and (b) spectra for the first two modes corresponding to the large scale shedding for $\alpha = 40°$.

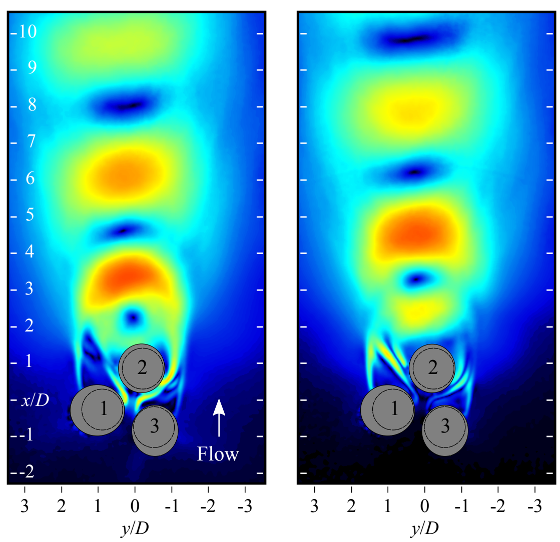

(a) ϕ_1

(b) ϕ_2

Figure B.8: First and second spatial modes corresponding to the large scale shedding for $\alpha = 40°$.

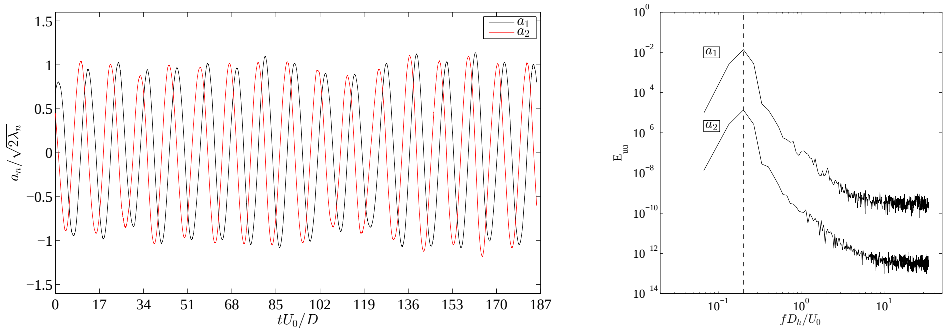

(a)

(b)

Figure B.9: Temporal coefficient (a) signal and (b) spectra for the first two modes corresponding to the large scale shedding for $\alpha = 50°$.

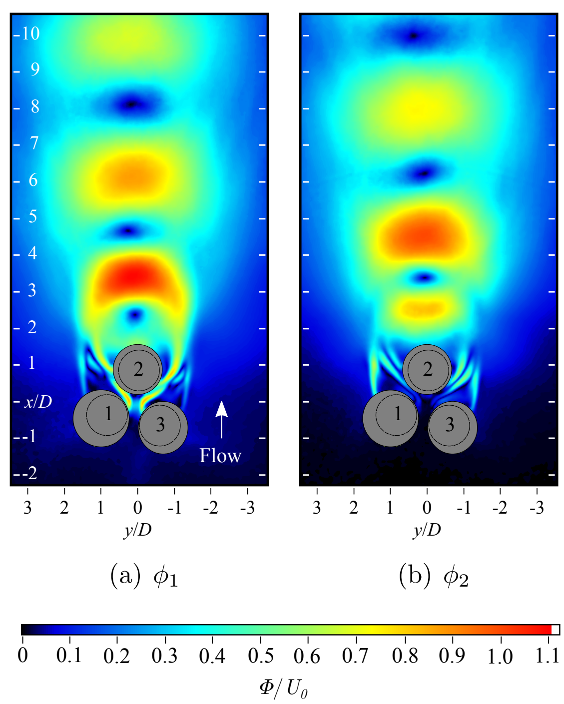

(a) ϕ_1

(b) ϕ_2

Figure B.10: First and second spatial modes corresponding to the large scale shedding for $\alpha = 50°$.

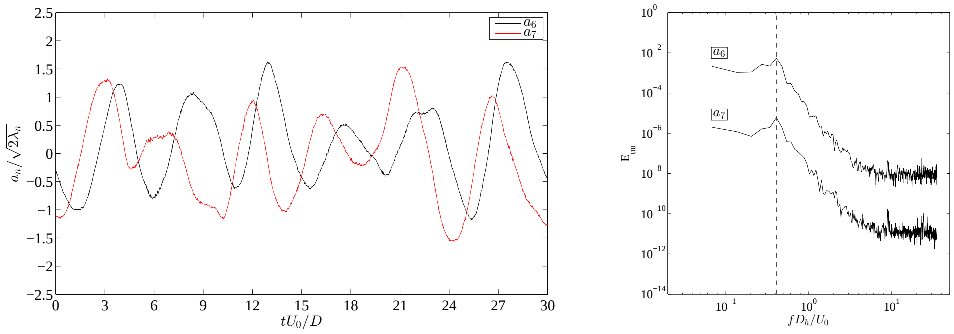

(a) (b)

Figure B.11: Temporal coefficient (a) signal and (b) spectra for the sixth and seventh modes corresponding to 2nd order harmonic of the large scale shedding frequency for $\alpha = 0°$.

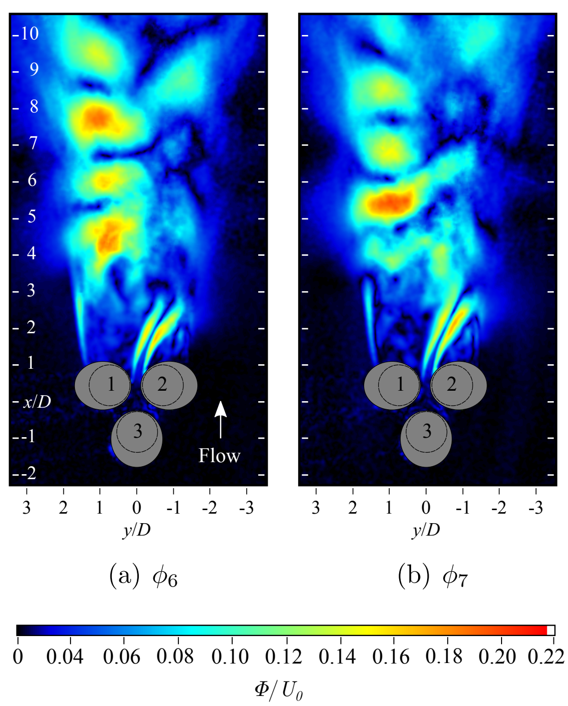

Figure B.12: Sixth and seventh spatial modes corresponding to 2nd order harmonic of the large scale shedding frequency for $\alpha = 0°$.

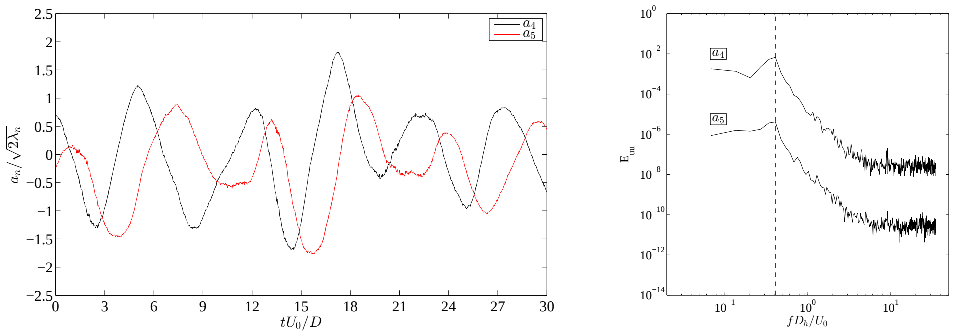

(a) (b)

Figure B.13: Temporal coefficient (a) signal and (b) spectra for the fourth and fifth modes corresponding to 2nd order harmonic of the large scale shedding frequency for $\alpha = 60°$.

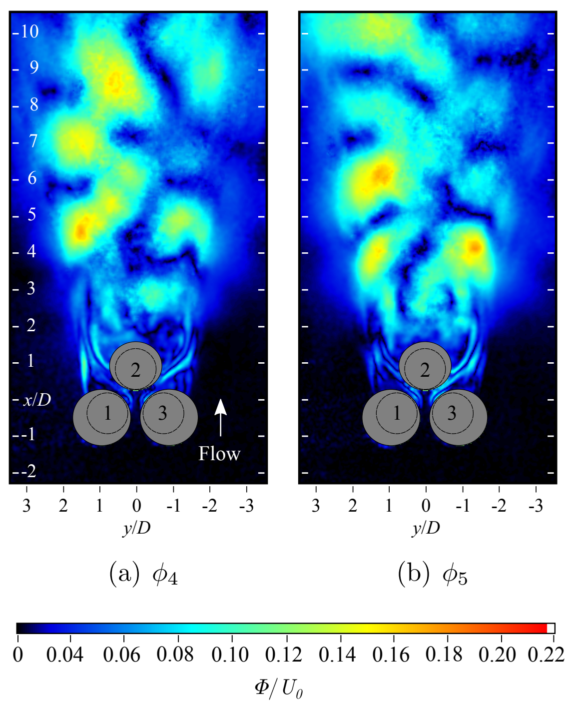

(a) ϕ_4 (b) ϕ_5

Figure B.14: Fourth and fifth spatial modes corresponding to 2nd order harmonic of the large scale shedding frequency for $\alpha = 60°$.

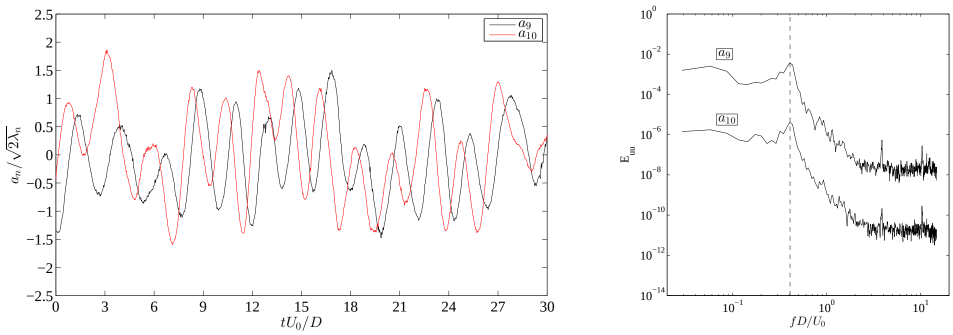

(a) (b)

Figure B.15: Temporal coefficient (a) signal and (b) spectra for modes corresponding to the small scale shedding for $\alpha = 10°$.

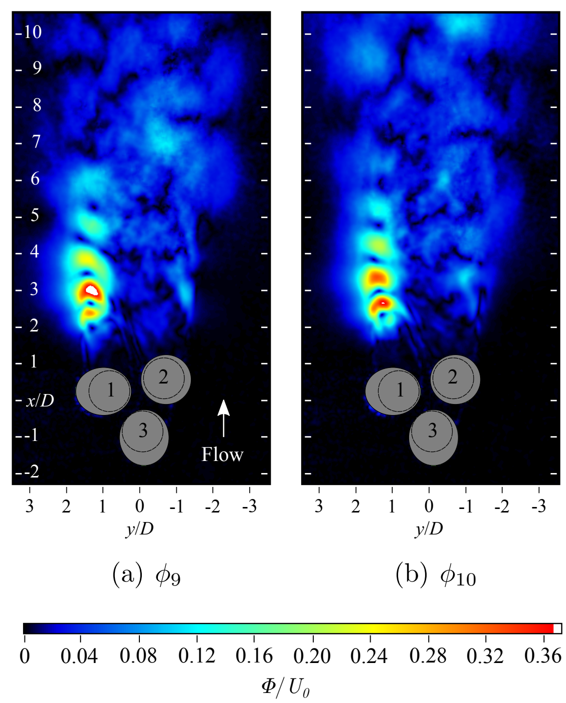

(a) ϕ_9 (b) ϕ_{10}

Figure B.16: Spatial modes corresponding to the small scale shedding for $\alpha = 10°$.

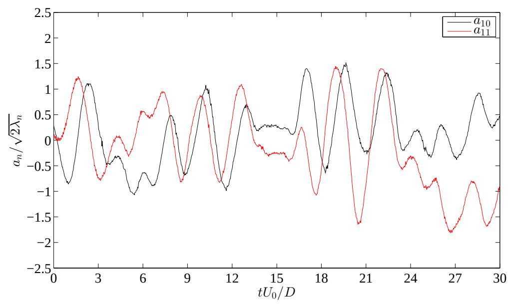

(a)

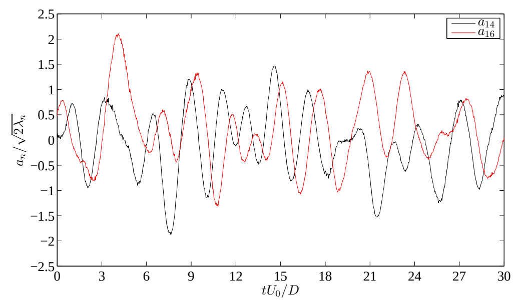

(b)

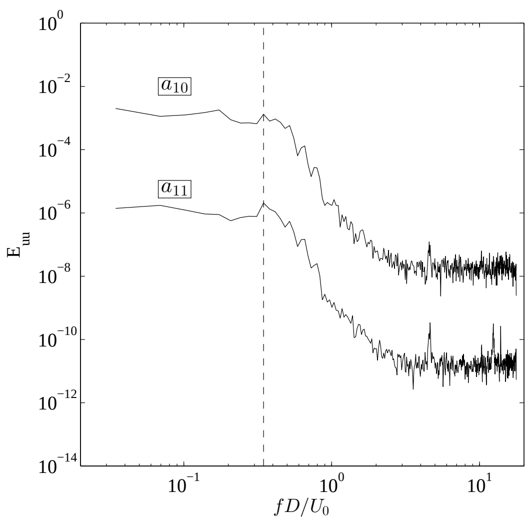

(c)

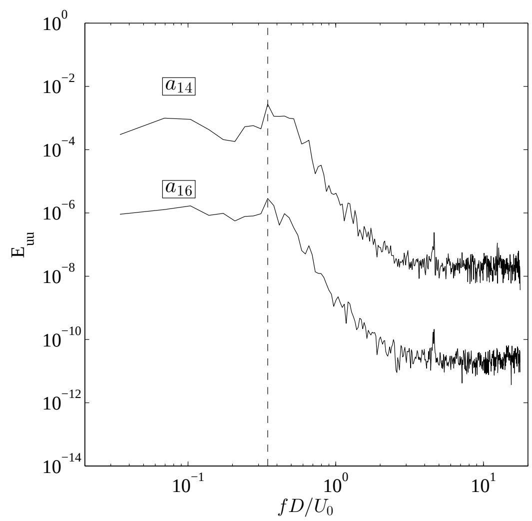

(d)

Figure B.17: Temporal coefficient (a) & (b) signal and (c) & (d) spectra for modes corresponding to the small scale shedding for $\alpha = 20°$.

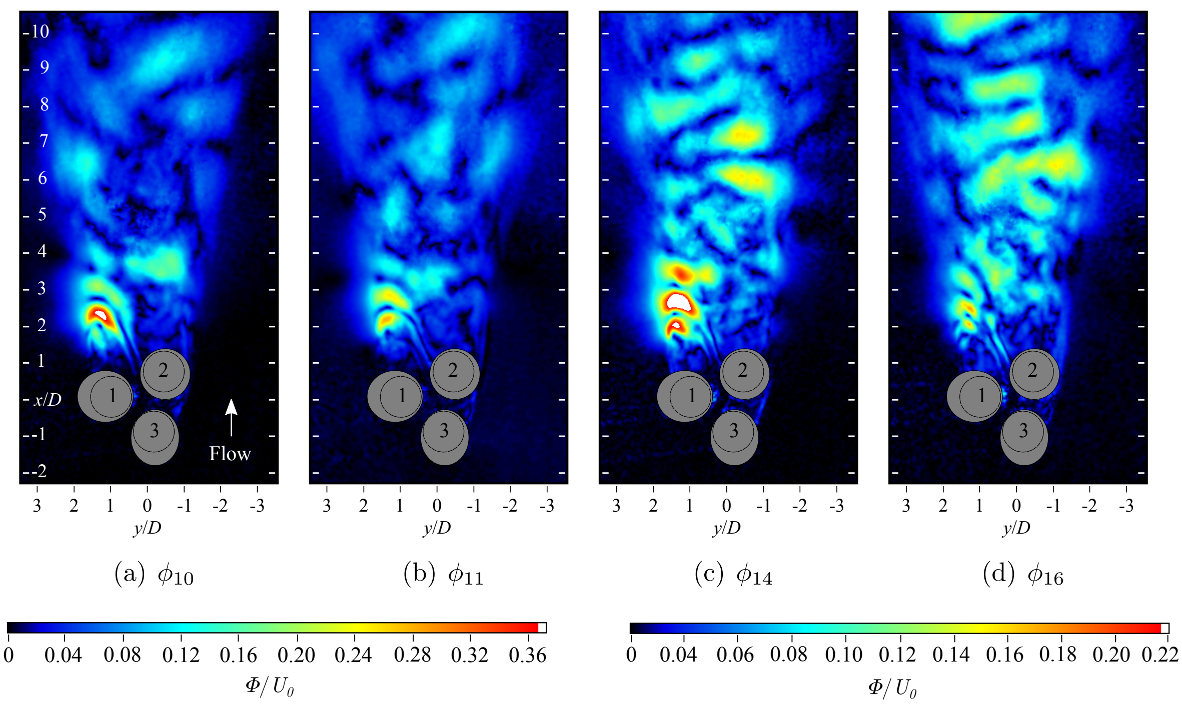

(a) ϕ_{10} (b) ϕ_{11} (c) ϕ_{14} (d) ϕ_{16}

Figure B.18: Spatial modes corresponding to the small scale shedding for $\alpha = 20°$.

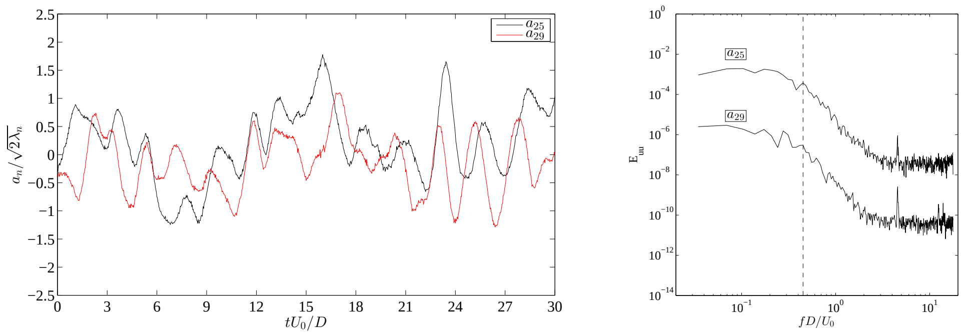

(a)

(b)

Figure B.19: Temporal coefficient (a) signal and (b) spectra for modes corresponding to the small scale shedding for $\alpha = 30°$.

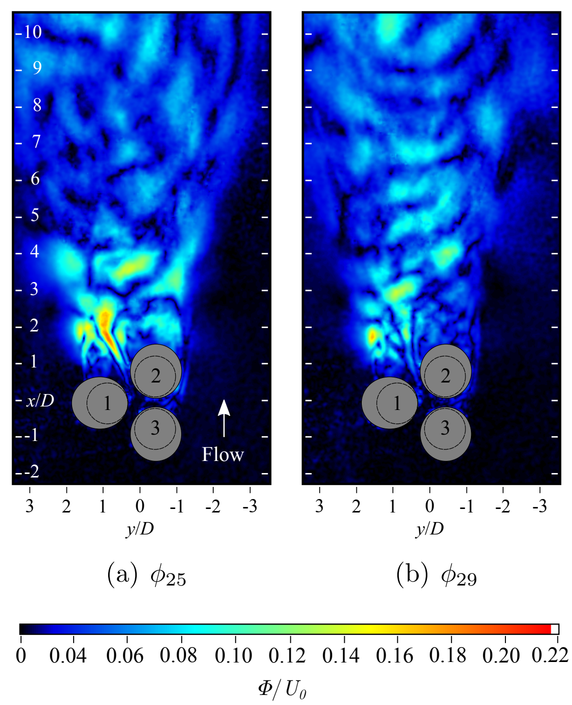

(a) ϕ_{25}

(b) ϕ_{29}

Figure B.20: Spatial modes corresponding to the small scale shedding for $\alpha = 30°$.

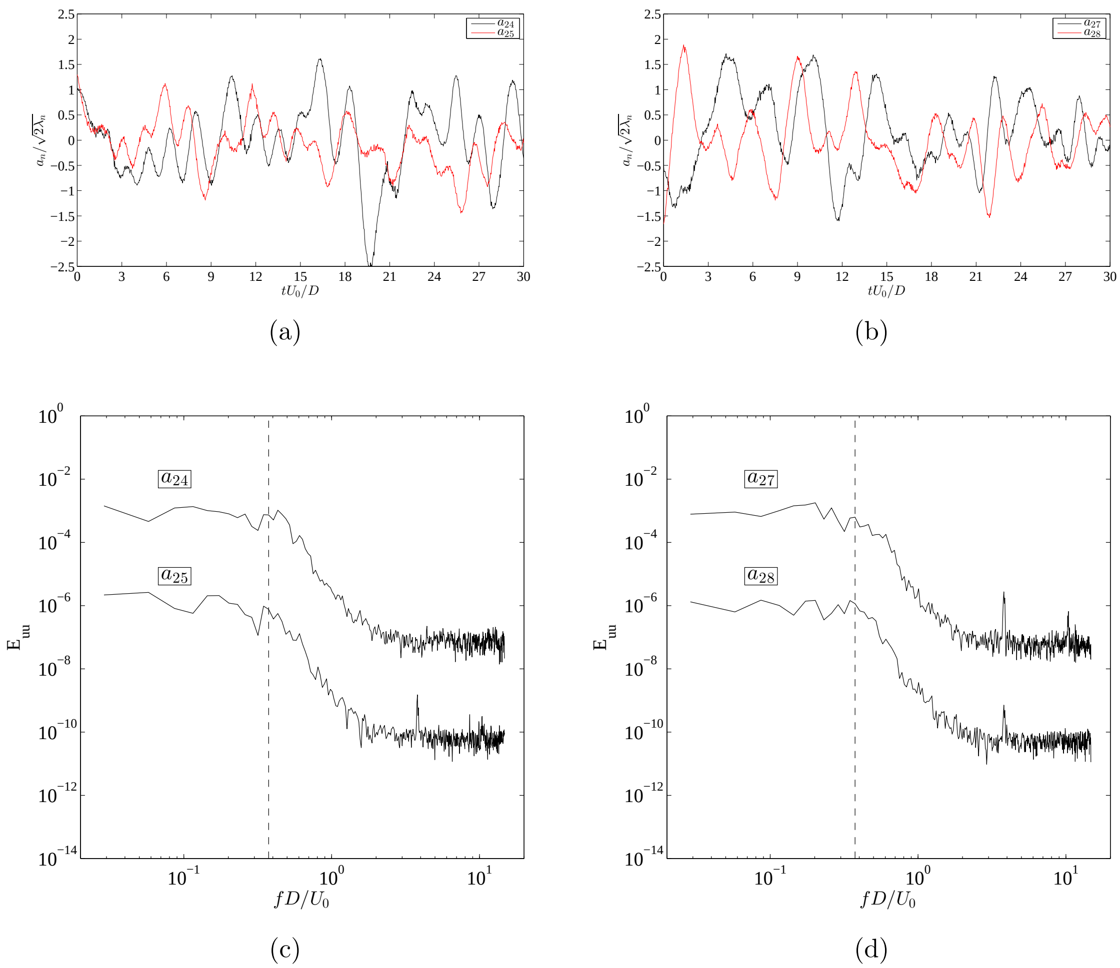

Figure B.21: Temporal coefficient (a) & (b) signal and (c) & (d) spectra for modes corresponding to the small scale shedding for $\alpha = 40°$.

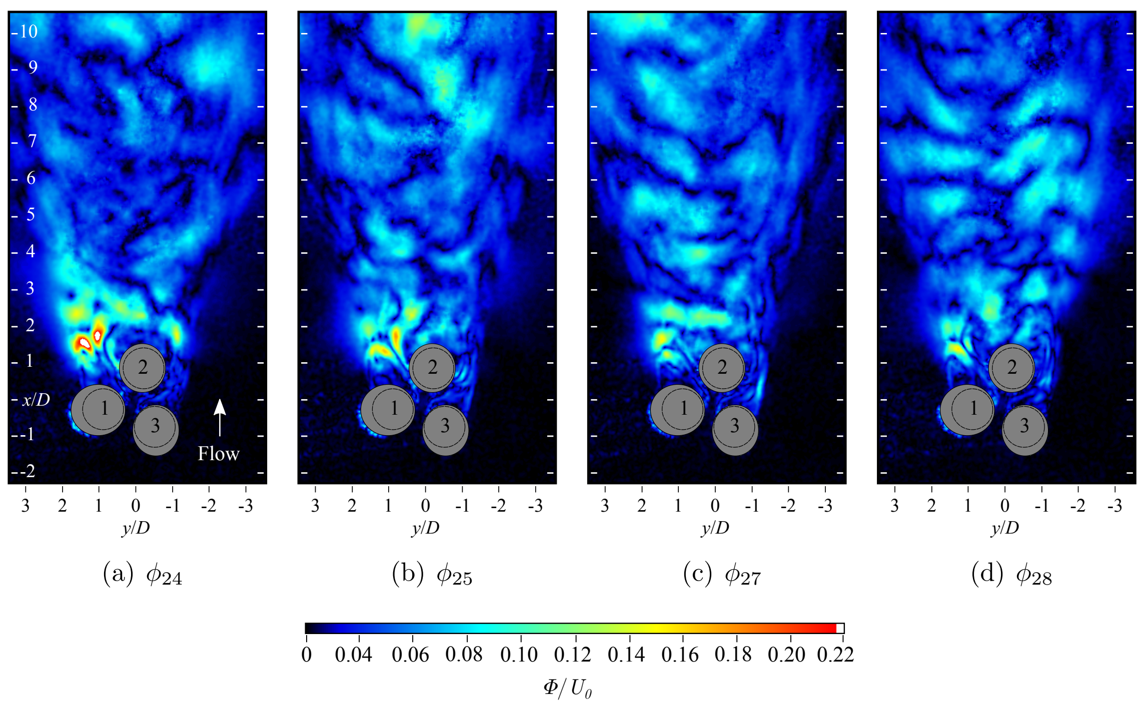

Figure B.22: Spatial modes corresponding to the small scale shedding for $\alpha = 40°$.

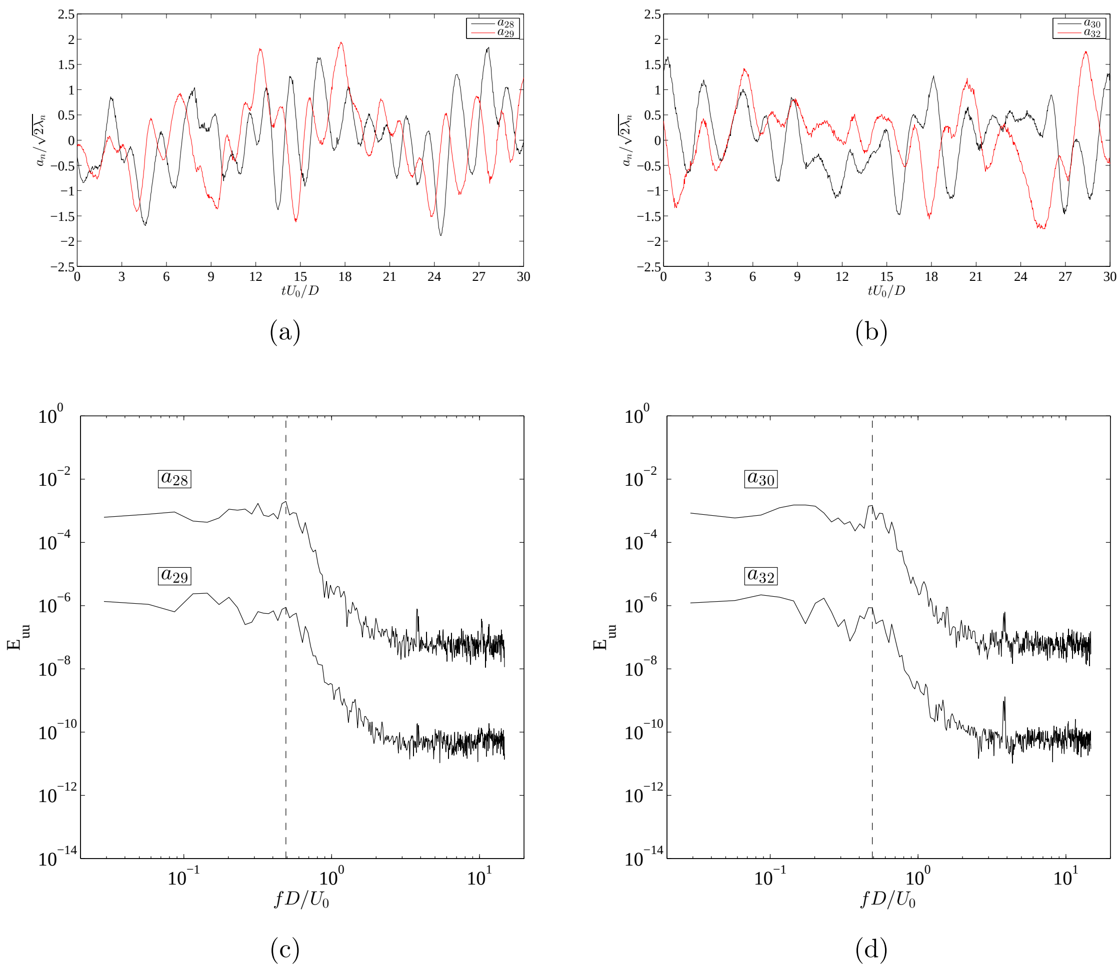

Figure B.23: Temporal coefficient signal for modes corresponding to the small scale shedding for $\alpha = 50°$.

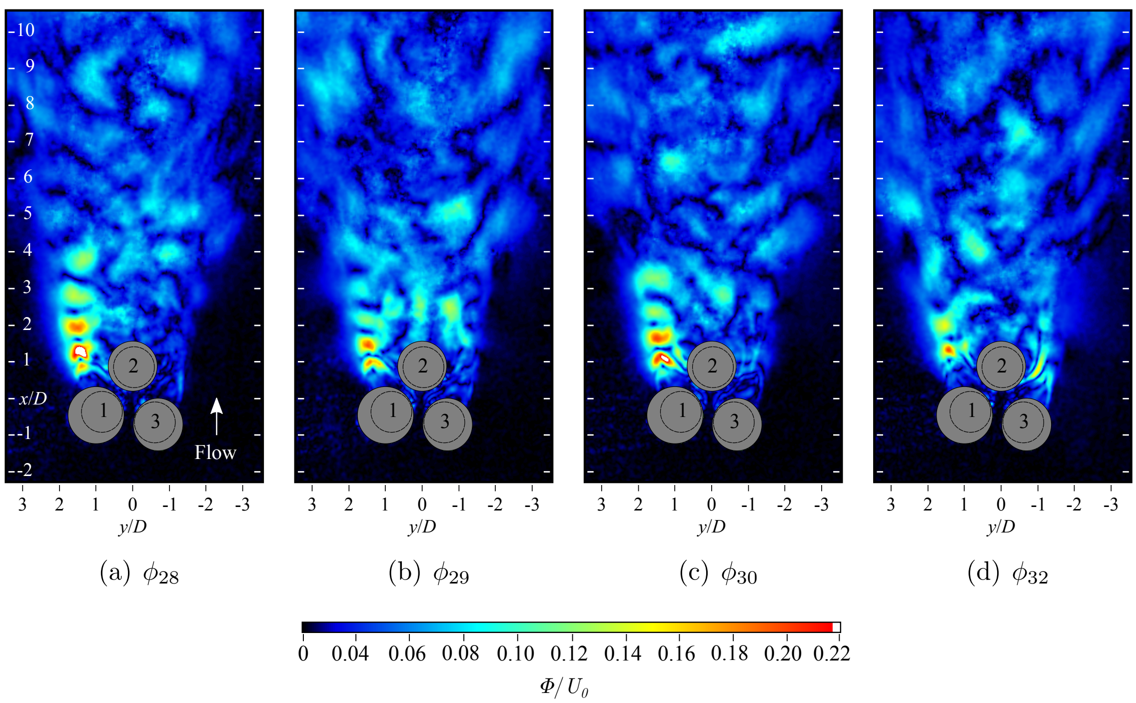

(a) ϕ_{28} (b) ϕ_{29} (c) ϕ_{30} (d) ϕ_{32}

Figure B.24: Spatial modes corresponding to the small scale shedding for $\alpha = 50°$.

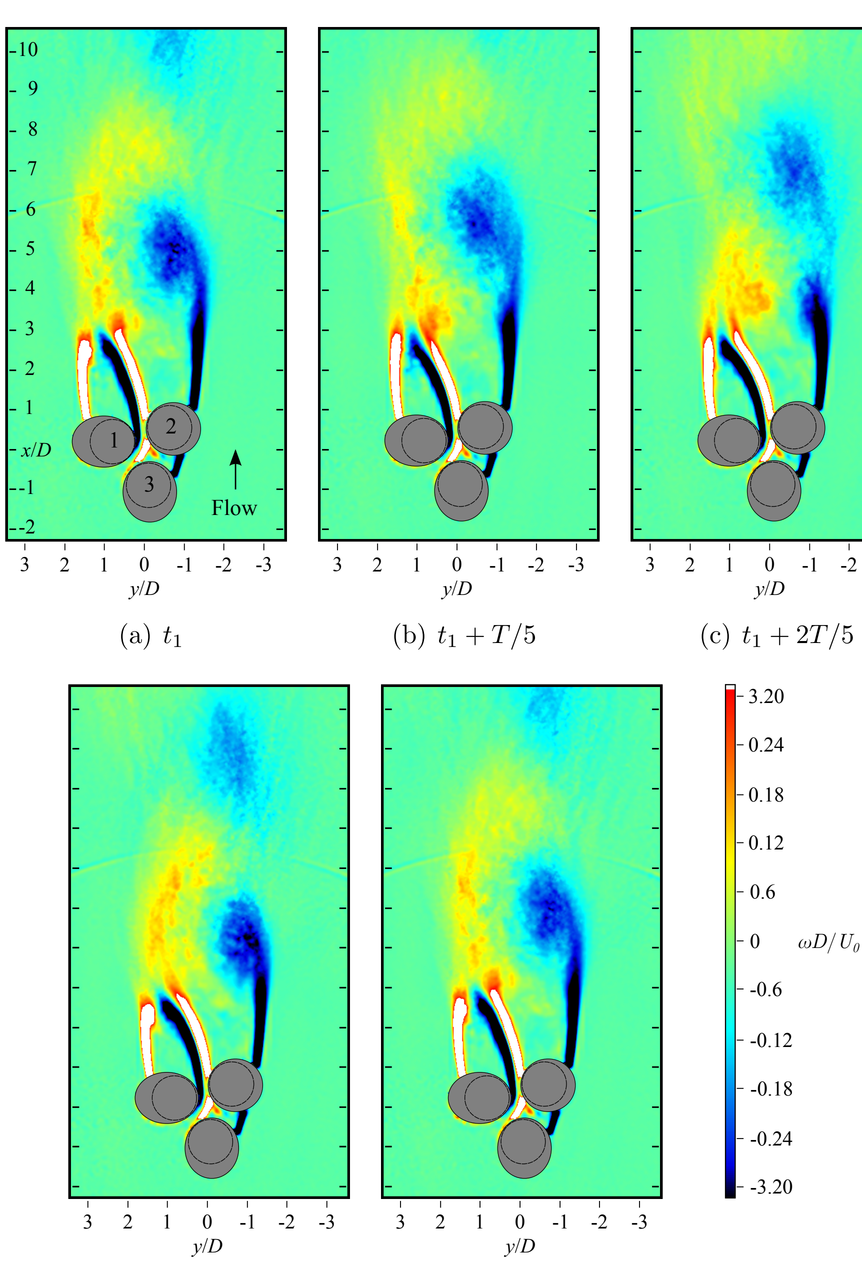

(a) t_1 (b) $t_1 + T/5$ (c) $t_1 + 2T/5$

(d) $t_1 + 3T/5$ (e) $t_1 + 4T/5$

Figure B.25: Vorticity contours of the reduced-order model consisting of the first two modes for $\alpha = 10°$.

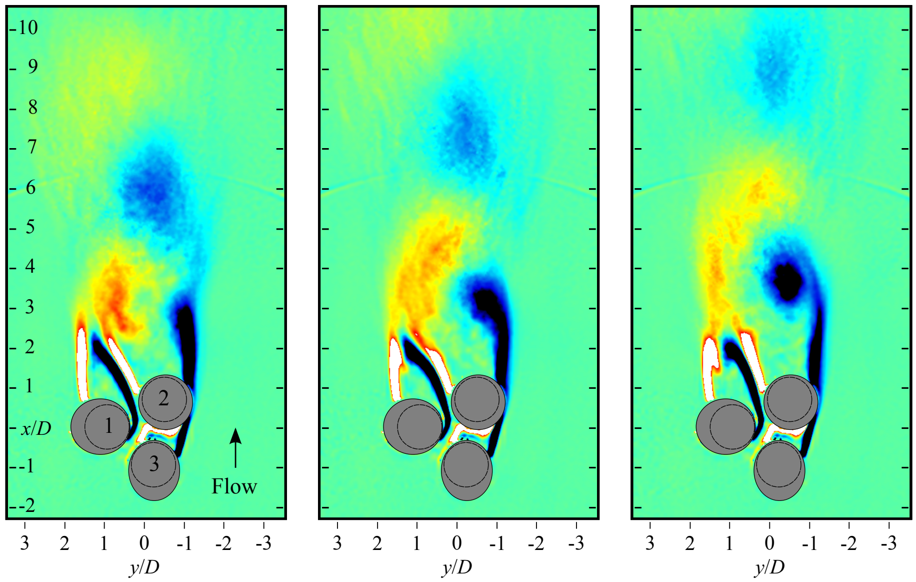

(a) t_1 (b) $t_1 + T/5$ (c) $t_1 + 2T/5$

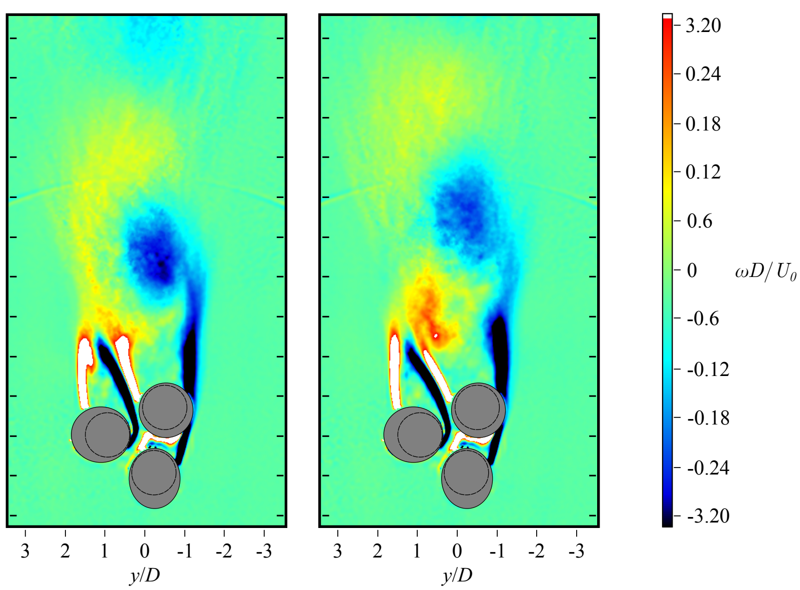

(d) $t_1 + 3T/5$ (e) $t_1 + 4T/5$

Figure B.26: Vorticity contours of the reduced-order model consisting of the first two modes for $\alpha = 20°$.

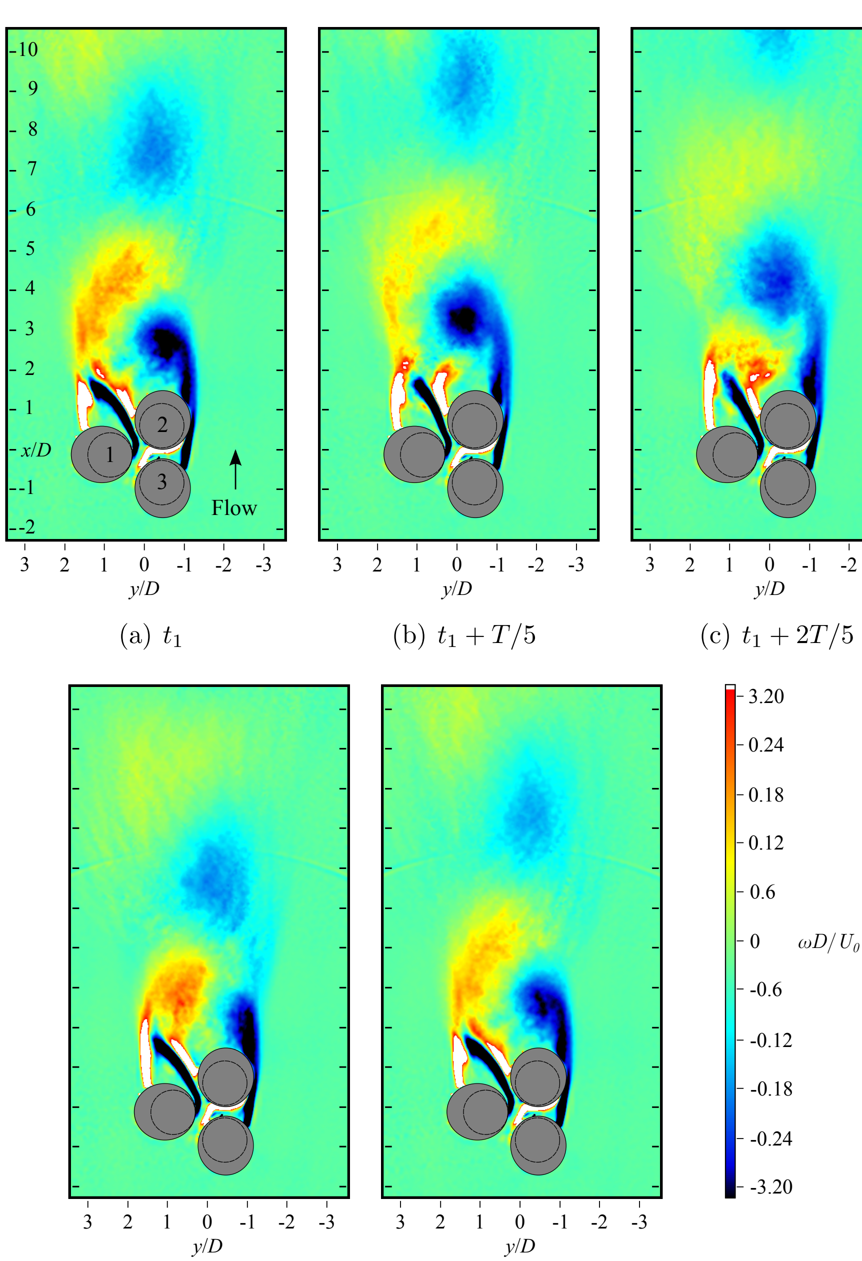

(a) t_1 (b) $t_1 + T/5$ (c) $t_1 + 2T/5$

(d) $t_1 + 3T/5$ (e) $t_1 + 4T/5$

Figure B.27: Vorticity contours of the reduced-order model consisting of the first two modes for $\alpha = 30°$.

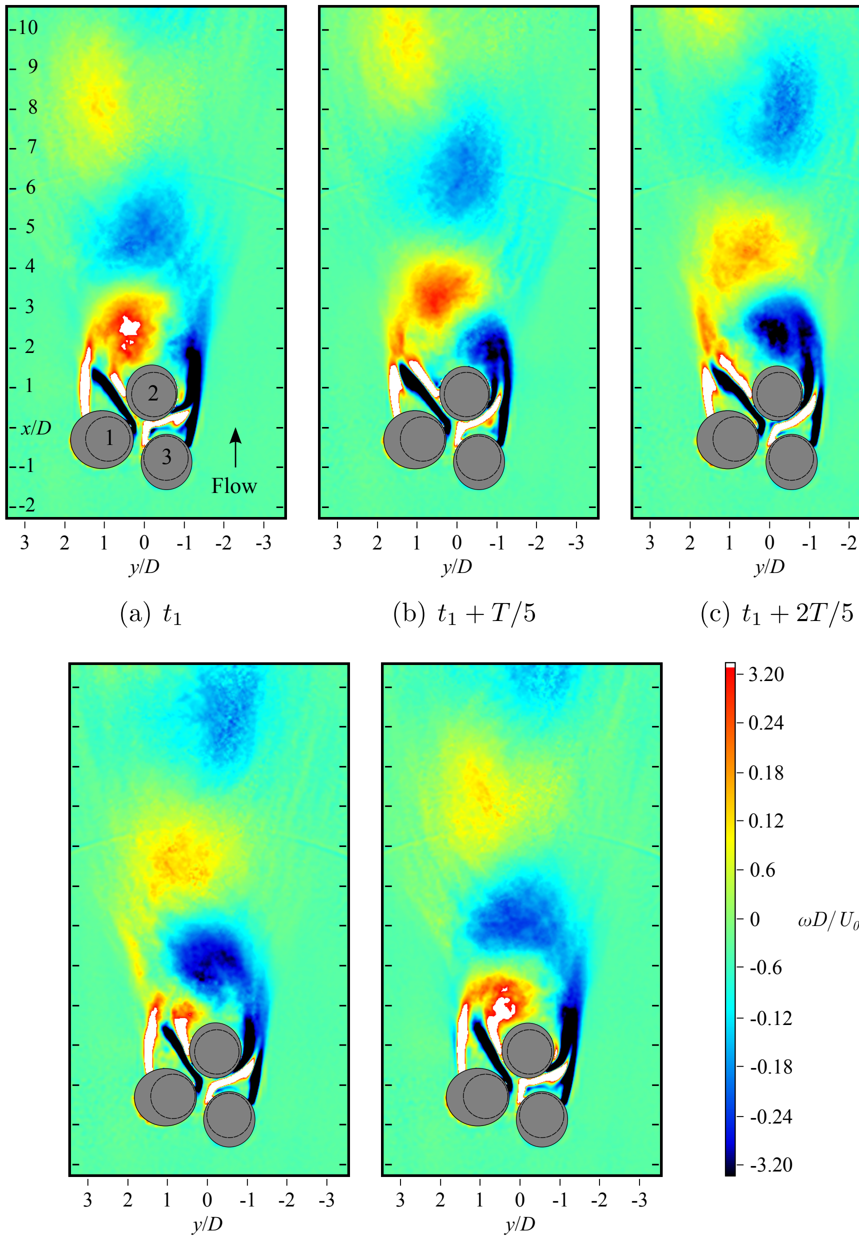

(a) t_1 (b) $t_1 + T/5$ (c) $t_1 + 2T/5$

(d) $t_1 + 3T/5$ (e) $t_1 + 4T/5$

Figure B.28: Vorticity contours of the reduced-order model consisting of the first two modes for $\alpha = 40°$.

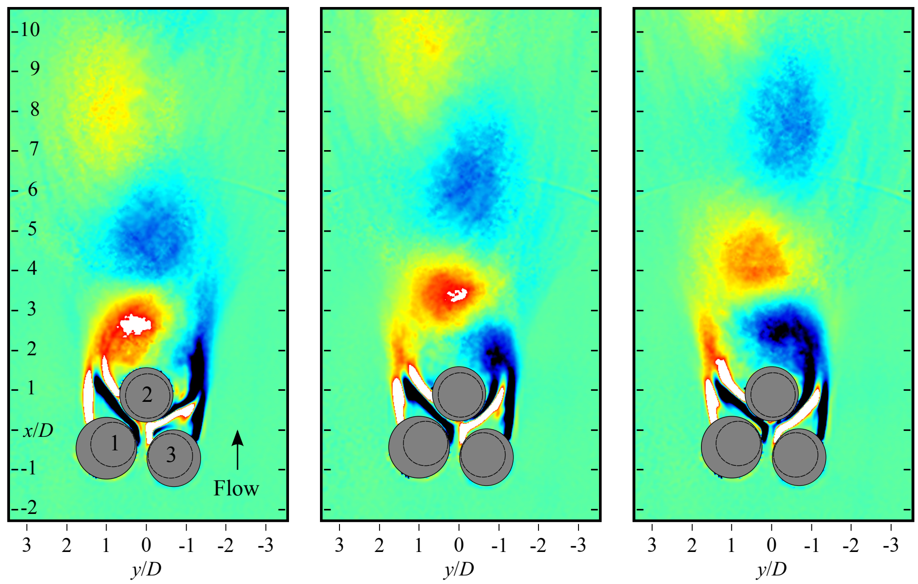

(a) t_1 (b) $t_1 + T/5$ (c) $t_1 + 2T/5$

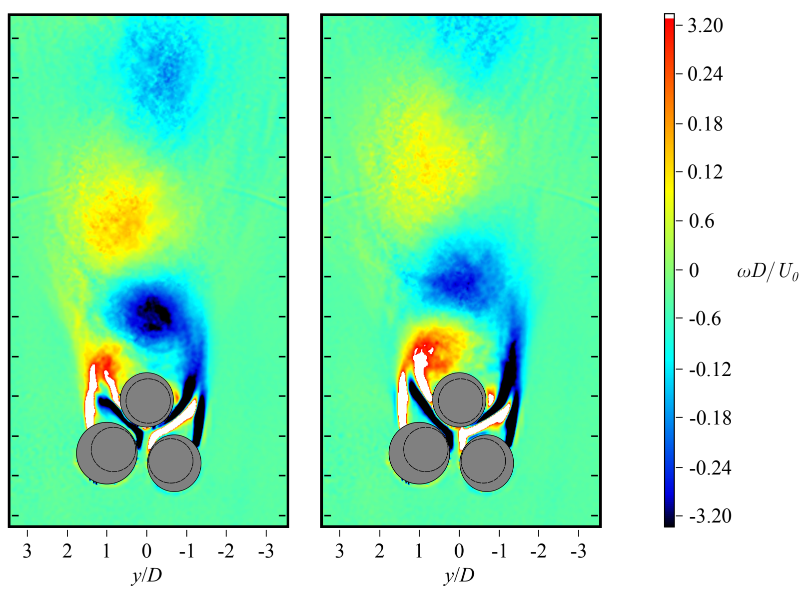

(d) $t_1 + 3T/5$ (e) $t_1 + 4T/5$

Figure B.29: Vorticity contours of the reduced-order model consisting of the first two modes for $\alpha = 50°$.

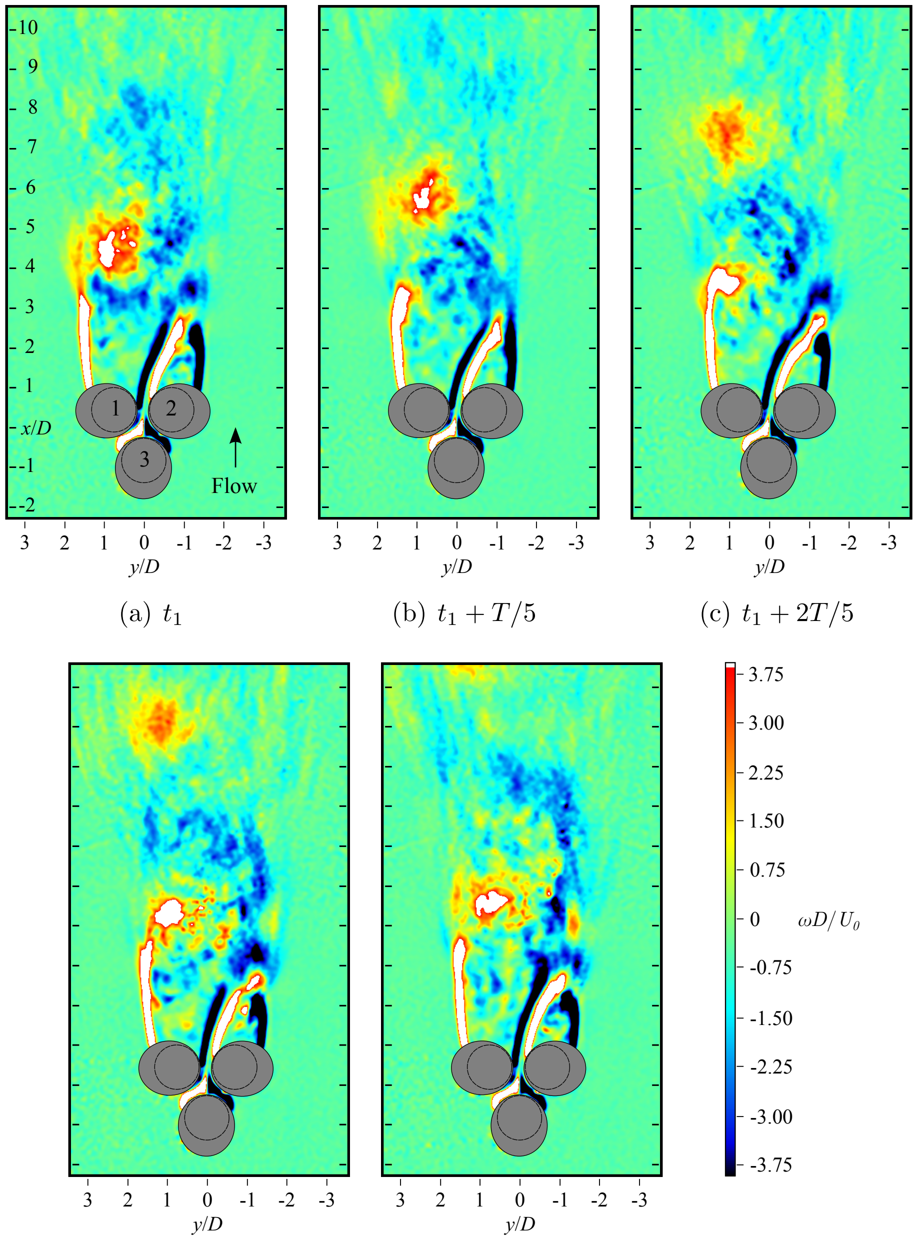

(a) t_1

(b) $t_1 + T/5$

(c) $t_1 + 2T/5$

(d) $t_1 + 3T/5$

(e) $t_1 + 4T/5$

Figure B.30: Vorticity contours of the reduced-order model consisting of the first forty modes for $\alpha = 0°$ (gap flow directed towards cylinder 2).

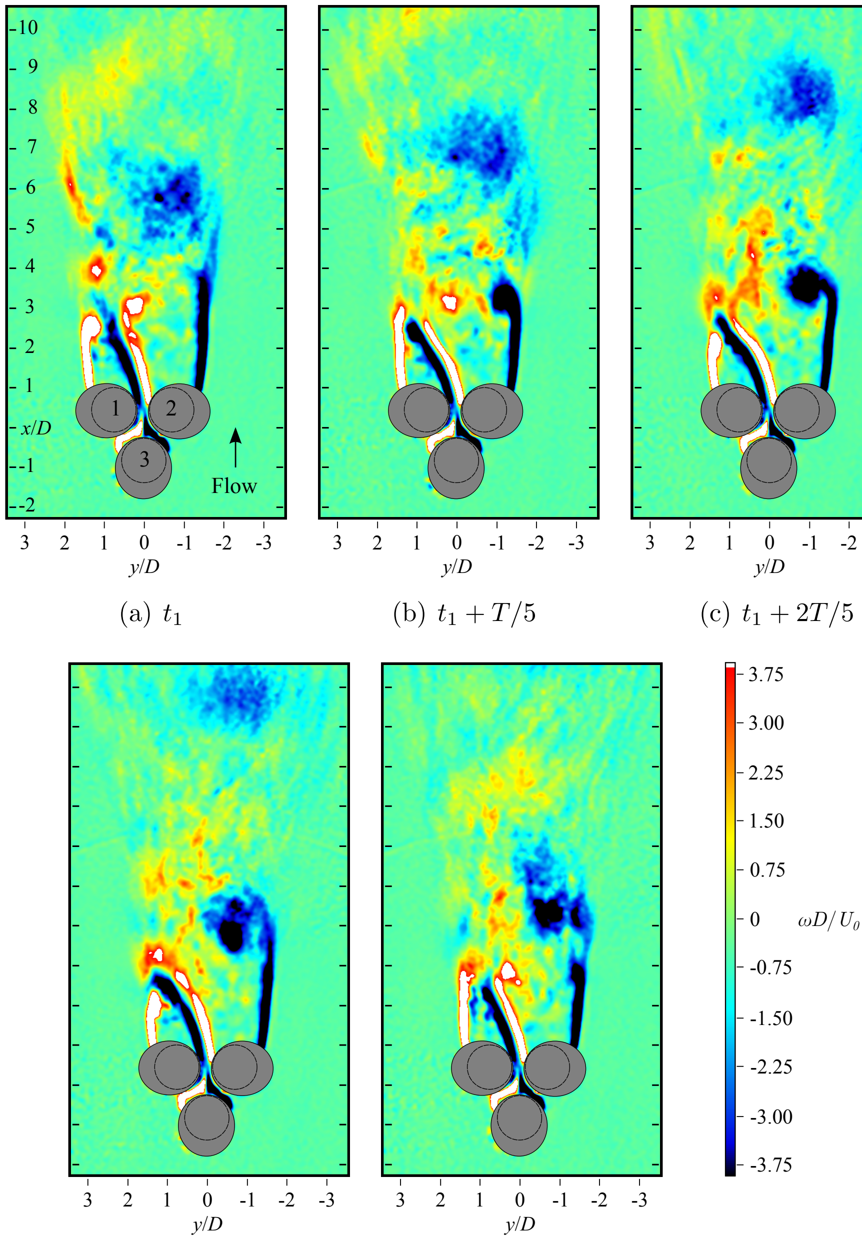

(a) t_1

(b) $t_1 + T/5$

(c) $t_1 + 2T/5$

(d) $t_1 + 3T/5$

(e) $t_1 + 4T/5$

Figure B.31: Vorticity contours of the reduced-order model consisting of the first forty modes for $\alpha = 0°$ (gap flow directed towards cylinder 1).

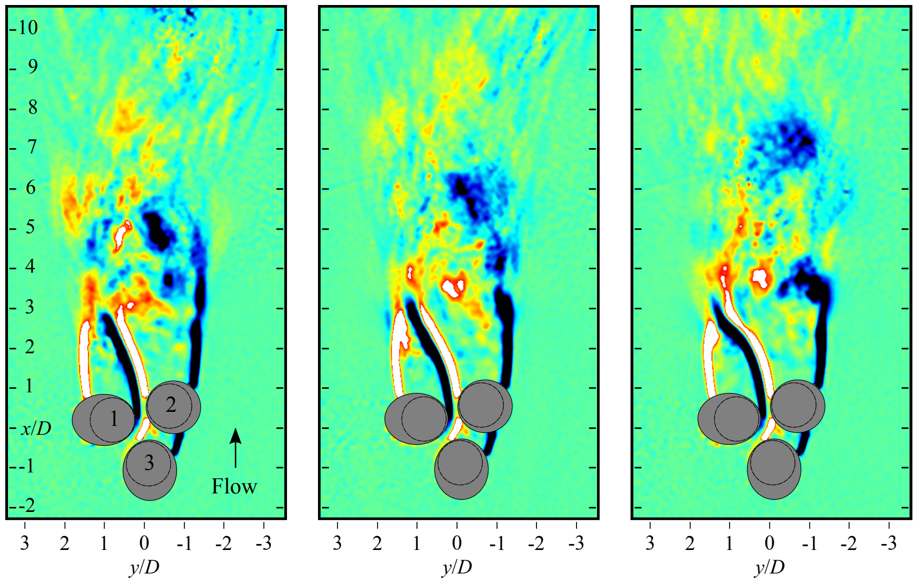

(a) t_1 (b) $t_1 + T/5$ (c) $t_1 + 2T/5$

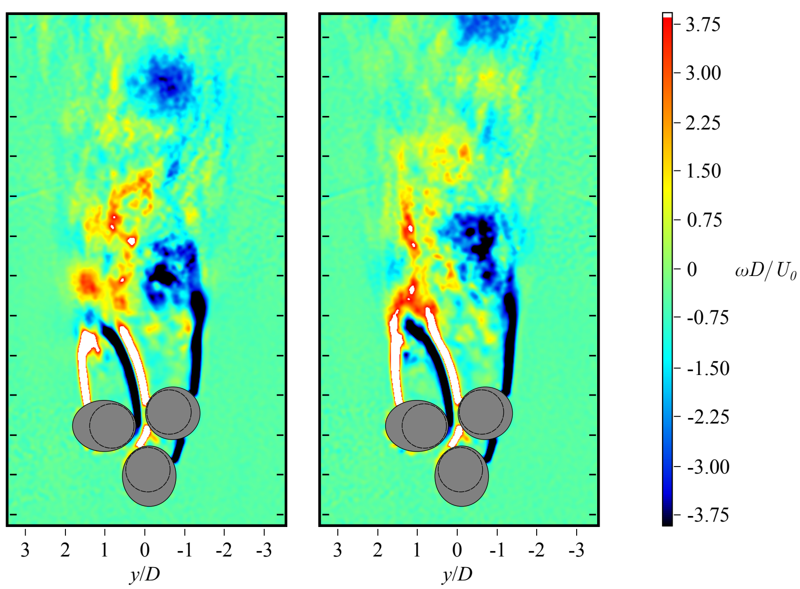

(d) $t_1 + 3T/5$ (e) $t_1 + 4T/5$

Figure B.32: Vorticity contours of the reduced-order model consisting of the first forty modes for $\alpha = 10°$.

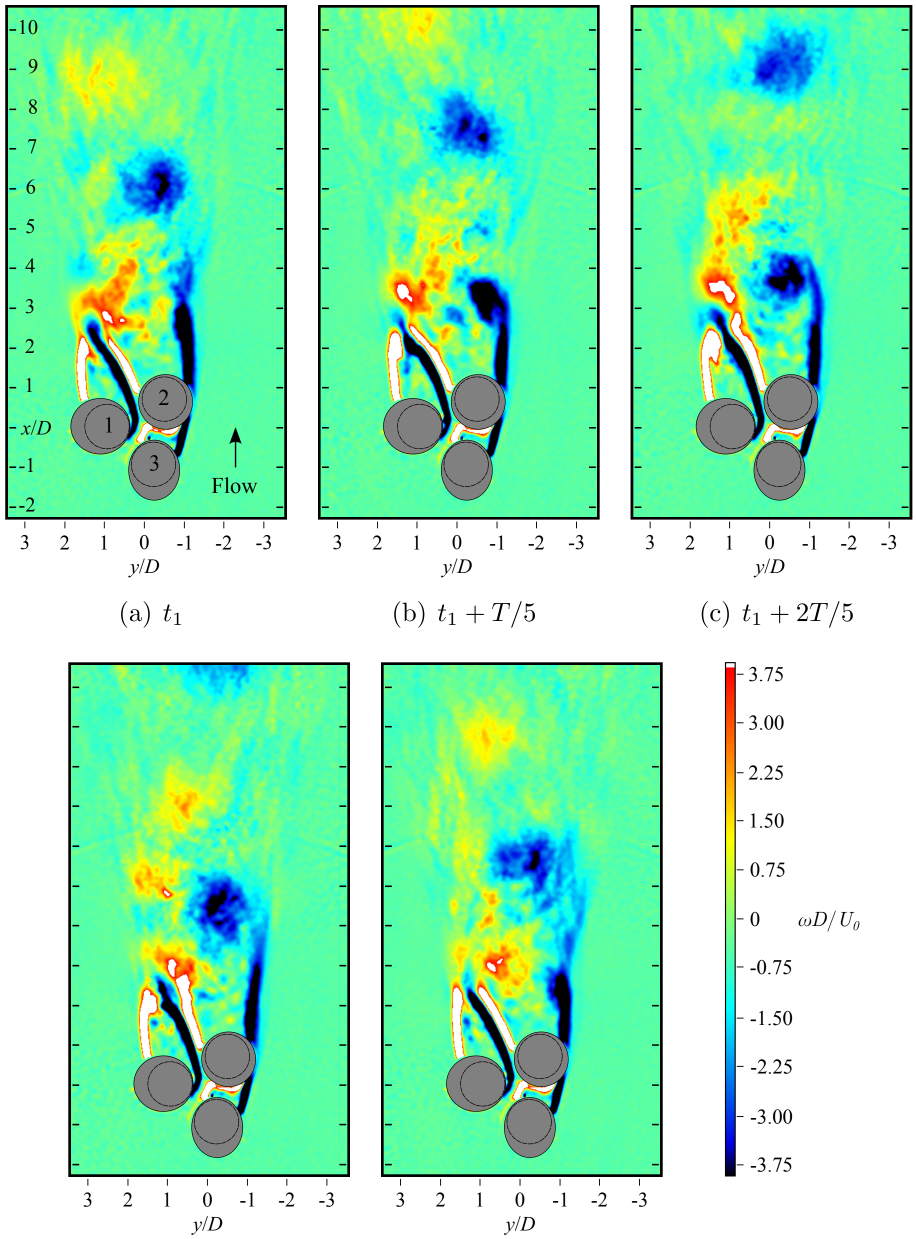

(a) t_1

(b) $t_1 + T/5$

(c) $t_1 + 2T/5$

(d) $t_1 + 3T/5$

(e) $t_1 + 4T/5$

Figure B.33: Vorticity contours of the reduced-order model consisting of the first forty modes for $\alpha = 20°$.

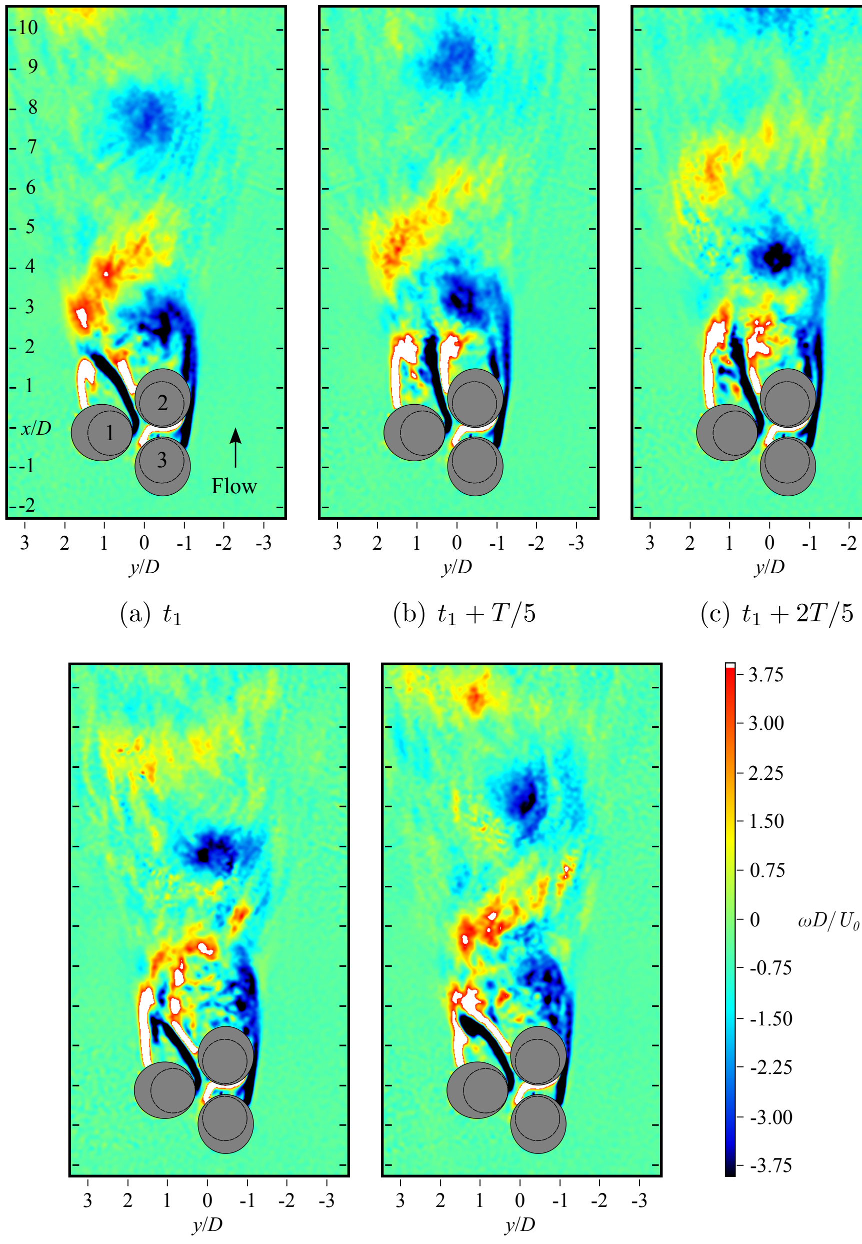

(a) t_1 (b) $t_1 + T/5$ (c) $t_1 + 2T/5$

(d) $t_1 + 3T/5$ (e) $t_1 + 4T/5$

Figure B.34: Vorticity contours of the reduced-order model consisting of the first forty modes for $\alpha = 30°$.

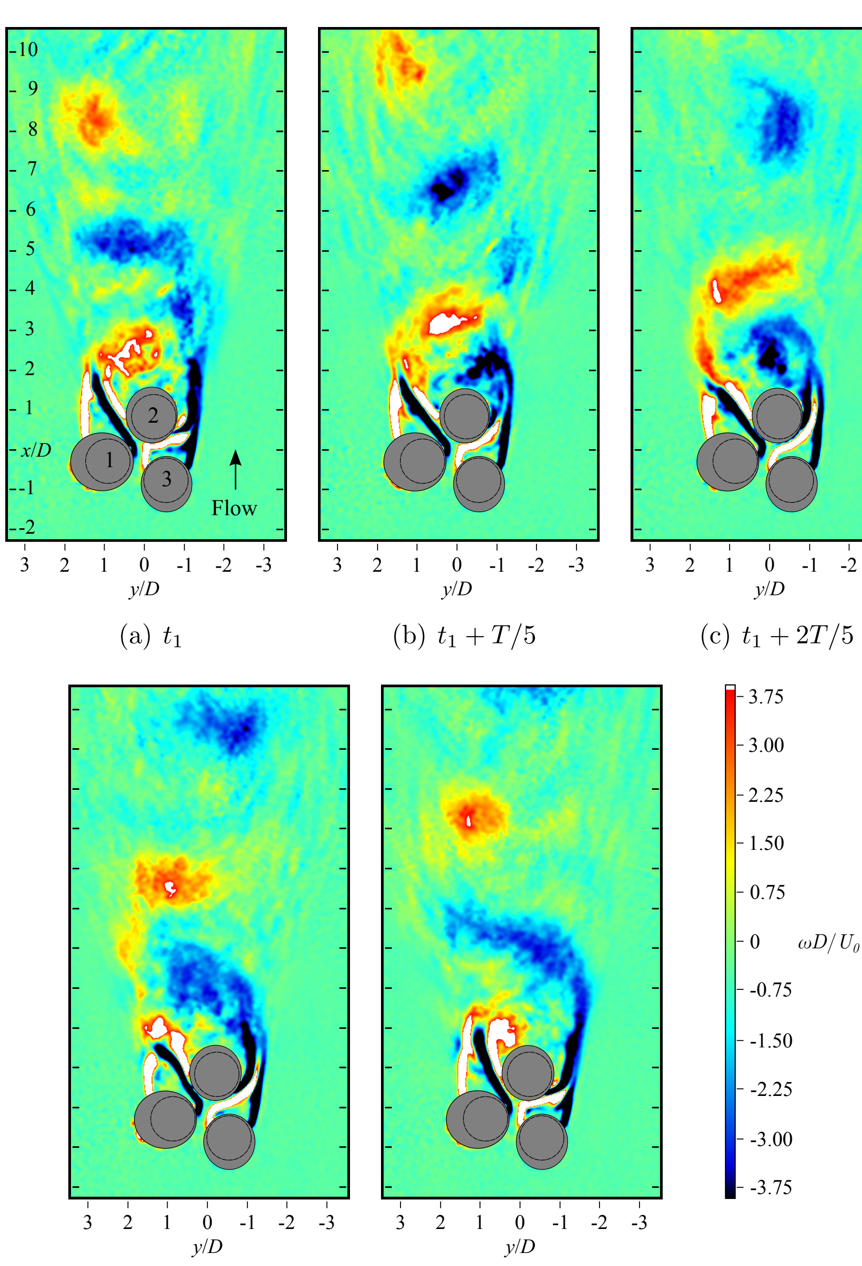

(a) t_1 (b) $t_1 + T/5$ (c) $t_1 + 2T/5$

(d) $t_1 + 3T/5$ (e) $t_1 + 4T/5$

Figure B.35: Vorticity contours of the reduced-order model consisting of the first forty modes for $\alpha = 40°$.

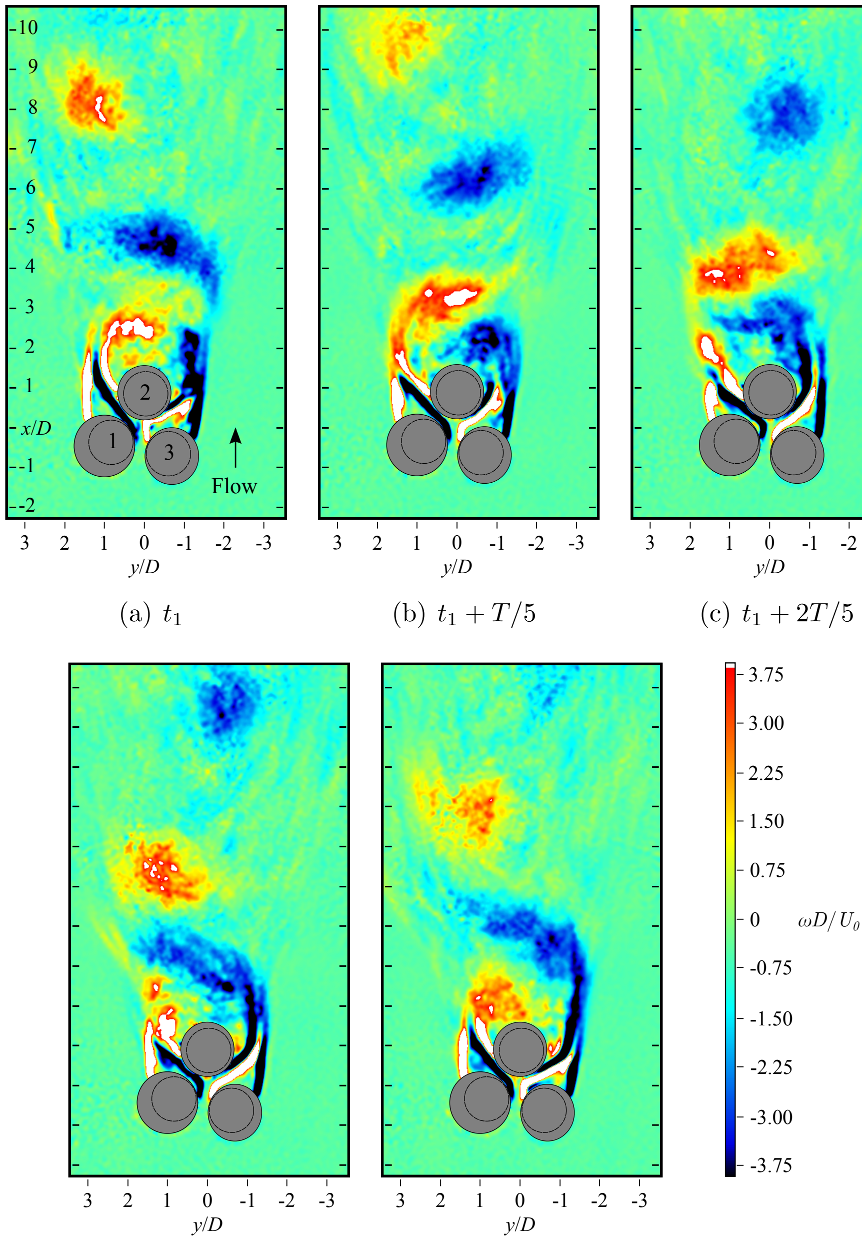

(a) t_1 (b) $t_1 + T/5$ (c) $t_1 + 2T/5$

(d) $t_1 + 3T/5$ (e) $t_1 + 4T/5$

Figure B.36: Vorticity contours of the reduced-order model consisting of the first forty modes for $\alpha = 50°$.

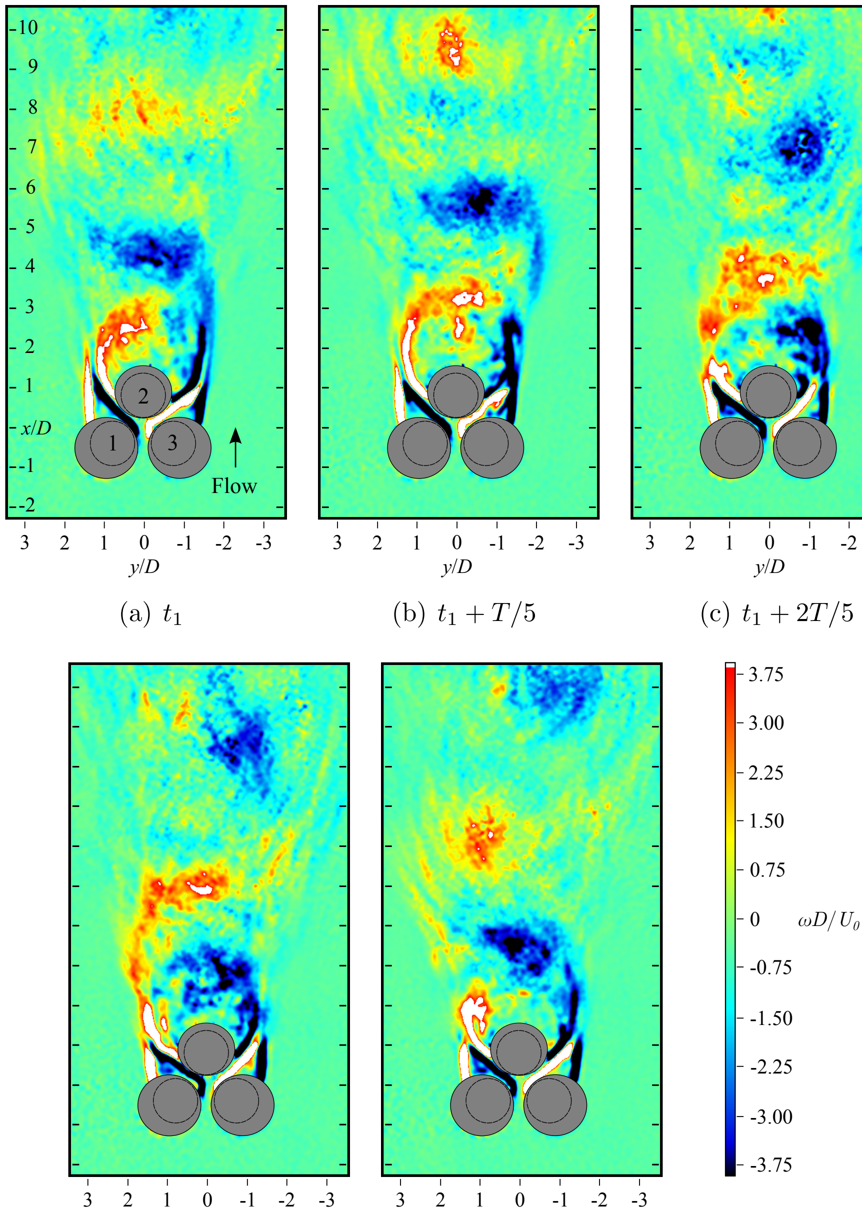

(a) t_1 (b) $t_1 + T/5$ (c) $t_1 + 2T/5$

(d) $t_1 + 3T/5$ (e) $t_1 + 4T/5$

Figure B.37: Vorticity contours of the reduced-order model consisting of the first forty modes for $\alpha = 60°$.

Appendix C

Check for bistability

Figure C.1 shows some of the cases tested to ensure no bistable wake for $\alpha = 0°$ at $Re_D = 100$. The case with the two cylinder setup show a bistable wake development, whereas the results for triangular cluster, under the same conditions, do not. The discussion based on these figures is given in Chapter 6.

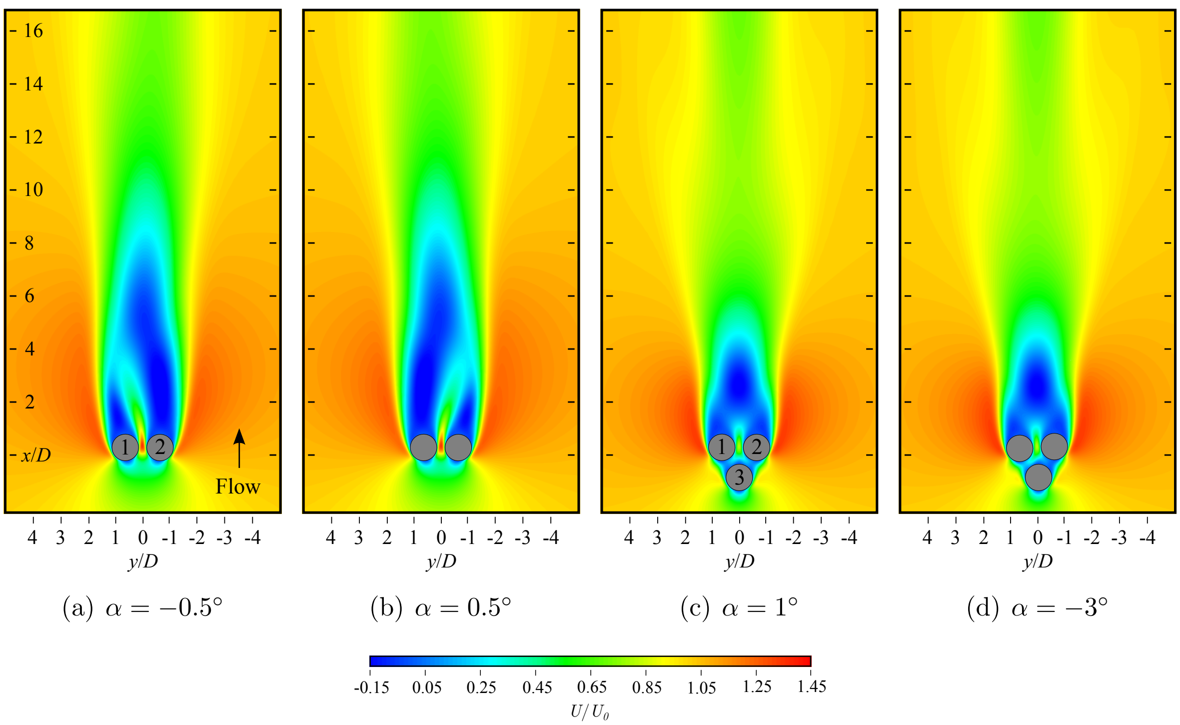

(a) $\alpha = -0.5°$ (b) $\alpha = 0.5°$ (c) $\alpha = 1°$ (d) $\alpha = -3°$

Figure C.1: Mean streamwise velocity field for two cylinder setup for $\alpha = \pm 0.5°$ and triangular cluster for $\alpha = 1°$ and $\alpha = -3°$.

Appendix D

Experimental uncertainty

This section provides an uncertainty analysis for the techniques used in the present study.

D.1 Laser Doppler velocimetry

Measurement error and uncertainty in LDV can arise from multiple sources. The most important and common error is bias in the velocity data [89]. The quantity of collected data points are proportional to the velocity of the seed particles crossing the probe volume. This introduces bias towards the higher velocities from the average local velocity. McLaughlin & Tiederman [90] proposed an order-of-magnitude estimate for such a bias, which is expressed as

$$\frac{\overline{U}_m}{\overline{U}} \approx 1 + \frac{\overline{u'^2}}{\overline{U}^2} \tag{D.1}$$

where $\overline{U}_m$ is the raw measured mean streamwise velocity and $\overline{U}$ is the real value. The real value can be found by iteratively solving for $\overline{U}$ in Equation D.1. For computing the velocity bias in the LDV measurements, a velocity signal in the wake ($x/D = 13$ and $y/D = -1.5$) of the cluster at $\alpha = 60°$ was investigated. For this particular case, the re-sampled mean velocity was 65.12 mm/s and the real value was 63.5 mm/s (Equation D.1), resulting in a velocity bias error of 1.62 mm/s. The MSE miniLDV probe is a dual-beam configuration with special optics inside the enclosure to ensure the two beams are parallel and cross at the same plane. Therefore, uncertainty due to fringe divergence [89] is negligible in the present setup. As stated in the manufacturers specifications, the sensor has a repeatability uncertainty of 0.1% and an accuracy of 99.7%. The total error, ϵ_t, due to velocity bias, sensor repeatability, and accuracy was found using a root-sum-square method [91]

$$\epsilon_t = \left(\sum_{k=1}^{N} \epsilon_k^2 \right)^{1/2} \tag{D.2}$$

where ϵ_k is the error from each individual source. The resulting total error was approximately 2.6%.

Other sources of errors in the LDV setup include horizontal alignment of the sensor, measurement location (i.e., location of probe volume), and variability in seed particle size. The LDV probe was aligned horizontally with care using digital level to an uncertainty within 0.1°. The position of the probe volume was measured using images from the high-speed camera. The uncertainty in both x and y directions was approximately $\pm 0.008D$. Lastly, the seed particles used have variable size and shape as they cross the probe volume. The average seed particle diameter is 10 μm with a variable range from 0 to 20 μm, resulting in random error in the velocity measurements.

D.2 Particle image velocimetry

When performing PIV experiments, several conditions must be satisfied for obtaining accurate measurements. Random errors in the average particle displacement for each interrogation window arise from variations in seed particle size and shape, acquisition procedure, noise in image output, or cross-correlation algorithm. Adrian [49] related the random errors to a proportionately constant, c, and the particle-image diameter, d_τ, as

$$\epsilon = \frac{cd_\tau}{\Delta X} \tag{D.3}$$

where ΔX is the average particle displacement. The random error is inversely proportional to the particle displacement (or velocity). Typical values of c range from 0.05 to 0.1 [92,93]. The particle-image diameter, d_τ, is expressed as [49]

$$d_\tau = \sqrt{M^2 d_p^2 + d_s^2} \tag{D.4}$$

where $M = 0.1$ is the magnification and $d_p = 10\,\mu$m is the seed particle diameter. The diffraction limited diameter, d_s is [49]

$$d_s = 2.44(1 + M)f^{\#}\lambda \tag{D.5}$$

where $f^{\#} = 5.6$ is the focal ratio and $\lambda = 532$ nm is the wavelength of the laser sheet. All PIV experiments were conducted at an acquisition rate of 100 Hz ($\Delta t = 0.01$ s). For evaluating the random error, an average value for c of 0.075 was selected. The near-wake region of the cluster is comprised of velocities ranging from approximately 5% to 110% of the free-stream velocity (86 mm/s), resulting in a range of particle displacements from 0.04 mm to 0.95 mm. The particle-image diameter is computed to 8.1 μm. Therefore, the random error in the velocity measurements in the cluster wake ranges from 1.5 mm/s to 0.064 mm/s.

Previous studies (e.g., [47,49,50,94]) suggest the following to minimize errors in particle displacements:

1. $N_i = C_p \Delta z_0 d_i^2 / M^2 > 10$ (seeding density), where N_i is the image-density parameter, C_p is the particle concentration, Δz_0 is the light sheet thickness, and d_i is the length of the interrogation window. This allows the evaluation of a stronger correlation peak between images. Larger signal-to-noise ratio provides less ambiguous detection of the peak.

2. $\Delta X < d_i/4$ (temporal resolution). It is important to perform this check when selecting the interrogation window size. The smaller the interrogation window, the higher risk in the particles leaving the window between frames.

3. $d_\tau/d_x > 2$ (pixel locking), where d_x is the pixel size of the camera sensor. Pixel locking can lead to bias error in the velocity results because there will be bias toward an integer-pixel value during cross-correlation. In the present work, the ratio of $d_\tau/d_x \approx 0.6$, which does not satisfy the condition. Overmars et al. [95] suggested that pixel locking can be avoided if the image is slightly defocused. This procedure was conducted during experimentation, such that the particle-image diameter is greater than 2 pixel units.

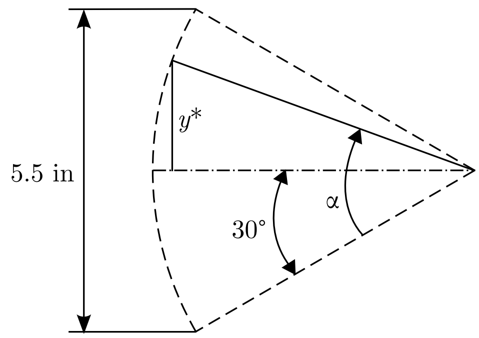

Figure D.1: Relationship between the orientation angle and yoke translation.

D.3 Scotch yoke mechanism

The rotating mechanism for the cluster was controlled by a scotch yoke mechanism. The yoke piece was attached on a linear guide rail, which was controlled by a stepper motor. Due to the slot in the yoke, the linear motion of the yoke rotated the top endplate. The orientation of the cluster was calculated using

$$\alpha = sin^{-1}\left(\frac{y^*}{5.5}\right) + 30 \tag{D.6}$$

where y^* is the yoke translation (Figure D.1). The maximum travel of the yoke to cover the desired orientations is 5.5 in. With this mechanism, the error in the accuracy of the orientation angle is $\pm 0.7°$. Also, multiple iterations showed that the repeatability uncertainty is $0.3°$.